Joanna Peszka

Laser-cooled Be^+ for improved antihydrogen trapping and magnetometry

Swansea University
Prifysgol Abertawe

Submitted to Swansea University in fulfilment
of the requirements for the Degree of Doctor of Philosophy

Declarations

This work has not previously been accepted in substance for any degree and is not being concurrently submitted in candidature for any degree.

Joanna Peszka, 31th October 2023

This thesis is the result of my own investigations, except where otherwise stated. Other sources are acknowledged by footnotes giving explicit references. A bibliography is appended.

Joanna Peszka, 31th October 2023

I hereby give consent for my thesis, if accepted, to be available for photocopying and for inter-library loan, and for the title and summary to be made available to outside organisations.

Joanna Peszka, 31th October 2023

The University's ethical procedures have been followed and, where appropriate, that ethical approval has been granted.

Joanna Peszka, 31th October 2023

Abstract

We have laser-cooled beryllium ions in a Penning-Malmberg trap dedicated for antihydrogen formation. This trap is combined with a magnetic minimum trap to confine antihydrogen. This can be used to assist in the studies of antihydrogen in two distinct ways. The first application of the cold $^9Be^+$ is to sympathetically cool positrons, which are used for antihydrogen formation. With this assistance we expect to produce colder antihydrogen and ultimately enhance the trapping rates of antihydrogen inside a magnetic trap by at least an order of magnitude. This would greatly improve measurements of antihydrogen properties allowing for increased precision. Cold Be^+ could also be used for in-situ measurements of magnetic fields in our antihydrogen traps. The method proposed in this work is to measure an electron spin-flip transition frequency in the ground state of Be^+, which is highly sensitive to the external magnetic field strength. The electron spin-flip transition could be induced by microwave radiation and detected via fluorescence from laser-cooling transition. Magnetometry plays a crucial role in trapped antihydrogen research, especially for antimatter gravity measurement performed at high magnetic fields. Also, with increasing precision of the antihydrogen spectroscopy measurements, the uncertainty of the magnetic field will increase the contribution to the systematic errors. Additionally, the benefit of using electron spin-flip in Be^+ is that it could be used to characterise the strength of the microwaves inside the ALPHA-2 trap. In this work, the feasibility of magnetometry using $^9Be^+$ inside the ALPHA's Penning trap was studied. The microwave induced electron spin-flip in Be^+ was observed for the first time within the ALPHA apparatus. The uncertainty of the external magnetic field derived from this proof-of-principle measurement was comparable to the currently used *Electron Cyclotron Resonance* method and there are prospects for significant improvement. The laser-cooling procedure was improved, which should allow further study with sympathetic cooling of positrons and application of this technique to antihydrogen production sequence.

Acknowledgement

A huge acknowledgement to all the *beryllium team*! First of all, Daniel Maxwell and Jack McCauley Jones, who taught me how to laser-cool beryllium ions and with whom we had *fun* running beryllium shifts for nearly entire year to achieve great results of sympathetically cooled positrons. A great thank to Kurt Thompson and Maria Beatriz Gomes Goncalves, who helped me to upgrade the laser setup for the Be^+ electron spin-flip experiment and who pushed to make this measurement happen even when I already lost hope. I am especially thankful to Maria who volunteered for a month of night shifts with me to run the experiment. Extra thanks go to Steven Armstrong Jones, who helped us write the control software, and Graham Stutter, who helped us with *the sticks*. Both Steve and Graham taught me a lot about laser physics and it was a pleasure to work with you. And finally, thanks to my supervisor Niels Madsen for watching over the course of the *beryllium* work and useful advice on ALPHA's experimental operations. I am very grateful to senior members and postdocs of the ALPHA Collaboration, who were always willing to answer technical and physics questions: William Bertsche, Joel Fajans, Michael Hayden, Claudio Lenz Cesar, Chris Rasmussen, Tim Friesen, Alexander Khramov, Eric Hunter, Andrew Evans, Joseph McKenna, Pierre Grandemange, Muhammed Sameed, April Cridland, Celeste Carruth Torkzaban, Alvaro Nunes de Oliveira, Janko Nauta and probably many more.

Thanks to all the *CERN gang* with whom we survived *ALPHA-g critical path*, we spent countless days on shifts and a few days cycling around the French countrysides or doing other activities: Mark Johnson, Jack Jones, Adam Powell, Patrick Mullan, Alex Khramov, Nathan Evetts, Peter Granum, Andrew Christensen, Danielle Hodgkinson, Siara Fabbri, Ted Thorpe-Woods, Jaspal Singh, Joos Schoonwater and others who stayed at CERN for some time.

Thanks to the Polish community at CERN for all the barbecues, bonfires and others. Especially great, great, greatest thanks to my Polish friends Piotr Konopka and Wojciech Bryliński for all the socialising events and cooking parties, which helped me to survive the COVID times and my PhD with residues of my sanity. *Dzieki ziomeczki!*

Many thanks to my family for all your support, especially to my parents who raised me to be open-minded, curious of the world, and to whom I owe who I am now. Special thanks to my grandma and Krysia with whom I can always talk and who believed in me all the time. */ Bardzo dziekuje mojej rodzinie za wsparcie, a w szczególności rodzicom, którzy wychowali mnie na osobe otwarta i ciekawa świata i którym zawdzieczam to, kim teraz jestem. Szczególne podziekowania dla mojej babci i Krysi, które zawsze wspierały mnie rozmowa i które cały czas we mnie wierzyły.*

I would like to express my gratitude for the help of my current supervisors at ETH Zurich, Klaus Kirch and Aldo Antognini, who gave me the opportunity to work in their group while still writing this thesis. I want to thank all the *Muon Group* at ETH and PSI for their support during my part-time work. Thank you for the trust that you put in me and for believing that I could finish this thesis.

And finally, the greatest possible word of thanks to Patrick for all the physics discussions concerning my work and other topics, for all the non-physics discussions and all the massive support you gave me during all the process of doing Ph.D.

Geneva - Racibórz - Zurich

2022 - 2023

Contributions

Author contributions

I joined the ALPHA Collaboration in 2018 under CERN Technical Student Programme. For over a year I worked on the construction of ALPHA-g experiment, which involved *i.a.* assembly of the vacuum system and setting up and testing control hardware and software.

I started my PhD studies in 2019 and I joined the *Beryllium Experiment Team*: a postdoc Daniel Maxwell, PhD student Jack McCauley Jones and our supervisor Niels Madsen. The experiment involves laser cooling $^{9}Be^{+}$ ions in the ALPHA-2 Penning trap. We worked together on sympathetic cooling of positrons with beryllium ions and we have demonstrated feasibility of using sympathetically cooled positrons for the antihydrogen production [1].

In 2020 I took over the responsibility for the beryllium experiment, when Daniel and Jack left. At the end of summer 2020 a new postdoc Kurt Thompson started working with us and year after a new PhD student Maria Beatriz Gomes Goncalves joined us. At the end of 2021 we got support from Steven Armstrong Jones.

Within the scope of my PhD project, I worked on the upgrade of the laser system for beryllium ions laser cooling, to make a positrons cooling more efficient and compatible with antihydrogen production sequence. I designed and prepared the proof-of-principle experiment with microwave induced electron spin-flip in Be^{+} for testing it as an alternative magnetometry technique in the ALPHA Experiment. Kurt and Maria helped me to perform this experiment and together we demonstrated the potential of using beryllium ions for probing magnetic field and characterise the strength of microwaves inside the ALPHA-2 trap.

Through the time working in the ALPHA Collaboration I took part in shift work of other ALPHA's physics programmes, making a contribution to results presented in the *List of publications*.

List of publications

As one of the main authors:

[1] ALPHA Collaboration, *Sympathetic cooling of positrons to cryogenic temperatures for antihydrogen production*, Nat Commun 12, 6139 (2021). doi: 10.1038/s41467-021-26086-1

As a contributing author

[2] ALPHA Collaboration, *Laser cooling of antihydrogen atoms*, Nature 592, 35–42 (2021). doi: 10.1038/s41586-021-03289-6

[3] ALPHA Collaboration, *Observation of the effect of gravity on the motion of antimatter*, Nature 621, 716–722 (2023). doi: 10.1038/s41586-023-06527-1

[4] ALPHA Collaboration, *Design and performance of a novel low energy multispecies beamline for an antihydrogen experiment*, Phys. Rev. Accel. Beams 26, 040101 (2023). doi: 10.1103/PhysRevAccelBeams.26.040101

[5] ALPHA Collaboration, *Precision spectroscopy of the 1S-2S transition in antihydrogen: hyperfine structure and CPT invariance*, in review by *Nature Physics*

[6] ALPHA Collaboration, *Measurements of Penning-Malmberg trap patch potentials and associated performance degradation*, in review by *Physical Review Research*

TABLE 1 Timeline of the beryllium experiment

2013	Procurement of the 313nm laser (35 mW)
2014	Design and procurement of a test vacuum chamber for the demonstration and characterisation of ablation of a beryllium metal target.
2015	Construction of the test chamber and first demonstration of laser ablation with an aluminium target.
2016	Continued ablation experiments with aluminium and beryllium targets in the test chamber. Design of ion source and other diagnostics to be mounted on a linear translator in ALPHA-2
2017	Installation of the linear translator (stick) assembly in the ALPHA-2.
2018	First Beryllium ions trapped in ALPHA-2. Successful demonstration of laser cooling of $^{9}Be^{+}$ ions in the ALPHA-2 Penning trap.
September 2019	Demonstration of positrons sympathetic cooling with laser-cooled beryllium ions
December 2019	Observation of centrifugal separation between beryllium ions and positrons and sympathetic cooling of positrons in an octupole magnetic field (with a smaller number of ions)
February 2020	Stick intervention: MCP shields added and on-axis mirrors installed
Aug-Sep 2020	Ablation and loading study, Be^{+} preparation only in RCT, catching in SolA
June 2021	New 313nm laser installed (800mW)
July 2021	Stick intervention: MCP shileds improved and additional big mirror on DS stick added
February 2022	UV fibres installed, USAT stick bellow replaced
March 2022	On-axis laser demonstration, study of cooling and fluorescence detection
July 2022	Demonstration of electron spin-flip in $^{9}Be^{+}$
September 2022	Further study on on-axis laser cooling with rotating wall compression

Contents

Thesis outline

In this thesis I will discuss all the physics fundamentals necessary to perform laser cooling of $^{9}Be^{+}$ in a Penning-Malmberg trap. This work was performed in the context of antihydrogen physics research. Therefore, in *Chapter 1* the motivation behind antimatter research and an overview of the ALPHA Experiment will be given. *Chapter 2* discusses physics of trapping charged particles, non-neutral plasma and diagnostics methods. In *Chapter 3* introduction and fundamentals of laser cooling and atom light interactions will be given.

Further chapters will present the work I have performed within my postgraduate research project. *Chapter 4* discusses pulsed laser ablation method to produce Be^{+} ions. In *Chapter 5* information regarding laser cooling in the ALPHA Experiment will be given. In that chapter, I will discuss all the hardware upgrades I performed to the laser system. *Chapter 6* presents results of the first proof-of-principle experiment of microwave induced electron spin-flip in Be^{+} performed in the ALPHA-2 trap. In the final *Chapter 7* I will summarise the work that has been done and discuss the future prospects of using laser-cooled beryllium ions for magnetometry and improved antihydrogen production in the ALPHA Experiment.

Chapter 5 and *Chapter 6* contain a lot of technical information, where I discuss all the possible failures we went through. I collected these in the highlighted box, to hopefully help save time for future generations that might want to perform a similar type of experiment. They look like the box below:

Advice: How to laser cool beryllium ions?

1. Produce ions via laser ablation
2. Trap ions in the Penning trap
3. Use 313 nm laser

...

Chapter 1

Introduction and physics motivation

1.1 Antimatter research

1.1.1 The history of antimatter research

The existence of antimatter was theoretically predicted by relativistic quantum theory, as a consequence of the mathematically possible negative energy state of an electron. When Paul Dirac derived his theory in 1928 [8], he did not interpret it yet as a prediction of a new particle, but J. Robert Oppenheimer interpreted his result as a positively charged electron [9]. Just a few years after, in 1932 Carl David Anderson observed positively charged electrons in the cosmic rays [10], which were called positrons. This was the evidence confirming the existence of antimatter, so it was also expected that other particles like protons should also have their antimatter counterpart.

The antiproton was first produced in 1955 by the physicists Emilio Segrè and Owen Chamberlain at the University of California Radiation Laboratory in Berkeley, USA [11]. This was achieved by using the Bevatron particle accelerator to smash protons into a copper target, producing numerous types of particles, including pairs of protons and antiprotons. They have detected six antiprotons and determined the energy threshold for proton-antiproton pair production to be 4.3 GeV. A detailed review of the work that led to the discovery of antiprotons was published by *K. Orrman-Rossiter* [12]. A year later, antineutrons were also produced from antiprotons through a charge exchange process with scintillators [13]. After the discovery of the antiproton, numerous experiments were performed to study this newly discovered antiparticle. A significant experiment was the observation of antiproton-proton

annihilations, giving insights into the energy released during matter-antimatter annihilation [14]. This research led to the development of the technique for detecting antiprotons using their annihilation signatures, a method that is used in current antimatter experiments (see Subsection 1.2.1). After the initial experiments at the Bevatron in Berkeley, the antiproton research moved to Tevatron in the Fermilab and Low Energy Antiproton Ring (LEAR) at CERN.

A single positron was first trapped in a Penning trap by Schwinberg, Van Dyck and Dehmelt in 1981 [15] to compare its g-factor with an electron. Later, Cliff Surko and collaborators developed a technique to accumulate large numbers of positrons by cooling them with a nitrogen buffer gas [16]. Antiprotons were trapped for the first time by Gerald Gabrielse and collaborators in 1986 [17]. They developed cooling techniques to reduce antiproton energies to < 100 meV [18]. Trapping positrons and antiprotons began the era of precision measurements of charged antimatter properties: charge-to-mass ratio [19] and magnetic moment measurements [20], pioneered by the ATRAP Collaboration and later continued by the BASE Collaboration [21, 22].

Having antiprotons and positrons naturally led to the idea to combine them to form the first antimatter atom: antihydrogen. It was already predicted that the most efficient method for antihydrogen production would be merging cold $\bar{p}$ and e^+ plasmas [23], but a proof of principle of antihydrogen atom production was carried out on a 2 GeV antiproton beam from the LEAR at CERN in 1995 [24]. The antiproton beam was sent through the xenon gas target. The positrons came from the production of pairs e^+e^-, which occurs when the antiproton passes through the Coulomb field of a Xe nucleus

$$\bar{p} + \mathrm{Xe} \longrightarrow \bar{p} + e^+e^- + \mathrm{Xe} \longrightarrow \bar{\mathrm{H}} + e^- + \mathrm{Xe}^- \tag{1.1.1}$$

The condition for $\bar{\mathrm{H}}$ production is that the difference between antiproton and positron energy is ≤ 13.6 eV. If the antiproton captures a positron, the antihydrogen atom is formed. In that experiment 11 highly energetic antihydrogen atoms were observed. The validity of this experiment was confirmed two years later by scientists from Fermilab [25]. To study antihydrogen properties, longer interaction times are needed: cold antihydrogen beams or trapped antihydrogen must be produced. Very soon after the first antihydrogen production, the Low Energy Antiproton Ring was converted into a Low Energy Ion Ring (LEIR) to provide heavy ions to the Large Hadron Collider (LHC) and the Antiproton Collector, which

was previously providing $\bar{p}$ beams to the LEAR, was converted to the Antiproton Decelerator (AD), which produces the low energy antiproton beams since 2000 until today. Multiple experimental groups are studying antiprotons [26], antihydrogen [27], antiprotonic atoms [28]. Since the shutdown of Tevatron at Fermilab in 2011, the Antiproton Decelerator is the only source of antiprotons in the world. The Facility for Antiproton and Ion Research (FAIR) at GSI in Darmstadt is under construction, but this will deliver antiproton beams in the GeV energy scale. There is a possible extension to low-energy antiproton beams (FLAIR) [29], which could allow for similar types of experiments as those performed at CERN.

Trapping antihydrogen requires producing cold antihydrogen atoms of sub-Kelvin temperature. Cold, trappable antihydrogen can be formed if the constituent antiparticles have significantly lower kinetic energies than in the beam experiment performed at *LEAR* and those cold antiprotons and positrons can be achieved by using various cooling techniques that are available for trapped ions in Penning traps (more about it in Section 2.4.1). Cold antiprotons and positrons were the key components to increase the antihydrogen production rate, as demonstrated by the ATHENA Collaboration at CERN [30]. In 2011, the ALPHA Collaboration confined antihydrogen in the magnetic bottle trap for the first time, demonstrating a storage time of over 15 minutes [31, 32]. This allowed for spectroscopic measurements of the structure of lowest energy levels ($1S \rightarrow 2S$ [33] and $1S \rightarrow 2P$ transition [34], hyperfine structure of the $1S$ ground state [35] and investigating the fine structure of the excited levels [36]), as well as the recently made first free-fall test of antihydrogen [3]. Other experiments (ASACUSA, AEgIS and GBAR) at the Antiproton Decelerator facility are working on hydrogen beam production for the ground-state hyperfine spectroscopy [37] and gravitational free-fall experiment [38–41]. Recently ALPHA has applied the laser cooling technique to antihydrogen atoms [2], which is very promising for future improvement of precision antihydrogen measurements. There is ongoing work to introduce a hydrogen [42–44] inside the ALPHA trap to perform a direct *CPT symmetry* test using the same experimental protocol, in the same apparatus and at the same time.

Currently, a great effort is being focused in the antimatter community on developing a technology to transport antimatter. In principle, this should be possible, since the mobile Penning trap was already built by C. H. Tseng and G. Gabrielse in the early 1990s [45]. At the moment two project at CERN are working on the transportable Penning trap for antiprotons.

A STEP project [46], which is part of the BASE Collaboration, wants to move the antiprotons out of the AD experimental hall to reduce the background magnetic noise level for their precision measurements with antiprotons. The second is a PUMA experiment, which aims to bring antiprotons to the ISOLDE facility to measure their annihilation with radioactive nuclei to study the effects of nuclear physics [47]. Transportable antiprotons would not only benefit the fundamental research community, there are also expected medical applications for antiprotons such as the generation of radioisotopes for PET and radiotherapy [48]. Early studies on the use of antiprotons for medical purposes were carried out by the Antiproton Cell Experiment (ACE) at CERN [49, 50], which studied the biological effects of antiprotons. They demonstrated that antiprotons were four times more effective than protons in killing cancer cells.

1.1.2 Fundamental physics tests with antimatter

Antimatter provides a unique platform for testing the fundamental principles of physics. Standard Model of particle physics makes precise predictions about the properties of antimatter, and any deviation from these predictions could hint at new physics that could explain one of the biggest mysteries of modern physics: why is there so much more matter than antimatter in the observable universe? Several experiments have been designed to perform high-precision measurements of antimatter's properties, like antiproton's mass [51], charge-to-mass ratio [21] and magnetic moment [22] and frequencies of quantum transitions in the antihydrogen atom [33–36].

The antihydrogen is a great test bench for testing the symmetries between matter and antimatter by measuring its energy level structure and it is the only neutral, entirely antimatter system that can be used to test the gravitational interaction. Testing gravity on charged particles, such as positrons and antiprotons, in a free-fall experiment is not feasible, since the interaction with electromagnetic field suppresses the effects of gravity (i.e. the gravitational interaction is 10^{42} times smaller than the electrostatic interaction between two electrons and 10^{36} for two protons), while other neutral systems like positronium [52, 53] and muonium [54, 55] are bounded states of electron and antilepton.

Baryon-antibaryon asymmetry problem

The observed Universe seems to be strongly dominated by matter, whereas most of the currently known physical processes produce an equal amount of matter and antimatter. A few mechanisms that do not produce exactly equal amounts of matter and antimatter have been observed, but the imbalance is not sufficient to explain the observed dominance of matter particles. If there was any significant amount of antimatter around us, eventually it should annihilate with matter and produce γ rays that could be detected. There are searches for these annihilation signals, for example, looking for candidates for hypothetical antimatter stars [56]. The Alpha Magnetic Spectrometer (AMS) installed on the International Space Station is looking for cosmic-ray charged particles including searches of antihelium nuclei, detection of which would be an argument for existence of antimatter sources in space. They have observed some antihelium signatures, but these events were not confirmed with high confidence [57].

Many physicists believe that in the early Universe there was an equal amount of baryonic[1] and antibaryonic[2] matter and at some point this symmetry has been broken by some process called *baryogenesis*, which cannot be explained so far. This is known as a baryon-antibaryon asymmetry problem. Sakharov introduced three conditions to classify whether any process could be responsible for causing baryon-antibaryon symmetry breaking [58]:

a) baryon number violation - the total baryon number $B = (n_q - n_{\bar{q}})/3$, where n_q is number of quarks and $n_{\bar{q}}$ is number of antiquarks, must change during the process.

b) *C-symmetry* and *CP-symmetry* violation - breaking C symmetry means that there must be more processes that favour matter production over processes favouring antimatter production, while CP symmetry violation is needed to introduce the imbalance between matter and *mirror reflection* of antimatter (antimatter for which the spatial coordinates were transformed) production.

c) departure from *thermal equilibrium* - the decay rate in the process that violates B number and C and P symmetries must be much smaller than the expansion rate of the Universe, so produced matter and antimatter does not achieve thermal equilibrium, decreasing the annihilation rates.

[1] Protons, neutrons, systems built from 3 quarks.

[2] Antiprotons, antineutrons, systems built from 3 antiquarks.

A detailed review of the concept of baryogenesis can be found in Ref. [59]. Alternatively, antimatter world might be ruled by different physics. Antimatter might have slightly different properties than matter (mass, charge, magnetic moment, etc.), interact differently with known forces (e.g. different gravitational constant), or even be subject of other not yet discovered interactions. Therefore, it is important to study and measure precisely all possible properties of antimatter in search for any even small deviation from the properties of matter.

CPT invariance theorem

Wigners formulation of quantum mechanisms used a parity quantum number as a symmetry property of wave functions of the states of the atom. This parity quantum number predicts that physical processes are unchanged in mirrored systems (parity transformed). By 1956 no violations to parity symmetry were observed in strong interactions, electromagnetic interactions nor gravitational interactions. However, a review by Lee and Yang illustrated that violations were not yet excluded in the weak sector. Informed by Lee and Yang [60], Chien-Shiung Wu in collaboration with the low temperature group of the National Bureau of Standards (NIST nowadays) performed an experiment to test the conservation of parity in weak interaction [61]. Their experiment used Cobalt-60, which decays via negative beta decay. This spin polarisation within a magnetic field allowed for a parity test, as the Cobalt-60 nucleus has a spin of +5 prior to the beta decay to Nickel-60 with a nuclear spin of +4, which can be verified by the directionality of gamma emissions of the produced nucleus with respect to a spin polarising magnetic field. The Cobalt-60 beta decay emits an electron with its quantum spin aligned parallel to the nuclear spin. By cooling Cobalt-60 atoms to low enough temperatures within a magnetic field, a 60% nuclear spin polarisation was obtained by *Wu et al.* The emission direction of beta decay electrons could be either parallel or antiparallel to the applied magnetic field due to conservation of quantum angular moment. The experiment observed an electron emission bias direction, antiparallel to the nuclear spin direction. This bias can be understood as the electron momentum direction being opposite to the electron spin direction; the projection of spin onto the direction of momentum is called helicity, categorised as left-handed and right-handed. This experiment observed that the weak interaction only couples to left-handed particles, not to right-handed particles, which was a discovery of the parity symmetry violation.

With this observed parity breaking in the weak interaction, an alternative symmetry was proposed, which was known to be satisfied by the other interactions, CP-symmetry. At the time, this symmetry was also conserved in all known interactions from the strong, electromagnetic and gravitational sector. It was proposed that one of the fundamental symmetries of physics is a CP-symmetry [62], together with momentum and energy conservation laws.

However, CP violating processes have been observed in kaon decays: in 1964 a long-lived neutral kaon was observed to decay into two pions [63], which was forbidden for if CP-symmetry was conserved. Subsequently CP violation was characterised by NA31/48 experiments at CERN [64, 65] and the KTeV Collaboration at Fermilab [66]. Additionally, the CP violation was also observed in the decays of B-mesons by the BABAR Collaboration at SLAC in the US [67] and the Belle Collaboration at KEK in Japan [68]. To theoretically explain the CP-violation Kobayashi and Maskawa introduced a third generation of fundamental particles , which were not observed at the time [69].

Neither C nor CP operation does a true transformation between matter and antimatter physics, even though for most interactions transforming only C or CP already gives a correct physical description. CPT symmetry which includes additional time reversal is believed to be a fundamental symmetry of physics. Modern particle physics theories assume the CPT symmetry, which considers the previous C and CP violating processes and includes additional time reversal, is a fundamental symmetry of physics. Since parity and CP-symmetry have been violated in the weak interaction, it is rather expected that a possible CPT asymmetry (if it exists) would also occur in the weak interaction. Comparisons of matter and antimatter's properties allow for direct CPT symmetry tests. Antihydrogen is of interest because the 1S-2S transition in hydrogen is the most precise spectroscopic measurement and is the best theoretically understood atomic system.

Possible violations of CPT symmetry can be quantified using the Standard Model Extension framework (SME) [70]. SME is an effective theory of the Standard Model of Particle Physics, which allows for Lorentz and CPT symmetry violation. The model has additional coefficients that quantify the strength of the violations. SME framework allows for the comparison of results of various independent experiments by placing limits on the coefficients of Lorentz and CPT violating terms [71]. A very broad overview of the antimatter tests in the context of the Standard Model Extension can be found in Ref. [72] and [73].

Gravitational interaction of antimatter

Standard Model of Particle Physics does not include gravitational interaction and General Relativity, a theory of gravitation, does not include antimatter. One of properties of General Relativity is the universality of the free fall, which means that the gravitational mass and inertial mass are the same. This is known as a *Weak Equivalence Principle* (*WEP*), which so far holds in all experiments performed on test bodies made of matter. Performing a free fall experiment of antimatter in the Earth's gravitational field is called a free-fall Weak Equivalence Principle (WEP_{ff}).

Up until recently, there was no direct observation of antimatter interacting with matter gravitationaly, therefore multiple contradicting models of antimatter's gravitation were made. Many were predicting the same attractive gravitational force between matter and antimatter particles [74], but also some investigated the possibility of *antigravity* [75–77] that would cause antimatter particles to be repelled by matter. Previous attempts at free-fall measurements of gravity with charged particles have failed, due to systematic effects, such as stray charges [78]. Gravity measurements of neutral systems containing antimatter became possible recently:

a) antihydrogen - progress in cold antihydrogen production and trapping, allows for the free-fall measurements [79], and pulse antihydrogen beam would allow for the interferometry type measurement [80]

b) positronium - metastable positronium beam is promising for the interferometry measurement [81],

c) muonium beams are being produced at the Paul Scherrer Institute (PSI) in Switzerland [82, 83] and ultracold muonium beams produced from the superfluid helium are under the development [84].

Positronium and muonium are exotic atoms containing an antilepton (positron or antimuon) and an electron. (Anti)muon is 207 times heavier than an electron. Therefore, muonium mass is dominated by mass of the antiparticle, which makes it a better candidate for testing antimatter's gravitational interaction. Interferometry measurements are proposed to test the gravity of positronium (AEgIS Collaboration at CERN [81] and David Cassidy at UCL [52, 53]) and muonium (LEMING Collaboration at PSI [54, 55]).

Antihydrogen is the only neutral and fully antimatter system available so far. There are three experiments proposed to test the behaviour of an antihydrogen under gravity:

i. AEgIS: interferometry measurements, similar to that of positronium and muonium, performed in the zero magnetic field [39],

ii. GBAR: free-fall of the ultracold hydrogen atom produced from the antihydrogen ion by photodetachment of the positron (scheme proposed by J. Walz and T.W. Hänsch [85]), experiment performed in the zero magnetic field [40, 41],

iii. ALPHA-g: release many antihydrogen atoms from the high magnetic field Ioffe-Pritchard trap [86].

The first ALPHA-g experiment aims to determine the sign of the interaction, to test the idea of antigravity [3]. Although the antiproton mass (same as proton mass) mostly originates from gluon interactions, it was expected that the most likely outcome of that measurement would be the same as for matter. The first free-fall measurement in the ALPHA-g apparatus has been performed last year showed the local gravitational acceleration of antihydrogen in Earth's gravitational field to be consistent, within the experimental errors [3], with $+1g$ and it ruled out the idea of antigravity. The precise value of the gravitational constant for the antihydrogen, denoted as $\bar{g}$ or $a_{\bar{g}}$, to the level of $< 1\%$ could inform us about the gravitational masses of the quarks. The GBAR experiment has been designed to achieve even higher precision [87]. The ALPHA-g experiment could achieve this precision with careful assessment of systematic errors generated by the magnetic field of the antihydrogen trap. Higher precision could be achieved by an antihydrogen atomic fountain experiment [88].

Another fundamental consequence of General Relativity is that the existence of mass curves the space-time and the clock's frequency is changed by the mass nearby the clock, which is known as *gravitational redshift* of clock's frequency. Charged particle in the magnetic field can be considered as a clock, since the cyclotron motion has its own characteristic frequency, which is redshifted by the gravitational field. By measuring the cyclotron frequency of the antiproton or positron in a Penning trap, the gravitational interaction of antimatter with Earth's gravitational field can be tested. If the universality of clocks Weak Equivalence Principle (WEP_{cc}) in the antimatter system holds, then the redshift of matter and the equiv-

[3]Measured gravitational acceleration of antihydrogen was $0.75g$, where $g = 9.81\ m/s^2$, with statistical and systematic error of ± 0.13 and error originating from the simulations used to model the magnetic field in the trap being ± 0.16.

alent antimatter clock should be the same [89]. As Earth moves around the Sun during the year, it gets closer or farther away from the Sun, changing the total gravitational potential experience on Earth. The magnitude of the redshift should change throughout the year, so measuring the cyclotron frequency of the antimatter charged particle would be a universality of clocks Weak Equivalence Principle test. This experiment was recently performed on antiprotons by the BASE Collaboration and they constrained the possible WEP_{cc}-violations to be < 0.03 [21]. Similarly, the transition frequency in the antihydrogen atom is a different type of antimatter clock. Measuring the antihydrogen's $1S - 2S$ transition frequency, which is the best characterised transition in hydrogen, at different times of the year and comparison with hydrogen would be a test of the Weak Equilibrium Principle of the clock, which could potentially offer higher precision [90].

Other fundamental physics tests

Assuming that antimatter properties are the same as matter (within some uncertainty), antimatter can be used for testing other physics theories and hypothesis. For example the *QED* can be tested in various ways:

a) positronium and muonium spectroscopy [91, 92]: both exotic atoms are purely leptonic, so their atomic levels can be calculated with greater precision than of the hydrogen atom, which contains proton, due to the proton's internal structure.

b) muonic and antiprotonic atoms [93,94]: atoms with muon or antiproton bounded instead of one of the valence electrons; Since muon is 207 times heavier and antiproton is 1836 times heavier than electron, they are stronger bounded to the atomic nucleus, therefore more sensitive to nuclear effects.

Additionally antimatter can be used to test the coupling to the axion-like dark matter to constrain the strength of their interactions. The interaction with axion-like dark matter with antiparticle in the Penning trap is expected to introduce noise at characteristic frequency. The BASE Collaboration has analysed their recorder frequency spectra of antiprotons in search of this coupling to axion-like dark matter [95]. So far no interaction has been observed, and they managed to set constraints on the coupling between axions and antiprotons.

1.2 ALPHA antihydrogen experiment

ALPHA is one of the experiments installed in the *Antiproton Decelerator* (AD) facility at CERN. It uses traps for charged particles, called Penning-Malmberg traps, to confine antiprotons and positrons that are used to form antihydrogen atoms. The Penning-Malmberg trap is a stack of cylindrical electrodes inside a vacuum chamber, installed inside a solenoid magnet, which produces a combination of magnetic and electric fields that allows for three-dimensional confinement of charged particles and low-energy plasmas. The principle of operation of charged-particle traps will be discussed in Chapter 2. ALPHA apparatus consists of 4 independent Penning-Malmberg traps and two of them, called *Atom Traps* (which could also be referred to as *Mixing Trap*), where antiproton and positron plasma are mixed and where antihydrogen is formed. Each of *Atom Traps* is combined with a *magnetic minimum trap* called a *Ioffe-Pritchard trap* [96] (also referred to as a *neutral trap*), which is used to trap antihydrogen atoms. The ALPHA apparatus consists of:

1. *Catching Trap*, which captures antiproton beam from the AD and performs initial cooling and compression of the antiproton plasma and sends it further to the *Atom Trap*.
2. *Positron Accumulator* is a specialised trap to store large quantities of positrons, emitted by a radioactive source, by cooling them with a buffer gas; from the accumulator positrons can be transported to the *Atom Trap* whenever they are needed.
3. *ALPHA-2 Atom Trap*, antihydrogen synthesis trap, overlaid with an antihydrogen trap, which is used for spectroscopy measurements: it has laser access ports and a waveguide for microwaves. It is installed horizontally along the antiproton beamline.
4. *ALPHA-g Atom Trap*, antihydrogen synthesis trap, overlaid with an antihydrogen trap, which is used for the gravity measurement, so it is installed vertically. It also contains a microwave waveguide to perform magnetic field measurements (using the *ECR* method, described in Section 6.1.1) and the laser access port for future use of the laser-cooling technique [2] 1.2.2.

Each of these traps, except for the positron accumulator, operates under *Ultra High Vacuum* (*UHV*) and cryogenic conditions and uses superconducting solenoid magnets to generate external magnetic field (1T in both *Atom Traps* and 3T in the *Catching Trap*). The *Positron Accumulator* uses a 0.14T magnetic field, which is generated by a standard electromagnet.

The *Positron Accumulator* uses a nitrogen gas to cool positrons, therefore, the internal pressure in this trap is higher than in the traps operating with antiprotons. The accumulator operates at room temperature, since there is no need for the cryogenic temperatures of the trap - positrons are warmer and will be accelerated anyway during the transport to one of the mixing traps. Antiproton traps must operate in the *UHV* and cryogenic environment, because the annihilation cross-sections with the background gas is significantly higher for antiprotons than for positrons, and to achieve the lifetimes of antiprotons long enough for the plasma preparation (longer than a few minutes, preferably at the level of hours), the operational pressures must be below 10^{-12} mbar. For the same reason, the antihydrogen lifetime in the traps is limited by the condition of the vacuum. In the current state of art, the antihydrogen lifetime in the ALPHA-2 trap is 66 hours [111].

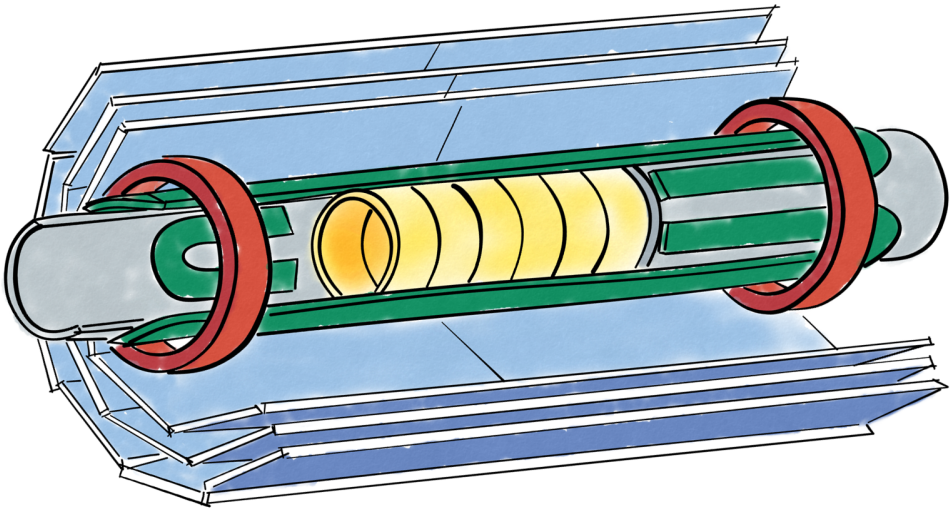

Figure 1.1 – Schematic of a ALPHA-2 trap adapted from Ref. [97]. The innermost is a stack of cylindrical electrodes (yellow), which together with external solenoid magnet (not shown on the diagram) form a Penning-Malmberg trap. The electrodes are installed in the *ultra-high vacuum* chamber (grey), which is placed in the liquid helium cryostat (not shown). Superconducting wires winding around the vacuum chamber (referred to as *inner vacuum*) for a magnetic Ioffe-Pritchard trap for neutral atoms. *Octupole magnet* (green) provides radial confinement, while *mirror coils* (red) restricts the axial motion of antihydrogen atoms. There are also two short superconducting solenoids magnets included in the internal magnet assembly, not shown in this diagram, which are used to increase the magnetic magnetic field locally from 1T to 3T to boost plasma compression (see Section 2.4.2). The cryostat is enclosed by an *outer vacuum chamber* (not shown). This is surrounded by a charged pion detector, a *Silicon Vertex Detector* (blue). The outermost assembly is an external solenoid (not shown) producing a background 1 T magnetic field.

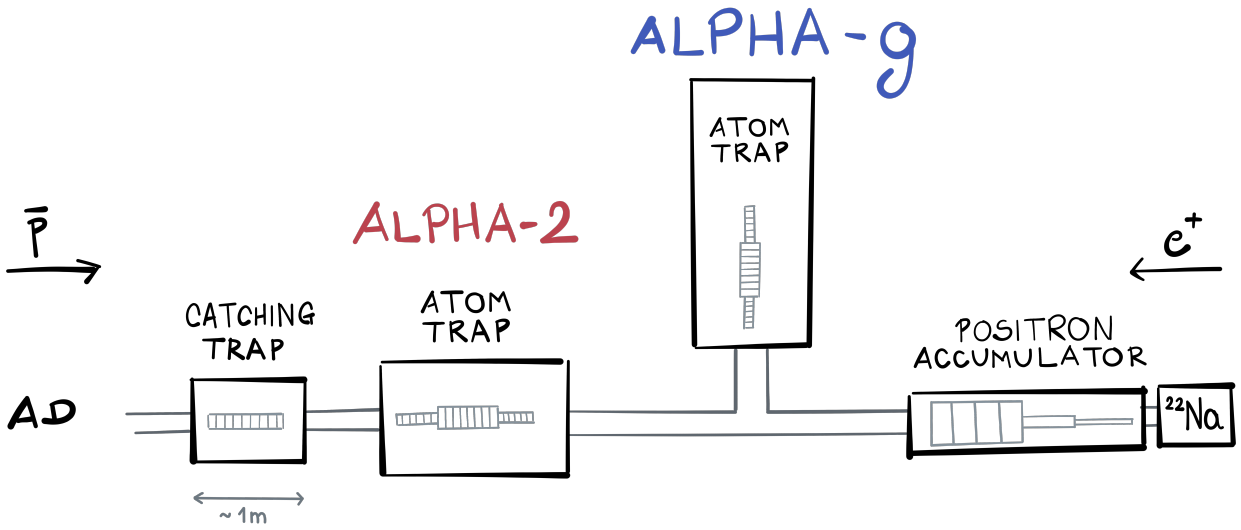

Figure 1.2 – Schematic of all of the ALPHA apparatus. Only bottom electrode stack is shown in the ALPHA-g trap, as a current hardware status, since the top electrodes stack was not installed yet.

Both *Atom Traps*, are joint charged particle traps and neutral atoms, and in principle they have the same design. The stack of cylindrical electrodes is the most inner and the external solenoid magnet is the most outer component, they together form a Penning-Malmberg trap. A vacuum chamber with electrodes is installed inside a liquid helium cryostat. The internal superconducting magnets, forming an Ioffe-Pritchard trap, are winded around the vacuum chamber and submerged in the liquid helium bath. The cryostat is placed inside the *outer vacuum chamber* (*OVC*) to reduce the heat transfer from the outside of the trap. There is a multilayer insulation (*MLI*) surrounding the cryostat to reduce thermal radiation that reaches the liquid helium volume. Between the outer vacuum chamber and the external solenoid magnet, there is a charged particle detector, which is used to record products of the antihydrogen annihilation.

The ALPHA-2 trap is installed horizontally between the Catching Trap and Positron Accumulator. The ALPHA-2 cross-section is presented in Figure 1.1. ALPHA-g trap is a vertical trap installed on top of the beamline that connects the ALPHA-2 trap to the Positron Accumulator. The beamline allows for positrons to be sent to both the ALPHA-2 and ALPHA-g traps and to send antiprotons to the ALPHA-g, through the ALPHA-2 trap. The ALPHA-g experiment uses a more complex trap than ALPHA-2: there are two stacks of cylindrical electrodes, one above the other, and the Ioffe-Pritchard trap contains nearly 30 internal superconducting magnets.

Those internal magnets in fact form two Ioffe-Pritchard traps, separated vertically by around 1 meter and there is additional magnetic trap in the middle aimed for a precision measurement of antihydrogen's gravity, called *precision* or *analysis trap*. Multiple internal magnets allow for expanding the trapping volume and transport of the antihydrogen vertically upward and downward. There is an electrode stack inside the bottom Ioffe-Pritchard trap to allow for antiproton and positron preparation and mixing to form antihydrogen within the trapping volume. In the future, a second electrode stack is intended to be installed inside the top Ioffe-Pritchard trap to be able to produce antihydrogen in the top trap as well. A double trap system was designed for a precision measurement of the gravity of antihydrogen. When the magnetic field of the internal magnets are changed Eddy currents are induced, which could influence the result of the precision measurement. By having a system of magnets that is symmetric around the centre of the z-axis of the trap, both magnetic traps could be changed simultaneously at the same rate, so the induced fields are expected to be symmetric as well [98]. An overview diagram of the entire ALPHA apparatus is shown in Figure 1.2

1.2.1 Antihydrogen production and trapping

To probe antihydrogen before it annihilates, it must be confined in an ultra-high vacuum region. ALPHA uses magnetic traps designed to trap neutral atoms, which are only capable of trapping sub-Kelvin antihydrogen atoms. Therefore, the antihydrogen produced within ALPHA experiments must have a sufficiently low energy to be trapped. The reaction used for the cold antihydrogen production is three-body recombination (*TBR*). The three-body collision process involves two positrons and one antiproton:

$$p^- + e^+ + e^+ \longrightarrow \bar{H}^{**} + e^+$$

An additional positron scatters, causing energy to be extracted from the positron that then binds to an antiproton, which increases the reaction rate [99, 100]. The reaction rate of the three-body recombination Γ_{TBR} scales with the temperature of the reagents T and the density of the positrons n_e as [23, 101]

$$\Gamma_{TBR} \sim n_e^2 \, T^{-9/2} \tag{1.2.1}$$

which means that at cold temperatures this process is highly enhanced, but negligible even at room temperatures.

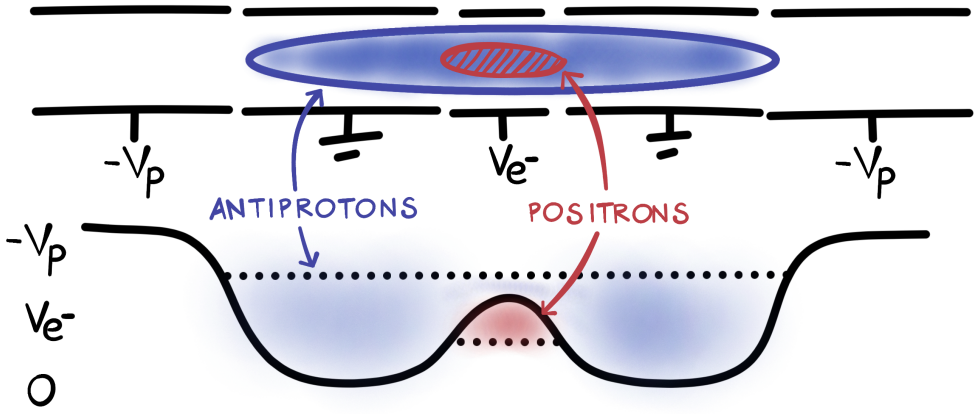

Figure 1.3 – Nested trap for positron and antiproton plasma, where both species overlap spatially allowing for collisions between antiprotons and positrons. On the top a schematic of electrodes confining plasma and electrostatic potentials at the bottom. Figure adapted from Ref. [104].

The antihydrogen atom produced in this process is in a highly excited state $\bar{H}^{**}$ (high Rydberg states, with high principal quantum numbers n), which can be easily ionised back to the antiproton and positron via collisions with positrons or via field ionisation process as they travel through electric field gradients (for example exiting the non-neutral plasma). Some collisions with positrons cause the antihydrogen atoms to deexcite to lower Rydberg states, from which they deexcite to the ground state via photon emission. Those deexciting antihydrogen atoms undergo many scattering events, in which their kinetic energy changes. They remained trapped in the Ioffe-Pritchard trap as long as their kinetic energy is smaller than the confining magnetic-field potential. The fraction of antihydrogen atoms that are trapped from the entire population produced is highly dependent on the positron density [102]. The temperature of the trapped antihydrogen can be reduced in an *adiabatic cooling* process, which is performed by slowly expanding the length of the Ioffe-Pritchard trap by manipulating the magnetic potentials. For this reason there are multiple mirror coils in the ALPHA's neutral trap, which allow to increase the separation of the axial magnetic potential barriers by ramping up the outer coils and ramping down the inner ones. More information about the adiabatic cooling process can be found in Danielle Hodgkinson's Ph.D. thesis [103].

Cold antihydrogen synthesis

Large quantities of antihydrogen can be synthesised in a three-body recombination process by mixing cold plasmas of positrons and antiprotons; this is a scheme that ALPHA Experiment uses. Each species population is trapped and cooled to < 50 K before mixing. The temperatures of each population affect the energy distribution of the produced antihydrogen. The antihydrogen production is enhanced with an increase in the density of both plasmas and with a maximum in their spatial overlap.

Antiprotons are sourced from CERN's Antiproton Decelerator and are initially caught by the Catching Trap. The antiproton catching protocol uses preloaded electrons for compression and sympathetic cooling [4]. The antiprotons are transferred to the ALPHA-2 Atom Trap, where they undergo the same cooling and compression procedure. The resulting antiproton plasma has a radius of 0.4 mm and a temperature of roughly 100 K.

Before antihydrogen synthesis the antiprotons are cooled down to 40 K by using the evaporative cooling technique. The remaining antiprotons have a radial extent of 1 mm and a population size of around $9 \cdot 10^4$. The positrons are source from the Positrons Accumulator. $1.6 \cdot 10^6$ positrons are transferred to the ALPHA-2 atom trap in parallel with the previously mentioned antiproton preparation protocol. Positrons are transferred between traps at energies of tens of eV, and once the positrons are caught within the ALPHA-2 trap, they undergo cyclotron cooling in the high magnetic field of 3T, causing the positrons to be deeply trapped. In addition, the positron temperature is cooled by adiabatic expansion to 30 K. The radial size of the positron plasma is similar to that of the antiproton plasma. Positrons are slowly mixed with antiprotons, so that the positrons undergo evaporative cooling. On average $2.2 \cdot 10^4$ antihydrogen atoms are produced and ~ 10 are trapped per mixing.

Plasma preparation and cooling techniques have been developed in the configuration with the Ioffe-Pritchard trap energised and this trap can remain energised continuously for hours, allowing the mixing process to be repeated multiple times allowing accumulation of the antihydrogen [105].

[4] Plasma manipulation and cooling techniques will be explained in the Section 2.4

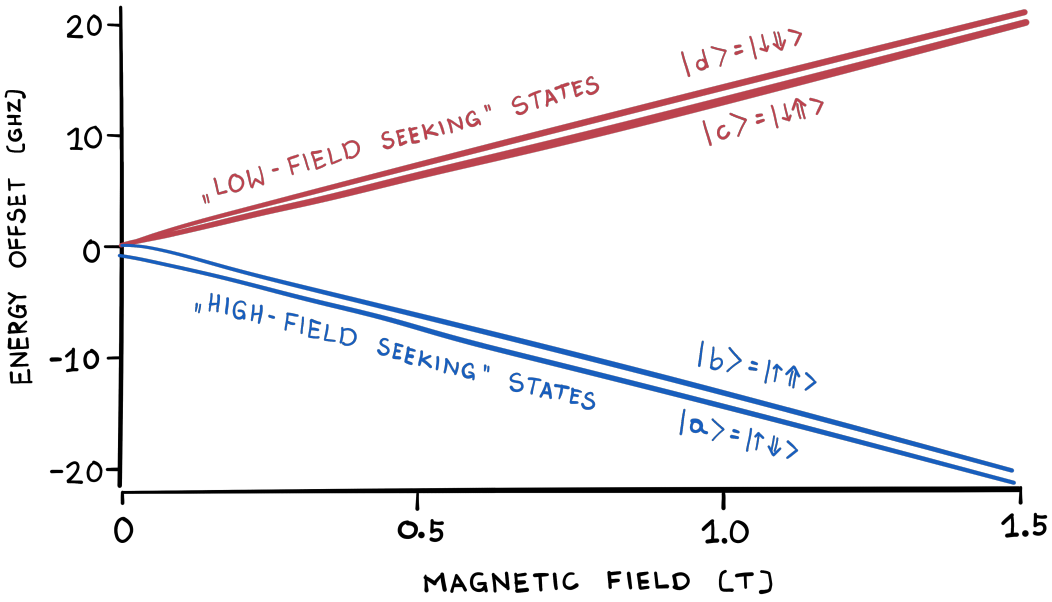

Figure 1.4 – The relative energy of the antihydrogen ground states as a function of magnetic field. Trappable (*low-field seeking*) and non-trappable (*high-field seeking*) states depend on the alignment of the positron spin with the direction of the magnetic field. The figure was adapted from Ref. [35].

Antihydrogen trapping

Antihydrogen atoms can be trapped by a magnetic field due to their magnetic moment $\bar{\mu}$. Magnetic moment is a vector quantity that describes the magnetic strength and orientation of the object. A particle placed in a magnetic field has a potential energy proportional to its magnetic moment and to the strength of that magnetic field

$$U = -\bar{\mu} \cdot \bar{B} \tag{1.2.2}$$

Depending on whether the magnetic moment vector and direction of the magnetic field are aligned or antialigned, the potential energy decreases or increases with increasing magnetic field value. If it decreases, then that magnetic moment will be attracted towards regions of higher magnetic field. In the same way, if the potential energy increases with increasing B-field, the magnetic moment will tend towards the magnetic field minimum. Based on this phenomenon, one could design a magnetic field with a local minimum to confine the atom with magnetic moment $\bar{\mu}$. According to *Earnshaw's theorem* a three-dimensional minimum of the magnetic field potential can be obtained, but it is not possible to produce a local maximum [106]. The same trapping mechanism applies to any matter atoms or charged particles that have a non-zero magnetic moment.

The magnetic moment of antihydrogen results from the magnetic moments (spins) of positron and antiproton

$$\bar{\mu}_{\bar{H}} = \bar{\mu}_{e^+} + \bar{\mu}_{\bar{p}}$$

Antiproton spin can be aligned or anti-aligned with the positron spin, therefore there are two possible values of antihydrogen magnetic moment. Antihydrogen magnetic moment $\bar{\mu}_{\bar{H}}$ in the magnetic field can be aligned or anti-aligned with the field vector $\bar{B}$, therefore there are 4 possible states of the antihydrogen atom. The antihydrogen energy levels in the ground state are shown in Figure 1.4. In principle, only two out of for antihydrogen states can be trapped:

$|a\rangle = |\uparrow\Downarrow\rangle$ and $|b\rangle = |\uparrow\Uparrow\rangle$ are untrappable *high-field-seeking* states,

$|c\rangle = |\downarrow\Uparrow\rangle$ and $|d\rangle = |\downarrow\Downarrow\rangle$ are trappable *low-field-seeking* states.

The symbols $|\uparrow\rangle$ and $|\downarrow\rangle$ correspond to the spin states of the positron, and $|\Uparrow\rangle$ and $|\Downarrow\rangle$ correspond to the antiproton spin. The antihydrogen magnetic moment is dominated by the positron magnetic moment $\mu_{\bar{H}} \approx \mu_{e^+}$ and this, according to our current knowledge, equals the electron magnetic moment, which is one Bohr magneton:

$$\mu_B = \frac{e\hbar}{2m} \tag{1.2.3}$$

This type of trap was developed by David E. Pritchard to cool sodium atoms to ultra low temperatures [107]. The name Ioffe originates from the magnet configuration, which are two Helmholtz coils (in ALPHA referred to as mirror coils) and an even number of wires ($2n$) parallel to the central axis between the two coils and evenly spaced from that axis, where the direction of electrical current is opposite between each neighbouring wire, as shown in Figure 1.5. Ioffe configuration of magnets provides a magnetic field minimum at the centre of the trap. The minimum of the magnetic field is offset from zero in the same direction as the magnetic field generated by the magnetic trap because atoms crossing a zero-field region could undergo Majorana spin-flips between trappable and non-trappable states, leading to atom losses. These types of traps are used *i.a.* to produce Bose-Einstein condensates [106].

The trapping potential is a function of a magnetic field generated by the Ioffe-Pritchard trap in cylindrical coordinates [104]:

$$U(r, \theta, z) = -\mu_B \left| \bar{B}(r, \theta, z) \right| \tag{1.2.4}$$

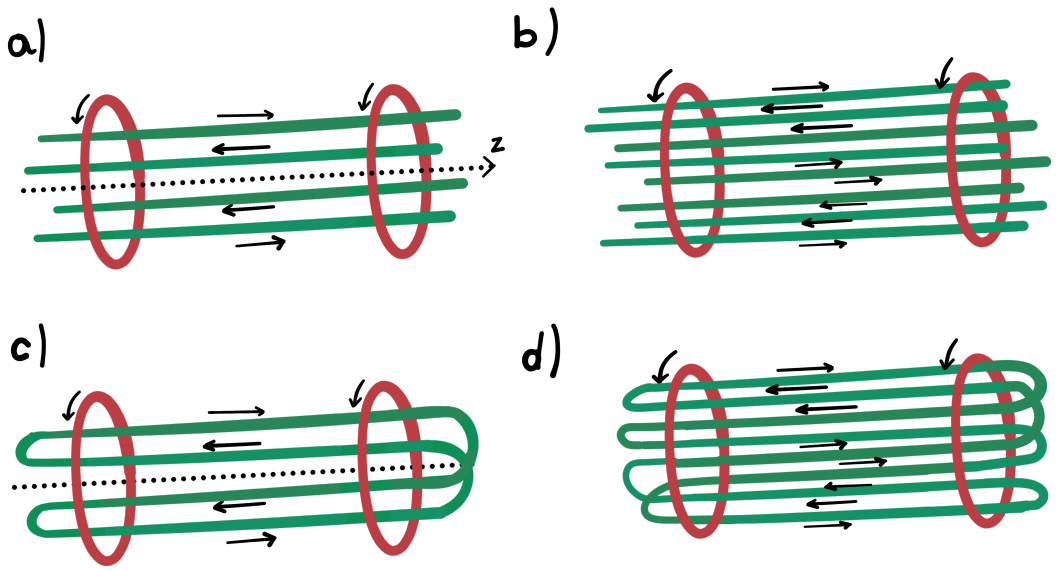

Figure 1.5 – In the top row there are schematics of an ideal Ioffe traps with infinitely long rods generating perfect quadrupole (a) and octupole (b) fields. The bottom row shows the real geometry of a (c) quadrupole and (d) octupole Ioffe-Pritchard trap with wire windings at the edges of the trap.

The potential energy of ground state low-field-seeking antihydrogen atoms near the centre of idea Ioffe trap (neglecting mirror coils at the end) depends on the number of parallel current wires $2n$ and their distance from the trap axis R:

$$U(r,\theta,z\approx 0) = -\mu_B\left|\bar{B}_\perp(r,\theta,z\approx 0)\right| = -\mu_B B_R\left(\frac{r}{R}\right)^{n-1} \tag{1.2.5}$$

In result the trapping potential of the octupole magnet ($2n = 8$) is stronger than that generated by a quadrupole ($2n = 4$). For the Ioffe-Pritchard trap combined with the Penning trap, the total magnetic field of is offset by the value of the magnetic field $B_0\hat{z}$ generated by an external Penning trap solenoid [5]. The magnetic fields generated by the Ioffe-Pritchard trap break the axial symmetry of the Penning trap, so the motion of charged particles is affected by the radial changes of magnetic field and it leads to increases losses of charged particles at higher radii. In the ideal Penning trap, the confinement time of charged particles is indefinite, and in practice it depends on the vacuum quality, e.g. the BASE collaboration demonstrated storage of antiprotons for a duration of more than a year [108, 109].

The ALPHA experiment uses an octupole version of the Ioffe-Pritchard trap (see Figure 1.5) combined with a 1T magnetic field generated by the Penning trap. This Ioffe-Pritchard trap is often referred to as a *neutral trap*.

[5] 1T in case of ALPHA's traps.

ALPHA's trap has multiple *mirror coils* that allow the trap volume to expand axially to perform *adiabatic cooling* of trapped antihydrogen atoms. There are also two additional solenoid magnets, around the region of a segmented electrode, to locally increase the magnetic field from 1T to 3T, which is used to compress the ion plasma by the *Rotating Wall* technique (more information in Section 2.4.2).

Antihydrogen detection

The antihydrogen atoms can be detected by annihilation events occurring when they are released from the magnetic trap. When antihydrogen atoms reach the apparatus wall (gold electrodes), the antiprotons annihilate with either protons or neutrons within the wall material. Unlike positron-electron annihilation, which produces two photons, antiproton annihilation is more complex due to the internal structure of the nucleons. The hadronisation process occurs and other particles, mostly pions (π mesons) are created [110]. Pions exist in two charged forms: π^+ and π^- and one neutral form π^0. Charged pions are detected with a charged particles detector. The number and type of pions produced depend on the energy of the antiproton at the moment of annihilation. For example, at low energies, typically two or three pions are produced (Table 6.1. in J.T.K. McKenna's PhD thesis [112]). Antihydrogen annihilation events are detected by reconstructing the trajectories of pions measured by a barrel detector surrounding a vacuum chamber. Pions produced from the same antihydrogen atom originate from the same point, so the intersection point of their trajectories, a vertex, is assigned as the annihilation position. A boosted decision tree algorithm is used to distinguish signals generated by a cosmic ray and reject them from the data analysis.

A detector used in the ALPHA-2 trap is a *Silicon Vertex Detector* (*SVD*) with three layers of *Double-sided Silicon Strip Detector* (*DSSD*) [112]. Pions give a *"hit"* signal in the position they pass through each silicon layer, and having three layers allows reconstructing their trajectory. Silicon detectors are expensive, so for the ALPHA-g trap, which is around 3 times longer, a *radial Time Projection Chamber* (*rTPC*) is used [113]. The time projection chamber is a gas detector in which charged particles are detected by ionising the gas mixture (90% argon + 10% CO_2) as they pass through a detector volume. The ionisation products, electrons and gas ions, are accelerated in opposite directions by concentric electrodes installed on the outer and inner bore of the detector. Electrons drift towards the outer

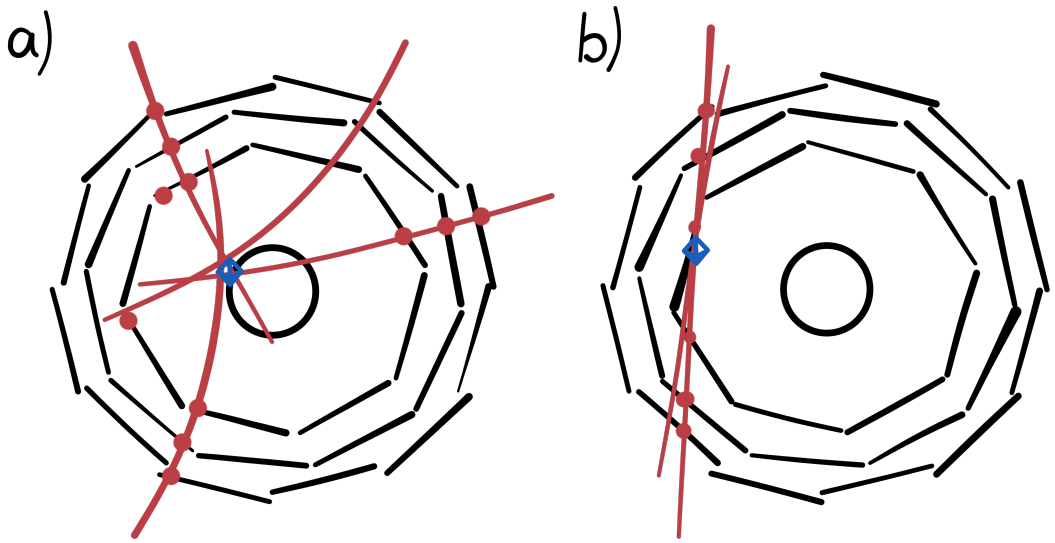

Figure 1.6 – Schematic diagram of the Silicon Vertex Detector and the charged pions trajectories reconstruction. Single counts in each of the detector layer, that are closely correlated in the time and position, are used to reconstruct the track of charged particle. The vertex is found on the intersection of the reconstructed tracks. If the vertex is on the inner wall of the apparatus, the event is classified as antiproton annihilation (a). If the vertex is outside of the trapping volume (b) or no vertex has been found, it is classified as an event caused by a background cosmic radiation. This figure was adapted from Ref. [31].

electrode, where readout pads are installed. Reading the positions where electrons drifted to the outer electrode gives a projection of the charged particle track. Annihilation detection is a destructive detection method, which has the obvious downside of losing the antihydrogen sample. To combat this, the ALPHA Collaboration is currently working on introducing photon detectors inside the ALPHA trap to measure the fluorescence light emitted by the antihydrogen.

1.2.2 Spectroscopy of antihydrogen

Spectroscopic measurements probe the electromagnetic forces acting on atoms. By measuring the electronic transitions of the antihydrogen, we can compare the energy-level structure to that of the hydrogen. Due to its simplicity and lack of nuclear structure, hydrogen is the best theoretically understood atom. The transition between the ground state and the excited state $1S$-$2S$ of hydrogen is the most precisely measured transition, measured to a few parts per 10^{15} [114] by the Theodor Hänsch group at Max-Planck-Institut für Quantenoptik (*MPQ*). Other transitions in the hydrogen atom have also been extensively studied [115,116].

Comparisons of antihydrogen and hydrogen transitions provide a very precise test of *Quantum Electrodynamics* (*QED*) and the Lorentz and CPT invariance [5, 72]. The same transition in antihydrogen has been measured to parts per 10^{12} [33].

The experimental protocol for hydrogen spectroscopy performed at *MPQ* differs significantly from the antihydrogen measurement performed at CERN by ALPHA: they use a 6K hydrogen beam and detect 121nm photons emitted in decay from excited to ground state, while in ALPHA magnetically trapped antihydrogen of less than 1K is used and detection relies on ionising antihydrogen atoms in excited state and detecting released antiprotons. Antihydrogen measurement is performed in a strong magnetic field of 1 T, while hydrogen measurement is performed in a weak magnetic field of 0.5 mT. Both experiments are performed with different methods and in different laboratories, therefore the systematic errors of both measurements differ, which will become more relevant with increasing precision. The best test of the CPT invariance would involve measuring antihydrogen and hydrogen with the same protocol, in the same reference frame: in the same apparatus and at the same time. This is challenging because the antimatter community would have to either develop the same measurement technique as *MPQ* and other groups measuring hydrogen beams or hydrogen would have to be trapped in an antihydrogen trap. ALPHA is currently looking for ways to introduce hydrogen atoms into their Ioffe-Pritchard trap in a few independent ways:

a. synthesis from protons and electrons in a similar way as antihydrogen is produced [44],

b. photodissociation hydrogen from molecular ion BaH^+ [42],

c. laser ablation of hydrogen ions from solid target of LiH [43].

All of these methods plan for the production of cold trappable hydrogen *in situ*. Commercial sources of protons and hydrogen are not practical for antimatter experiments because of the very strict vacuum requirements. An additional challenge is to develop detection methods that are compatible with both hydrogen and antihydrogen. Hydrogen/protons obviously do not annihilate when released towards apparatus walls, therefore photon detection for antihydrogen fluorescence would have to be developed. There is work to introduce photon counting, possibly by using silicon photon multiplying chips *SiPM*, which is ongoing [117], but this is technically challenging. Alternatively, protons and antiprotons could be detected using charged particle detectors, for example, a *MCP*, after ionisation of hydrogen/antihydrogen in the excited $2S$ state.

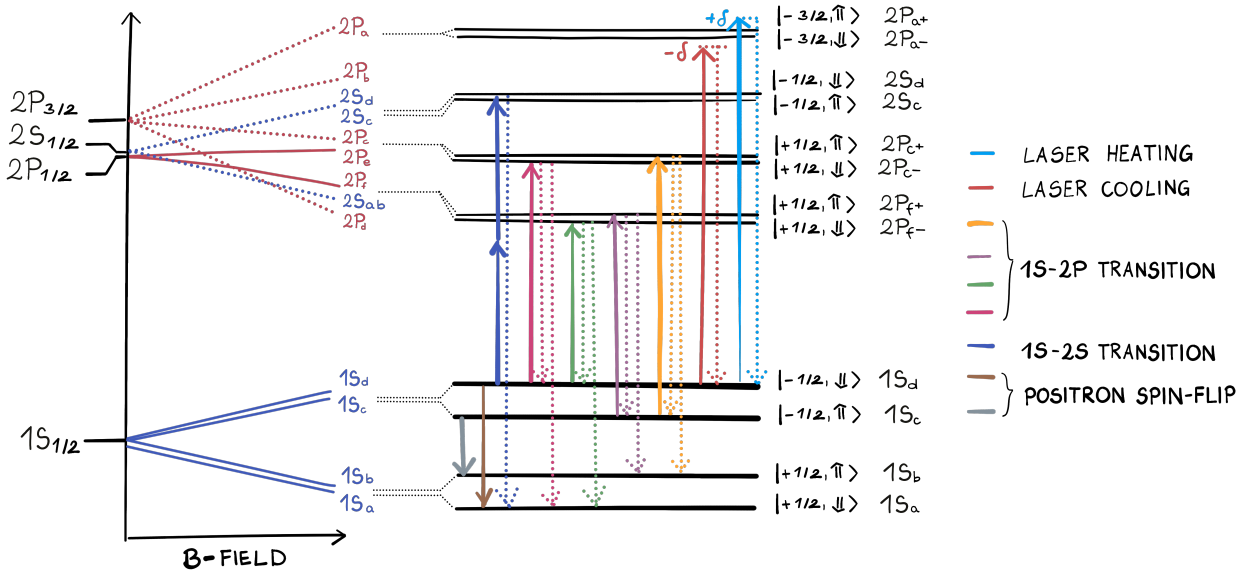

Figure 1.7 – Schematic diagram of transition in the antihydrogen atom that are being excited (solid lines) in the ALPHA Experiment and the decay channels from those levels (dashed lines). The energy levels in the zero magnetic field are marked with the spectroscopic notation nL_J. The *ket* notation for the high magnetic field (left side of the diagram) uses the m_J values of the positron and the orientation of the antiproton spin ($\Uparrow$ or $\Downarrow$). Figure adapted from Ref. [103].

1S-2S transition

The ground and first excited level in the (anti)hydrogen are separated by the energy corresponding to 121.6 nm wavelength, called a Lyman-α line. Although the $1S$ and $2S$ are both states of the same parity, i.e. an electric dipole transition is forbidden by selection rules, meaning that the transition mediated by a single photon is very unlikely. This means that the lifetime of the $2S$ state in the (anti)hydrogen is relatively long, ~ 0.12 ms, so the state is metastable. This means that the transition linewidth is very narrow (1 Hz), making a $1S$-$2S$ transition frequency a value that can be determined very precisely.

The $1S$-$2S$ transition is measured in the two-photon spectroscopy scheme, meaning that two counter propagating photons of 243 nm wavelength are absorbed by an atom, which conserves the angular momentum. The first-order Doppler shift is cancelled in the two-photon absorption, so the broadening of the transition linewidth is reduced. The laser used for the spectroscopy is a commercial Toptica laser, which uses two second harmonic generation crystals to convert 972 nm light produced by a laser diode into the 243 nm laser beam. The two-photon transition is achieved with an enhancement cavity built around the antihydrogen trapping volume, allowing the absorption of two counter propagating photons.

The enhancement cavity also allows for the building up of laser power to about 1 W. High precision measurement of the transition requires stable and accurate frequency reference for the 243 nm laser. To precisely measure the frequency of that laser, a frequency comb is used [118] in both hydrogen and antihydrogen measurements (more information can be found in Steven Jones' Ph.D. thesis [119] in Section 5.2.2). To achieve relative precision at the level of 10^{-15}, the hydrogen group at *MPQ* used a caesium fountain clock [120, 121]. To achieve competitive precision of $1S$-$2S$ transition frequency in antihydrogen, ALPHA Experiment has also installed a caesium fountain in the Antiproton Decelerator facility, which is currently under commissioning.

1S-2P (Lyman-α) transition

The Lyman-α transition in the hydrogen [122] is a transition between a ground state $1S_{1/2}$ and second excited state $2P_{3/2}$. The S and P states have different parity, so an electric dipole transition between these states with a single photon is allowed. This transition is highly probable and the $2P_{3/2}$ is a short living state, which means that it is a cycling transition:

$$1S_{1/2} \longleftrightarrow 2P_{3/2}$$

that can be used for laser cooling hydrogen and antihydrogen atoms. The transition occurs with a wavelength 121.6 nm that is extreme ultraviolet, which propagates only in vacuum. The 121.6 nm laser light is very difficult to generate, especially as an intense continuous radiation. To measure the Lyman-α transition, ALPHA uses a pulsed source of 121.6 nm radiation, which is produced in two stages: initially the 730 nm laser pulse is frequency doubled, and next the third harmonic is generated from the 365 nm in a high-pressure Kr/Ar gas cell. The third harmonic generation efficiency is very low, below 10^{-6}. Pulses of 121.6 nm of around 12 ns are injected into the ALPHA-2 ultra-high vacuum system through an MgF_2 window. The antihydrogen atoms in two ground *trappable states* are exposed to the Lyman-α laser pulses at the 10 Hz repetition rate for few hours, since the transition rate of antihydrogen in ALPHA-2 magnetic trap is very low due to the low density of antihydrogen atoms (500 antihydrogen atoms interrogated with laser pulses for 2 hours in the first $1S$-$2P$ measurement [34]). At resonance $\bar{H}$ the atoms are excited to one of the $2P_{3/2}$ states (denoted $2P_c$), from which they can decay back to the *trappable* or *non-trappable* ground state and the later events are detected by annihilations of antihydrogen atoms escaping from the trap.

$1S$-$2P$, but between different sublevels of excited state, was also used for Doppler laser cooling of antihydrogen atoms [2]. Exposing antihydrogen atoms to 121.6 nm radiation detuned slightly below the resonance of the $1S_d \rightarrow 2P_a$ transition for 4-5 hours resulted in a reduction in the antihydrogen temperature by around a factor of 2. Those laser cooled antihydrogen samples were used to perform the $1S \rightarrow 2S$ spectroscopy, resulting in narrowing of the transition linewidth. Laser cooling is a highly promising tool not only for antihydrogen spectroscopy, but also for gravitational experiments [86, 88].

Hyperfine transitions

The hyperfine structure is the result of the interaction of the electronic spin with the nuclear spin. In the case of antihydrogen, we have a positron spin interacting with antiproton spin, which results in splitting of the energy levels. The ground state $1S$ splits into two branches: lower energy singlet state and higher energy triplet. The triplet state in fact contains 3 sublevels that separate from each other in the presence of magnetic field. The energy splitting between singlet and triplet state, the hyperfine splitting, in zero magnetic field equals 1.42 GHz, the transition between the two hyperfine levels is the famous *21 centimetre hydrogen line* studied in astronomical observations. In a high magnetic field, this energy structure reorganises, since the interaction of electron/positron spin with magnetic field dominates the hyperfine interaction between spins of both particles. The energy of states with positron spin aligned with the magnetic field direction, referred to as *spin-up* $|\uparrow\rangle$, increases with increasing magnetic field strength, while the energy of states with anti-aligned positron spin, *spin-down* $|\downarrow\rangle$, decreases with increasing magnetic field. This is the origin of the *trappable* and *non-trappable* states - the *spin-up* states are *low-field-seeking* and *spin-down* states are *high-field-seeking*.

The hyperfine interaction in antihydrogen is studied by ALPHA [35]. Antihydrogen atoms trapped in the magnetic Ioffe-Pritchard trap are equally distributed between the two *trappable* ground states. The energy splitting between those states and the *non-trappable* states in the 1T field used in the ALPHA-2 trap is around 29 GHz. Microwave radiation at the frequencies around the resonance of the two transitions $1S_d \rightarrow 1S_a$ and $1S_c \rightarrow 1S_b$ is used to drive transitions from trapped to non-trapped states. Both transitions correspond to changes in the alignment of the positron spin with respect to the magnetic field direction.

These transitions are commonly referred to as *positron spin-flip* transitions. Microwave radiation is produced by an Agilent 8257D PSG frequency synthesiser and a Miteq AMF-4B amplifier and delivered to the ALPHA-2 trap through a waveguide. The hyperfine transition strength is measured by counting the number of annihilation events after the antihydrogen atoms are released from the magnetic trap for given microwave frequency. The difference in frequency between the two transitions $1S_d \rightarrow 1S_a$ and $1S_c \rightarrow 1S_b$ is the hyperfine ground-state splitting, which is independent of the magnetic field strength. The higher frequency transition, $1S_d \rightarrow 1S_a$, has been measured to have a wider line width and a lower intensity than the other transition. This is explained by the technical limitations of the experimental apparatus: The Penning trap interior and the electrode stack are a complicated boundary surface for the injected microwaves. The microwave radiation inside the ALPHA-2 trap, instead of being a freely propagating wave, is a mixture of standing and travelling waves, and the pattern of those standing waves changes for different microwave frequencies. Therefore, the strength of microwave radiation at a given location in the trap is a function of its frequency. The strength of the electric field component of the injected microwave in the region of the trapped antihydrogen is measured by studying the electron cyclotron resonance heating of the electron plasma trapped in the same volume as the antihydrogen atoms (ECR technique of magnetic field measurement is discussed in Section 6.1.1). These studies have indicated that when the microwave source power is kept fixed, its electric field strength at the lower resonant frequency is seven times larger than the upper resonant frequency. Currently, this difference in electric field strength is managed by using an injected microwave strength of 160 mW for the lower transition frequency and 320 mW for the upper transition frequency. However, the *positron spin-flip* is a magnetic dipole transition, so it is the magnetic field component of the microwaves that drives the transition between hyperfine levels. The relationship between the microwave electric and magnetic field components has not been measured so far. Since the magnetic field component of the microwave radiation cannot be measured directly with current experimental methods used in ALPHA, it has been proposed to use beryllium ions [6] to probe strength of the magnetic component of the microwaves. The energy structure of the ground state of $^9Be^+$ is well characterised, and a microwave transition of *electron spin-flip* is also induced by the magnetic field component of the microwaves.

[6] Originally used for sympathetic cooling of positrons with laser-cooled Be^+, which will be discussed in the Section 1.3.2

The *electron spin-flip* transition frequency in $^9Be^+$ in the $\sim$ 1 T field of the ALPHA-2 Penning trap is around 27.6 GHz, which can be produced by the same synthesiser used for the antihydrogen hyperfine transition and electron cyclotron resonance study, can be performed in the ALPHA-2 trap without any hardware modification, since the beryllium ions source and all the laser system and detectors are already installed. This measurement will be the key part of the work presented in this thesis, and the results of the first proof of principle measurement will be presented in Chapter 6.

1.2.3 Antimatter - matter gravitational interaction

A new antihydrogen trap, called ALPHA-g, has been built to test the gravitational behaviour of antimatter. The principle of the gravity measurement relies on the fact that the trapping potential of the magnetic Ioffe-Pritchard trap in the axial direction (along the central axis of the trap) is a combination of the potential generated by the magnetic field of the trap and the gravitational potential:

$$U_{\bar{H}} = \bar{\mu}_{\bar{H}} \left| \bar{B} \right| + M_{\bar{H}} g z \tag{1.2.6}$$

where $M_{\bar{H}}$ refers to the gravitational mass of antihydrogen, g is the gravitational acceleration acting on antihydrogen and z is its vertical position in the gravitational field. The idea is to vary the height of the potential barrier on one axial end of the trap by changing the magnetic field generated by one of the magnets, such that it compensates or not for the potential difference due to gravity, as shown in the Figure 1.8. If the gravitational potential is compensated, an equal number of antihydrogen atoms should escape through the bottom and upper ends of the trap. If the gravitational potential is undercompensated or overcompensated, there should be an asymmetry in the number of annihilation events detected below and above the vertical centre of the trap. From this measurement the strength of the gravitational potential acting on the antihydrogen could be deduced and the gravitational mass of antihydrogen $M_{\bar{H}}$ could be compared to its inertial mass $m_{\bar{H}}$ known from interactions with other forces in the trap. The ratio of gravitational mass to inertial mass

$$F = \frac{M_{\bar{H}}}{m_{\bar{H}}} \tag{1.2.7}$$

is the quantity being tested and if the Weak Equivalence Principle of the free-fall holds this value should equal to 1.

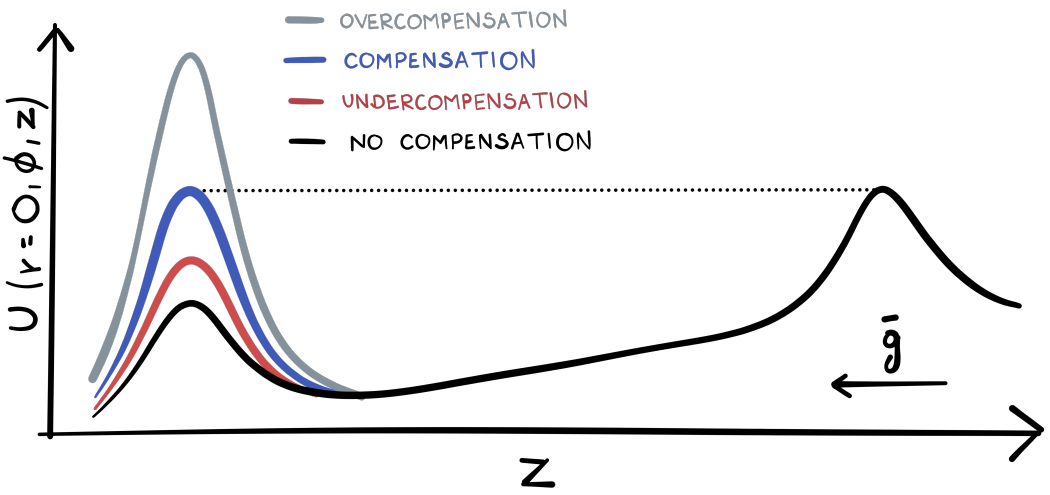

Figure 1.8 – Gravity potential compensation with magnetic field potential generated by *mirror coils* of the Ioffe-Pritchard trap. The gravity experiment is performed by varying the height of potential well barrier around the value that compensates for gravitational potential and compare the numbers of antihydrogen atoms released on the top and bottom of the trap (corresponding to right and left on this diagram).

This experimental protocol was proposed 10 years ago and was tested by analysing annihilation data collected in the first ALPHA spectroscopy trap [79]. The horizontal symmetry of the original ALPHA trap meant that first of all the gravitational potential gradient was very small because the vertical dimension of the antihydrogen trap was limited to the radius of the Penning trap's electrodes, just a few centimetres. Second, the horizontal geometry of the Ioffe-Pritchard trap meant that the confinement in the vertical direction was provided by the octupole magnet, and independent manipulation of bottom and upper trapping potential was not possible. In the vertical configuration of the Ioffe-Pritchard trap, the bottom and upper confinement is provided by mirror coils, which can be energised independently, allowing one to set the potential barrier difference in vertical direction as desired. The vertical configuration also allows the antihydrogen to span a greater range of vertical positions, since the diameter of the electrodes is no longer a limit. The ALPHA-g experiment is designed with around 40 cm of vertical trapping length [123].

Recently, the first *up/down* measurement was performed to determine the direction of the antihydrogen fall in the Earth's gravitational field. being the same as for ordinary matter [3]. The force acting on the $\bar{H}$ atoms has been shown to be attractive and the gravitational acceleration $\bar{g}$ was measured to be consistent with g for ordinary matter:

$$\bar{g}/g = 0.75 \pm 0.13 \text{ (statistical + systematic)} \pm 0.16 \text{ (simulation)} \tag{1.2.8}$$

To further improve the sensitivity of gravity measurements, ALPHA-g will aim to reduce the kinetic energy of antihydrogen atoms via laser cooling [2] and adiabatic expansion cooling [103]. Systematic errors could be reduced mostly by improved precision on magnetic field measurements: the electron cyclotron resonance technique, nuclear magnetic resonance (NMR) probes, and possibly beryllium magnetometry, which will be discussed in this dissertation. The statistics can be improved by increasing the number of $\bar{H}$ atoms trapped by implementing sympathetic cooling of positrons with laser-cooled Be^+ [1] to the ALPHA-g.

1.3 Laser cooling beryllium ions in ALPHA

1.3.1 Enhanced antihydrogen production

The antihydrogen production mechanism used in the ALPHA experiment is a three-body recombination process, one antiproton and two positrons, where an additional positron mediates the recombination by carrying away excessive kinetic energy. The three-body recombination rate increases with decreasing temperature of antimatter plasmas and it is a dominant process at low temperatures, below 4 K [100], therefore, the coldest possible antiproton and positron plasmas are desired. Currently antiproton plasmas or around 40 K and positron plasmas of ~ 30 K are used for antihydrogen synthesis. A single mixing of antiproton and positron plasma at these temperatures results in the production of tens of thousands of antihydrogen atoms, but only about 10 have temperatures below 0.5 K, so they could be confined in the ALPHA magnetic trap. In the ALPHA mixing scheme antiprotons thermalise with positrons before antihydrogen formation, therefore the rate of antihydrogen formation depends on the positron temperature. To produce colder antihydrogen the positron temperature needs to be lowered. Enhancement of cold antihydrogen production would benefit the trapping efficiency, since there would be more antihydrogen atoms that are sufficiently cold to be trapped in the ALPHA Ioffe-Pritchard trap. Positrons cool down by cyclotron radiation (described in Section 2.4.1), but their temperature stops decreasing when various heating mechanisms inside the trap start counteracting the cooling effect and some thermal equilibrium is established. These heating mechanisms are *i.a.* radiation temperature and noise temperature of the surroundings. Temperatures below the surrounding temperature can be achieved by removing positrons of the highest kinetic energies in so-called evaporative

cooling process (see Section 2.4.1), but those lower temperatures cannot be maintained due to the heating mechanisms. The evaporative cooling causes radial expansion of the plasma, and if the magnetic antihydrogen trap is energised, the octupole magnet generates a non-homogeneous radial field, which causes heating of plasma at higher radii [124]. To maintain the temperatures below the surrounding temperature an active cooling mechanism is needed.

1.3.2 Sympathetic cooling of positrons with laser-cooled Be^+

The active method of cooling available for atoms and ions is laser cooling, but this requires many-body systems that possess an electronic structure. Positrons cannot be laser-cooled directly, but they can be sympathetically cooled by interacting with other ions that are actively cooled with a laser. Sympathetic cooling is based on kinetic energy transfer between two species in collisions until a thermal equilibrium between both species is reached. If one of the species is laser-cooled during the interaction with hotter species, heat can be effectively removed from the system and the achieved final equilibrium temperature could be maintained as long as the cooling power of the laser is provided. In principle, laser cooling could obtain milli-Kelvin temperatures, which is significantly below the environment temperature of the trap (~ 4 K for cryogenic traps). $^9Be^+$ ions are one of the most common choice for laser-cooled species, since the cooling laser sources of 313 nm are commercially available and beryllium ions are not difficult to produce. The benefit of using $^9Be^+$ to cool positrons is that beryllium is the lightest ion that can be laser cooled because on average more momenta are transferred per collision due to the smaller mass difference between the species than if using other heavier ions. We require laser-cooling ions, not atoms, to trap them in large quantities in the Penning trap and manipulate them together with positrons.

The idea of sympathetically cooling positrons with laser-cooled Be^+ to temperatures $\leq$ 4K was proposed by *Wineland, Weimer & Bollinger* in 1993 [125]. They suggested that these cold positrons could be used for antihydrogen production, even before the first antihydrogen was formed. A pioneering experiment of laser cooling positrons with Be^+ in a Penning trap was performed by *Jelenković et al.* at NIST in 2002 [126,127]. They used the simplest method of Doppler laser cooling. They have cooled roughly 1700 positrons of density $\geq 4 \cdot 10^9$ cm^{-1} to temperatures of at least 5 K using $1.3 \cdot 10^5$ Be^+. They suggested that this technique could be used to accumulate large amounts of cold positrons ($\sim 10^9$) in room temperature traps.

The feasibility of using this technique to form antihydrogen in ALPHA was theoretically studied by *N. Madsen, F. Robicheaux and S. Jonsell* [128]. It is required to cool down $2 \cdot 10^6$ positrons, which are typically used in a mixing process with antiprotons to form antihydrogen. A sympathetic cooling of this number of positrons was theoretically studied with laser cooled Be^+ and Mg^+ and beryllium, resulting in a more promising route. Later, Muhammed Sameed and Daniel Maxwell studied a method of pulsed laser ablation of beryllium ions from the metal target to introduce Be^+ into ALPHA-2 without unnecessary contamination of the ultrahigh vacuum system [129,130]. After successful Be^+ ablation tests, the beryllium source was installed in the ALPHA-2 apparatus and the work has been continued by Daniel Maxwell, Jack McCauley Jones and myself. We have demonstrated sympathetic cooling of $2.6 \cdot 10^6$ positrons with $3 \cdot 10^5$ Be^+ to temperatures below 7 K [1, 131]. We have used a very similar scheme as group at NIST with a major difference, that in ALPHA Penning traps we cannot use a perpendicular laser beam for efficient laser cooling of beryllium ions nor rotating wall technique at the location of ion cooling, so the preparation time of beryllium ion plasma was lengthy, ~ 10 min which is longer than our usual positrons & antiprotons mixing cycle for the antihydrogen formation. Additionally, due to significant large radial extent of beryllium ion plasma and difficulties to compress it, standard number of positrons used for antihydrogen synthesis could not be successfully cooled with magnetic Ioffe-Pritchard trap energised as required for antihydrogen accumulation because of the heating caused by radially homogeneous magnetic field generated by the octupole magnet. We have successfully managed to sympathetically cool smaller numbers of positrons $\sim 10^5$, using similar numbers of Be^+, with the octupole magnet energised to the standard magnetic field used for antihydrogen trapping, proving that, in principle, it is possible for small enough plasmas. To combat the problem of radial size of beryllium ion plasma, we have upgraded the hardware of the laser system to introduce an additional cooling laser beam, well aligned *on-axis* of the Penning trap, to allow simultaneous laser cooling and rotating wall compression of Be^+. We have also obtained a new 313 nm laser of significantly higher power (800 mW) to efficiently improve the cooling and shorten the preparation time for beryllium ions. Implementing those technical upgrades was the main part of my Ph.D. work in the ALPHA experiment. In the meantime, I have been pursuing the idea of using the laser-cooled Be^+ for characterising magnetic fields in the ALPHA-2 trap, which will be introduced in the next section.

1.3.3 Cold Be^+ for magnetometry in ALPHA traps

We propose an alternative method to measure the magnetic fields inside ALPHA's Penning traps using beryllium ions. The idea is to measure the electron spin-flip transition frequency in the $2S_{1/2}$ ground state of Be^+, which depends on the magnetic fields strength. The $|\uparrow\rangle \rightarrow |\downarrow\rangle$ transition is induced by microwave radiation, which opens an interesting possibility of using Be^+ to characterise the microwave intensity distribution in the ALPHA-2 trap. The strength of the electric field component of the microwaves can be extracted by measurements of the cyclotron frequency of electrons, but there was no method so far to characterise the magnetic field component of the microwaves propagating inside the ALPHA-2 trap. The spin-flip of the electron in Be^+ is a magnetic dipole transition, which means that it is sensitive to the amplitude of the oscillating magnetic field. Information about the strength of the magnetic component of the microwaves would benefit the antihydrogen hyperfine structure measurements. The hyperfine transition in the antihydrogen is a positron-spin flip, which is also a magnetic dipole transition that depends on the amplitude of the oscillating magnetic field in the same way as the electron spin-flip in the beryllium ion does.

This measurement was inspired by the experiment performed by *Shiga, Itano & Bollinger* at NIST with laser-cooled $^9Be^+$ in a Penning trap to characterise the hyperfine energy level structure of those ions [132]. The basic idea is to look at the fluorescence of the trapped $^9Be^+$ (fluorescence is induced by the 313 nm cooling laser), while sending microwave pulses of changing frequency. A sudden drop in the fluorescence signal level would indicate that the electron spin-flip transition has occurred and the size of the drop should correlate with the amount of beryllium ions that changed the electron spin state.

In this work I will present the results of our progress towards *beryllium magnetometry* in the ALPHA experiment. We have demonstrated the spin-flip of electrons in $^9Be^+$ induced by microwave absorption within the ALPHA-2 trap. Based on this we have measured spectra of the electron spin-flip transition in around 1 T magnetic field. The resonance frequency value of the electron spin-flip transition can be used to calculate the magnetic field strength experienced by beryllium ions with precision up to around 5 μT. This is still a two orders of magnitude worse performance than the current precision of the *ECR* measurement, but the electron spin-flip measurement, presented in this thesis, was a proof of principle experiment performed in only 3 days. Therefore, there is plenty of room for improvement.

The experiment performed by *Shiga et al.* used a Rabi method, in which the duration of the microwave pulse was chosen such that it gives the highest possible spin-flip transition probability, called a π-pulse (the physics of Rabi cycles and π-pulse will be explained in Section 3.1.2). We used microwave pulses that were tens to hundreds milliseconds long, so it is expected that the beryllium ions undergo many cycles between the *spin-up* and *spin-down* states and those and those oscillations are no longer coherent with each other, which would cause a broadening of the electron spin-flip transition linewidth. Additionally, the beryllium ions samples, not the parameters of the cooling and probing laser beam were not optimised and systematic errors were not studied.

Chapter 2

Trapping ions and plasmas

2.1 Ion trapping

In many research applications, like e.g. quantum computing, mass spectrometry, precision measurements of fundamental constants, it is essential to isolate ions from the bulk materials to remove interactions that are in the domain of solid state physics and access the properties of single particles. It is beneficial not only to produce isolated ions but also to be able to store them in order to increase the interaction time for the processes studied. Since we speak of charged particles, we can benefit from their interaction with electric fields to confine them. We want to find a shape of the electric potential that can provide stable confinement of the charged particle motion within a closed volume of space. The *Earnshaw theorem* tells us that only electrostatic potentials cannot be used to trap ions, because any potential U must satisfy the *Laplace equation*

$$\nabla^2 U = 0 \tag{2.1.1}$$

which means that there are no three-dimensional minimum or maximum of electrostatic potential. Although the electrostatic potential U can have a location with a saddle point. If the electric potential around that saddle point becomes varied over time in such a way that the electric potential at that point does not change in value and the high potential around the saddle point *rotates* fast enough around that point (at the radio-wave frequencies), the ion can see a stable minimum of the effective potential. In this way by using fast oscillating electric field we can trap charged particles. The device operating on this principle is called a Paul trap or radiofrequency trap [133].

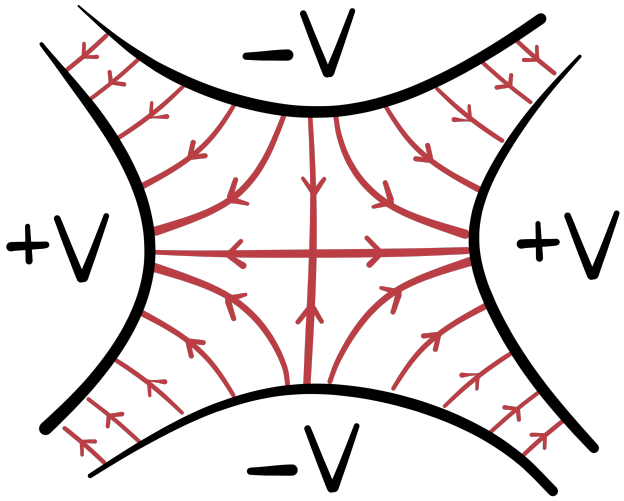

Figure 2.1 – Schematic diagram of a shape of quadrupolar potential. In the Penning trap the quadrupolar potential has a cylindrical symmetry around the z axis, meaning that the electrostatic potential has this shape in any r-z plane, where r is an axis lying in the radial plane (x-y).

If we want to use static electric fields, there is another way to walk around the *Earnshaw theorem*. We can add a magnetic field on top of our electrostatic potential, in a special configuration, to provide a stable three-dimensional confinement. The ion trap that uses a combination of static electric and magnetic fields is called the Penning trap [1], even though it was developed by Hans Georg Dehmelt in 1960s [134].

2.1.1 Penning Trap

In this section, the mechanism of trapping charged particles by combined static electric and magnetic fields will be discussed. Presence of the magnetic field introduces a circular motion of the ions, which is used to confine the ion's motion in the direction(s) of the de-confining electric potential, which in total provides a stable 3D confinement. Let us introduce a uniform magnetic field along the z-axis. A charged particle moving in the direction $\bar{v}$, which is perpendicular to the magnetic field direction $\bar{B}$ would experience a Lorentz force, perpendicular to the direction of the $\bar{B}$ and to the direction of motion $\bar{v}$. This results in a circular motion of the particle that is called *cyclotron motion*.

[1] The name Penning trap comes from the fact that the original device built by Dehmelt was inspired by a geometry of a vacuum gauge designed by Frans Michel Penning. Dehmelt did not get enough credit for his invention, and the device remained referred to as Penning trap. At least in 1989 Dehmelt received a Nobel Prize for his work on trapping ions

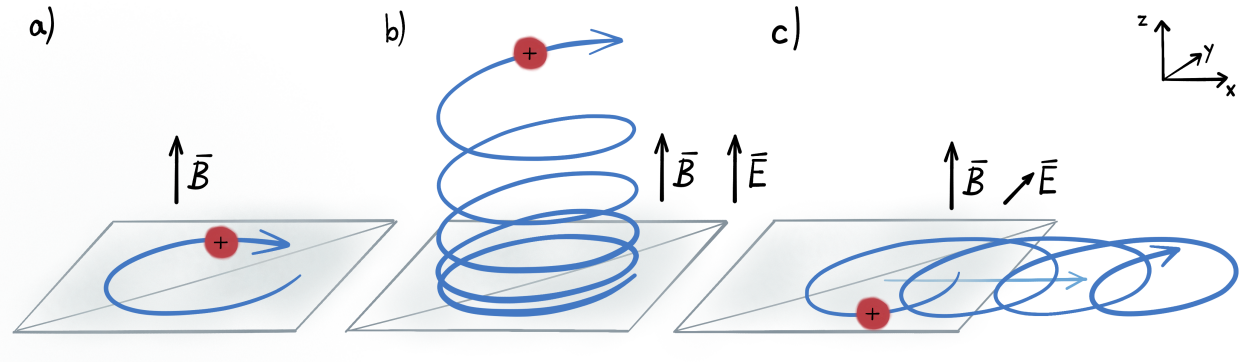

Figure 2.2 – The direction of $E \times B$ motion depending on the orientation of the electric field $\bar{E}$ in respect to the magnetic field $\bar{B}$. a) $\bar{E} = 0$, b) $\bar{E} \parallel \bar{B}$ and c) $\bar{E} \perp \bar{B}$. Figure adapted from [135].

If the particle is placed only in the constant and uniform magnetic field ($\bar{v} \perp \bar{B}$) without an electric field present (situation in Figure 2.2.a), the cyclotron motion of the ion will form a closed orbit. Adding a constant electric field $\bar{E}$ introduces a drift of the centre of cyclotron motion, and the ion trajectory no longer follows a closed orbit. The direction in which the centre of motion drifts depends on the alignment of the electric field vector with respect to the magnetic field. If the electrostatic field is parallel to the magnetostatic field $\bar{E} \parallel \bar{B}$ (as in Figure 2.2.b), the drift of the centre of motion occurs in the direction parallel to both of the fields. In the situation when the electrostatic field is perpendicular to the magnetostatic field $\bar{E} \perp \bar{B}$, the centre of cyclotron motion will drift in the direction perpendicular to both of the fields (Figure 2.2.c), which is called a *E×B drift*.

We confine the motion of the charged particle in the direction perpendicular to the magnetic field $\bar{B}$ (projection on the *x*-*y* plane in Fig. 2.2) in the first and second scenarios, but there is no stable confinement for the particle in the direction out of that plane (*z*-direction). In the case of the magnetic field only, we do not have any restoring force in the direction perpendicular to the *x*-*y* plane, so any distortion of the cyclotron motion that gives an ion additional energy in the *z* direction would lead to loss of the ion. For the parallel fields $\bar{E} \parallel \bar{B}$ configuration, if the electric field is uniform, we already see that there is a force acting on the ion in the direction out of the plane. If we wanted to limit the motion in the direction of $\bar{E}$, we would have to vary the strength of the field to create a minimum of the electrostatic potential in the *z*-direction. But we already know from *Laplace equation* that the existence of the potential minimum in one direction at a given point in space automatically enforces this point to be a potential maximum for at least one or even both perpendicular directions.

This means that by creating a minimum of electrostatic potential along the direction parallel to the magnetic field $\bar{E} \parallel \bar{B}$, we must introduce the maximum in the other direction(s) and that means that we have just introduced a vector of electric field in the direction perpendicular to the magnetic field $\bar{E} \perp \bar{B}$. In consequence we need to consider the $E{\times}B$ motion nevertheless.

The $E{\times}B$ *drift* shifts the centre of the cyclotron orbit in the direction that is a cross product of the $\bar{E}$ and $\bar{B}$ fields vectors. For constant $\bar{E}$ and $\bar{B}$ the $E{\times}B$ *drift* velocity is constant, but if any of the fields are changing, the $E{\times}B$ *drift* will experience a velocity change. Now consider an electric field $\bar{E}(x, y)$ with a radial symmetry such that an electric force acting on the test ion will always point outward from the same point on the x-y plane (we can assign the coordinates $x = 0, y = 0$ to this point). This means that the electric field vector $\bar{E}$ points inwards to the central point for a negatively charged particle and $\bar{E}$ outwards for a positively charged particle. Electrostatic potentials of this type can be realised by electrodes with radial symmetry (e.g. inside a cylindrical electrode). As the electric force vector is spinning around, the direction of drift velocity of the centre of cyclotron motion ($E{\times}B$ drift) changes to always point in the direction perpendicular to both $\bar{E}$ and $\bar{B}$. The centre of the cyclotron motion will move on a closed circular orbit (called the *magnetron orbit*), with the acceleration vector always pointing towards the $(0, 0)$ point and the drift velocity vector $\bar{v}$ tangent to the orbit. In this way we confined the particle's motion in the x-y plane, although the range of motion on that plane is bigger than initially considered pure cyclotron motion. The $E{\times}B$ drift is called *magnetron motion* in distinction from the cyclotron motion, which is the result coming purely from the magnetic field. In the presence of $E{\times}B$ drift, the *cyclotron orbit* is modified and the radius of cyclotron motion r_c increases and decreases periodically, as shown on Figure 2.4. This is called *modified cyclotron motion*. It happens because we have defined the electric force to point outwards from the centre of the magnetron orbit, so the point of coordinates $(x, y) = (0, 0)$, and this means that the direction of motion of the ion changes between being aligned and antialigned with the electric field $\bar{E}$ during a single period of cyclotron motion, and this causes the ion to periodically accelerate and slow down. This changes the magnitude of the velocity vector perpendicular to the magnetic field $v_\perp$ and is directly related to the cyclotron radius:

$$r_c = \frac{m v_\perp}{|q| B} \tag{2.1.2}$$

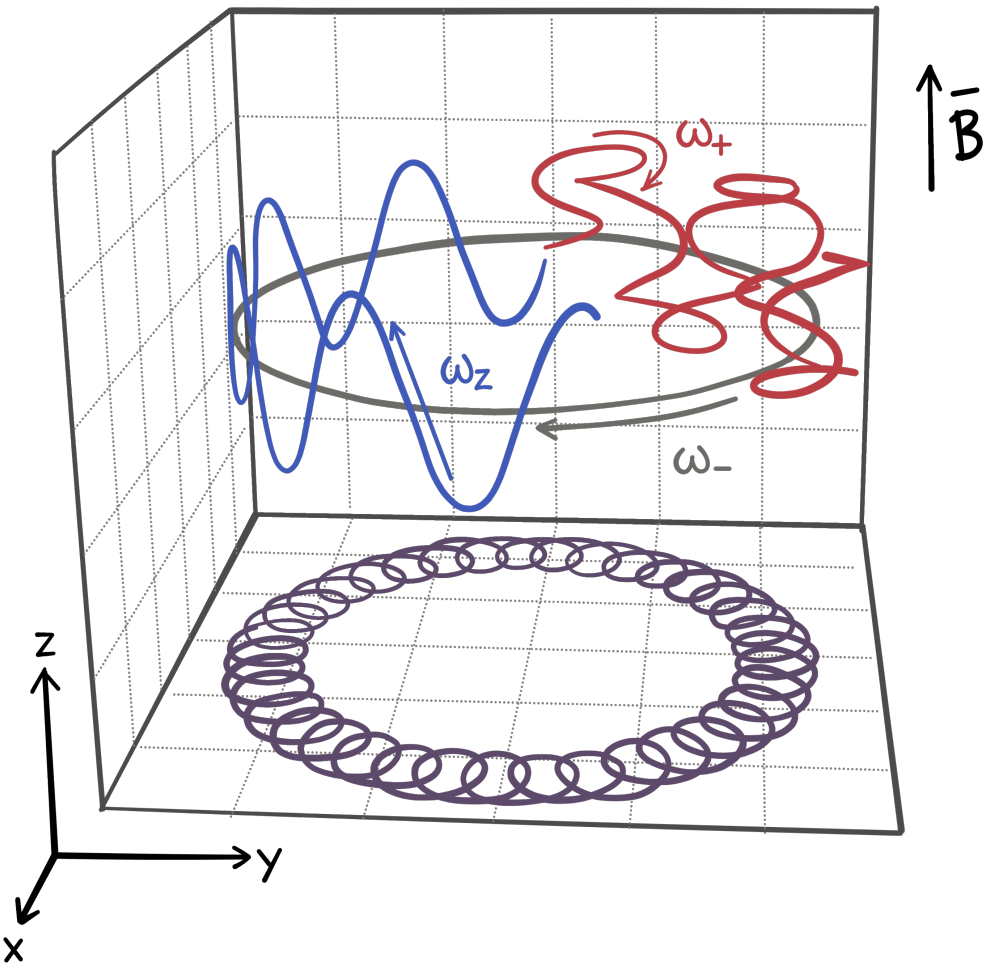

Figure 2.3 – Motion of the charged particle in the Penning trap. The axial motion (blue line) occurring in the z direction has a frequency ω_z. The projection on the x-y plane (dark violet line) is the radial motion of the ion, which is the result of combined cyclotron and magnetron motion with frequencies ω_c' and ω_m respectively (magnetron motion is represented by grey line and the fragment of a full combined motion in red). Figure was adapted from [136].

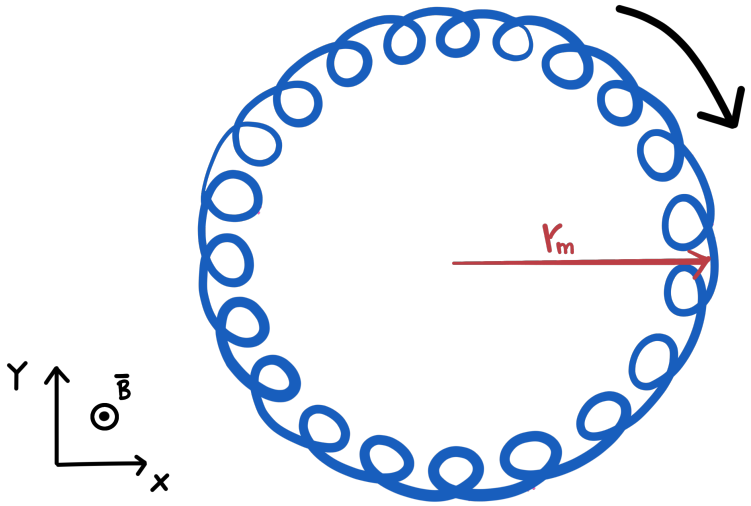

Figure 2.4 – Motion of a charged particle in the Penning trap in the radial direction is a combination of cyclotron motion and $E \times B$ drift.

A combined magnetron motion and modified cyclotron motion are referred to as a *radial motion*. So far we described a method for trapping ions in the x and y direction, but we are still missing the last ingredient to prevent the ion from escaping in the z direction. This can be solved by introducing the electrostatic potential minimum on the z-axis to obtain a confining potential. This can be done since the electrostatic potential in the x and y directions is deconfining already (without the B-field, charged particles would be repelled away from the central point). This configuration of electric potential is called a quadrupole potential. The ion will be bouncing back and forth inside the potential well along the z direction, which we call an *axial motion*. The combined radial and axial motions in the trap are shown in Figure 2.3 (the red line represents a fragment of the combined motion trajectory).

2.1.2 Charged particle motion and energy in a Penning trap

Charged particles confined in the Penning trap are moving on closed trajectories that are a superposition of previously discussed axial, cyclotron and magnetron motions. Each of these motions is periodic and it could be characterised by a characteristic frequency and energy [137,138]. Let us simplify the description of motion by using the harmonic electrostatic potential ϕ_E, represented in a cylindrical coordinate system (r, z):

$$\phi_E(r, z) = -U_r r^2 + U_z z^2 \tag{2.1.3}$$

where constants U_z and U_r defining the depth of the potentials in axial and radial direction.

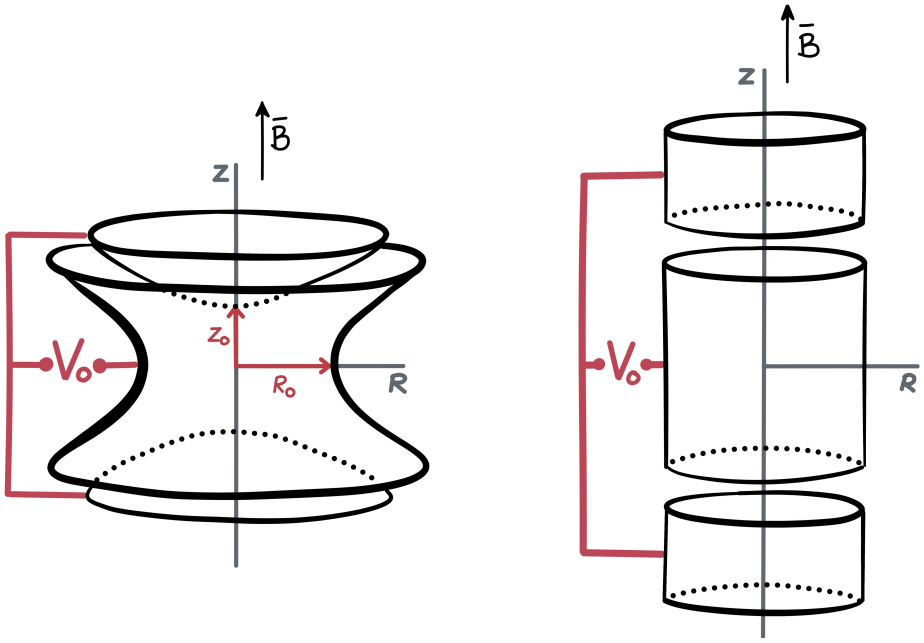

Figure 2.5 – Schematic of a Penning trap. On the left there is an original design with electrodes in shapes of the equipotential lines. On the right cylindrical electrodes used in the Penning-Malmberg trap, which is the most common modern design. Figure was adapted from [136].

We define harmonic potentials because we want to use the description of harmonic oscillator motion. The potential in the axial direction is confining (potential energy is increasing with increasing distance away from central location) and potential in the radial direction is deconfining (potential energy decreasing with increasing radial position). In the absence of magnetic field there is no $E \times B$ force and the ion in the central point $r = 0$ is in an unstable equilibrium and if it happens to be in any other position $r \neq 0$ it would be repelled radially outwards (in practice that means the ion would be attracted towards the electrodes walls). This means that the magnetron motion is unstable and it requires strong magnetic fields to overcome the deconfining electrostatic potential (usually on the order of $\geq 1T$). Potentials in the radial and axial directions are defined to generate a quadrupolar electrostatic potential (symmetric equipotential lines in the (z, r) plane, the quadrupolar field has cylindrical symmetry), which is the case if the condition $U_z/2 = U_r$ is satisfied. The classic Penning trap is built by electrodes shaped as hyperboloid of revolution (left diagram in Figure 2.5), which surfaces are the equipotential lines of the quadratic potential (of the type as in Eq. 2.1.3), which gives a condition

$$2z^2 - r^2 = const \tag{2.1.4}$$

Classical Penning trap consist a ring electrode in the shape defined by the equation:

$$2z^2 - r^2 = -r_0^2 \tag{2.1.5}$$

placed in the middle and two end electrodes defined as:

$$2z^2 - r^2 = 2z_0^2 \tag{2.1.6}$$

The potential generated by ideal [2] Penning trap has a quadratic form:

$$\phi_E(r, z) = V_0(2z^2 - r^2)/(r_0^2 + 2z_0^2) \tag{2.1.7}$$

where r_0 and z_0 are the distances of electrodes from the central position $(r, z) = (0, 0)$ and V_0 is the voltage applied between the ring electrode and each of two endcaps. These electrodes are placed in a uniform magnetic field along the z-axis

$$\bar{B} = B_0\hat{z} \tag{2.1.8}$$

The electric force is the only restoring force acting in the axial direction, so this motion is a simple harmonic oscillator, described by a single frequency ω_z, which is independent of the amplitude of the oscillation (it is defined directly by the shape and strength of the electric potential).

$$eV_0 = \frac{m\omega_z^2}{2}(r_0^2 + 2z_0^2) \tag{2.1.9}$$

Axial frequency:

$$\omega_z = \sqrt{\frac{4eV_0}{m(r_0^2 + 2z_0^2)}} \tag{2.1.10}$$

The equation of motion in axial direction for single ion in a Penning trap:

$$\ddot{z} + \omega_z^2 z = 0 \tag{2.1.11}$$

The radial motion is determined by the cyclotron motion introduced by the magnetic field $\bar{B}$. The frequency of that motion is called *cyclotron frequency* and is proportional to the strength of the magnetic field and the charge-to-mass ratio of the particle.

[2] To be more precise, the ideal quadratic potential would be generated by electrodes are placed infinitely far away from the trap centre and this geometry gives approximately ideal quadratic potential.

Cyclotron frequency:

$$\omega_c = \frac{qB_0}{m} \tag{2.1.12}$$

It is convenient to represent the motion in the radial direction as a motion in the complex plane, by writing equation for complex variable $u = x + iy$:

$$\ddot{u} - i\omega_c\dot{u} - \frac{\omega_z^2}{2}u = 0 \tag{2.1.13}$$

which corresponds to equation of motion in x and y respectively:

$$\ddot{x} - \omega_c\dot{y} - \frac{\omega_z^2}{2}x = 0 \tag{2.1.14}$$

$$\ddot{y} + \omega_c\dot{x} - \frac{\omega_z^2}{2}y = 0 \tag{2.1.15}$$

The solution of Equation 2.1.13 must have the form of

$$u = e^{-i\omega t} \tag{2.1.16}$$

which transforms this equation to a quadratic equation of variable ω:

$$\omega^2 - \omega_c\omega + \frac{1}{2}\omega_z^2 = 0 \tag{2.1.17}$$

Roots of Equation 2.1.17 correspond to two frequencies characterising the radial motion. The higher frequency ω_+ is the modified cyclotron frequency (also denoted as ω_c') and the lower frequency is the magnetron frequency ω_+ (also referred to as ω_m).

Modified cyclotron frequency:

$$\omega_+ = \omega_c/2 + \sqrt{(\omega_c/2)^2 - \omega_z^2/2} \tag{2.1.18}$$

Magnetron frequency:

$$\omega_- = \omega_c/2 - \sqrt{(\omega_c/2)^2 - \omega_z^2/2} \tag{2.1.19}$$

We put condition for frequencies ω_+, ω_- to be positive and from that we get the *trapping condition*:

$$\omega_c^2 - 2\omega_z^2 > 0 \tag{2.1.20}$$

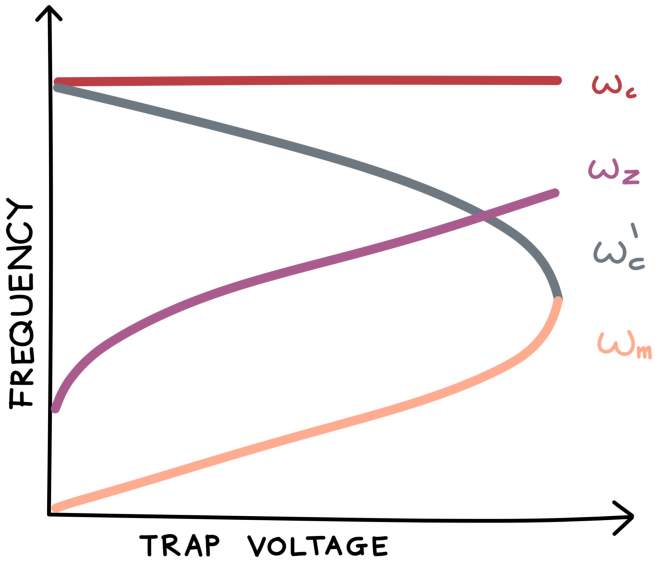

Figure 2.6 – Frequencies of motion in a Penning trap as a function of voltage V_0 applied between electrode.

Stable trapping of charged particles also requires the condition that the modified cyclotron frequency is greater than the magnetron frequency ($\omega_c' \gg \omega_m$). The standard operation of a Penning trap should fulfil the hierarchy of frequencies:

$$\omega_c \gtrsim \omega_c' \gg \omega_z \gg \omega_m \tag{2.1.21}$$

The true cyclotron frequency ω_c is independent of the trapping voltage, but all other frequencies depend on V_0. Magnetron and axial frequency increase with increasing trapping voltage and modified cyclotron frequency decreases (see Figure 2.6).

From Equations 2.1.18 and 2.1.19 we see that the sum of magnetron and modified cyclotron frequency are always equal to true cyclotron frequency:

$$\omega_c = \omega_c' + \omega_m \tag{2.1.22}$$

According to Brown-Gabrielse invariance theorem [139] the sum of squares of modified cyclotron frequency, axial frequency and magnetron frequency is equal to square of the true cyclotron frequency:

$$\omega_c^2 = \omega_c'^2 + \omega_z^2 + \omega_m^2 \tag{2.1.23}$$

This relation holds even if the trap electrodes are slightly misaligned in respect to the B-field direction or field is not ideally quadratic. We can measure the true cyclotron frequency in experiments. This makes the Penning trap the best tool for high precision mass comparison and g-factor measurements of various nuclei [140] and fundamental particles [19–22].

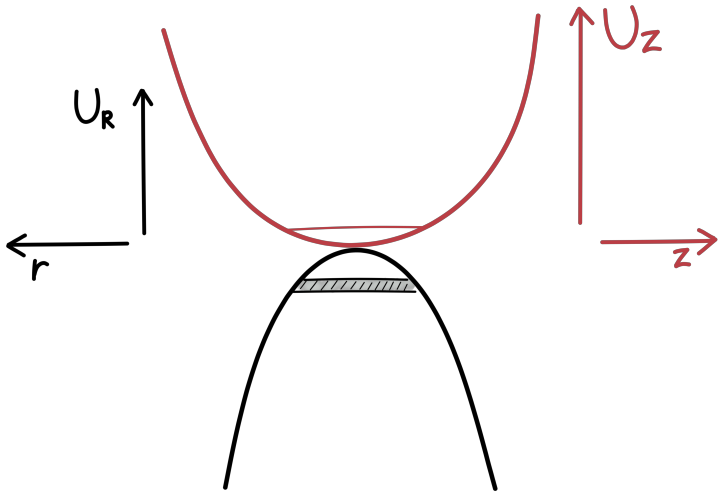

Figure 2.7 – The potential of electric field experienced by particle is confining in the axial direction U_z, but deconfining in the radial direction U_R. The shaded area corresponds to the range of radial potentials experienced by particle moving with a combined cyclotron and magnetron motion.

The important thing to discuss is the energies associated with each of the motions. We already said that the potential energy of the axial motion increases with increasing distance z away from the trap centre, while for the modified cyclotron and magnetron the potential energy decreases with increasing radial distance r. The kinetic energy of any type of motion is always positive and increases with increasing amplitude of the oscillation. Total energies are the sums of the corresponding potential energy and kinetic energy. The potential energies are defined to be zero at centre of the trap and when the ion is motionless. The kinetic energy of the axial motion is equal to the potential energy of the axial motion (equipartition of energy), which is not the case for the two radial motions.

Total energy of the axial motion:

$$E_z^{\,tot} = \frac{mz^2\omega_z^2}{2} + \frac{mv_z^2}{2} = \frac{mz_0^2\omega_z^2}{2} \tag{2.1.24}$$

Total energy of the modified cyclotron motion:

$$E_{c'}^{\,tot} = -\frac{mr_c^2\omega_z^2}{4} + \frac{mv_c^2}{2} = \frac{mr_c^2\omega_c'(\omega_c' - \omega_m)}{2} \tag{2.1.25}$$

Total energy of the magnetron motion:

$$E_m^{\,tot} = -\frac{mr_m^2\omega_z^2}{4} + \frac{mv_m^2}{2} = -\frac{mr_m^2\omega_c'(\omega_c' - \omega_m)}{2} \tag{2.1.26}$$

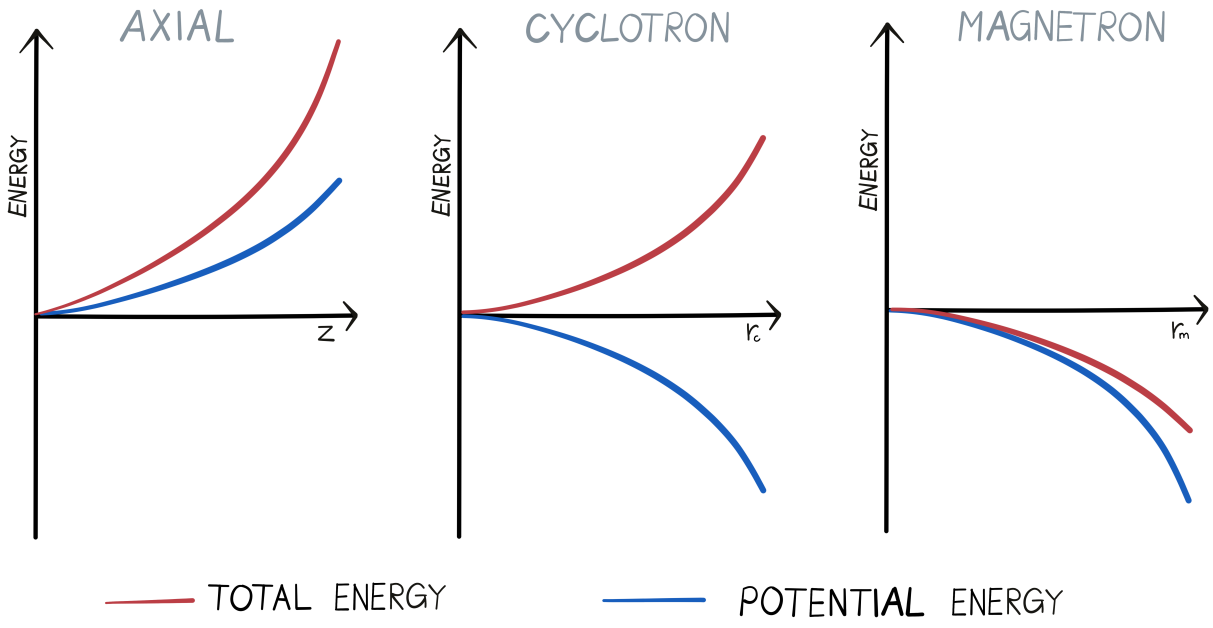

Figure 2.8 – Penning trap energies as a function of a distance away from the trap centre for the axial, cyclotron and magnetron motion.

The relationships between potential energy and total energy for axial, (modified) cyclotron and magnetron frequency are shown on Figure 2.8. Radial motions see decreasing potentials for increased radial positions, which means that removing energy from the magnetron motion causes an increase in the magnetron radius r_m, so the volume within which the charged particle moves increases. This will have a practical consequences for laser cooling in the Penning trap, because reducing the total energy of a magnetron motion increases the ion orbit and in the application of laser cooling of ion plasma it would increase the radius of the plasma. People quite often say *cooling magnetron motion* when they mean decreasing the radius r_m, which can be confusing. The name *"cooling"* refers there to decreasing the kinetic energy of the ion, which causes reduction of the magnetron radius r_m (see example in Ref. [143]).

All considerations so far have been concerned with the trapping of single charged particles in the Penning trap. Adding any more ions makes the motion more complicated, because we need to consider the Coulomb interactions between ions as well. Especially if we want to trap large numbers of ions and plasmas, we will look at the collective behaviour of all the ions ensemble in the next Section 2.2.

2.1.3 Penning-Malmberg trap

The ideal Penning trap is made with electrodes shaped as equipotential surfaces of the harmonic well (left diagram in Figure 2.5). The voltage V_0 is applied to the middle ring electrode and the two end caps are grounded. This configuration allows for the trapping of single ions in a well defined volume of space, but it does not allow for much manipulation of the ions (the depth of the quadrupole well can be manipulated by the applied voltage V_0, but we cannot change the shape of the axial or radial well independently, neither ions can be shifted from one location to another). Moreover, in the traditional Penning trap ions of the opposite charge, like antiprotons and positrons, cannot be trapped jointly, and this aspect is crucial for the low energy antihydrogen production. For this reason, plasma physicist John Malmberg developed a new design of a Penning trap, which consists of a stack of simple cylindrical electrodes [144, 145] (see right drawing on Figure 2.5). The inner cylinder acts as the ring electrode, and two neighbouring cylinders are grounded. Applying the same voltage V_0 creates an anharmonic potential well, but for deep wells the bottom of the potential well can be approximated as a harmonic potential [3]. In fact, many cylindrical electrodes can be stacked together, which makes it possible to introduce multiple neighbouring wells of varied depth, length and also opposite polarity. Penning-Malmberg trap allows for flexible manipulation of the axial well depth and length, which allows the length of the plasma to expand or squeeze very rapidly, and it can also accommodate multiple species of varied mass but the same charge sign in the same potential well, which is necessary for studying multiple-species plasma. While the cyclotron and axial motions are stable oscillations around a minimum of potential energy, the magnetron motion is an oscillation around a maximum of potential energy. The total energy of the magnetron motion is negative, which implies that the magnetron motion is unstable. This makes the magnetron motion sensitive to any perturbations, which could cause the particle to drift away from the centre of the trapping field. This could be caused by, for example, collision of the trapped particle with another atom or molecule of a residual gas in the trap. For this reason, high or even ultra-high vacuum conditions are required within the Penning trap. Additionally, precision measurements in Penning traps often require operating in cryogenic conditions (≤ 4 K) to minimise the heating of trapped particles due to the thermal radiation emitted by the interior of the trap.

[3] This is no longer true for trapped plasma, if the potential generated by charged particles significantly shifts the value of ϕ_E.

Penning-Malmberg traps have been realised to be the best approach to confine the antimatter particles, since they allow to suspend large quantities of antiprotons and positrons in vacuum and manipulate the properties of trapped charged antimatter clouds to change their size, density and temperature. Long term storage of antimatter plasma allowed production of antihydrogen atoms in large quantities [30].

2.2 Plasma in Penning trap

Penning-Malmberg trap is a great tool to confine many charged particles ($> 10^6$ particles), which means that storage of non-neutral plasma is possible. In this section, the physics of non-neutral plasma trapped in the Penning trap will be discussed. Fundamentals necessary to understand operations on charged particles in the ALPHA Experiment will be presented here, based mostly on work done by the plasma group at University of California, San Diego (UCSD) [144–149]. A detailed review on plasma manipulation techniques in the context of positrons was written by *Danielson, Dubin, Greaves and Surko* [150].

2.2.1 Plasma definition

Plasma is an ensemble of many ions with a density high enough that it produces non-negligible electric and/or magnetic fields, which affect the motion of individual ions. Inside the plasma, the ions are *shielded* from the external electrostatic fields. Electrostatic fields are still present on the surface of the plasma, but they decrease exponentially (by a factor $1 - 1/e$) on the distance Λ_D, called the Debye length. The Debye length depends on the density of the plasma n_0, charge of the ion species q (in our application we always consider singly charged ions, so we will use the charge of the electron) and plasma temperature T:

$$\lambda_D = \sqrt{\frac{\epsilon_0 k_B T}{n_0 q^2}} \tag{2.2.1}$$

Beneath the skin depth on the order of few Debye length the plasma is fully screened from the external electric fields. For a collection of ions to show plasma properties, its physical size L must be significantly greater than the Debye length:

$$\lambda_D \ll L \tag{2.2.2}$$

Additionally the density cannot change too fast on the scale of the mean inter-particle spacing $a = n_0^{-1/3}$, which gives condition:

$$\lambda_D \gg \frac{1}{\sqrt[3]{n_0}} \tag{2.2.3}$$

A large enough size of the plasma shields the inner ions from the static electric fields. Shielding occurs because ions reorganise to provide sufficient enough density to shield the external field. If the oscillation of the electric fields occurs faster than the ions could rearrange, then the collection of ions does not exhibit plasma behaviour. The time at which plasma responds to changing electric field τ_p is the inverse of the so-called *plasma frequency*:

$$\omega_p = \sqrt{\frac{q^2 n_0}{\epsilon_0 m}} \tag{2.2.4}$$

which depends on the ions species charge q, mass m and plasma equilibrium density n_0. Usually plasma is the ionised atomic gas, so it contains electrons and ions. In this context, the plasma oscillation at ω_p will refer to oscillation of electron density and the mass in the Equation 2.2.4 would be an effective mass of the electron m^*. The phenomenon is known as Langmuir waves [151].

Plasmas are usually created from very dense and hot gases by ionising the atoms. Most of the plasmas occurring in nature (ionised gases in interstellar space, lightnings, auroras, stars) are the mixtures of ions and electrons with zero net electric charge and this is referred as a *neutral plasma*. Neutral plasmas can also be created by heating up dense gas, e.g. neon lights in glass bulbs or in fusion reactors. Another type of plasma contains only particles of the same charge (only electrons or ions), and this is called a *non-neutral plasma*.

Non-neutral plasmas experience similar collective effects as neutral plasma: Debye shielding of electric fields and plasma waves [144]. Non-neutral plasma has a few advantages over neutral plasma:

- it is easier to confine the plasma with a single sign of charge that neutral plasma, since electron-ion collisions increase the rate of radial expansion [147, 148];
- longer storage time of many ions of the same electric charge are available thanks to Penning-Malmberg traps, potential wells can be made deeper by increasing the applied voltage and this allows for confinement of high number of ions;
- longer confinement time allows the plasma to evolve to the thermal equilibrium [149];

- non-neutral plasma can be stored in the state of thermal equilibrium, which is easier to control the plasma properties (size and density) and diagnose the temperature;
- non-neutral plasmas can achieve lower temperatures than neutral plasmas (even cryogenic temperatures), because in neutral plasmas electrons start to recombine with ions while cooling [147];

2.2.2 Non-neutral plasma in Penning-Malmberg trap

Instead of considering a motion of each individual ion in a trap, we will describe a shared behaviour of all the ions in the non-neutral plasma. Ions in the plasma exhibit various collective effects like plasma heating, instabilities, waves and oscillatory motions that are not present in a single-particle regime. These plasma phenomena will turn out to be crucial in diagnostics and preparation of charged particles (electrons, positrons, antiprotons and single charge ions) for the antihydrogen experiments.

Space charge in plasma

Having a plasma in the Penning trap causes each individual charged particle to see the electric field generated by other ions. The field generated by the plasma itself is called *space charge* (or *self-potential*) ϕ_P and adds an offset to the electric trapping potential generated by electrodes ϕ_T (denoted as ϕ_E in Section 2.1.2) [4]. There is also an additional term coming from the potential induced on electrodes due to the presence of trapped ions $\phi_{ind}(r,z)$, but this term can be neglected if the dimensions of the trap are significantly greater than the size of the plasma [147]. The ions inside the plasma see an effective electric potential:

$$\phi(r,z) = \phi_T(r,z) + \phi_P(r,z) + \phi_{ind}(r,z) \approx \phi_T(r,z) + \phi_P(r,z) \tag{2.2.5}$$

The trapping potentials ϕ_T used in ALPHA Experiment are usually tens of volts (up to 140V in the *normal* traps: *Recatching Trap* and *Positron catching* and 100V in the thin electrodes of the *Atom Trap*, while the space charge of typical plasmas of singly-charged ions, that we operate with, varies from sub-electronvolts up to a few electronvolts (eV) for small plasmas, used for antihydrogen synthesis, up to tens of eV for the initial plasmas trapped in ALPHA

[4] The trapping potential generated by electrode are denoted in some previous ALPHA theses, e.g. [152], as potentials in vacuum ϕ_{vac} to distinguish them from potential experienced by particle inside the plasma

Penning traps ($\bar{p}$ from Antiproton Decelerator, e^+ transferred from the Positron Accumulator and e^- generated by *e-gun*, see Section 2.5 on particles sources in ALPHA experiment). For small plasmas in deep wells, ions are well confined and the potential experienced by each particle is mainly originating from the trapping potential, so usually we can safely use the approximation $\phi \approx \phi_T$. This is good if we manipulate only the particles [5], but we do not study the plasma properties in detail. In the case of large reservoirs of charged particles or if the exact value of the potential experience by particles is needed (to obtain precise values of ions numbers, plasma densities or motional frequencies), the space charge needs to be evaluated carefully. This type of evaluation is performed by solving the Poisson equation and requires readjusting the value of ϕ_P until the density profiles obtained from the measurements match the $n(r, z)$ profiles from Equation 2.2.17 (more about the plasma density measurements in Section 2.3.2).

Ions motion in the plasma

We want to discuss the motion of ions inside the plasma trapped in Penning-Malmberg trap. Penning-Malmberg trap has a cylindrical symmetry, so its cylindrical coordinate system (r, θ, z) will be the simplest way to describe the system. The non-neutral plasma is placed in the static axial magnetic field (Eq. 2.1.8). The vector potential of the magnetic field is:

$$\bar{A} = \hat{\theta} A_\theta(r) \tag{2.2.6}$$

where $A_\theta(r) = Br/2$. The potential of electrostatic field is described by Eq. 2.2.5. The Hamiltonian describing N charged particles (charge q and mass m), inside the plasma:

$$\mathcal{H}^N = \sum_{j=1}^{N} \frac{m}{2} v_j^2 + \sum_{j=1}^{N} e\phi\left(\bar{r}_j\right) = \sum_{j=1}^{N} \frac{m}{2}\left(\dot{r}_j^2 + (\dot{\theta}_j r_j)^2 + \dot{z}_j^2\right) + \sum_{j=1}^{N} e\Big(\phi_T\left(\bar{r}_j\right) + \phi_p\left(\bar{r}_j\right)\Big) \tag{2.2.7}$$

The canonical momenta of j^{th} ion moving in the Penning-Malmberg trap are

$$p_{r_j} = m\dot{r}_j \tag{2.2.8a}$$

$$p_{\theta_j} = mr_j^2\dot{\theta} + \frac{q}{c} A_\theta(r_j) r_j \tag{2.2.8b}$$

$$p_{z_j} = m\dot{z}_j \tag{2.2.8c}$$

[5] For example to just get the rough values for the potential well depth and shape, e.g. for the particles transport or to get number of ions in the sample correct to the order of magnitude

Total canonical angular momentum of all N particles

$$P_\theta \equiv \sum_{j=1}^{N} p_{\theta_j} = L \tag{2.2.9}$$

Substituting Equations 2.2.5, 2.2.8to the Hamiltonian in Equation 2.2.7 we get:

$$\mathcal{H}^N = \underbrace{\sum_{j=1}^{N}\left(\frac{p_{r_j}^2}{2m} + \frac{\left[p_{\theta_j} - \frac{q}{c}\frac{Br_j^2}{2}\right]^2}{2mr_j^2} + \frac{p_{z_j}^2}{2m}\right)}_{\text{kinetic energy}} + \underbrace{\sum_{j=1}^{N} e\phi_T\left(\bar{r}_j\right)}_{\text{trapping potential}} + \underbrace{\sum_{j=1}^{N} e\phi_p\left(\bar{r}_j\right)}_{\text{space-charge}} \tag{2.2.10}$$

This Hamiltonian represents total energy of N-particles in the Penning-Malmberg trap, that is a conserved quantity since Hamiltonian is invariant under time translations (Hamiltonian is time-independent). Hamiltonian is also invariant to rotations θ, which means that the total canonical angular momentum P_θ is conserved for ideal cylindrical symmetry. Of course real particle traps are not ideal and the imperfections in the manufacturing of the electrodes or magnet and misalignments of the fields do occur, which breaks the cylindrical symmetry and contributes to the torque force acting on the plasma. Additionally, ions collide with the background gas atoms, which give an excess energy for the ion to move away from the centre of the trap and eventually get lost from the trap. The trapping region is a high vacuum environment, in order to reduce collision rates with residual neutral atoms, such that practical trapping lifetimes of ions are achieved. Depending on the requirements of the study, the operational pressure is typically 10^{-8} mbar or below. Plasma in the Penning trap naturally expands, but the ions that remain confined inside the trap will eventually reach thermal equilibrium, and in this state they can remain confined for many hours.

Plasma in thermal equilibrium

Ions within the trapped plasma undergo a complex motion, which can be approximated as bounce motion in the axial direction, and *B-field* induced cyclotron motion and $E \times B$ drift in the radial direction. But the situation with plasma is more complicated, because ions collide and interact with each other so there is energy exchange between the ions. Ions do not move on stable orbits with constant frequencies (ω_z, ω_c', ω_m), but the velocities and trajectories of the ions are constantly changing. After some time τ_{eq} (usually on the order of seconds), the heat exchange between ions brings all of the plasma to the thermal equilibrium [149].

The collisions between particles act as a shear force in the rotational flow, making the average angular velocity of ions the same in all of the plasma, thus independent of the radial position r. The plasma spins around the z-axis of the trap with a frequency ω_R (technically the plasma rotation frequency is $-\omega_R$ for a positively charged particle [147, 148]), which can be viewed as a rigid rotor rotation. When ions are in thermal equilibrium, their velocities can be described by the Maxwell-Boltzmann distribution function, where a single particle energy H is offset by the kinetic energy related to plasma rotation $-\omega_R p_\theta$:

$$f(\bar{v}) = n_0 \left(\frac{m}{2\pi k_B T} \right)^{3/2} exp\left[-\frac{1}{k_B T} \left(H + \omega_R p_\theta \right) \right] \tag{2.2.11}$$

which means that in the frame of reference rotating with a frequency ω_R, ions behave just like a thermal gas of the temperature T. A peak density n_0, plasma rotation frequency ω_R and the temperature T in the thermal equilibrium depend on the total number of ions N, angular momentum P_θ and energy of the system $\mathcal{H}^N$ [147].

By putting the expressions of $H = mv^2/2 + q\phi(r,z)$ and $p_\theta = mv_\theta r + qBr^2/2c$ [6], into Equation 2.2.11 gives the expression that looks like a thermal velocity distribution superimposed on rigid-body rotation, which offsets the standard Maxwell-Boltzmann velocity distribution by the value of the average velocity of the ions in the Penning trap

$$\langle \bar{v} \rangle = -\omega_R r \hat{\theta} \tag{2.2.12}$$

giving a velocity distribution:

$$f(\bar{v}) = n(r,z) \left(\frac{m}{2\pi k_B T} \right)^{3/2} exp\left[-\frac{1}{2} m \frac{(\bar{v} + \omega_R r \hat{\theta})^2}{k_B T} \right] \tag{2.2.13}$$

Ions within the plasma see the effective trapping potential $\phi_{\text{eff}}(r,z)$

$$q\phi_{\text{eff}}(r,z) = \underbrace{q\phi(r,z)}_{\text{electric potential}} \quad \underbrace{+ \frac{1}{2} m\omega_R \omega_c r^2}_{\text{rotation induced potential}} \quad \underbrace{- \frac{1}{2} m\omega_R^2 r^2}_{\text{centrifugal potential}} \tag{2.2.14}$$

where last two terms provide a radial confinement, if the condition below is satisfied

$$0 < \omega_R/\omega_c < 1 \tag{2.2.15}$$

and the confinement due to rotation through magnetic field is stronger than deconfining centrifugal force.

[6] Equivalent to Equation 2.2.8b, where $v_\theta = \dot{\theta} r$

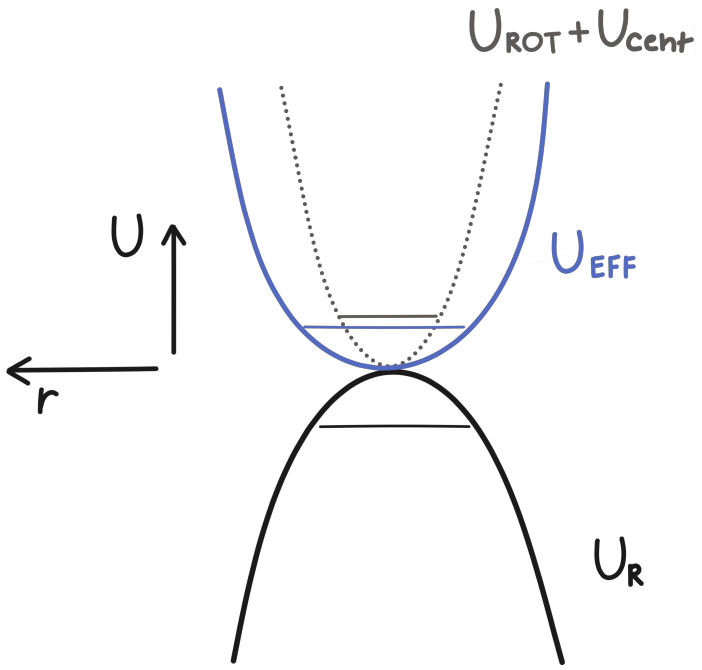

Figure 2.9 – Radial electric potential U_R generated by the cylindrical electrodes in red and rotation induced potential U_{ROT} with centrifugal potential U_{centr} in dashed grey. The resulting effective potential U_{eff} is represented in blue.

At low temperatures the density of ions inside the plasma is approximately constant and equal to n_0, but it drops exponentially at the edges of the plasma. The density change on the edge of the plasma is described by a plasma density profile:

$$n(r,z) = n_0 \ \exp\left[-\frac{q\phi(r,z) + \frac{1}{2}m\omega_R(\omega_c - \omega_R)r^2}{k_B T}\right] \tag{2.2.16}$$

where ω_c is the same as single particle cyclotron frequency (2.1.12).

The plasma rotation frequency ω_R is greater than magnetron frequency and smaller than cyclotron frequency of a single particle in a Penning trap [146, 153]:

$$\omega_m < \omega_R < \omega_c \tag{2.2.17}$$

The plasma density profile depends on the temperature of the plasma, and it scales as $n(r,z) \sim \exp(1/T)$. To avoid infinitely high densities inside the plasma for low temperatures ($T \to 0$), the condition is introduced:

$$q\phi(r,z) + \frac{1}{2}m\omega_R(\omega_c - \omega_R)r^2 = 0 \tag{2.2.18}$$

This means that the electric potential inside the plasma for zero temperatures would be independent of z position

$$\phi(r,z) = \phi(r) = -m\omega_R(\omega_c - \omega_R)r^2/2q \tag{2.2.19}$$

so there would be no force acting on ions in the axial direction (along *B-field* lines). Potential $\phi(r,z)$ includes the plasma space-charge (Equation 2.2.5), so the potential depends on the charge distribution $\rho(r,z)$ via Poisson equation:

$$\nabla^2\phi(r,z) = -\frac{\rho(r,z)}{\epsilon_0} = -\frac{qn(r,z)}{\epsilon_0} \tag{2.2.20}$$

Solving Poisson equation for the potential in Equation 2.2.19 obtained as the condition for $T \to 0$, we can obtain the maximum ions density n_0, which is constant inside the plasma [146]

$$n_0 = \frac{2\epsilon_0 m\omega_R(\omega_c - \omega_R)}{q^2} \tag{2.2.21}$$

From Equations 2.2.4 and 2.2.21 we can see that the plasma rotation frequency ω_R is related to the plasma oscillation frequency ω_p

$$\omega_p^2 = \frac{4\pi q^2 n_0}{m} = 2\omega_R(\omega_c - \omega_R) \tag{2.2.22}$$

A parameter characterising the plasma is the *Coulomb coupling constant* Γ_{plasma}

$$\Gamma_{plasma} = \frac{E_C}{k_B T} \tag{2.2.23}$$

which is a ratio of the Coulomb energy per particle inside the plasma E_C to the thermal energy $k_B T$. This Coulomb energy is given by

$$E_C = \frac{q^2}{4\pi\varepsilon_0 a_S} \tag{2.2.24}$$

where the effective ion-ion distance at a given ion number density n_0 is described by Wigner-Seitz radius a_S

$$a_s = \sqrt[3]{\frac{3}{4\pi n_0}} \tag{2.2.25}$$

Combining last three equations we get plasma coupling constant Γ_{plasma}

$$\Gamma_{plasma} = \frac{q^2}{4\pi\varepsilon_0 a_S k_B T} \tag{2.2.26}$$

which characterises the state of plasma. If the charged particles are cold enough and $\Gamma_{plasma} \geq 175$, the plasma can change state to a Coulomb crystal, which would rotate around the trap axis at frequency ω_R.

2.2.3 Centrifugal separation

Centrifugal separation is an effect that occurs in plasmas of mixed species with different masses and charges to mass ratios, when two species radially separate from each other due to the difference of their rotation frequencies [138, 148, 155, 156]. Shear between both species a and b due to difference of rotations $\omega_{R,j}$ and due to collisions between particles of both species at the rate ν_{ab} cause azimuthal drag forces

$$F_{\theta,a} = -m_a \nu_{ab} r(\omega_{R,a} - \omega_{R,b}) \tag{2.2.27}$$

which produces $F_{\theta,a} \times B$ radial drift, causing an inward radial flux Γ_{ra} of lighter species:

$$\Gamma_{ra} = \frac{cn}{qB} F_{\theta,a} \tag{2.2.28}$$

and similarly equivalent $F_{\theta,b}$ will produce outward flux Γ_{rb} of heavier species. This causes momentum transfer until thermal equilibrium is reached and both species rotate with the same frequency ω_R. In the state of thermal equilibrium, the density of each species will have different radial distributions [148]

$$n_a(r) = n_{a0} \exp\left[-\frac{q_a}{k_B T}\left(\phi(r) - \phi(0) + \frac{B\omega_r r^2}{2c} - \frac{m_a}{q_a}\frac{\omega_r^2 r^2}{2}\right)\right] \tag{2.2.29}$$

and equivalently for $n_b(r)$. One species has maximum density in the centre of the plasma $r_a = 0$ and the density exponentially decreases with higher radii. The other species has a maximum density at a radial position away from the trap centre $r_b > 0$ and its density decreases moving inwards to the radial centre and as well moving outwards. If one of the species a is dominant and the species b does not contribute significantly to the potential $\phi(r)$, then the factors inside the exponential function that determine the density distribution:

$$\psi_a = -\frac{q_a}{k_B T}\left(\phi(r) - \phi(0) + \frac{B\omega_r r^2}{2c} - \frac{m_a}{q_a}\frac{\omega_r^2 r^2}{2}\right) \tag{2.2.30}$$

$$\psi_b = \underbrace{\frac{q_b}{q_a}\psi_a}_{\text{charge difference}} + \frac{1}{kT}\underbrace{q_b\left(\frac{m_b}{q_b} - \frac{m_a}{q_a}\right)\frac{\omega_r^2 r^2}{2}}_{\text{centrifugal separation}} \tag{2.2.31}$$

The difference between both density distributions comes from a so-called charge difference separation and centrifugal separation caused by the mass-to-charge ratios difference. If two species have the same charge, the relative density distribution would be proportional to the centrifugal separation term

$$\frac{n_a(r)}{n_b(r)} \propto \exp\left\{\frac{1}{2k_B T}(m_a - m_b)\omega_R^2 r^2\right\} \tag{2.2.32}$$

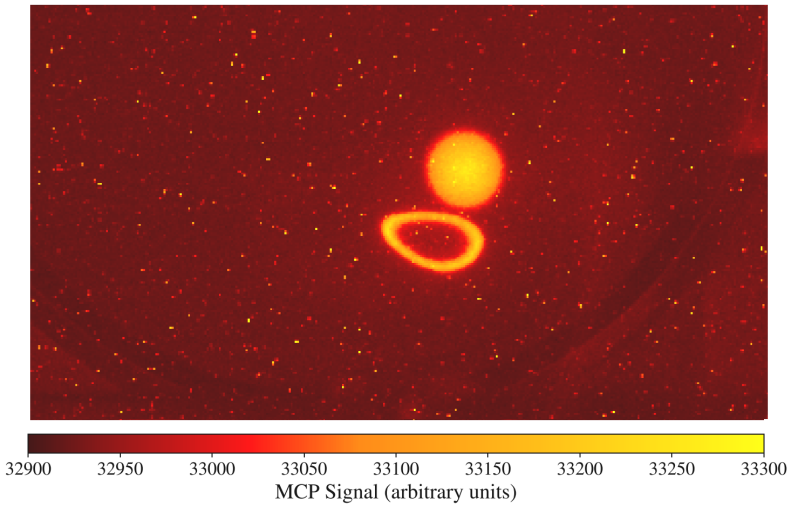

Figure 2.10 – Example MCP image of centrifugal separation between antiproton and electron plasma.The offset between the centres of both plasmas is caused by the high voltage tabs of the MCP electrodes generate a static electric field and the resulting force acts in opposing directions on particles of different charge.

For the centrifugal separation to be noticeable within the plasma of the radius R_P, the centrifugal term must be large in respect to the thermal energy:

$$q_b \left| \frac{m_b}{q_b} - \frac{m_a}{q_a} \right| \omega_R^2 R_P^2 > k_B T \tag{2.2.33}$$

Two species in the plasma can be partially separated if the separation length is smaller than radius of the plasma $l_{sep} < R_P$ and fully separated if separation is significantly larger than Debye lengths of both species $\Lambda_{Da}, \Lambda_{Db} \ll l_{sep}$. In the case of full separation, the heavier species will form a shell around the lighter species. The separation length between the two species depends on the equilibrium temperature T:

$$l_{sep} = \frac{k_B T}{|m_a - m_b| \omega_R^2 R_P} \tag{2.2.34}$$

Two-component plasmas in the ALPHA experiment are used to sympathetically cool one species with another species of lower temperature (more on sympathetic cooling in Section 2.4.1). For example, during the antihydrogen production sequence, antiprotons are cooled with electron plasma [157], since electrons cool by cyclotron radiation to around 20K. Another example is sympathetic cooling of positrons with Be^+, which we have recently demonstrated [1]. In both cases, centrifugal separation was observed with the MCP detector. Since the *sharpness* of separation depends on the equilibrium temperature, measurements of the radial profile can be used to extract information about the plasma temperature, which will be discussed in Section 2.3.3.

2.3 Plasma diagnostics

The detection methods used in the ALPHA experiment are mostly destructive, which means that the ions must be released from the Penning trap [7] and sent to the detector. This means that every sample of particles must be discarded to measure the properties of the plasma, and for any further study a new sample must be loaded to the trap. If we want to characterise the dynamical changes in plasma properties, we need to dump the ions into the detector at a desired step of particle manipulation and then load a new sample and repeat the same manipulation steps as before. This is a clear disadvantage of destructive measurement methods. The advantage is that they are relatively easy to implement from the hardware point of view. The number of particles and the equilibrium temperature of the plasma is measured using a *Faraday Cup* (*FC*), which is a metal plate with a simple electronic circuit. The plasma radial profile is measured using a single Chevron *Microchannel Plate* (*MCP*), which is a commercial detector from *Photonis*.

2.3.1 Plasma size, shape and density

In experiments with trapped plasmas, the size and shape of the plasma will determine the overlap volume between two species of plasma (e.g. positron and antiproton plasmas during antihydrogen formation [158], beryllium ions and positron plasma in sympathetic cooling [1], etc.) or the overlap with the laser beam for the spectroscopy measurements and laser cooling. Plasma size also defines the plasma density, which is important for interactions between constituent charged particles. The collision rate of charged particles within the plasma depends on its density and temperature. Plasma density is inferred from the number of particles within the plasma and plasma size. The number of particles is measured with a Faraday Cup technique that will be described in the next section. Plasma size in the x-y plane (radial profile of the plasma) can be measured using the *MCP* detector, while axial size cannot be measured directly and has to be calculated based on the knowledge of the shape of the trapping electric well. The *MCP* detector is a thin plate with an array of microchannels that amplify the signal of charged particles reaching its surface via an electron avalanche, then the amplified electrons reach the phosphor screen where they impact the surface to produce phosphorescence, which is detected on the CCD camera.

[7] Or antihydrogen atoms are released from the magnetic bottle trap.

The CCD camera consists of an array of pixels, which enables imaging the radial distribution of charged particles within the plasma. The signal intensity for each pixel corresponds to the sum of charged particles at a given radial position. Therefore, the values measured in the *MCP* picture are in fact the axially integrated radial density profile. To correlate the intensity of the signal recorded by the CCD camera pixels with the real number of charged particles that were deposited on the front surface of the MCP, a calibration is made by measuring the total number of charged particles inside the plasma using a *Faraday Cup* detector[8]. The measured radial intensity profile of the plasma is fitted by the Gaussian power law curve:

$$S_{MCP}(r) = a \exp\left\{-\left(\frac{r - r_0}{b}\right)^n\right\} + S_{bckg} \tag{2.3.1}$$

where a corresponds to the peak signal intensity in the plasma centre, b is the plasma radius defined as e^{-1} of the central intensity, r_0 is the centre position of the plasma on the *MCP* image and S_{bckg} is the background level offset.

Plasma Solver

Plasma density profile in the thermal equilibrium $n(r, z)$ is defined by Equation 2.2.16. The temperatures of the plasma is measured by the *Temperature Diagnostics* technique that will be described in Subsection 2.3.3. The unknown values in the density profile equation are the space charge (contributing to $\phi(r, z)$) and the plasma rotation frequency ω_R. The plasma size is calculated using a closed form method. The guess for an initial density profile $n_{guess}(r, z)$ is informed by an MCP measurement and knowledge of the trapping electric potentials. In each i^{th} iteration of the closed form method, the total electric potential $\phi_i(r, z)$ is obtained by solving the Poisson equation

$$\nabla^2 \phi_i(r, z) = -\frac{q n_{guess}(r, z)}{\varepsilon_0} \tag{2.3.2}$$

for the boundary conditions set by applied voltages on the surfaces of the electrodes and by the current guess of the density distribution [138].

[8]For the best result of a *MCP* calibration, the *Faraday Cup* detector should be placed in the same location as the *MCP* and both instruments should have a large enough surface, such that all particles in the plasma are deposited on the detectors surface. In the ALPHA experiment, detectors are installed on a linear translator inside a vacuum chamber, which allows detectors to be moved in and out of the axis of the Penning trap. In the case of the ALPHA-2 trap we use the same *MCP* instrument in two configuration: standard radial profile imaging and in the *Faraday Cup* configuration, with the front plate of the *MCP* connected to the *Faraday Cup* signal readout electronics.

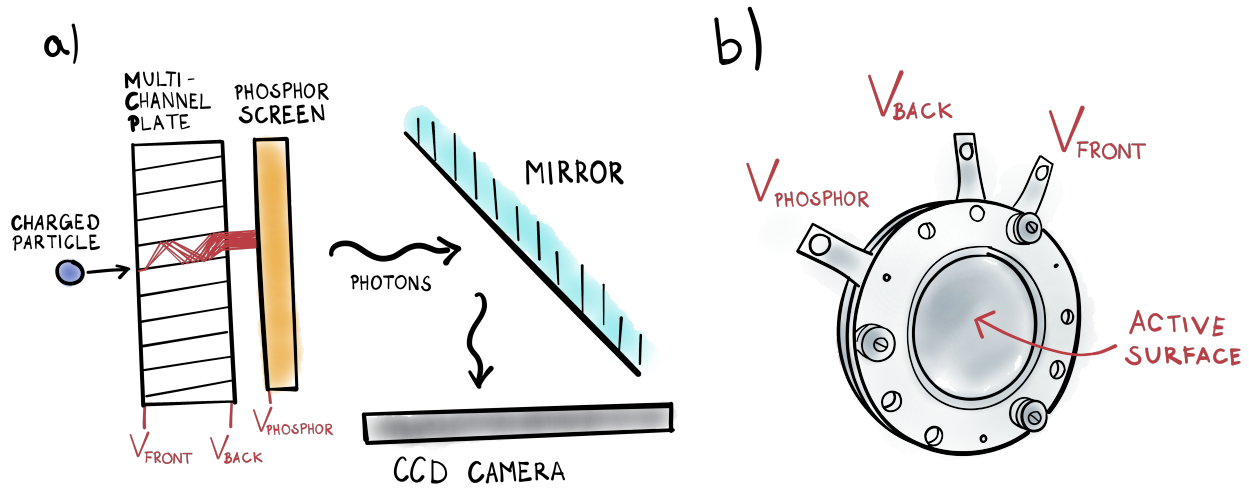

Figure 2.11 – Assembly of the MCP detector. Photon multiplier channels are placed between the *front* and *back* electrodes. The front of the phosphor screen is biased to ~ 5 kV. The voltages are delivered to the electrodes by the *tabs* extending out of the MCP assembly.

This electric potential $\phi_i(r,z)$ is used to calculate the plasma density distribution profile of the i^{th} iteration using Equation 2.2.16:

$$n_{i,j}(r,z) = C\exp\left\{-\frac{q}{k_B T}\left[\phi_i(r,z) + \frac{1}{2}m\omega_{R,j}(\omega_c - \omega_{R,j})r^2\right]\right\} \tag{2.3.3}$$

where C is a normalisation constant related to the maximum density n_0 inside of the plasma and $\omega_{R,j}$ is the plasma rotation frequency in the i^{th} iteration of the electric potential calculation and j^{th} iteration of the plasma rotation calculation. A plasma rotation frequency must be chosen to calculate $n_{i,j}(r,z)$. The plasma rotation frequency is set to an initial value ω_R^{guess} based on an educated guess to calculate the density distribution $n_{i,0}$. This calculated density distribution is then axially integrated and compared to the axially integrated density profile measured by the *MCP* detector. If the difference between the two axially integrated density distributions is greater than the chosen error value, then a new guess is made for the plasma rotation frequency $\omega_{R,j}$ and a new density distribution $n_{i,j}(r,z)$ is calculated. When the error falls below a desired value, the latest plasma density distribution $n_{i,J}$ is set as a guess value for the next evaluation of the Poisson equation. The plasma density distribution $n_{i,j}(r,z)$ is iteratively calculated until the difference between two consecutive iterations, $n_i(r,z)$ and $n_{i-1}(r,z)$, is below some defined threshold. More details about the *Plasma Solver* for the density distribution profile can be found in Chukman So's Ph.D. thesis [152].

MCP detector

The *MCP* detector is an array of microchannels covered on both sides with a metallic surface (see Figure 2.11). Metallic surfaces form *front* and *back* electrodes, to which a voltage is applied to accelerate charged particles. The voltages on the *MCP* detector are with respect to the ground of the apparatus. The *front* has a positive voltage for negatively charged particles (e^-, $\bar{p}$, anions) and a negative voltage for positively charged particles (e^+, Be^+, other cations) to accelerate particles toward the *MCP* detector. The absolute *front* electrode voltage is usually set at $|V_{front}| = 100$ V in the ALPHA experiment setup. Inelastic collisions between charged particles and atoms on the surface of the *MCP* cause emission of secondary electrons. All types of charged particles, independently of the sign of the electric charge, can initialise an avalanche of electrons within the microchannels of the *MCP* device, so the voltage applied to the *back* electrode is always positive: $V_{back} \simeq 1$ kV and the difference between the *front* and *back* electrodes defines the gain value for the *MCP* detector. Electrons are accelerated between the *back* electrode and the *phosphor screen* by applying high voltage to the surface of the *phosphor screen*. This high voltage is $V_{phosphor} \simeq 5$kV.

The overall *MCP* efficiency of detecting a single charged particle depends on the impact energy of the particle [159]. For the same gain settings (*front* to *back* electrode voltage), the detection efficiency depends on the particle type and mass - heavier ions have lower detection efficiency than leptons, since the same *front* voltage causes slower acceleration for heavier species, and antimatter particles have different detection efficiency than matter particles. The detection efficiency of ions can be improved by increasing the *front* voltage. An example using Be^+ is shown in Figure 2.12, where V_{front} was increased from -100 to -300 V, which allowed for the imaging of samples with a smaller number of Be^+ that could not be detected using standard *front* voltage setting.

2.3.2 Number of particles

Number of particles is measured using the *Faraday Cup* technique. *Faraday Cup* detector measures the number of charges arriving at the metal surface in units of time. Ions are deposited on a metal plate connected to the ground through a resistor. The plate charges as the ions arrive at its surface, which represents the integrated *time-of-flight* spectrum of ions released from the trap, and then it slowly discharges to the ground through a resistor.

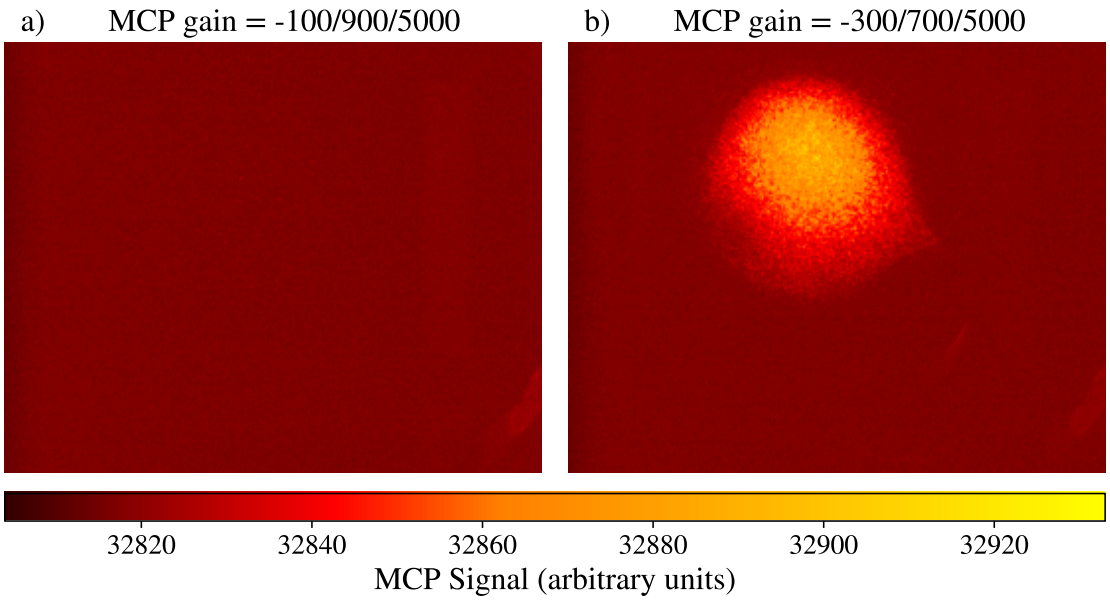

Figure 2.12 – The MCP image of small ($\ll 1M$) beryllium ions sample for different front voltage settings. a) $V_{front} = -100V$ and b) for the $V_{front} = -300V$. The MCP gain is denoted as $V_{front}/V_{back}/V_{phosphor}$.

The behaviour of this circuit can be described as an RC-circuit with a capacitance C and a resistance R:

$$\frac{dV}{dt} + \frac{1}{RC}V(t) = G\frac{I(t)}{C} \tag{2.3.4}$$

$I(t) = dQ(t)/dt$ is the amount of charge arriving at the detector in the time dt [9], V is a voltage difference between the metal plate and the ground reference and G is the signal amplification gain factor. The decay of the FC signal occurs on the time scale of $\tau \sim 1$ms, where

$$\tau = RC \tag{2.3.5}$$

and this should be much greater than the arrival time of the particle beam (usually $\sim \mu s$). There is an amplifier present in the circuit that allows adjustments to the gain level G. Our amplifier (Stanford Research Systems SR560) has built-in low-pass and high-pass filters to remove background noise and clean the signal. Ideally, we want to amplify the signal without amplifying the background, but avoiding saturating the voltage measurement device (National Instruments PCI-6132). The height of the voltage peak with good approximation corresponds to a total number of particles N in the sample (example FC signal in Figure 2.13). But if any ions arrive after the FC plate starts discharging, these charges will not

[9] Here we should account for the charge of single ion, but in our case we only measure singly charged particles

be accounted for when we take only the maximum peak value. To get an accurate number of particles, we need to fit the acquired signal with the function in Eq. 2.3.5. Fitting a signal with one peak originating from a single beam of single-ion species is simple. If we have multiple different species trapped in the same potential well (e.g. $\bar{p}$ and e^- or e^+ together with Be^+) their arrival time to the *FC* detector after release from the trap will be different, due to their mass difference: lighter species arrive faster to the detector. Depending on the distance travelled, different species can be well separated or multiple peaks can overlap with each other. Since the arrival of the second ion beam in principle happens at the same time as a discharge after deposition of the first beam, a more complex fitting routine is needed to extract the exact values of ions of each species (see example in Patrick Mullan's Ph.D. thesis, Chapter 5.6 [44]). For our application of Be^+, we also use a beryllium source as a Faraday Cup (since it is electrically isolated from the frame assembly) to see the amount of charges leaving the plate, which is sufficient to measure an order of magnitude of ablated ion number. The ablation process is highly non-reproducible and we lose some ions in the trapping process, so we are not able to infer an exact number of ions that were held in the potential well. The decay time of signals with this hardware is much longer than the duration of the arrival of charged particles, which allows for a suitable approximation of the total number of particles to be obtained by integrating Equation 2.3.5 between the period before particles arrive at the plate and the time at which the voltage signal reaches a peak

$$\int \frac{dV}{dt}dt + \frac{1}{RC}V(t)dt = \int G\frac{I(t)}{C}dt \tag{2.3.6}$$

In this situation the voltage peak value gives already a good enough estimate:

$$Q_{total} \approx \frac{V_{max}C}{G} \tag{2.3.7}$$

We have a few Faraday Cup detectors that are simple metallic surfaces (a beryllium source is a plate that looks like a standard Faraday Cup detector), but more commonly we use a front plate of the MCP detector as a Faraday Cup detector. In this mode of operation, the MCP voltages are disabled and the front MCP electrode is connected to the standard *FC* circuits and the same type of signal is measured. There is also a newer setup, more suitable for a smaller and colder plasma, which extracts the charge from the measurement of the intensity of photon emission caused by ions striking the MCP [160]. In this configuration a *Silicon Photomultiplier* (*SiPM*) converts the photons into an amplified electrical signal.

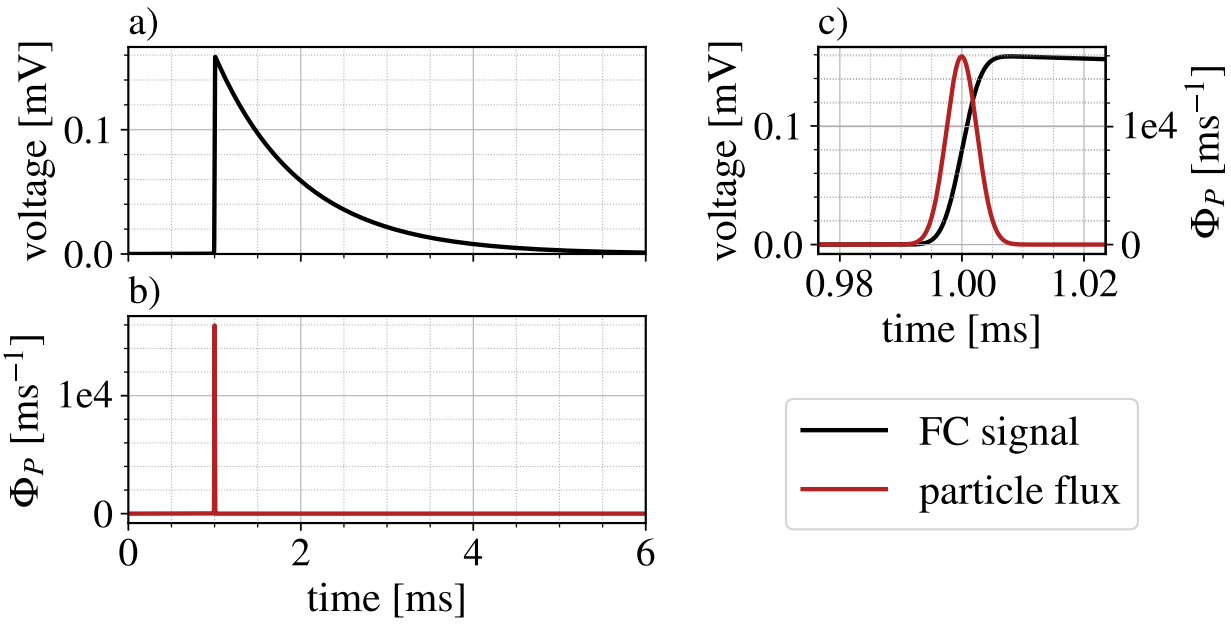

Figure 2.13 – a) Simulated signal of 1 million singly charged particles read by the Faraday Cup detector. b) Flux of particles arriving to the Faraday Cup detector. c) Comparison between charged particles current and voltage signal read by the Faraday Cup detector.

The integrated light intensity across the SiPM surface is measured as a function of time, similar to the FC signal, contrary to standard MCP measurement which measures spatial distribution of photons emitted from the MCP. The measured SiPM signal can be calibrated using a secondary FC to use the SiPM as a FC with improved sensitivity for plasmas with low numbers of particles because of the relatively low noise of the SiPM electronics.

2.3.3 Plasma temperature

Parallel temperature diagnostics

Plasma *Temperature Diagnostics* method (internally referred as *TDiag*) allows to measure the axial temperature of the plasma trapped in the Penning trap [161]. In certain scenarios, if the parallel and perpendicular energy are thermalised with each other, this measurement can inform about the global temperature of the plasma.

Plasma is released from the Penning trap by lowering one side of the confining potential well in a sequence of discrete steps by changing the voltage applied to one outer electrode in a series of $10^3 - 10^4$ steps of around 1-15 ms. Each step of lowering the wall of the potential well causes ejection of particles, with axial kinetic energies between the axial potential energy

of the trapping well before and after the voltage change (see Figure 2.14). The duration of each potential lowering step must be longer than the period of the axial bounce frequency ω_z, but shorter than the thermalisation timescale τ_{eq}, such as the velocity distribution of charged particles remaining inside the plasma does not change during the particles dump. The number of charged particles that escape from the trap for various confining potentials in each step is measured with a detector. In ALPHA we use a *phosphor screen electrode* of the MCP detector configured in a *Faraday Cup* mode. The electrical signal is amplified inside the MCP via electron avalanche, but instead of detecting the spatial distribution of the photons emitted by *phosphor screen*, the total current signal is measured. In the *Temperature Diagnostic* mode, the electrode voltages setting on the MCP are different from standard MCP operation: the *front-to-back* electrode gain is high, but the *phosphor* electrode is low.
If the plasma could be treated as a thermal gas, the number of particles ejected at each potential drop step would correspond to a certain energy interval $\Delta E_{k,\parallel}$ of the total Maxwell-Boltzmann distribution of the axial energy. Although, the space-charge ϕ_P (i.e. plasma's self-potential) plays a significant role in the total potential experienced by charged particles inside the plasma (see Equation 2.2.5). The kinetic energy of ions that escape the plasma

$$E_{k,\parallel} \geq -q(\phi_T - \phi_P) \tag{2.3.8}$$

The energy interval that is being probed with the *Temperature Diagnostics* method at each dump step corresponds to the changing effective potential $\Delta\phi = \Delta\phi_T + \Delta\phi_P$. Plasma self-potential changes as charged particles are extracted from the plasma, but for first few steps of decreasing the trapping potential, the space-charge does not change significantly $\Delta\phi_P \approx 0$. The change in the trapping potential $\Delta\phi_T$ can be related to the energy slice $\Delta\phi$ of the Maxwell-Boltzmann distribution of the axial kinetic energies:

$$\Delta E_{k,\parallel} \approx q\Delta\phi_T \tag{2.3.9}$$

Particles released from the trap during these first steps of *Temperature Diagnostics* dump are those of the highest kinetic energy out of all the population, which corresponds to the high-energy tail of the Maxwell-Boltzmann distribution. The number of particles with the highest energy in the population can be well approximated by the exponential function

$$N(\phi_T) \propto \exp\left\{\frac{\phi_T}{k_B T_\parallel}\right\} \tag{2.3.10}$$

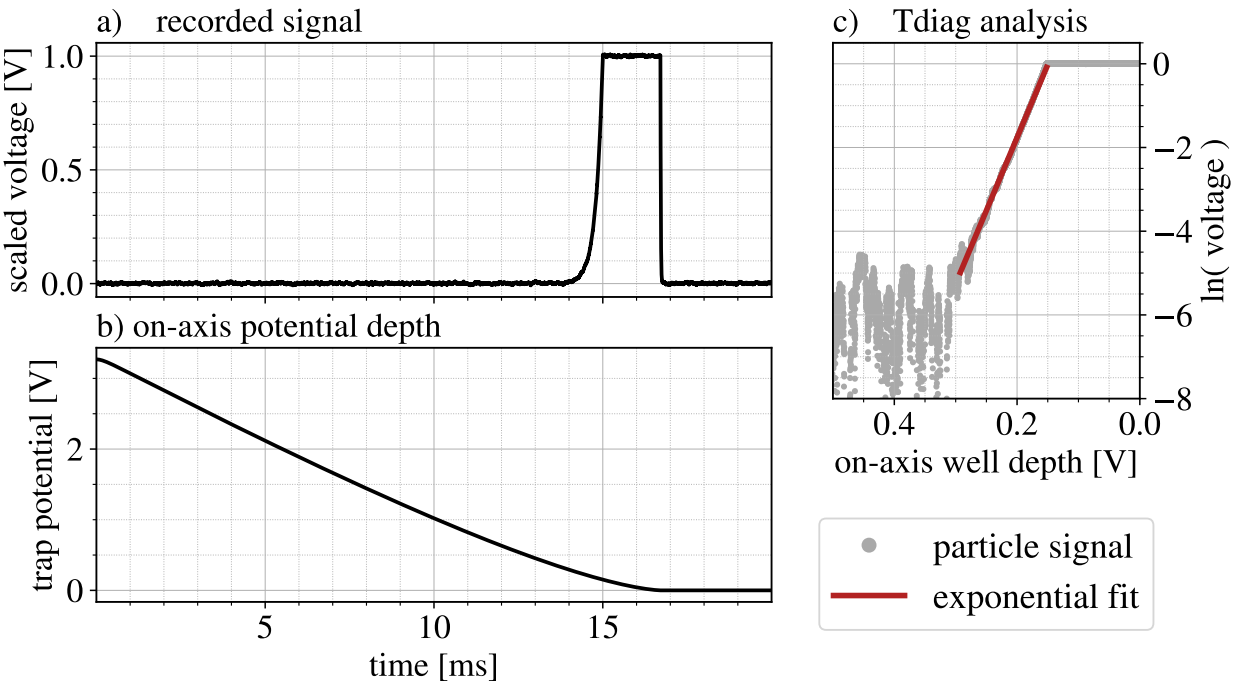

Figure 2.14 – a) Signal recorded by the Faraday Cup for the Temperature Diagnostics (*TDiag*) measurement. b) Change in the on-axis trapping potential during the release of the plasma. c) *TDiag* in the analysis format with the fit to the exponential tail. An exponential function is fitted to the initial part of the measured signal, but we display this in a logarithmic scale as it is visually easier to identify the period of time when the signal increases exponentially across orders of magnitude.

Given the voltages applied to the electrodes we can calculate the vacuum trapping electric potentials experienced by the particles at various axial and radial positions of the trap, which determines the well depth. The most weakly confined particles in a plasma are those close to the central axis of the trap and the confinement increases with increasing radial position. Therefore, when the well depth is reduced, the first particles extracted from the trap are the on-axis particles. This means that, in fact, during the first dump steps, we are sampling the upper energy distribution of the core of the plasma. As the well depth is further reduced, the radially outer regions of the plasma begin to be ejected onto the detector, which causes the signal measured at later steps to be a convolution of information about energy distribution and particles location within the plasma: lower energy slices from the axial position will be mixed with higher energy intervals from radially outer positions. For simplicity, only the initial high energy distribution is analysed and fitted with the exponential tail of the Maxwell-Boltzmann distribution. Since, according to the assumption, the plasma was in thermal equilibrium before the *TDiag* dump, the temperature of the plasma core is the same

as the temperature of the entire plasma, therefore the information extracted from the initial signal of particles ejected from the centre is representative of the temperature of the plasma in its entire volume. To perform the *Temperature Diagnostics* method in a way that gives correct temperature information and does not change plasma properties during the first few steps, multiple parameters of the dump process must be adjusted for each specific plasma, based on the type of charged particles, space-charge of the plasma, size of the plasma, etc. These dump parameters are

- what is the initial and final applied electric potentials,
- how many voltage steps are performed,
- what is the total duration of all steps,
- and the magnitude of the amplifier gain used on the detector's signal.

Trapping potentials will produce different axial frequencies for various species, which affects how quickly you can perform the voltage steps. When the amplification gain on the detector signal is chosen to increase the signal-to-noise ratio of the Maxwell-Boltzmann exponential tail, disregarding the signal quality of later steps. In practise, there is no universal temperature diagnostic configuration for all plasmas within these experiments; the parameters of the *TDiag* dump need to be optimised with a trial and error method.

The *Temperature Diagnostics* method was developed to measure low energy plasmas in Penning traps. We found this method to work reliably in the range from tens of kelvins to tens of thousands of Kelvins. Initially only larger plasmas could have been measured, but the application range was expanded by *E.D.Hunter et al.* [160] by using silicon photomultiplier (*SiPM*) to improve the signal-to-noise ratio of small and cold plasma. *SiPM* measures light emitted from the *phosphor screen* instead of directly measuring the current of *phosphor screen* directly, which reduces the microphonic noise. This allowed for reproducible measurements of plasmas of only 300 electrons at temperatures of 10-30 Kelvins. This improved technique of measuring plasmas' temperatures allowed us to develop an improved method for *Electron Cyclotron Resonance* measurement, called a *Reservoir ECR* [162]. More details on *Reservoir ECR* can be found in Section 6.1.1. We used this improved *Temperature Diagnostics* method with *SiPM* to measure the temperature of the plasma of beryllium ions in the sympathetic cooling experiment of positrons [1] performed in 2019. We have measured cold beryllium

ion plasma temperatures of 5-30 K with the *Temperature Diagnostics* method, and we also extracted plasma temperatures by measuring the prominence of the centrifugal separation between Be^+ and positrons (more details concerning the centrifugal separation effect in Section 2.2.3). These two methods gave a good agreement, which confirmed the applicability of the *Temperature Diagnostics* method in this low temperature regime (above 5 K). More information about those temperature measurements can be found in Jack Jones' Ph.D. thesis in Section 7.6.3 [131].

It should be stressed that this *Temperature Diagnostics* method measures only the axial temperature of the plasma. The axial temperature and plasma temperature are equivalent when the plasma is non-magnetised. A plasma is considered magnetised when the cyclotron radius is smaller than the distance of closest approach for Coulomb scattering at mean kinetic energy, which means that the collisions can be viewed as collisions of point-like particles and energy of the cyclotron motion is not transferred to other motions. More information about collisions in magnetised plasma can be found in Ref. [194]. If the plasma can be shown to be non-magnetised then the Temperature Diagnostic method measures the plasma temperature.

Centrifugal separation analysis

Centrifugal separation is an effect that occurs in a mixed plasma of multiple species with different charge and/or mass, which causes heavier species to drift outward and lighter species to locate in the centre of the plasma. The migration of charged particles occurs until a thermal equilibrium is reached. The phenomena was discussed in Section 2.2.3 in more detail, but now it is only needed to know that the separation length depends on the mass difference between the species and the final temperature that the mixture reaches. We have used this effect to measure the temperature of beryllium ions and positron mixture in sympathetic cooling measurement [1, 131] by measuring the integrated radial profile of beryllium ions. Positron plasma at around $20 - 30\ K$ was mixed with laser cooled Be^+ of $< 1\ K$. There were around $0.1M$ positrons and around twice as many beryllium ions. The mixed plasma was exposed to the cooling laser, the frequency of which was chirp towards the cooling transition resonance frequency. The final frequency of the laser defines cooling power and, as a result, determines the final plasma temperature. For each sample, the positrons were removed from the mixture using the *e-kick* technique (described in Section 2.4.4). Be^+ were

ejected to the MCP immediately after removing the positrons to maintain the hollow shape and unaffected density profile of beryllium plasma [10]. The axially integrated radial profiles of beryllium plasmas for different final laser frequencies were measured to compare these profiles with results of calculations of the density profiles at various equilibrium temperatures (more information about these calculations can be found in Jack Jones' Ph.D. thesis in Section 7.6. [131] and in Ref. [157]). Temperatures obtained from radial profiles measurements were compared with the measurements obtained using our standard *Temperature Diagnostic* method and showed very good agreement. We have demonstrated sympathetic cooling of positrons with laser-cooled Be^+ and reached temperatures as low as $6 - 7K$. By using centrifugal separation measurements, we have cross-validated the *Temperature Diagnostic* method and we have proven that this method can also be used for plasmas at $T \gtrsim 5K$.

2.4 Plasma manipulation and cooling

Multiple plasma manipulation techniques are used to prepare samples of particles with desired properties, such as plasma size, density, and temperature. Most of these properties can be controlled by manipulating in a very specific way the trapping electric potential well depths and shapes. A technique of evaporative cooling, plasma length adjustment, radial compression or radial tailoring of the plasma and removal of lighter particles is performed by changing voltages applied to the electrodes. When it comes to the temperature control, charged particle plasmas can be cooled by interaction with other particles by transferring the energy via collisions, which is known as sympathetic cooling. The temperature of the ions inside the Penning trap can also be controlled by adjusting the magnitude of the external magnetic field, which defines the strength of the cyclotron cooling effect. The controllability and reproducibility of plasma samples is a key aspect in the ALPHA experiment, as destructive detection techniques are used. Reproducibility is key to reliably performing systematic studies. Preparation of the antimatter plasmas for the antihydrogen synthesis involves many complicated steps in order to manipulate its properties in such a way that the next operation can be efficiently performed. A systematic studies of scanning various experimental parameters at each step (e.g. electrodes potential shapes and well depths and speed at which they are being changed, changes of external magnetic field and alternating electric fields, number

[10] Hollow plasmas are not stable and they are known to collapse towards the centre due to Helmholtz instabilities

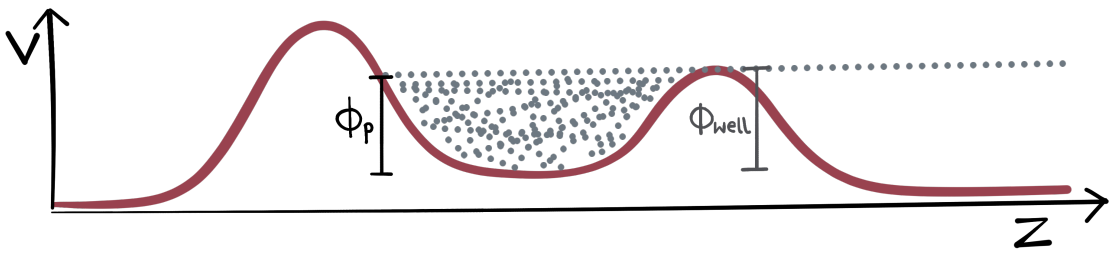

Figure 2.15 – Evaporative cooling diagram, adapted from Ref. [164]. When particles begin to evaporate from the trapped plasma, the space charge ϕ_P is limited by the depth of the trapping potential well ϕ_{well}. Adjusting the trapping potential allows to control the space charge within the plasma.

of other charged particles introduced to the system) requires that previous steps reliably led to a plasma of the same properties. These changes are diagnosed by discarding the plasma samples towards a detector at each step multiple times. If the plasma properties are reproducible at a given step, we assume that we have control over this preparation step. For the entire experiment to be performed successfully, individual steps must be performed in a reproducible manner. For example, the *Strong Drive Regime Evaporative Cooling* (*SDREVC*) technique [163, 164], which improves the repeatability of positrons and electrons preparation, allowed some trappable antihydrogen atoms to be produced in every mixing cycle.

2.4.1 Cooling techniques

Evaporative cooling

Evaporative cooling is a technique of reducing plasma's temperature by removing the particles that have the highest kinetic energy, which causes the mean kinetic energy of the remaining plasma to be reduced. This is performed by reducing the depth of the trapping electric well to the level of the plasma's space charge so that most energetic particles will have enough kinetic energy to escape the trap, referred to as *evaporation*. Collisions between particles within a plasma lead to thermalisation of the particles' energy towards a Maxwell-Boltzmann distribution. The mean average kinetic energy after evaporation is reduced, and there are more particles occupying lower thermal energy states. The clear consequence of this cooling method is that some of the particles are lost. If plasma before the evaporation was in a thermal equilibrium state, then the highest energies of particles within the population corresponded to the exponential tail of the Maxwell-Boltzmann distribution, which means that removing a very small fraction of the population can lead to a significant cooling effect.

Cyclotron cooling

Cyclotron radiation is an effect of an electromagnetic wave emission by a charged particle due to its acceleration in the magnetic field. A charged particle in a magnetic field performs a cyclotron motion in the plane perpendicular to the magnetic field direction, with a velocity $v_\perp$ tangent to the orbit of motion and an acceleration vector $a_\perp = \omega_c v_\perp$ pointing along the radius of motion. This charged particle emits an electromagnetic wave in the same perpendicular plane. The energy of the emitted wave depends on the velocity of the particle $E_\perp = mv_\perp/2$, so the particle loses energy at the rate given by the Larmor formula [138]:

$$\frac{dE_\perp}{dt} = \frac{2}{3}\frac{q^2 a_\perp^2}{4\pi\epsilon_0 c} = \frac{q^2\omega_c}{3\pi\epsilon_0 mc^3}E_\perp \tag{2.4.1}$$

For a thermal Maxwell-Boltzmann distribution of charged particles the perpendicular temperature changes as

$$\frac{dT_\perp}{dt} = -\frac{3T_\perp}{2\tau_r} \tag{2.4.2}$$

with a radiation time τ_r dependent on the particles mass, charge and the B-field strength

$$\tau_r \equiv \frac{9\pi\epsilon_0 m^3 c^3}{2q^4 B^2} \tag{2.4.3}$$

When the relaxation time is significantly greater than the timescale of of collisions between charged particles, the perpendicular and parallel temperatures are equal $T_\perp = T_\parallel = T$ and an entire plasma is in a thermal equilibrium. If the perpendicular and parallel temperature is coupled, the energy stored in all three degrees of freedom is irradiated by the perpendicular direction, reducing the total temperature at the rate

$$\frac{dT}{dt} = -\frac{T}{\tau_r} \tag{2.4.4}$$

which is a good approximation of the cyclotron cooling rate of hot plasmas in the Penning trap, when the plasma temperature is significantly higher than the surrounding heat bath temperature and the quantum effects do not play a significant role. For the temperature T approaching the temperature of the interior of a Penning trap, the black-body radiation of the surrounding environment becomes a significant contribution to the balance of energy absorbed and emitted by charged particles. This causes the cooling rate at temperatures close to the trap's temperature to differ from Equation 2.4.4 and the cooling rate to slow down. It has been shown, in Ref. [165], that in practise the cooling rate starts deviating

from the exponential decay at higher temperatures than close to the heath bath, which is an indication of addition heating sources acting on the plasma.

Cyclotron radiation causes efficient cooling of light particles (electrons and positrons), as the radiation time is $\tau_r \approx 3.87\,\mathrm{s}\,/B\,[\mathrm{T}]^2$, which corresponds to less than 0.5 s in a 3 T magnetic field used in the ALPHA Experiment. Although this is not practical for ions as the radiation time of ions in the same magnetic field would take years, for example 84 years for the proton and more than 60 thousands years for Be^+. Heavier particles must be cooled by dissipating the energy via collisions with different species at lower temperatures, which is known as sympathetic cooling, and this will be discussed in the next section. Cyclotron cooling is limited to the temperatures of the surrounding environment. The black-body radiation of the interior of the Penning trap is the practical limit for cyclotron cooling and for this reason modern precision measurements are performed in the cryogenic condition. Cryogenic temperatures are necessary to obtain the cold antimatter plasmas that can lead to the production of trappable antihydrogen atoms.

By effectively converting the particles' axial kinetic energy into cyclotron energy and then radiatively dissipating it as electromagnetic waves, cyclotron cooling can substantially reduce the overall energy (and thus temperature) of the plasma. This plays a key role in long-term confinement and manipulation of the antimatter plasmas.

Sympathetic cooling

The sympathetic cooling method relies on the principle of energy exchange between different species of charged particles through their mutual interactions. In a Penning trap, a cloud of ions of one species, the *coolant* ions, is first cooled down by other techniques, e.g. cyclotron cooling for electrons or laser cooling for some atomic ions like $^9Be^+$. These coolant ions are then mixed with the ions of a second species, the *target* ions, which are intended to be cooled. Through repeated Coulomb collisions, energy is transferred from the warmer target ions to the colder coolant ions. This leads to a reduction in the temperature of the target ions. Cooling of target ions occurs until a thermal equilibrium is reached. Ion species of two different masses in a Penning trap would start radially separating as their temperatures become closer to each other, which decreases the sympathetic cooling rate.

In the ALPHA experiment we use sympathetic cooling for cooling antiproton plasma with electron plasma. Electrons can reach temperatures of around 20 K due to the cyclotron cooling mechanism. Collisions between electrons and antiprotons allow to achieve temperatures of $\sim$ 100 K [105]. Electrons are later removed from the mixture by using an *e-kick* method, which will be described in Subsection 2.4.4. Further reduction of antiproton plasma temperature is made by evaporative cooling.

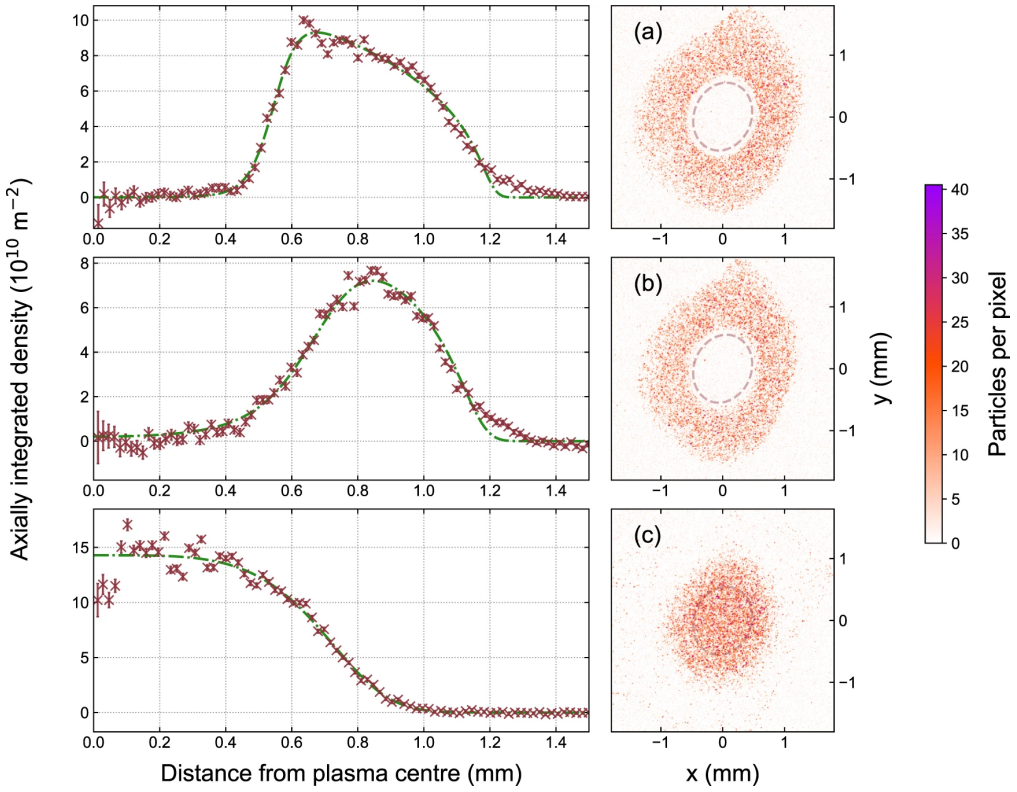

Figure 2.16 – The figure and caption is adapted from [1]. The images (right) show Be^+ ejected to the MCP/Phosphor imaging assembly 5 μs after the ejection of e^+ in the opposite direction immediately following the laser cooling of the Be^+. (a) Laser detuning $-20\gamma_0$, (b) detuning $-36\gamma_0$, and (c) detuning $-128\gamma_0$. The measured longitudinal temperatures were (a) 7.1±0.5 K, (b) 10.1±0.2 K, and (c) 370±100 K, respectively. To the left of each image is a plot of the extracted axially integrated radial density profile, overlaid with the best fit distribution from calculations assuming thermal equilibrium at the temperatures stated. The fit results were (a) 6.2 ± 0.6 K, (b) 19 ± 2 K and (c) 253 ± 54 K. The corresponding e^+ densities were (a), (b) $6.2 \pm 0.1 \times 10^7$ cm^{-3} and (c) $1.2 \pm 0.2 \times 10^8$ cm^{-3}. The calculations were made using the *N2DEC* code in ref. [157] where thermal equilibrium of the two species is assumed. Note that due to the distortion in the imaging, the plasma image is elliptical; the extraction of the radial profile took this into account. Additionally, at higher radii (> 1.25 mm) the images are distorted by stray electric fields near the MCP as well as physical aperture effects.

Low temperatures of antiproton and positron plasmas are required to form cold antihydrogen, such as few of the produced antihydrogen atoms would have low enough temperature ($< 0.5\ K$) that we can trap it in the magnetic Ioffe-Pritchard trap. The thermal distribution of the antihydrogen produced has been observed to correlate with the temperature of the positron plasma. Therefore, it is expected that further cooling of positron plasmas would enhance cold antihydrogen production [128]. We have recently developed a method to sympathetically cool the positron plasma by interaction with laser-cooled $^{9}Be^{+}$. Beryllium ions can be cooled to at least $\sim 0.2\ K$ in the ALPHA-2 Penning trap, while positrons on their own can only reach the same temperatures as electrons due to the cyclotron cooling mechanism. We have achieved a reduction by more than a factor of 2 in positron temperatures and there are prospects for future improvement.

Sympathetic cooling is particularly useful when the target ions cannot be directly cooled by other techniques, for example, due to the absence of appropriate laser cooling transitions or too heavy a mass for applying cyclotron cooling. It is used not only in the context of cooling non-neutral plasmas, but in general for cooling ions, atoms and molecules. A final example of sympathetic cooling in the ALPHA experiment is buffer gas cooling used in the positron accumulator, where high energy positrons (545 keV) emitted from the source are cooled via collisions with the nitrogen gas molecules (more information in Section 2.5.2).

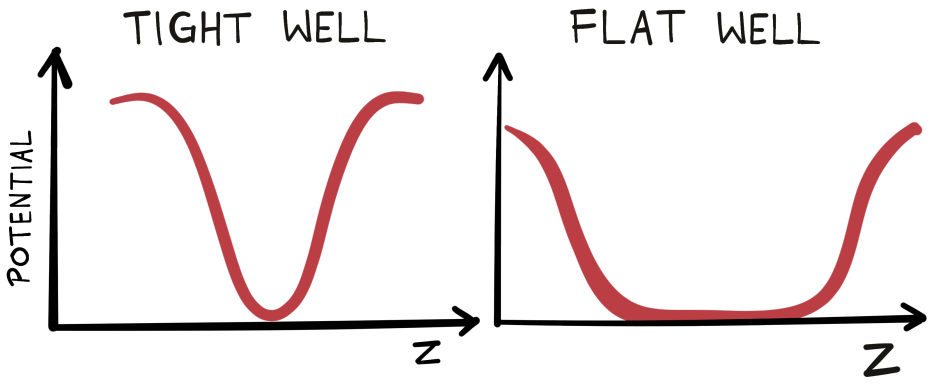

Figure 2.17 – Axial expansion of the potential well involves increasing the length along z axis, where the potential has minimum value. This applies to the minimum of the electrostatic potential in the Penning trap, as well as magnetic field potential in the Ioffe-Pritchard trap for antihydrogen. Axial expansion of the trapping well increases length of the plasma/antihydrogen cloud and it can be used for the adiabatic cooling of antiprotons/antihydrogen atoms [103].

2.4.2 Plasma size and density control

Axial size control

The length of the plasma can be easily changed in the Penning-Malmberg trap by adjusting the voltages on the neighbouring electrodes, as shown in Figure 2.17. In the ALPHA-2 trap, when the axial length of the plasma is expanded, the plasma radius typically does not change. Therefore, axial expansion can be used to reduce the plasma density. When the plasma gets compressed axially, the density increases, and the radial size might also increase, if the space charge changes significantly with respect to the trapping potential. We typically use a single or double electrode well, especially as at least two electrode wells are needed for the Rotating Wall compression, which will be discussed in Section 2.4.2. The main application of axial expansion of the plasma is adiabatic cooling, which is performed by slow expansion of the trapping potential well. Adiabatic cooling is one of the methods to reduce the temperature of the antiproton plasma [166].

Rotating Wall compression

Confined non-neutral plasmas might radially expand due to imperfections in the Penning trap assembly or the charged particle collisions with the residual gas. Maintaining or even reducing the radial size of the plasma is important while overlapping two plasmas of different species to maximise the rate of interactions, for example sympathetic cooling between Be^+ and e^+ or antihydrogen production by merging antiprotons with e^+. Controlling the radial size of the plasma is more complicated than controlling the axial size, which can be done just by adjusting static voltages applied to the cylindrical electrodes. Plasma can be radially compressed or expanded by azimuthally rotating multipolar electric field, which is called a *Rotating Wall* (*RW*) technique developed by *Huang et al.* at UC San Diego in 1996 [167] and also applied to positron accumulator design by C.M. Surko group [168].

Plasma in a Penning-Malmberg trap rotates around its central axis at the frequency ω_R, this rotation is the net drift from the Penning trap solenoid magnetic field and the plasma's own radial electric field and it relates to the plasma density as in Equation 2.2.21. The radial electric field in the Penning-Malmberg trap is azimuthally symmetric, so the plasma's radial profile is a circle. Applying a dipolar radial field breaks the plasma's symmetry around the trap axis, and the plasma's radial profile becomes elliptical.

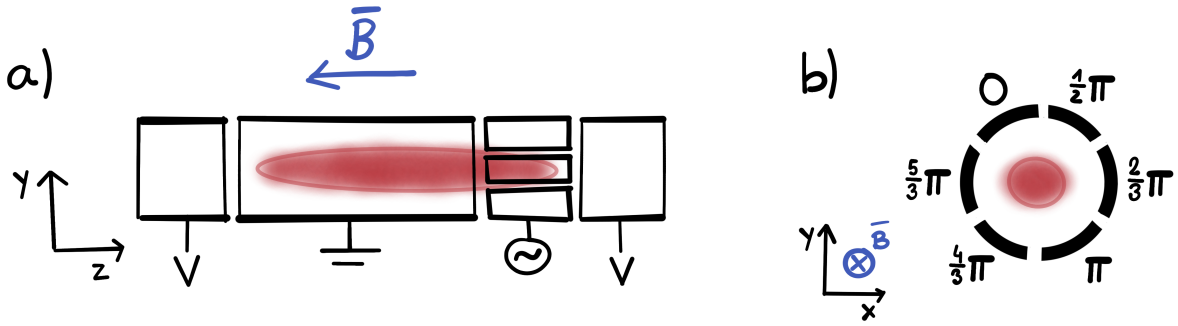

Figure 2.18 – *Rotating Wall* electrode is one of the cylindrical electrodes, which is azimuthally divided into multiple segments (6 in the case of ALPHA traps). *Rotating Wall* electrode should be placed on one of the ends of the plasma, as shown in Figure *a)*. The voltage applied to each segment changes sinusoidally with a different phase offset for each of the segments; see Figure *b)*, which generates a dipolar electric field rotating around the radial centre of the trap at frequency ω_{RW}. Figure adapted from [138].

Rotating this dipolar electric field around the trap axis with a frequency ω_{RW} would apply a torque on the plasma, which modifies the rotation frequency of the plasma ω_R. If $\omega_{RW} > \omega_R$ and rotation of the electric field occurs in the same direction as plasma rotation, the plasma is compressed [11], otherwise the plasma is expanded. In practise the rotating electric field is generated by applying suitably phase shifted sinusoidal signals on to each segment of an azimuthally segmented electrode, see the Figure 2.18. The applied rotating electric field must spatially overlap with the plasma, and for optimal performance this should overlap with one of the axial ends of the plasma, as the coupling mechanism involves certain plasma modes. This means that the plasma should be axially longer than the length of the *RW* electrode, which should be position on one of the ends of the plasma to apply a torque on one of the plasma ends, as shown in Figure 2.18. In practise controlling the plasma rotation frequency is much more complicated, and it depends on the properties of specific plasma. Typically coupling to the plasma requires coupling to the plasma modes at a very specific frequency of the rotating wall field, which can cause a slow, gradual change of the plasma's rotation frequency ω_R, this is known as *weak drive regime*. For low oscillation amplitudes of the *RW* drive, plasma compression occurs then only at discrete frequencies ω_{RW}. If the density of the plasma is sufficiently high and the temperature is low enough, the plasma can be in a *Strong Drive Regime* (*SDR*) and efficient compression can be achieved over a broad range of frequencies without tuning to plasma modes.

[11] In literature [167, 169, 170] the Rotating Wall is usually expressed in frequency f_{RW}, not angular frequency ω_{RW} and for consistency the plasma rotation is also expressed as rotation rate f_E, so the compression condition is given as $f_{RW} > f_E$.

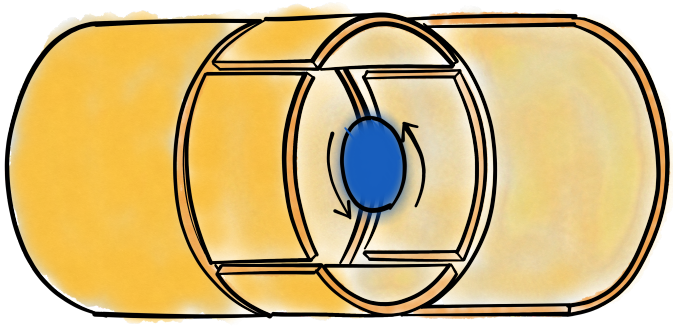

Figure 2.19 – Segmented electrode of the Penning-Malmberg trap that allows to apply *Rotating Wall* compression technique. Here the *RW* electrode is splitted into 4 segments for simplicity of the drawing. In case of the ALPHA Penning traps, the *RW* electrodes are splitted into 6 segments.

This Strong Drive Regime was first observed by J. R. Danielson and C. M. Surko at UC San Diego in 2005 and it was obtained by increasing the *RW* drive amplitude from 0.1 to 1 V [169]. In this regime there is a linear relationship between the applied *RW* frequency and plasma density. Therefore, Rotating Wall technique can be used to control plasma's density. In the ALPHA Experiment we are using the *Rotating Wall* technique in the *Strong Drive Regime* to be able to precisely control the number of particles (positrons or electrons) by combining rotating wall compression with evaporative cooling (*SDREVC* technique which will be discussed in Section 2.4.3).

In ALPHA traps the *RW* electrodes are split into six segments, which can produce a rotating electric dipole field with a distinct direction of rotation, unlike a four-segmented electrode (see Figure 2.19). The peak-to-peak voltage of the rotating wall signals used in ALPHA experiments are typically between 0.1 Vpp and 5 Vpp. Larger amplitudes improve the coupling strength between the plasma and the rotating field, though this causes too much heating. The typical rotating wall frequencies used in ALPHA experiments are $0.1 - 1$ MHz and the plasma density response is linearly proportional to the *RW* drive in this frequency range in the Strong Drive Regime. There are two Rotating Wall electrodes in the ALPHA-2 trap, one on the antiproton end and the other on the positron end, which allows simultaneous preparation of two species. Both Rotating Wall electrodes are placed under short solenoid magnets, built into the internal superconducting magnet setup of the Ioffe-Pritchard trap, to boost the magnetic field from standard 1 T to 3 T in order to enhance the Rotating Wall in the Strong Drive Regime via increasing the cyclotron cooling of the trapped leptons.

The undesired consequence of the plasma compression using Rotating Wall is plasma heating. During the compression, particles' magnetron orbit decreases and since magnetron energy is negative, this causes the energy of magnetron motion to increase. Without a cooling mechanism to compensate for this effect the plasma heats up. The method used for efficient laser cooling of a plasma in the Penning trap is to combine *RW* compression with cooling using a perpendicular laser beam. Laser cooling of the radial motion compensates the magnetron heating induced by compression and Rotating Wall mixes the degrees of freedom, allowing to achieve three dimensional cooling with only one perpendicular cooling laser.

Radial size tailoring

In our work on Be^+ plasma, we initially struggled to efficiently compress all the plasma with the Rotating Wall method, since some of the ions loaded by the laser ablation occupied very high radii. The density on the outer shell of the beryllium was so low that collisions might not have occurred frequently enough for those ions to experience the plasma behaviour. Therefore, the *RW* compression did not work well. We developed an alternative method to tailor the radial size of the plasma by cutting its outermost parts, which we called *centre-extraction*. We relied on the fact that whenever the confining potential is lowered and plasma is released from the well, the extraction of particles begins from the radially central part of the plasma. We released the inner core of the Be^+ plasma and recaptured it in the neighbouring potential well, while blocking ions that were extracted later, so the outer shell. Depending upon how soon the blocking of remaining ions occurs, we can extract a bigger or smaller fraction of the plasma's core. The downside of this method is that some of the particles are lost in this process. Using the *centre-extraction* method on Be^+ plasmas allowed us to remove the ions at very high radii, which were preventing compression with *RW*.In the next step we have applied a *RW* field and managed to successfully compress the remaining plasma.

2.4.3 Plasma reproducibility

Strong Drive Regime Evaporative Cooling (*SDREVC*)

We never load exactly the same number of particles with exact same energies and as we learnt in previous sections, plasma parameters (number of particles, density, size and shape, temperature) are related to each other. At the same time, plasma properties and plasma

stability (plasma expansion, particle losses) are dependent on the environmental conditions. Changing the number of ions, shape of potential well, or magnetic field strength can greatly change plasma properties. In a real experimental setup, the conditions of background gas level, trap temperature, electric field generated by electrodes, magnetic fields, etc. fluctuate. That means that even consecutive ion samples, loaded for the same trapping configuration, can produce plasmas of different properties. Controlled and reproducible ions sample with approximately similar parameters are crucial for the success of antihydrogen production and diagnostics of the magnetic field inside the trap. In the ALPHA Experiment, we can already prepare reproducible samples of electrons for the *Electron Cyclotron Resonance* (See Section 6.1.1) and reproducible positron samples for $\bar{H}$ formation, but heavier charged particles, such as antiprotons or beryllium ions, are more difficult to cool down. A method to prepare reproducible samples of lepton plasmas uses an *Evaporative Cooling* applied to the plasma in a *Strong Drive Regime* developed by Celeste Carruth Torkzaban in her Ph.D. thesis [164].

The *Rotating Wall* drive at the *Strong Drive Regime* allows us to tune the plasma's density, while the *Evaporative Cooling* gives control over the space charge of the plasma by lowering the trapping potential wall to a desired value of ϕ_P as shown in Figure 2.15. A space charge and the density define the number of particles within the plasma, therefore *Strong Drive Regime Evaporative Cooling* technique allows the control of the number of particles within the plasma. As long as the initial number of particles is sufficient to bring plasma to the *Strong Drive Regime*, adjusting the Rotating Wall frequency and amplitude together with choosing a depth of evaporation gives reproducible control over plasma parameters: particles number, density and space charge. In principle, using the same *SDREVC* sequence should result in the same final properties of the plasma, but in practise the initial number of particles might fall below the minimum threshold required. Whenever *SDREVC* stops working properly, sometimes increasing the number of particles loaded into the trap (longer accumulation time of positrons or running the electron source for longer) allows us to bring the operation back to the *Strong Drive Regime*.

For the *SDREVC* method to work properly, the plasma must be sufficiently cold. This is easy to achieve for leptons, electrons, and positrons, since they cool down to around $20-30$K via cyclotron radiation (see Section 2.4.1). The *SDREVC* on the antiproton plasmas has been unsuccessful so far, since the antiprotons heated up too much during the Rotating

Wall drive (from around 100 K to $3000 - 4000$ K, see C.Carruth Torkzaban Ph.D. thesis [164], Section 5.4.). Applying *SDREVC* on beryllium ions seems to be more promising, since those ions can be directly laser cooled to counteract the *RW*-induced heating. The application of the *SDREVC* method to prepare reproducible Be^+ samples is currently under development, carried out by Kurt Thompson and Maria Gomes Gonçalves. So far, the Be^+ samples loaded into the ALPHA-2 trap varied significantly between shots. Since the number of ions, their momentum and spatial distribution produced in the laser ablation process are not well reproducible, then trapping a beam of those ablated ions does not produce consistent plasmas either. We tried multiple methods to obtain more reproducible samples, mainly trapping multiple bunches from consecutive ablation shots to average the variation in number of ions and then we tried to radially and axially reduce the plasma size and apply the Rotating Wall compression, but this never provided good reproducibility of beryllium plasma samples (see Section 4.0.4). Successful *SDREVC* on Be^+ plasma and preparation of reproducible samples would greatly benefit any systematic study on beryllium ions, e.g. Be^+ electron spin-flip magnetometry (Chapter 6), and it will be a key for implementing laser-cooled beryllium ions to the antihydrogen production sequence, since positrons need to be reliably cooled in every e^+ and $\bar{p}$ mixing cycle.

2.4.4 Purifying the plasma

Light particles removal (*e-kick*)

In the mixed plasma of two species with greatly different masses, e.g. electrons and antiprotons or Be^+ and positrons, the lighter species can be removed from the mixture by briefly removing the potential barrier. The potential wall is lower for a short period of time, on the order of 100 ns, allowing the light particles to escape, and the wall is raised up to block the ejection of heavier particles. This is possible since the axial bounce frequency of charged particles in the Penning trap scales with mass as $\sim m^{-1/2}$ (Equation 2.1.10), so leptons have 43 higher axial frequency than antiprotons and 129 times greater than $^9Be^+$. This method of removing lighter species from ion plasmas is internally referred to as *electron-kick* or *e-kick* for short. The *e-kick* duration must be adjusted carefully to avoid heating of the remaining ion plasma.

Heavy particles removal (*ion heating*)

After charged particles are transferred between Penning traps through the magnetic beamline guide secondary ion production is observed. Charged particles are transferred between Penning traps with energies of 50-100 eV within approximately 10 μ s. There is a negligible amount of secondary ions produced during the transfer that would be trapped together with the original charged particles. Instead, most of the secondary ion production is observed during the capture and thermalisation. The charged particles are caught with kinetic energies of the order of 1 to 10 eV and inelastic collisions between trapped charged particles and background gas are enhanced at these energies. While the charged particles thermalise, on the order of milliseconds to tens of milliseconds, they can inelastically collide with the residual gas, causing the produced ions to be captured within the electrostatic potentials of the Penning trap. This production of ions spoils the plasma with impurities that might act as heating sources or suppress physical processes. These secondary ions are removed from the trap in the process called *ion heating*, which is a standard technique within the ALPHA Experiment. This is done by resonantly driving the ions out of the trapping potential well by using an oscillating electric field. ALPHA's Penning traps were not designed to produce ideal harmonic electric potentials, rather anharmonic potentials are produced. An anharmonic potential causes the trapped charged particles to oscillate at different frequencies depending upon their axial energies. The oscillating electric field is generated by the sinusoidally changing voltage applied onto a cylindrical electrode with the chirp of the oscillation frequency. The oscillating signal is applied into the outermost electrode confining the plasma and it changes the potential well shape on one of the plasma ends, which can affect the trapped particle motions. When the frequency of the oscillating signal is close to the particle's frequency of axial motion, the particle's motion will couple to the signal. The anharmonic trapping potential causes the oscillation frequency of the particle to decrease for larger axial kinetic energies. When the frequency sweeps downward, the particle motion is amplified, causing its kinetic energy to increase, reaching sufficient energies to overcome the trapping potential barrier. The axial frequency of trapped charged particles is defined by their charge-to-mass ratio, so secondary ions can be targeted for removal by a suitable configuration of a frequency sweep. The process of ion heating is routinely performed on positron plasma after transfer from the accumulator to the Atom Trap.

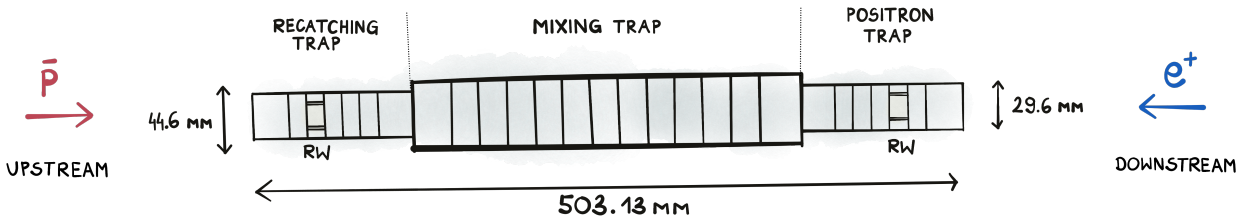

Figure 2.20 – Diagram of ALPHA-2 Penning trap electrodes.

2.5 Charged particles in ALPHA

ALPHA uses very specialised Penning traps to prepare antimatter plasmas. *Positron Accumulator* uses buffer gas to cool e^+ and uses cylindrical electrodes that increase in diameter moving away from the positron source to decrease the gas density in the accumulation region. *Catching Trap* is a cryogenic Penning trap that aims to capture antiproton bunches from the Antiproton Decelerator and perform initial preparation of antiproton plasma. ALPHA-2 and ALPHA-g are Penning traps combined with the magnetic Ioffe-Pritchard trap to trap antihydrogen that has been produced by mixing plasmas of positrons and antiprotons. Those traps are also referred to as *Atom Trap* or *mixing trap*. Electrodes of smaller diameter on the sides of *Atom Trap* are intended to trap transported bunches of antiprotons and positrons and compress them using *Rotating Wall* electrodes. Thinner traps in the middle are where antiprotons are mixed with positrons and where antihydrogen atoms are made. The middle electrodes have larger radius to increase the trapping volume of the antihydrogen, and they are thinner to reduce the amount of material with which the antiproton annihilation products could interact for better vertex reconstruction.

The particles are transported between the traps using magnetic guides. In the past *Catching Trap*, ALPHA-2 trap and *Positron Accumulator* were connected with a short vacuum section with only a few steering magnets between. Installation of the ALPHA-g experiment, located between the ALPHA-2 trap and the *Positron Accumulator*, required to introduce a specialised beamline capable of transporting positrons and antiproton in opposite directions (positrons to ALPHA-2 and antiprotons to ALPHA-g) and to guide both species around the 90° bending upward towards the ALPHA-g trap [4]. This beamline was designed by Mark Johnson, all details concerning the beamline can be found in his Ph.D. thesis [171].

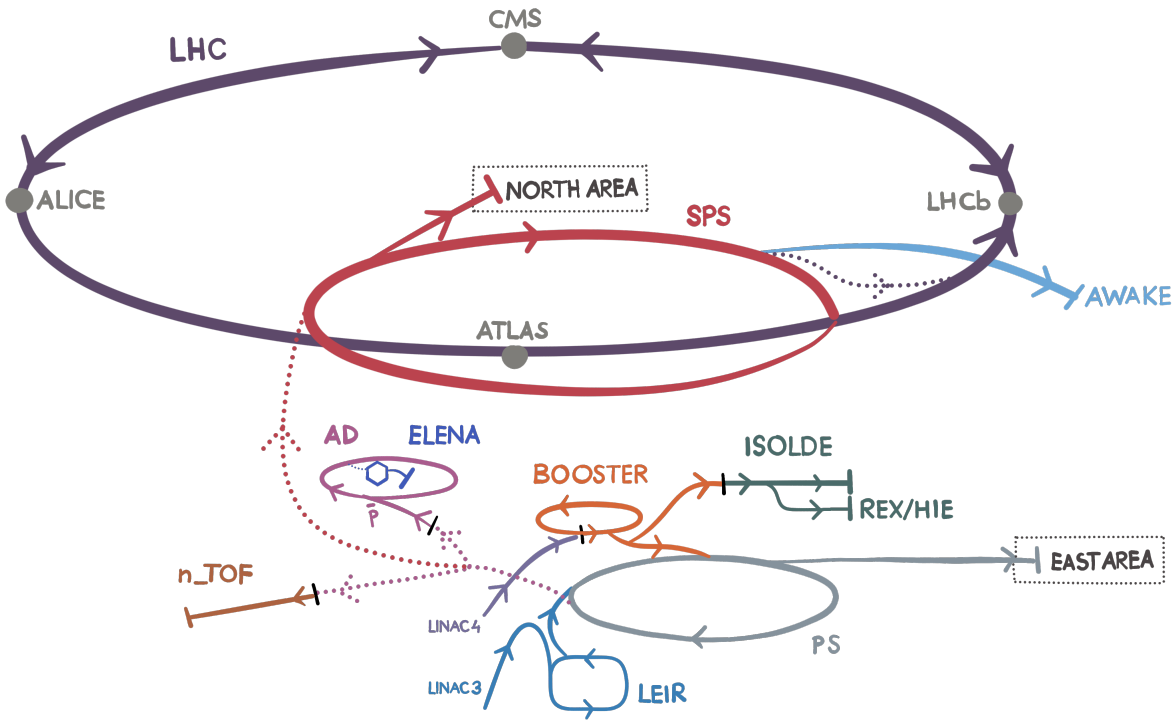

Figure 2.21 – Schematic diagram of CERN accelerators complex. Antiproton Decelerator (AD) with newly commissioned in 2018 Extra Low Energy Antiproton ring (ELENA) are located in the southern campus in Meyrin. The proton beam used to produce antiproton is sourced from the Proton Synchrotron (PS), currently the oldest accelerator at CERN, which is still in operation. Low Energy Ion Ring (LEIR) is a former Low Energy Antiproton Ring (LEAR), where first antihydrogen atoms were produced in 1995.

2.5.1 Antiprotons

Antiproton production at CERN involves a series of complex processes aimed at creating and cooling antiprotons for use in various experiments. The process begins with the *Proton Synchrotron* (*PS*), which accelerates protons to an energy of 25 GeV. The resulting proton beam from the PS is used to produce antiprotons by colliding it with an iridium target [172], resulting in pair-produced proton-antiprotons [173]. After the collision, antiprotons are selected by a mass separator and are guided to the *Antiproton Decelerator* (*AD*) complex [174]. The *AD* plays a crucial role in reducing the energy of the antiproton beam from an initial energy of 2.69 GeV to a final energy of 5.3 MeV, after going through processes of stochastic cooling and electron cooling, as well as RF cavities for phase space compression. The energies after the first and second stochastic cooling are 1.27 GeV and 47 MeV, respectively. The energy is further reduced by AD using electron cooling to 5.3 MeV. All of these steps are performed in a cycle of 120 min.

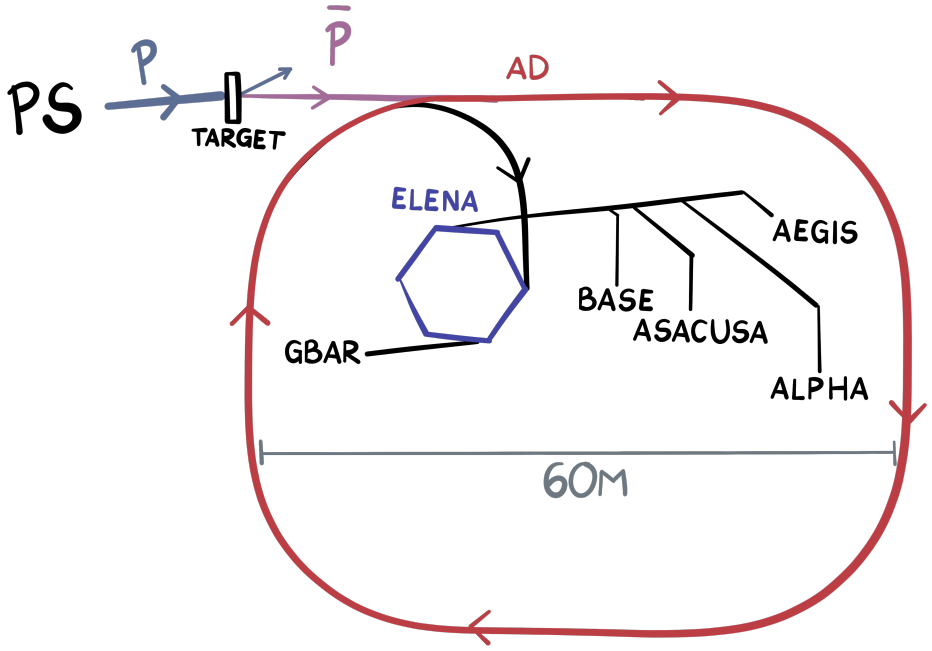

Figure 2.22 – Antiproton Decelerator facility with location of all the user experiments present in 2022. Antiprotons are produced in the collision of proton beam on the iridium target. Proton beam of 25 GeV is provided by the *Proton Synchrotron*, CERN's primary accelerator. Antiprotons are separated from protons and formed in a beam, which is reduced in the kinetic energy in the Antiproton Decelerator ring. This beam is further cooled down in a phases space by new decelerator ELENA installed inside the *AD* ring. From the ELENA decelerator, antiproton beams of $\sim$ 100 keV are delivered to the experimental areas over magnetic beamlines.

In 2018, an additional decelerator named *Extra Low Energy Antiproton*, abbreviated as *ELENA*, was introduced to further reduce the energy of the AD beam from 5.3 MeV to 100 keV [175]. Reduced beam energy is expected to increase antiproton trapping efficiencies by two orders of magnitude, which was typically 1% with the beam from the AD. The deceleration cycle duration of ELENA is 13 s, with an injected beam population of $3.2 \cdot 10^7$. The decelerated antiproton beam is split into four bunches, then delivered on request to experimental areas through electrostatic beamlines, and the extracted beam efficiency across four bunches is 80%.

In the ALPHA experiment, the antiproton beam passes through a degrader that moderates the beam to lower energies and gets injected into the *Catching Trap*. The emittance of the antiproton beam increases after passing through the degrader, resulting in 1% trapping efficiencies. The antiproton annihilation lifetime within the Penning traps is sensitive to vacuum quality, so the Catching Trap must operate in the ultrahigh vacuum condition.

ELENA's antiproton beamlines are designed to operate at a vacuum pressure of 10^{-10} mbar, which is 100 times higher pressure than inside the Penning traps. The degrader used before the ELENA decelerator was introduced was thick enough to act as a primary vacuum window, disconnecting the ALPHA *UHV* from the AD vacuum. Since the antiproton beam provided by ELENA has significantly lower energy, the degrader foil must also be thinner and the Catching Trap vacuum system had to be upgraded to include the differential pumping region [176].

The Catching Trap is designed to catch antiprotons with axial energies up to 5 keV. The moderated beam is then captured by applying high voltage to electrodes on both ends of the trap, in a well time-controlled manner. Antiprotons caught in a Penning trap form the non-neutral plasma, which is further cooled by sympathetic cooling with a preloaded electron cloud. The cooled antiprotons are then transferred to one of the Penning traps, ALPHA-2 or ALPHA-g, where the antiprotons will be mixed with positrons to form an antihydrogen. The last cooling step of antiprotons inside the mixing trap involves evaporative cooling [124].

2.5.2 Positrons

ALPHA obtains positrons from a radioactive sodium-22, which is a beta positive decay emitter with a half-life of 2.6 years [177].

$$^{22}_{11}\mathrm{Na} \rightarrow ^{22}_{10}\mathrm{Ne} + \mathrm{e}^{+} + \nu_{\mathrm{e}} \tag{2.5.1}$$

One alternative solution for sourcing positrons is shooting an accelerated electron beam on the target of specialised material to produce bremsstrauhlung light leading to the production of electron-positron pairs [178]. This method is used by the GBAR experiment [87], it can produce beams of higher intensity of positrons than typical radioactive sources. This source takes more of the floor space, and its positron intensities are beyond the current needs of ALPHA's antihydrogen experiments.

The energies of the positrons emitted from the sodium source are above 545 keV, which is too high to be caught directly in a Penning trap. A solid neon moderator is used to reduce the energies of the positrons and increase the flux of trappable positrons [179]. A disk of sodium-22 is placed on the end of a cold finger inside a vacuum chamber and cooled to 7 K. Neon gas is injected into the chamber such that it sublimates onto the surface of the source

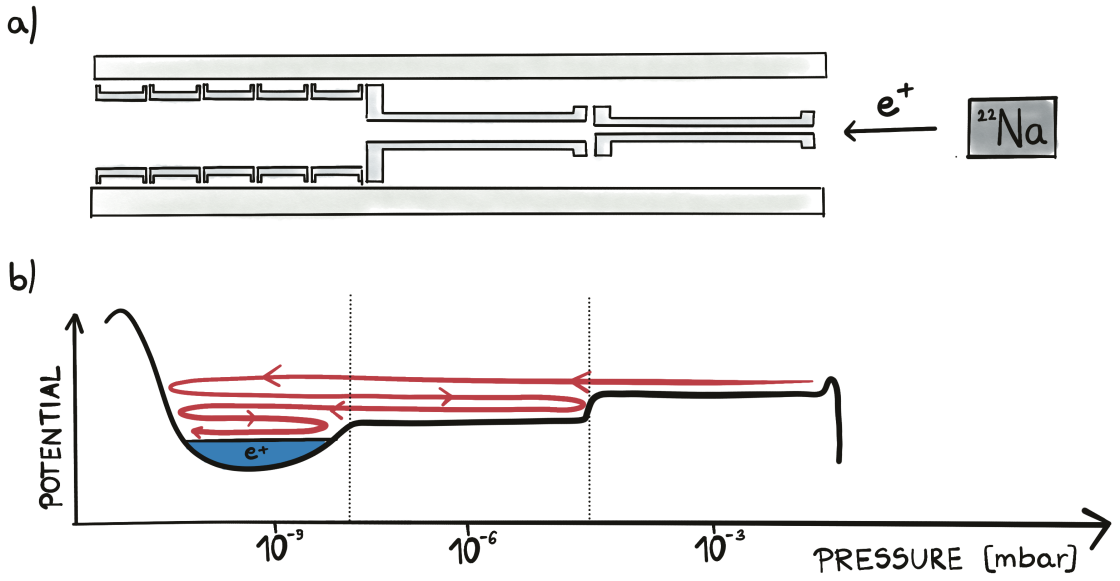

Figure 2.23 – Schematic diagram of 3 stage positron accumulator. a) Cross-section of the Penning trap system: external electromagnet and cylindrical electrodes of varied diameter. b) Nitrogen gas pressure change along the electrostatic potential well due to changing size of the electrodes. Electrostatic well is shaped to accumulate positrons in the lowest gas density region.

to produce solid neon. The positron and neon moderator are cooled to 6 K. Positrons lose energy while passing by the solid neon moderator, most of them getting stopped inside the moderator. About 1% of the positrons diffuse out of the moderator and they are transferred by a surrounding magnetic beamline, which guides the beam towards *Positron Accumulator*.

Positron Accumulator is a specialised Penning trap system to capture, cool and compress positrons [180]. Cooling of the positrons is achieved with a buffer gas present within the trapping volume, causing the positrons to cool sympathetically via scattering. Molecular nitrogen gas is leaked into the Penning trap vacuum system through a needle valve. The Penning trap is formed by a conventional electromagnet that generates a 0.14 T field and a stack of cylindrical electrodes of varying size. The diameters of the Penning trap electrodes increase axially along the path of the positron beam, creating a pressure differential across the axial length of the trap by restricting the flow of nitrogen gas. The electric potentials applied onto electrodes create a biased electric field that directs positrons towards the lower pressure regions, such that the positron lifetime is increased. The accumulated positron cloud is radially compressed using the rotating wall method from a continuously rotating field generated by a six-segmented electrode. This type of trap is known as a Surko-type buffer gas trap or a three-stage positron accumulator [16].

During operation, this system can accumulate 30 million positrons over $\sim$ 70 seconds. The vacuum pressure is $3 \cdot 10^{-6}$ mbar at the positron cloud, which is much worse than other Penning trap systems. During accumulation, a gate valve connecting the accumulator to the magnetic beamline towards other traps is closed. Before the positrons are transferred to other Penning traps the vacuum must be improved by using a turbomolecular pump to evacuate the nitrogen gas.

2.5.3 Electrons and ions

Other types of charged particles trapped within ALPHA Penning traps are electrons and beryllium ions. Electrons are used for sympathetic cooling of antiprotons and $^9Be^+$ are used for sympathetic cooling of positrons. Electrons are generated by an *electron gun*, a thermionic metal wire, which emits electrons when heated, and neighbouring electrodes guide electrons into a beam. Beryllium ions are generated by pulsed laser ablation from a beryllium target installed inside the ALPHA-2 apparatus. Details concerning beryllium ions production will be presented in Chapter 4.

Additionally, other (usually unwanted) ions are generated inside the ALPHA Penning trap by ionising background gas during transporting charged-particle beams between the traps. These are mostly hydrogen ions. The residual gas also comprises some He, N_2 and O_2 [181]. Nitrogen originates from the Positron Accumulator and it is transferred together with positrons. The N_2 contamination in the ALPHA-2 trap improved, as the accumulator was moved farther away to install the beamline and the ALPHA-g experiment. Hydrogen ions generated from the background gas could be used in the ALPHA Experiment. A large amount of protons could serve as an antiproton mock-up for a plasma dynamics study and they could also be used for hydrogen formation in an analogue scheme to antihydrogen formation [44]. H^- ions, of a mass very similar to the antiproton mass could be used for beamline transfer commissioning, during the time when antiprotons are not available. However, in current experimental conditions of the ALPHA Experiment the negative hydrogen ion production is not feasible.

Chapter 3

Light and atoms interaction

3.1 Atoms in electromagnetic field

3.1.1 Atomic transitions induced by electromagnetic field

An atom placed in the electromagnetic (*EM*) field will interact with the field and this interaction is usually described in a semi-classical way: the atom behaves according to quantum-mechanical rules, but the *EM* field is introduced as a classical wave. If the frequency of the *EM* wave matches the difference between two energy levels, the atom will continuously cycle between the ground level $|g\rangle$ and the excited energy level $|e\rangle$. This cycling between states lasts as long as the *EM* field is present and the state of the atom changes from the ground state to the excited state with a characteristic frequency called the Rabi frequency. Rabi frequency is denoted as Ω and depends on the specific transition and intensity of the *EM* wave. The probability of a transition between two energy levels depends on the coupling strength between these levels, which is characterised by a *transition matrix element* $\bar{d}_{ge}$. A very simplified idea is based on the symmetries of those two electronic states, the transition conserves or breaks specific quantum numbers (generally referred to as *selection rules*). The transitions within the atom are induced by an oscillating electric or magnetic field. If an atomic transition between states $|g\rangle \rightarrow |e\rangle$ causes a change of the charge distribution, then we say that this is an *electric multipole transition*, so we have *electric dipole transition* (*E1*) if there is an electric dipole present and the transition is induced by the dipolar electric fields, *electric quadrupole transition* (*E2*) for the electric quadrupole present, *electric octupole transition* (*E3*) for the octupole moment and so on. Similarly, if there is a resulting magnetic

moment present for the transition of the electron within the atom, we call it *magnetic multipole transition* and in the same way we have *magnetic dipole transition* (*M1*), *magnetic quadrupole transition* (*M2*), etc. In general, *electric transitions* couple states of opposite parity (e.g. S and P) and *magnetic transitions* couple states of the same parity (e.g. S with another S). The probability of an *electric dipole transition* depends on the intensity of the oscillating electric field, while the probability of an *magnetic dipole transition* depends on the intensity of the oscillating magnetic field. Transitions between strongly coupled states are *dipole transitions* and are characterised by higher transition probabilities. Other multipole transitions (quadrupole, octupole, etc.) decrease in probability with increasing order of the multipole [182]. So the hierarchy of the transition probabilities is

$$E1 \gg M1 \gg E2 \gg M2 \gg E3 \gg M3 \gg ... \tag{3.1.1}$$

Electric dipole transition changes the parity of the electronic state and requires changing the electronic angular momentum $\Delta l = \pm 1$; magnetic moment may change $\Delta m = 0, \pm 1$ and a spin remains unchanged $\Delta s = 0$. The example of *electric dipole transitions* is $1S \rightarrow 2P$ transition used for laser cooling.

The *magnetic dipole transitions* do not change the parity and the selection rules for these transitions are [1]

1. $\Delta J = 0, \pm 1$, except of $J = 0 \leftrightarrow 0$
2. $\Delta M_J = 0, \pm 1$
3. $\Delta J = 0$ and $\Delta M_J = 0$ together are not allowed

The example of the *magnetic dipole transition* is the hyperfine transition in the ground state $^2S_{1/2}$ of the antihydrogen (positron spin-flip) and in beryllium ion (electron spin-flip). Since an electron spin-flip transition in Be^+ is an equivalent of the hyperfine transition in $\bar{H}$ that we study in the ALPHA Experiment [35], the transition frequencies are similar and the same *EM*-wave source (microwave synthesiser installed in the ALPHA-2 *Atom Trap*) can be used to drive those transitions. For this reason, we proposed to use beryllium ions as a probe for the magnetic field in the ALPHA Experiment. Hyperfine transitions in the ground state of $^9Be^+$ are well known and commonly studied as *qubit states* for quantum computing [183,184].

[1] There are addition selection rules for H-like ions: $\Delta L = 0$, $\Delta S = 0$ and no change in electronic configuration.

3.1.2 Rabi flopping

An atom exposed to continuous electromagnetic radiation of angular frequency ω_0, connecting states $|i\rangle$ and $|j\rangle$, will oscillate between two states with Rabi frequency Ω. If the angular frequency ω of the *EM* wave is close to the resonance frequency, the change in the state of the atom will occur with higher frequency, at the so-called *generalised Rabi frequency*:

$$\Omega\,' = \sqrt{\Omega^2 + \delta^2} \tag{3.1.2}$$

where δ is the frequency detuning of the *EM* wave

$$\delta \equiv \omega_0 - \omega \tag{3.1.3}$$

This continuous change of atom's quantum state is referred as *Rabi flopping*. The frequency of Rabi flopping depends on the strength of the oscillating field and the coupling between the two energy levels $|i\rangle$ and $|j\rangle$. For the electric dipole transition, the Rabi frequency is [2]

$$\Omega = \frac{\bar{d_{ij}} \cdot \bar{E}_0}{2\hbar} \tag{3.1.4}$$

where $\bar{E}_0$ describes the intensity of the oscillating electric field and d_{ij} is the dipole matrix element for the electric dipole transition. For the magnetic dipole transition, the intensity of the electric field would be replaced with the magnetic field intensity $\bar{M}_0$ and the equivalent matrix element. Therefore, the Rabi frequency Ω depends on the intensity I of the electromagnetic wave that induces the $|i\rangle \leftrightarrow |j\rangle$ oscillation.

The probability of finding the atom in the excited state $|j\rangle$ at time t (if the atom-wave interaction started at $t = 0$) depends on the Rabi frequency Ω and frequency detuning of the wave δ, which is expressed by *Rabi formula*:

$$\mathcal{P} = 1 - \frac{\Omega^2}{\Omega^2 + \delta^2}\ sin^2\Big(\frac{t}{2}\sqrt{\Omega^2 + \delta^2}\Big) \tag{3.1.5}$$

That means that for no detuning ($\delta = 0$) after time $t = \pi/\Omega$, we know that atom will be in the excited state $|j\rangle$ and after the time $t = 2\pi/\Omega$ it will be back in the lower state $|i\rangle$.
In real systems Rabi flopping decays at the rate

$$1/\tau_c = \xi \cdot \Omega \tag{3.1.6}$$

where τ_c is the decoherence time and ξ is the damping coefficient.

[2] In fact there are two definitions of Rabi frequency different by a factor of 2. Another definition is $\Omega = \bar{d_{ij}} \cdot \bar{E}/\hbar$.

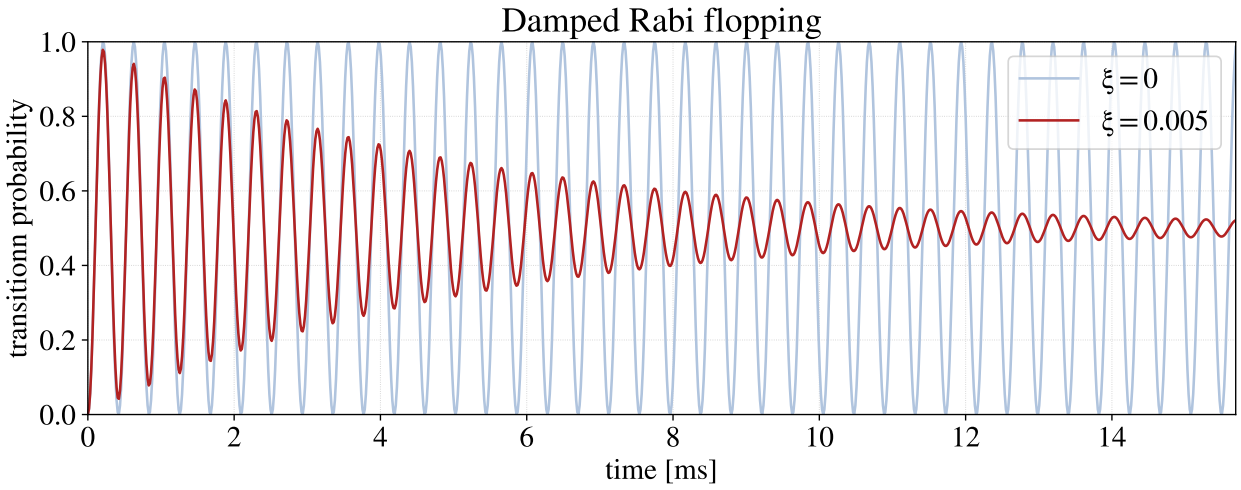

Figure 3.1 – Example of Rabi flopping at frequency $\Omega = 15\ kHz$ with damping coefficient $\xi = 0.005$ (red line) compared to undamped Rabi flopping (bright blue line).

The decoherence time depends upon environmental conditions (interaction with magnetic field, with electromagnetic radiation, and thermal fluctuations) and interaction with other atoms via collisions. The coherence time is ultimately limited by the spontaneous emission lifetime [3]. The decoherence effect modifies the *Rabi formula* in Fig.3.1.5 to behave as

$$\mathcal{P} = \frac{1}{2}\frac{\Omega^2}{\Omega^2 + \delta^2}\left[1 - cos\left(t\sqrt{\Omega^2 + \delta^2}\right) \cdot \exp(-t/\tau_c)\right] \tag{3.1.7}$$

Let us neglect the damping of Rabi oscillation for now. If the *EM* wave is detuned from the resonance frequency of the atom, the probability decreases and the frequency of oscillation changes to Ω' (see Figure 3.2). The atom still oscillate periodically and, if there is no damping present, achieve the maximum transition probability for $\Omega t = (2n+1)\pi, n \in \mathbb{W}$.

In an ideal Rabi flopping scenario, with no detuning, at every moment for which the relation $\Omega t = (2n+1)\pi, n \in \mathbb{W}$ holds, the atom will be in the upper state, for $\Omega t = 2n\pi, n \in \mathbb{W}$ in the lower state and for any other value of Ωt the atom will be in the superposition of both states. This phenomenon could be used to prepare the atoms purely in the upper state by using a π-pulse, so radiation of the duration equal to

$$t_\pi = \frac{\pi}{\Omega} \tag{3.1.8}$$

If we would expose an atom to the *EM* radiation for a time shorter by half (a $\frac{\pi}{2}$-pulse) the atom would be in an equal superposition of both states. π-pulse is a basis of a *Rabi experiment*, which allows to measure the lineshape of atomic transition.

[3] For the hyperfine states that will be considered in this work the spontaneous emission is not a practical problem.

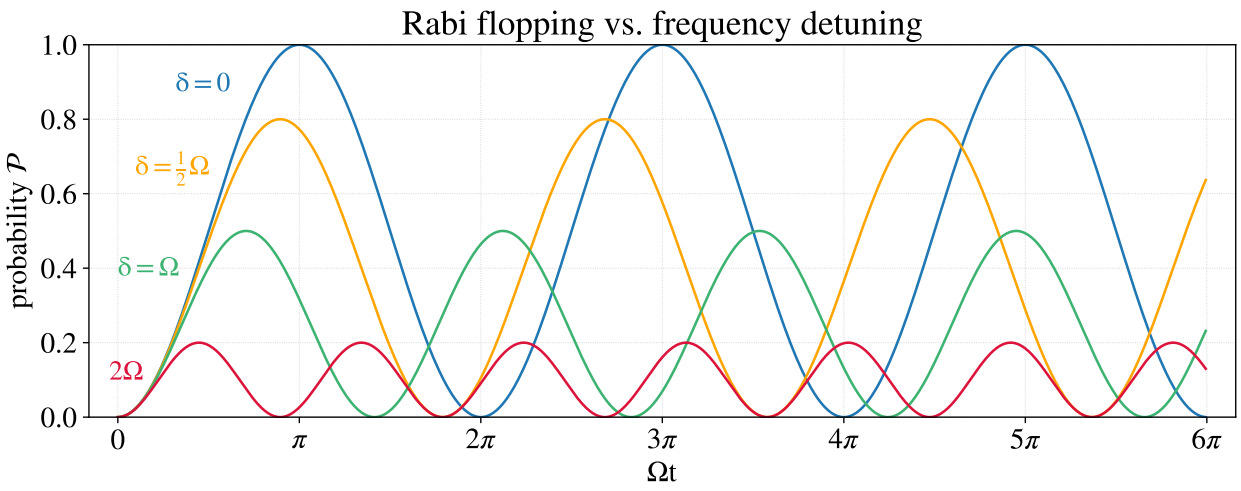

Figure 3.2 – Rabi flopping for various values of frequency detuning δ. Here ideal Rabi flopping with no damping of oscillation is presented.

In the Rabi experiment, the initial state atoms are exposed to consecutive pulses of *EM* waves of different frequencies, each pulse of duration t_π. The probability of transition is the same as in Equation 3.1.5, so for pulse at frequency ω_i the probability is

$$\mathcal{P}_i = 1 - \frac{\Omega^2}{\Omega^2 + (\omega_0 - \omega_i)^2} \; sin^2\Big(\frac{t}{2}\sqrt{(\Omega^2 + (\omega_0 - \omega_i)^2}\Big) \tag{3.1.9}$$

After the each π-pulse, the state of atoms is measured, which breaks the superposition state and makes the atoms to manifest in one of the states with a probability $\mathcal{P}_i$. For an ensemble of atoms, the probability $\mathcal{P}_i$ can be viewed as a fraction of ions that changed their quantum state. A plot of the fraction of ions that underwent the transition as a function of pulse frequency gives a *Rabi resonance curve*, from which the resonance frequency ω_0 and the linewidth of the transition can be extracted.

The π-pulse duration depends on the intensity of the *EM* radiation, which defines the Rabi frequency. The relationship between Rabi frequency and π-pulse time is shown in Figure 3.5. Experiments are usually performed in the regime when t_π is on the order of hundreds of microseconds [132, 186]. Longer pulses would make the time of probing full lineshape longer, on longer time scales this could mean that for example the resonance frequency ω_0 is changing due to *B-field* drift of fluctuations, which changes the effective detuning of of later pulses. Short pulses require a higher power of *EM*-waves. For longer pulses, the same absolute intensity fluctuations lead to larger change in the associated π-pulse duration.

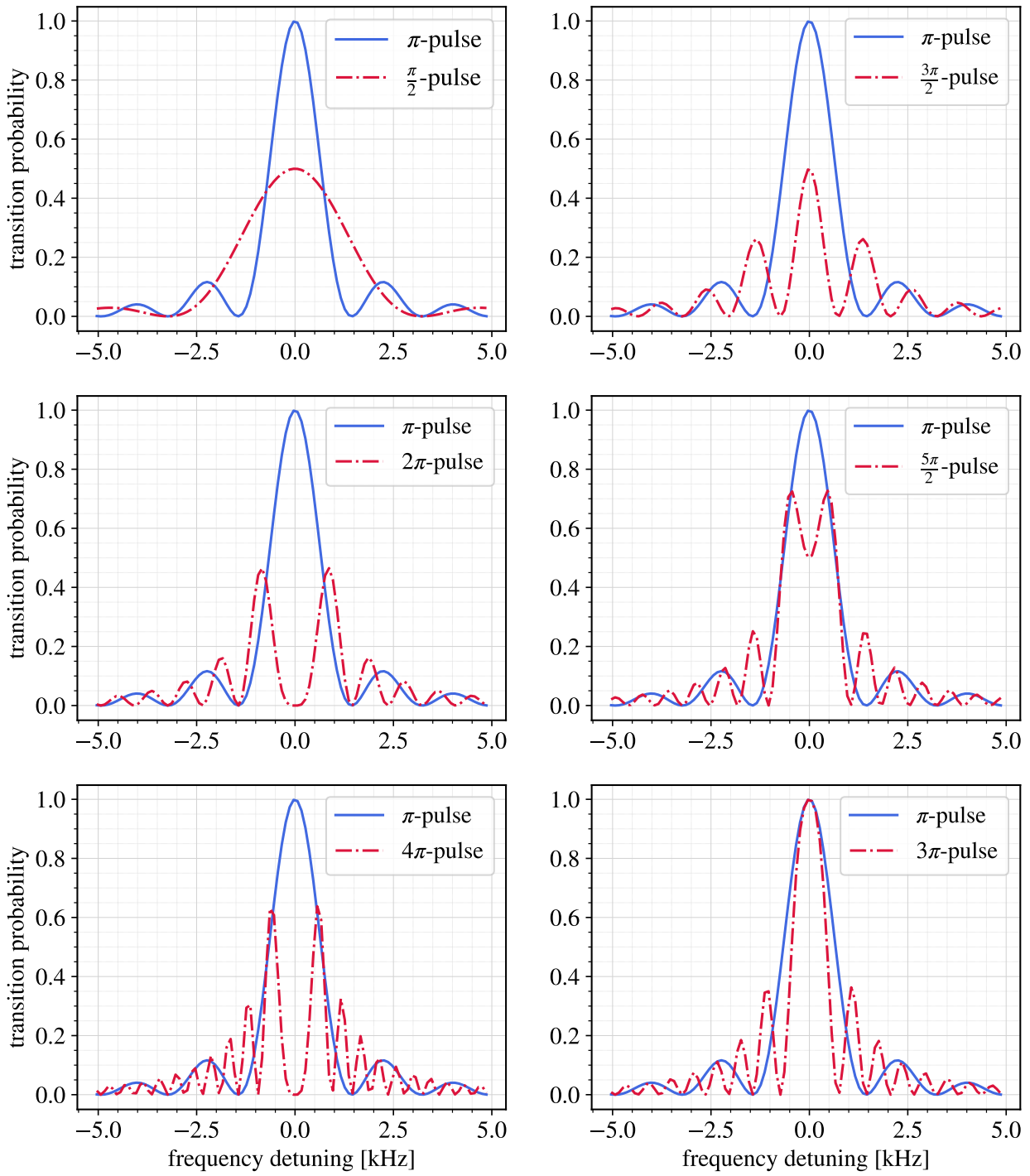

Figure 3.3 – Rabi resonance curve generated by pure π-pulse (blue lines) in comparison to various different pulse durations (red lines). The π-pulse resonance curve is meant to reconstruct the microwave induced electron spin-flip in the $2S_{1/2}$ ground state of Be^{+} measured by *Shiga et al.* in Ref. [132] (FIG. 5. in Section C). The π-pulse duration used was 600 μs and Rabi frequency ($\Omega \approx 5.235\ kHz$) was adjusted such as on resonance the transition probability is $\mathcal{P} = 1$, which means all the Be^{+} have changed the electron spin state.

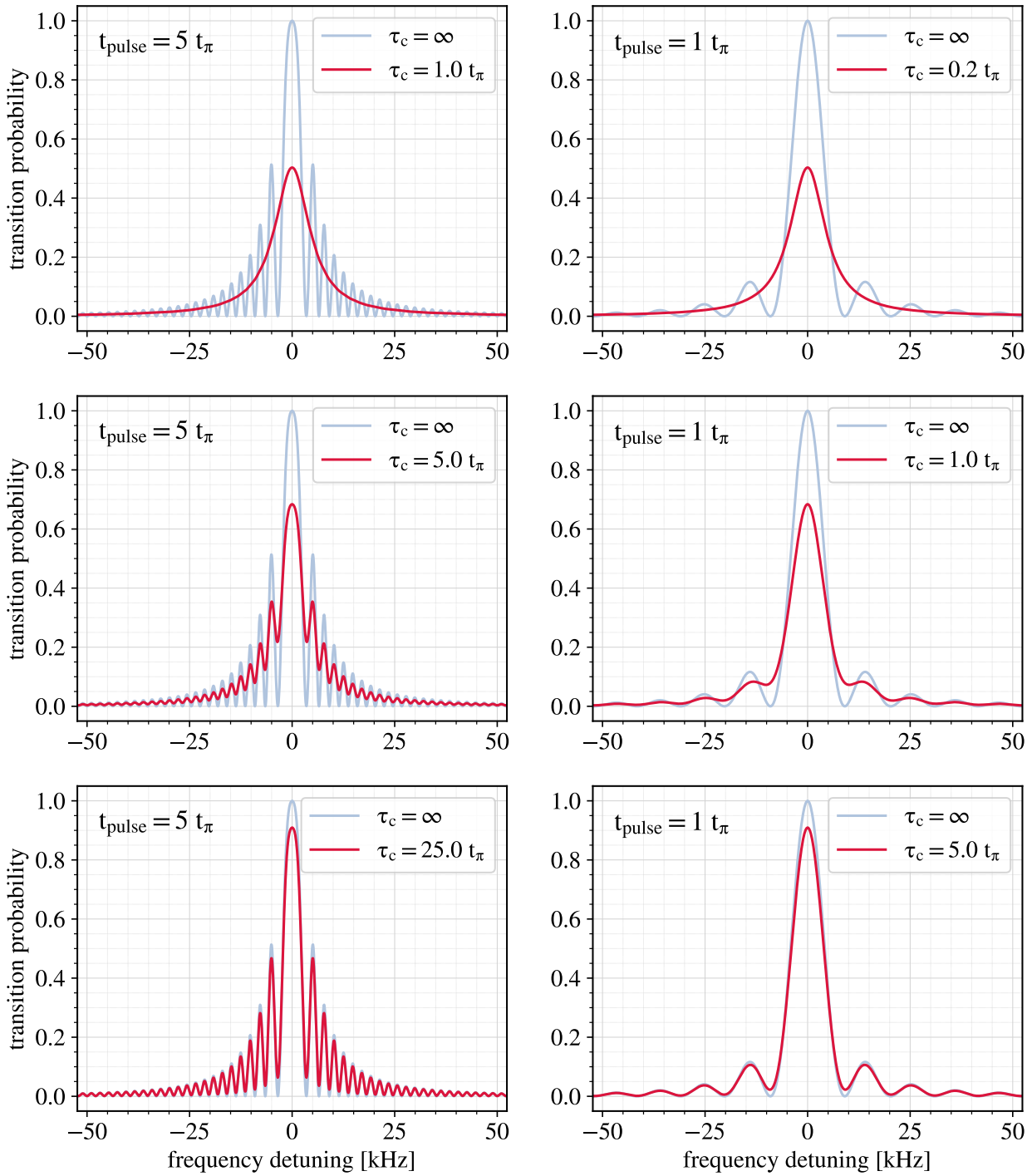

Figure 3.4 – Rabi resonance curves with decoherence effect (red line) in comparison to Rabi resonance curves generated for the infinite coherence time (light blue lines). The coherence time is varied in respect to the π-pulse duration.

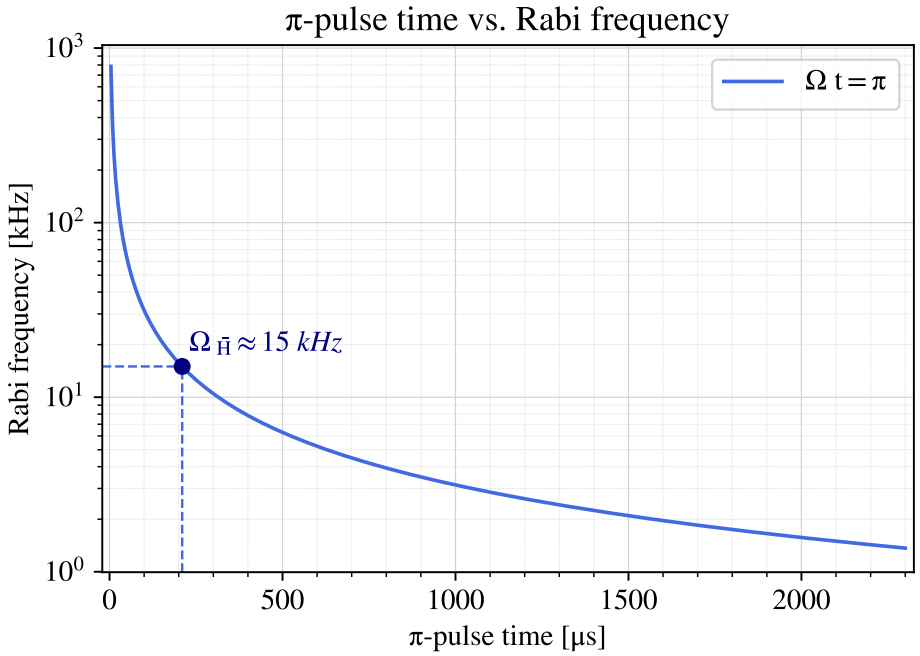

Figure 3.5 – Relationship between Rabi frequency Ω and time t_π corresponding to a π-pulse. For the future reference a Rabi frequency measured in ALPHA-2 trap for antihydrogen ($\approx \cdot 15$ kHz) [187] is marked. The duration of the π-pulse is around 210 μs.

Experimentally the Rabi frequency can be found by exposing the atom to resonant pulses ($\omega_i = \omega_0$) of varied duration but constant intensity. Plotting the transition probability as a function of pulse duration should give a data set that would look like the plot in Fig. 3.1. From this plot, the time corresponding to the π-pulse could be extracted and the Rabi frequency calculated. For an unknown resonance frequency, this scan should be performed for multiple pulse frequencies ω_i. As we can see in Figure 3.2, for constant Ω, the period of probability change in time decreases with increasing frequency of detuning. This means that the Rabi flopping measured with the slowest oscillation and also with the highest initial amplitude will occur at a frequency that is closest to the resonance frequency ω_0. Alternatively, a π pulse can be found by setting a constant pulse duration and adjusting the pulse power to obtain variable Rabi frequencies.

The duration of the *EM*-wave pulse with respect to the Rabi frequency changes the transition probability for the off-resonant ($\delta_i \neq 0$). Figure 3.3 presents how the Rabi resonance curve changes depending on the duration of the *EM* pulse compared to the use of the perfect π-pulse. The damping of the Rabi oscillation is neglected here. We can see that for the same phase of the $\Omega' t$ factor, the transition probability on resonance is the same, for example:

- for $t = \pi, 3\pi, ..$ the probability is $\mathcal{P}(f_0) = 1$;
- for $t = \frac{1}{2}\pi, \frac{3}{2}\pi, \frac{5}{2}\pi, ...$ it is $\mathcal{P}(f_0) = 0.5$;
- for $t = 2\pi, 4\pi, ..., \mathcal{P}(f_0) = 0$.

Examples of Rabi resonance curves, as in Equation 3.1.9, for even and odd multiple of π and $\frac{\pi}{2}$-pulse are presented in Figure 3.3. For longer pulses (corresponding to odd multiple π-pulse, which gives the maximum signal at resonance frequency) the main resonance line becomes narrower, sidebands increase in magnitude, and approach closer to the 0^{th} order peak. For an ideal Rabi resonance, without decoherence playing a role, increasing the pulse duration would infinitely narrow the central peak, infinitely increasing the resolution of the measured resonance frequency ω_0. For a real experiment, the decoherence of quantum states between atoms in the sample must be considered. Decoherence causes damping of Rabi flopping, which means that with increasing pulse duration, the fraction of atoms in each state oscillates closer to the value $\frac{1}{2}$ (see Figure 3.1), eventually reaching an equal population distribution when atoms are subjected to continuous *EM* radiation. The effect of the decoherence on the shape of Rabi resonance curve is that the heights of the main peak and sidebands decrease and the values of local minima between the sidebands increase, which leads to smoothing the curve. Whenever the pulse duration is a few times longer than the decoherence time τ_c, the sidebands merge into a single broad peak with a maximum value equal to $\frac{1}{2}$. A comparison between resonance curves with and without the effect of decoherence is presented in Figure 3.4. In conclusion, if the pulse at resonance frequency ω_0 is too long, the maximum fraction of atoms that will change the quantum state is only half of the population.

Rabi experiment of this type was performed at NIST by *Shiga, Itano and Bollinger* with beryllium ions, where a microwave π-pulses induced an electron spin-flip transition [132]. In that work they measured the frequency of the electron spin-flip transition:

$$|\uparrow\rangle = {}^2S_{1/2}(m_I = +3/2, m_J = +1/2) \rightarrow \ |\downarrow\rangle = {}^2S_{1/2}(m_I = +3/2, m_J = -1/2)$$

at a few values of the magnetic fields to extract the value of the diamagnetic correction of the hyperfine constant in the ground state of $^9Be^+$.

The fraction of ions that changed the electron spin state was measured via fluorescence induced by 313 nm laser tuned to the laser cooling transition , since ions in the $|\uparrow\rangle$ state takes part in the cooling transition and emit photons while decaying from the excited state.

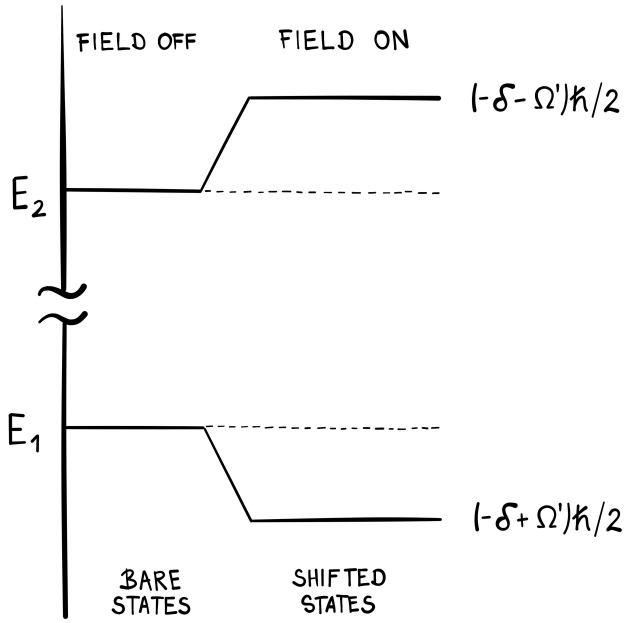

Figure 3.6 – Light induced shift of energy levels of two coupled states. Ω is the Rabi frequency for the transition between the two states and δ is the frequency detuning of the lightwave driving the transition from the resonance frequency. The figure was adapted from Ref. [185].

The work of *Shiga et al.* was an inspiration for us to use the beryllium ions we already have in the ALPHA Experiment (for the purpose of positron sympathetic cooling [1]), to perform a similar experiment in order to measure the magnetic field and to characterise the strength of the microwave radiation inside the ALPHA Penning trap. Magnetometry with $^9Be^+$ was the main subject of this Ph.D. project and the initial results will be presented in Chapter 6.

It is important to underline here that the presence of laser field introduces shift of energy levels called a *light shift* [185], as shown in the Figure 3.6. The magnitude of the shift depends upon the intensity of the laser field. If the microwave pulse is sent during the time that the ions interact with the laser, the resonance frequency would be offset and the peak broadened as reported by *Nakamura et al.* [186]. They reported a transition linewidth 8 kHz for the Rabi method (laser off during microwave pulses), while the linewidth obtained in the so-called continuous method (laser on during microwaves) was 5 times greater and light shift changed the resonance frequency by -16 kHz. Precise measurement of the magnetic field requires obtaining a narrow transition linewidth. Therefore, future magnetometry with beryllium in the ALPHA Experiment should use the proper protocol for the Rabi method.

3.2 Laser cooling theory

Here laser cooling process will be discussed, which is a phenomena of reducing a kinetic energy of atoms (or atomic ions) by interaction with coherent light radiation. Atom is a complex system containing internal energy structure, the photon will interact with the internal degrees of freedom (electronic levels) and with the external degrees of freedom related to its motion. It relies on the fact that atoms absorb photons from a laser beam of very well defined momentum, but then it spontaneously emits a photon in the random direction, which causes that the final momentum of the atom in the direction parallel to the laser beam gets reduced. The momentum in the perpendicular direction increases in the single scattering event (atom absorbing and re-emitting a photon), but it averages to zero over many absorption-emission cycles. This leads to a final reduction in the kinetic energy, which can be associated with decreasing temperature. The explanation presented in these chapters is based mostly on Wineland and Itano's papers [143, 188] and few popular atomic physics textbooks [182, 189, 190].

A requirement for laser cooling of a specific atom is the existence of a so-called *closed cycle transition*. The closed cycle transition means that the electron gets excited from a ground state $|1\rangle$ with high probability to the short lived excited state $|2\rangle$ and that the vast majority of atoms spontaneously decay back to the same ground state $|1\rangle$ from which it can be excited again by the cooling laser (electric dipole transitions fulfil this requirement). There is always some non-zero probability of the electron to fall down into another state $|3\rangle$ than the initial one $|1\rangle$, which does not interact with our cooling laser, we call it a dark state [4]. Even though the probability of the transition $|2\rangle \rightarrow |3\rangle$ is very small compared to the decay $|2\rangle \rightarrow |1\rangle$, after many laser cooling cycles the state $|1\rangle$ gets depopulated due to increasing number of atoms trapped in the $|3\rangle$ state. In order to maintain the number of atoms that interact with the laser and take part in the laser cooling process, people introduce additional laser(s) that drive the transition $|3\rangle \rightarrow |2\rangle$, to bring atoms back to the excited state $|2\rangle$ from which the initial ground state $|1\rangle$ can be repopulated. This process is called repumping, and an additional laser for $|3\rangle \rightarrow |2\rangle$ transition is called a repump laser.

[4] Technically dark state is a state that does not couple to any EM radiation, since any transition out of this state is forbidden (to the first order). But often researchers refer to **dark states** in the respect of the transition of interest driven by the light source existing in the experimental setup.

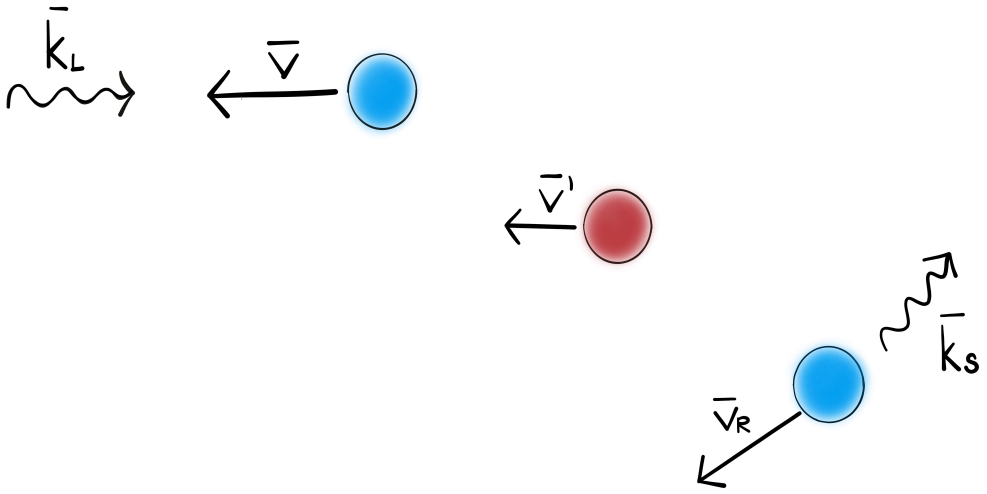

Figure 3.7 – a. photon from the laser beam of momentum $\bar{k}_L$ interacting with the atom moving with initial velocity $\bar{v}$ (atom in a ground state $|g\rangle$; b. atom absorbs the photon, gets excited to the $|e\rangle$ state and continues moving with velocity $\bar{v}'$; c. atom spontaneously decays back to the ground state $|g\rangle$ emitting a photon of momentum $\hbar\bar{k}_s$

3.2.1 Doppler cooling

Doppler effect is a phenomena occurring for any type of waves including electromagnetic waves. The Doppler effect experienced by atoms in motion can give rise to a scattering force, which could reduce the kinetic energy of those atoms, which is called a *laser cooling*. The introduction to the theory behind laser cooling based on the Doppler effect will be given based on *"Laser cooling of atoms"* (*Phys.Rev.A, 1979*) by D.Wineland and W.Itano [188].

If we consider an atom of a mass m, moving with velocity $\bar{v}$ and a monochromatic beam of light: laser of a frequency ω_L, propagating with a wave vector $\bar{k_L}$, the atom will experience a shifted frequency of light comparing to the the observers sitting in the laser lab:

$$\omega_L^{at} = \omega_L - \bar{k}_L \cdot \bar{v} \tag{3.2.1}$$

For the case when atom is moving in the direction counter propagating to the laser beam ($\bar{k}_L \cdot \bar{v} < 0$), the atoms sees higher frequency of the photons than measured in the lab frame.

Now we should consider interaction of an atom with the laser. We use an approximation that atom is a two-level system with a ground $|g\rangle$ and excited $|e\rangle$ states separated by energy:

$$E_{eg} = \hbar\omega_0 \tag{3.2.2}$$

where ω_0 is a frequency of a photon that could cause transition $|g\rangle \rightarrow |e\rangle$.

The difference between laser frequency in the laboratory frame and the resonance frequency is called a *frequency detuning*:

$$\delta = \omega_L - \omega_0 \tag{3.2.3}$$

If the laser frequency seen in the atom's frame of reference is equal or greater than the transition frequency ($\omega_L^{at} \geq \omega_0$), atom can absorb a photon. The excessive energy is converted into the kinetic energy of the atom

$$\omega_L^{at} = \omega_0 + E_{rec}/\hbar \tag{3.2.4}$$

E_{rec} is called a *recoil energy* and equals to:

$$E_{rec} = (\hbar k_L)^2/2m \tag{3.2.5}$$

By combining Equations 3.2.1 and 3.2.4, we obtain the frequency of the absorbed photon [5]:

$$\omega_{abs} \equiv \omega_L = \omega_0 + \bar{k}_L \cdot \bar{v} + E_{rec}/\hbar \tag{3.2.6}$$

Detuning of the laser frequency in the absorption process is equal to

$$\delta = \bar{k}_L \cdot \bar{v} + E_{rec}/\hbar \tag{3.2.7}$$

Since the first term on the right side of the Equation 3.2.7, associated to the Doppler shift, is significantly greater in absolute value than second term with the recoil energy [6], the detuning is negative for the counter propagating laser beam and atom's velocity. Then the laser frequency ω_L is smaller than that of ω_0, which is referred to as *red detuning*. This means that the laser frequency tuned below the resonance of the atomic transition targets atoms that move towards the laser beam at velocity $\bar{v}$.

After photon absorption, the atom gets excited to a higher electronic state $|e\rangle$ and continues its motion with a velocity v'. The atom will decay back to the ground state $|g\rangle$ with a time constant $\tau = 1/\gamma_0$, emitting a photon of a energy $\hbar\omega_s$ and a wave vector $\bar{k}_s$, which causes a recoil of the atom [7]

$$\omega_{em} \equiv \omega_s = \omega_0 + \bar{k}_s \cdot \bar{v}' - E_{rec}/\hbar \tag{3.2.8}$$

[5] $\omega_L = \omega_0 + \bar{k}_L \cdot \bar{v} - \omega_0\beta^2/2 + E_{rec}/\hbar$, but the second order Doppler effect is very small $\beta = v/c << 1$, so we can neglect it.

[6] The recoil energy is small comparing to the energy lost due to the Doppler cooling, so quite often it is neglected in calculations.

[7] The recoil caused by emitting a photon is $E'_{rec} = (\hbar\bar{k}_s)^2/2m$, where $k_s^2 = (\bar{k}_L + \Delta\bar{k})^2 = k_L^2 + 2\bar{k}_L \cdot \Delta\bar{k} + (\Delta k)^2$, but $(\Delta k)^2$ is small and $\bar{k}_L \cdot \Delta\bar{k}$ averages to zero, so in approximation $E'_{rec} \simeq E_{rec}$

The process of spontaneous emission produces photons of random momentum $\hbar\bar{k}_s$ and the atom is recoiled due to momentum conservation. So in total the process of photon absorption and re-emission could be seen as photon scattering of the atom. A well defined initial velocity of the atom becomes a random final velocity $\bar{v}_R$. That causes the atom's kinetic energy in the direction defined by the incoming photons $\bar{k}_L$ to be reduced for every event in which $|\bar{v}_R \cdot \bar{v}| < |\bar{v}|$ and for the cases where the final velocity is parallel or antiparallel to the initial velocity $|\bar{v}_R| = |\bar{v}|$ the kinetic energy in that direction remains unchanged. The momentum change of the atom in the perpendicular plane can cause an increase or decrease in the kinetic energy, depending upon whether the perpendicular momentum change was aligned or antialigned with the original momentum of the atom before the scattering event. Since photons get scattered in all directions with equal probability, the average momentum change in the perpendicular direction after many scattering events is zero (we can set the second term of Equation 3.2.8 equal to zero). The energy transferred from atom to photon in one single scattering event

$$\Delta E_K(atom) = -\Delta E(photon) = -\hbar(\omega_{em} - \omega_{abs}) = -\hbar(\omega_s - \omega_L) = \hbar\ \bar{k}_L \cdot \bar{v} + 2E_{rec} \quad (3.2.9)$$

For $\hbar\bar{k}_L \cdot \bar{v} + 2E_{rec} < 0$ the kinetic energy of the in the direction of the laser beam is reduced. Recoil contributes to increasing kinetic energy by a small fraction, but as long as the laser frequency is red-detuned and detuning fulfils the condition

$$\delta < -E_{rec}/\hbar \quad (3.2.10)$$

the total kinetic energy will be reduced in a single scattering event. For the opposite case, if we would use a laser frequency with a detuning $\delta > -E_{rec}/\hbar$, after re-emission the kinetic energy would increase. The change of total kinetic energy can be related to the change of temperature

$$\Delta E_K = \frac{3}{2} k_B \Delta T \quad (3.2.11)$$

The total kinetic energy (and simultaneously the temperature) changes proportionally to the number of scattering events. If the kinetic energy of the atom decreases as a result of interaction with a *red-detuned* laser, the process is called *Doppler cooling*.

Specific detuning of the laser frequency ω_L targets atoms moving with a specific velocity $\bar{v}$. When that velocity is changed after the scattering event, the detuning of the laser must also change to increase the probability of the next scattering event to occur. With decreasing

temperature, the laser frequency must be shifted closer to the resonance frequency ω_0, which is often referred to as a *frequency chirp*. After a sufficient number of scattering, atoms can reach very low temperatures, on the order of millikelvin.

Absorption cross-section and cooling rate

The rate of change in kinetic energy for a single atom depends on the average energy charge per scattering event $\langle \Delta E \rangle_s$

$$\langle \Delta E \rangle_s = 2E_{rec} + \hbar \bar{k} \cdot \bar{v} \tag{3.2.12}$$

and the photon scattering rate γ_s, which is equal to the number of photons times the photon absorption cross-section $\sigma(\omega)$

$$\gamma_s = \frac{I}{\hbar\omega} \cdot \sigma(\omega) \tag{3.2.13}$$

which depends upon the intensity of the laser I [8] and the absorption cross-section $\sigma(\omega)$ for the photon at frequency ω:

$$\sigma(\omega) = \sigma_0 \frac{(\gamma_0/2)^2}{(\omega_{abs} - \omega)^2 + (\gamma_0/2)^2} \tag{3.2.14}$$

where γ_0 is the natural linewidth of the transition and σ_0 is the resonant scattering cross-section depending upon the electric-dipole moment of the transition $\hat{d}_{eg}$, its resonance frequency ω_0 and light's polarisation $\hat{\epsilon}$:

$$\sigma_0 = \frac{6\pi c^2}{\omega_0^2} |\hat{\epsilon} \cdot \hat{d}_{eg}|^2 \tag{3.2.15}$$

For a single laser beam, incoming from x-direction, rate of kinetic energy change for single atom equals to:

$$\frac{dE}{dt} = \frac{I}{\hbar\omega} \sigma(\omega)(\hbar k v_x + 2E_{rec}) \tag{3.2.16}$$

For a collection of atoms, the average cross section could be obtained by averaging velocities in the direction of the laser beam v_x, which are described by Maxwell-Boltzmann distribution:

$$\langle \sigma(\omega) \rangle = \sigma_0 \int_{-\infty}^{+\infty} \frac{exp[-(v_x/\sqrt{2k_BT/m})^2]}{\sqrt{\pi}\sqrt{2k_BT/m}} \frac{dv_x}{1 + [(2/\gamma_0)(\omega_0 + kv_x + E_{rec}/\hbar - \omega)]^2} \tag{3.2.17}$$

[8] Laser intensity across the atoms motion is assumed to be uniform to avoid necessity of considering the intensity gradient force acting on the atoms

The average rate of kinetic energy change for ensembles of atoms can be obtained by substituting this average cross-section to the Equation 3.2.16:

$$\left\langle \frac{dE}{dt} \right\rangle = \frac{I\sigma_0}{\hbar\omega} \int_{-\infty}^{+\infty} \frac{exp[-(v_x/\sqrt{2k_BT/m})^2]}{\sqrt{\pi}\sqrt{2k_BT/m}} \frac{(\hbar k v_x + 2E_{rec})dv_x}{1 + [(2/\gamma_0)(\omega_0 + kv_x + E_{rec}/\hbar - \omega)]^2} \tag{3.2.18}$$

Laser cooling of free atom would reduce the kinetic energy in the direction of the laser beam propagation, but increase the energy in the other directions due to the recoil heating. For this reason, three pairs of counter-propagating laser beams in x,y,z directions, are often used. This six-laser beam configuration is called an *optical molasses*. Two counter-propagating beams create a force on the atom that can be described as a viscous force. From that configuration, the maximum cooling rate occurs for a frequency $\omega = \omega_0 + E_{rec} - 1/2\gamma_0$ and it is equal to

$$\frac{dE_x}{dt} = \frac{2I\sigma_0}{\hbar\omega}\Big(- \frac{\hbar k^2 \langle v_x^2 \rangle}{\gamma_0} + E_{rec}\Big) \tag{3.2.19}$$

Doppler cooling limit

The minimum kinetic energy E_x is achieved when there is no further energy decrease

$$dE_x/dt = 0 \tag{3.2.20}$$

and this minimum kinetic energy is equal to

$$\langle E_x \rangle_{min} = \frac{1}{4}\hbar\gamma_0 \tag{3.2.21}$$

The minimum kinetic energy does not depend on the laser intensity. Since the thermal energy associated with a single degree of freedom is $E_x = \frac{1}{2}k_BT$, the minimum temperature of the atoms that can be reached with this method is

$$k_BT_D = \frac{1}{2}\hbar\gamma_0 \tag{3.2.22}$$

and the temperature T_D is called a *Doppler limit*. This lowest temperature predicted by the Doppler cooling mechanism was derived for the configuration of two counter propagating laser beams detuned by the same frequency δ and this is a temperature in the co-linear direction. To achieve cooling in all three dimensions, additional two pairs of beams, in the two other perpendicular directions are needed, referred to as *three-dimensional optical molasses*, in the case if there is no coupling between the degrees of freedom, which is a case for freely propagating atoms. Although Doppler cooling is not the only mechanism for cooling atoms and temperatures below Doppler limit can be achieved [141, 142].

3.2.2 Laser cooling in a Penning trap

The picture of laser-cooling freely propagating atoms is suitable for atomic beams, when atoms are given a certain initial velocity (for example from the thermal energy of the oven or laser energy in the ablation process), but for many modern applications, including this work, laser-cooling is performed on trapped atoms or ions. Here we will be discussing laser-cooling of ions trapped with electric and magnetic fields. For ions trapped in the potential wells, their motion is a combination of oscillations defined by the shape of the potential and the velocities of the ions are changing periodically. The mechanism of laser cooling of ions in a harmonic and Penning trap is well explained by W.M.Itano and D.J.Wineland in *"Laser cooling of ions stored in harmonic and Penning traps"* (*Phys.Rev.A, 1982*) [143]. Here, only key points regarding cooling of trapped ions will be presented.

Laser cooling in a harmonic trap

The motion of an ion trapped in the three-dimensional harmonic well can be described by oscillations in three directions and the frequencies of these oscillations are $\omega_x, \omega_y, \omega_z$. In the Penning trap we will look at the characteristic frequencies: axial ω_z, cyclotron ω_c and magnetron ω_m (Equations 2.1.10, 2.1.18, 2.1.19).

We distinguish two regimes depending upon the decay time from the excited level, related to the transition linewidth $\tau = 1/\gamma_0$, to the motional frequencies ω_i, $i = x, y, x$ in Cartesian coordinates in 3D harmonic trap or $i = c, m, z$ in a Penning trap:

– *weak binding regime*: $\omega_i \ll \gamma_0$

– *strong binding regime*: $\omega_i \gg \gamma_0$

During the oscillation period $T_i = 2\pi/\omega_i$ the velocity of the atom v_i changes, for the ideal harmonic trapping potential the relationship would be

$$v_i(t) = v_{i,max} sin(\omega_i t + \varphi) \tag{3.2.23}$$

For the non-harmonic potential the velocity change would have to be evaluated. The most important message at this moment is that the velocity of the trapped atom/ion changes periodically. For a given laser frequency ω , the Doppler-shifted frequency seen by the atom (Equation 3.2.1) will also change periodically.

In the weak binding regime the frequency of scattering of photons on the ion is much greater than the frequency of the ions's motion in the trap and in this regime Doppler cooling is applicable. The photon's scattering occurs on the time scales significantly shorter than a period of oscillation in a harmonic trap, so at each moment of atomic semi-constant velocity there are many absorption and emission events occurring (of course if the Doppler-shifted frequency lies in the absorption spectrum of the atom). It is a good approximation that the atom is propagating freely between scattering events with the photon. We can say that for each velocity of the atom we can apply the same energy change equations as for the unbounded atom (Eq. 3.2.16). Then one can find the average velocity $\langle v_i \rangle$ to get the average cooling rate for the atom in the harmonic potential well during one oscillation period. In the case of many ions, if the frequency of collisions between them is much higher than than the optical transition rate , we can average over a Maxwell-Boltzmann velocity distribution as for the case of free atoms in Equation 3.2.18. Rate of energy change for each direction in the case of one laser beam propagating in the x-direction:

$$\frac{dE_x}{dt} = \frac{I}{\hbar\omega} \left\langle \sigma(\omega, \vec{v}) \left[\hbar k v_x + E_{rec} \left(1 + f_{sx}\right)\right] \right\rangle_v , \tag{3.2.24a}$$

$$\frac{dE_y}{dt} = \frac{I}{\hbar\omega} \langle \sigma(\omega, \vec{v}) \rangle_v E_{rec} f_{sy}, \tag{3.2.24b}$$

$$\frac{dE_z}{dt} = \frac{I}{\hbar\omega} \langle \sigma(\omega, \vec{v}) \rangle_v E_{rec} f_{sz} \tag{3.2.24c}$$

where $f_i \equiv \hat{k}_i^2$ and $f_{si} \equiv \int \mathcal{P}_s(\hat{k}_s) \hat{k}_i^2 d\Omega$ are the parameters characterising the photons scattering angular distributions, so the recoil energy is distributed among the degrees of freedom according the probability $\mathcal{P}_s(\hat{k}_s)$ of scattering in the direction $\hat{k}_s$. As mentioned in the previous section, cooling in the direction of the beam, here in the x direction, occurs if the cooling due to the Doppler effect $\hbar k v_x$ is greater than the heating due to the recoil $R_{rec}(1 + f_{sx})$. For the remaining two degrees of freedom, there is only heating due to the recoil. If only one laser beam is used for the Doppler cooling, its intensity should be limited, such that the transition rate is small enough to avoid heating the motion in the directions perpendicular to the laser beam due to recoil heating. In many modern applications this is solved by using 3 perpendicular laser beams.Alternatively, another method of cooling the ion in the harmonic well with a single laser beam is to tilt the beam such that it is not parallel to any of the principal axes and it effectively has a cooling component in every of the x, y and z directions.

Laser cooling in a Penning trap

In the Penning trap, the motion of an ion is a combination of three fundamental motions: axial bounce along the z axis and a superposition of two circular motions in the xy plane, which are fast cyclotron motion due to the uniform magnetic field and slower magnetron orbiting in the xy plane due to the $E \times B$ drift. Axial motion can be a harmonic oscillation[9] ω_z (Equation 2.1.10), while the radial motion, instead of the frequencies in the Cartesian coordinates ω_x and ω_y, is described by two frequencies: magnetron ω_m and (modified) cyclotron ω_c' (see Equations 2.1.18 and 2.1.19). The term *"cooling"*, in the context of a Penning trap, refers to decreasing the kinetic energy. Laser cooling reduces the kinetic energy of an ion, so it reduces the amplitudes of motions (axial r_z , cyclotron r_c and magnet r_m). For the axial and cyclotron motion, cooling reduces the amplitude of motion and effectively causes that the total axial and cyclotron energy to decrease. In the case of magnetron motion, reducing r_m, reduces the radial position r away from the trap centre, causing an increase in total magnetron energy (see Figure 2.8). A laser beam aligned in the z axis would cool the axial motion but heat the magnetron and cyclotron motions by recoil. The cyclotron motion is cooled, hence r_c reduced, when the velocity change of the scattered photon $\Delta\bar{v} \equiv \hbar(\bar{k}-\bar{k}_s)/m$ is tangential to and in the opposite direction to the cyclotron motion, similarly to the axial motion (harmonic oscillator). The magnetron radius r_m is reduced, so the magnetron motion is cooled, when the photon scattering occurs in the tangential direction, but in the same direction as the magnetron motion. For the laser beam in the xy plane, e.g. aligned with the x axis, the axial motion is heated by the recoil, and when one of the radial motions is heated, the other gets cooled. Adding some beam component along the z axis can cool the axial motion, but the cyclotron and magnetron motions cannot be cooled at the same time with combination of multiple laser beams, aligned through the centre of the Penning trap, if the beams have uniform intensity. Cooling cyclotron and magnetron motion at the same time can be achieved with a non-uniform laser beam in the xy plane, which is offset from the trap's centre (with $y_0 > 0$), such as the higher intensity is on the side on which the laser beam is co-propagating with the magnetron motion, see in Figure 3.8.a.

[9] In the Penning-Malmberg trap with a stack of cylindrical electrodes, the electric potential well is in principle anharmonic, but the bottom of the well can be approximately a harmonic potential. If the particle has a lot of kinetic energy or is inside the plasma, which offsets the potential generated by the trap ϕ_T by a value of the plasma space-charge ϕ_P, it moves through potentials that are no longer harmonic.

Assume a linear change of the laser intensity along the y-axis

$$I(y) = I_1(1 + y/y_0) \tag{3.2.25}$$

where I_0 is the laser intensity in the middle of the trap $y = 0$ and that intensity increases as I_1/y_0. The laser beam intensity gradient causes cooling of the magnetron motion, while it heats up the cyclotron motion. The cyclotron motion is cooled due to the Doppler effect, if the laser detuning is negative $\delta_1 < 0$, which still causes heating to the magnetron motion. Axial motion can be cooled by having another red-detuned laser beam $\delta_2 < 0$ in the z-direction of the uniform intensity I_2. Here, the cooling of motion in the Penning trap is referred to as reduction of the amplitude of this motion. Therefore, the cooling rate would be expressed as the change of the radii associated with each motion.

Magnetron radius r_m change:

$$\frac{d\left\langle r_m^2\right\rangle}{dt} = \overbrace{-\gamma_{s1}\hbar k_1 \left\langle r_m^2\right\rangle / m y_0(\omega_c' - \omega_m)}^{\text{intensity gradient cooling}} \overbrace{+2\gamma_{s1}\delta_1\hbar k_1^2\omega_m \left\langle r_m^2\right\rangle / m(\omega_c' - \omega_m)\left[(\gamma_0/2)^2 + \delta_1^2\right]}^{\text{Doppler heating } (\delta_1 < 0)} \underbrace{+\left(\gamma_{s1}E_{rec}/m(\omega_c' - \omega_m)^2\right)\left[1 + (1 + \gamma_{s2}/\gamma_{s1})\left(f_{sx} + f_{sy}\right)\right]}_{\text{heating due to recoil}} \tag{3.2.26}$$

Cyclotron radius r_m change:

$$\frac{d\left\langle r_c^2\right\rangle}{dt} = \overbrace{\gamma_{s1}\hbar k_1 \left\langle r_c^2\right\rangle / m y_0(\omega_c' - \omega_m)}^{\text{intensity gradient heating}} \overbrace{-2\gamma_{s1}\delta_1\hbar k_1^2\omega_c' \left\langle r_c^2\right\rangle / m(\omega_c' - \omega_m)\left[(\gamma_0/2)^2 + \delta_1^2\right]}^{\text{Doppler cooling } (\delta_1 < 0)} \underbrace{+\left(\gamma_{s1}E_{rec}/m(\omega_c' - \omega_m)^2\right)\left[1 + (1 + \gamma_{s2}/\gamma_{s1})\left(f_{sx} + f_{sy}\right)\right]}_{\text{heating due to recoil}} \tag{3.2.27}$$

Axial bounce amplitude r_z change:

$$\frac{d\left\langle r_z^2\right\rangle}{dt} = \overbrace{-2\gamma_{s2}\delta_2\hbar k_2^2 \left\langle r_z^2\right\rangle / m\left[(\gamma_0/2)^2 + \delta_2^2\right]}^{\text{Doppler cooling } (\delta_2 < 0)} \overbrace{+\left(2\gamma_{s2}E_{rec}/m\omega_z^2\right)\left[1 + (1 + \gamma_{s1}/\gamma_{s2})\, f_{sz}\right]}^{\text{heating due to recoil}} \tag{3.2.28}$$

Scattering rates γ_{s1} and γ_{s2} of both laser beams ($l = 1, 2$) with wavenumber k_l:

$$\gamma_{sl} = \frac{I_l\sigma_{0l}}{\hbar\omega_l}\frac{(\gamma_0/2)^2}{(\gamma_0/2)^2 + (\omega_0 - \omega_l)^2} \tag{3.2.29}$$

where σ_{0l} are the absorption cross sections for both laser beams.

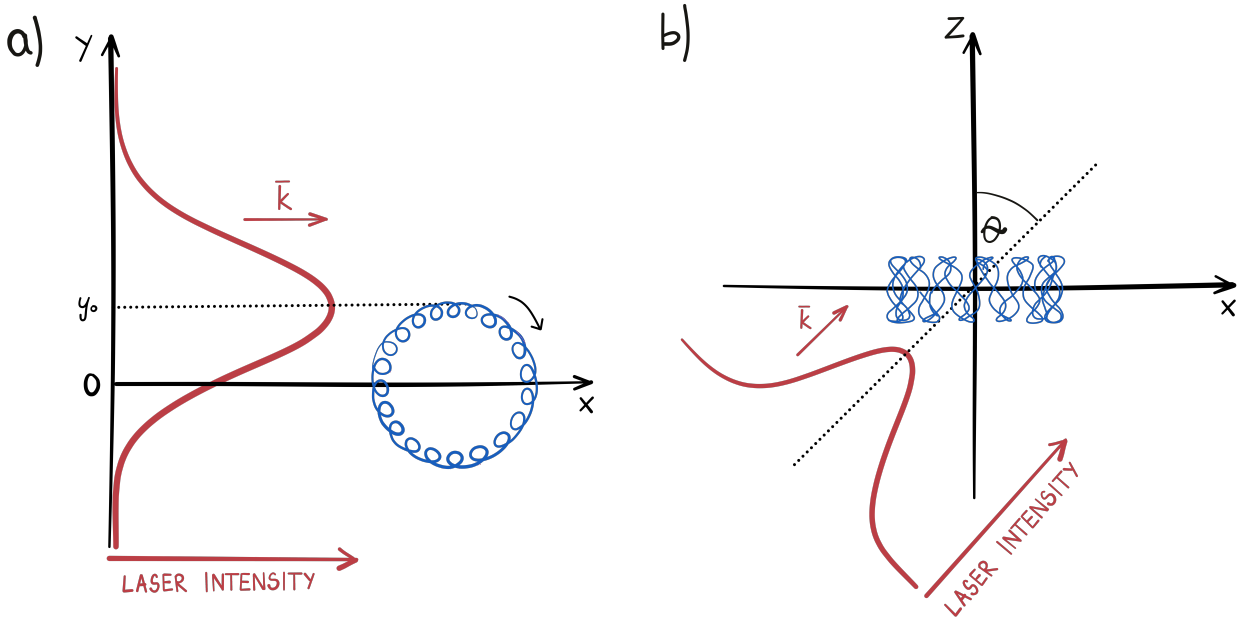

Figure 3.8 – Schematic diagrams representing cooling-laser orientation in space in respect to the ions motion in the Penning trap. a) Offset from the trap's centre in the x-y plane necessary to achieve gradient cooling of the magnetron motion. b) Tilt in the x-z plane to cool axial and radial motions with at the same time with just a single laser beam. Figure adapted from Ref. [191].

There is a regime in which the intensity gradient cooling is dominating in the magnetron motion and the Doppler cooling is dominating in the cyclotron motion:

$$\omega_m < \frac{(\gamma_0/2)^2 + \delta_l^2}{2k_1 y_0 \delta_l} < \omega_c' \tag{3.2.30}$$

The r_m, r_c and r_z will continue to change until a steady state is reach when the cooling and heating forces compensate each other. The total kinetic energy in this final state, therefore the minimal temperatures achievable depend on the detunings of both beams (ω_1 and ω_2) and their relative intensity γ_{s1}/γ_{s2}.

A cooling laser in the z axes could also be achieved with the first beam tilted out of the xy plane to introduce a laser beam component in the axial direction, intersecting the centre of the trap in the xz plane at the angle θ from the z-axis, as shown in Figure 3.8. This single laser beam still has the same intensity gradient along the y-axis. Equations 3.2.26, 3.2.27, 3.2.28 will be modified by inserting axial and radial component of that single laser beam, a function of $sin^2\theta$, instead of two beams (ω_1, k_1) and (ω_2, k_2) [10] and the condition for simultaneous cooling of cyclotron and magnetron motions is the same as in Eq. 3.2.30.

[10] See Eq. *65a-c* in Ref. [143]

In a Penning trap, these motions can be coupled to each other, meaning that cooling one of them can reduce the kinetic energy of the other motions and provide three-dimensional cooling. Coupling between ion's motion might be caused by the collisions between the ions for a trapped plasma or by the anharmonicity of the potential well, which is often used with Penning-Malmberg traps. The imperfections of the trap design and misalignments, e.g. between the electrodes and the axis of the magnetic field, also contribute to mixing of the ion's motion. Additionally, some special methods can be applied to couple the cyclotron and magnetron motions in the Penning trap:

- axialization, using radial field weakly oscillating at the true cyclotron frequency ω_c [192];
- *Rotating Wall* technique, driving the rotation frequency of the non-neutral plasma [167].

3.2.3 Laser cooling plasma in the Penning trap

In our experiment the plasma of beryllium ions is laser cooled. The main difference between the single particle regime and plasma in the Penning trap is that plasma rotates around the trap axis at a frequency ω_R. The velocity distribution of the charged particles within the plasma is shifted by a value of $\omega_R r$, where r is the radial distance away from the trap centre. For trapped plasmas, the kinetic energy is transferred between different degrees of freedom by collisions between charged particles, which means that in principle a single laser beam can provide three-dimensional cooling [193]. This laser beam should be perpendicular to the z-axis of the Penning trap with the offset along the y-axis (similarly to Fig. 3.8.a), but the laser beam size should be smaller than the radial extent of the plasma. For a laser beam co-propagating with the plasma rotation, the amplitude of radial motion is reduced. As the plasma cools, it becomes more magnetised and a collision rate decreases, leading to reduced energy transfer [194]. Due to the nature of magnetron motion, the perpendicular laser beam, which is reducing the amplitude of radial motion, will not allow to reach the Doppler cooling limit. To achieve the lowest temperature, a perpendicular beam that provides radial compression should be supplemented with a higher intensity axial beam of a detuning $\delta = -\gamma_0/2$. Alternatively, radial compression can be provided by the *Rotating Wall* technique (discussed in Section 2.4.2). The configuration of combined axial beam *Rotating Wall* compression was chosen for cooling Be^+, due to the fact that radial access for the laser is not possible in the ALPHA Penning trap.

Chapter 4

Beryllium ions production

4.0.1 Laser ablation of beryllium ions

Beryllium ions are generated by *pulsed laser ablation* (*PLA*). Laser ablation is a general term to describe a collection of processes that remove atoms, ions, and small clusters from the surface of the bulk material after impact of pulsed laser beam. It might be heating of the material's surface that causes evaporation, mechanical stress that affects the surface, or breaking structural bonds between atoms in the material [195]. The main advantages of pulsed laser ablation, as a production method for trapped ion experiments, are lower contamination of the vacuum compared to other methods such as atomic oven sources, and stricter control of loading in the form of an ion beam at a time well defined by the laser pulse trigger. Adjusting the laser pulse energy gives some control over number of ablated ions, but the number of ions trapped is the most difficult experimental parameter to control. The ablation process depends upon the energy deposited by the laser per surface area, this is defined as fluence. The minimum fluence required for the ablation process to occur is for singly charged beryllium ions Be^+. We require an increasingly higher fluence for production of increasingly higher charged ions: Be^{2+}, Be^{3+}, etc. Each of these minimal fluences is called *ablation thresholds*. We are interested in Be^+ generation, so we will use *ablation threshold* to refer to the minimal fluence required to produce Be^+. Increasing a fluence above the ablation threshold increases the number of ions produced. Since we do not want to generate any higher charged ions, we try to keep the fluence immediately above the ablation threshold. In the scenario when higher numbers of ions are required, we loaded many bunches of beryllium ions from consecutive ablation pulses, in the process we call *stacking*.

The average kinetic energy of the ion bunch also increases with increasing laser fluence. In our case we can modify the kinetic energy of the ion bunch with an electric field generated by electrodes within the beryllium source assembly (more details in Subsection 4.0.2). We can still use laser pulse energies just above the ablation threshold and accelerate ions to a desired velocity if needed. In general, we do not want ions to have too high kinetic energies, since we want to trap them in a Penning trap using a blocking potential of at most 140 V. All ions that have higher energies that blocking voltage will just pass through the trap. One can imagine tuning the ion beam energy to be high and to generate many more ions, such as we will be trapping only a low energy tail, but since increasing the fluence gives rise to the number of unwanted higher charged ions, this seems to be non-practical approach.

The next parameter that affects the process of ablation is the wavelength of the laser pulse. It has been observed that the shorter the wavelength, the higher the ion yield (Ref. [129, 130]). A shorter wavelength of the ablation laser would cause more atoms to be ionised in the process and eliminate the need for an additional ionising laser. In general, UV or near-UV lasers are desired for pulsed laser ablation [197]. The disadvantage of using shorter wavelengths is that the fluence threshold for double and higher ionised approaches the fluence threshold of the singly ionised products.

The last important aspect during ions generation in the laser ablation process is the angular distribution of the ablated ions. Unlike in the case of atomic oven sources, the angular distribution of the laser ablated ions is not isotropic. There is a maximum yield in the direction perpendicular to the source surface [196]. This produces ions in a collimated beam, giving the additional advantage of using the *PLA* method in the ALPHA trap.

1.	There is a minimum fluence required for the production of ions (*ablation threshold*)
2.	There is a higher fluence threshold for generation of doubly charged ions, then triply ionised, and so on.
3.	Shorter wavelengths of laser pulse give lower fluence threshold for ablation
4.	Increasing fluence increases number of ions generated
5.	Using shorter wavelengths increases the number of ions generated
6.	Ions ablated close to the ablation threshold can be well described by the Maxwell-Boltzmann distribution.
7.	Increasing fluence increases average kinetic energy of the ions.
8.	The maximum number of ions is generated in the direction normal to the surface of the source.

Table 4.1 – Summary of the most important characteristics of the pulsed laser ablation process. Adapted from Muhammed Sameed's Ph.D. thesis [130]

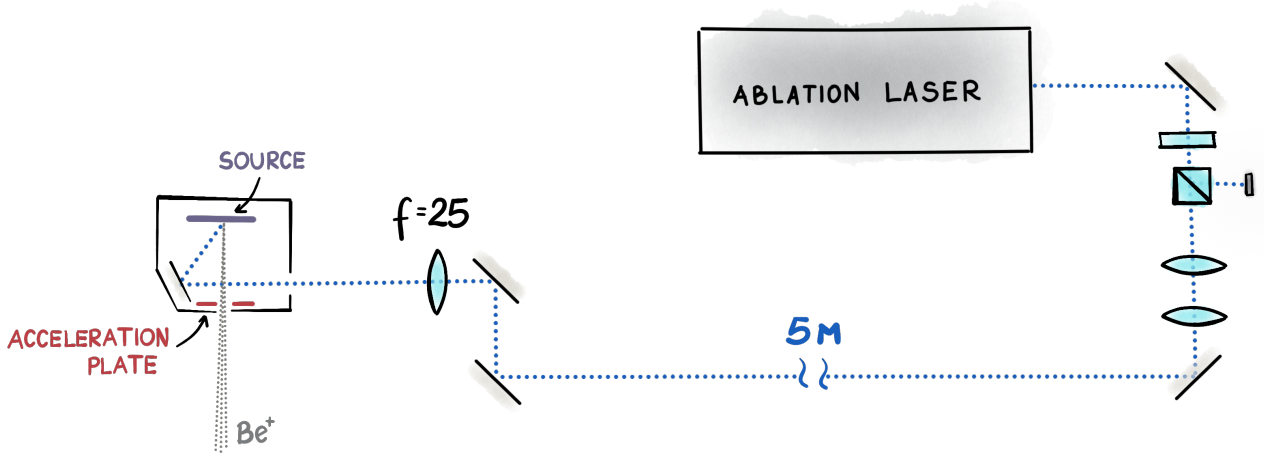

Figure 4.1 – Schematic of the laser setup for beryllium ions ablation. The 355nm pulsed laser is delivered from the laser lab to the experimental apparatus through a periscope.

4.0.2 Beryllium source

The source of Be^+ is a beryllium metal plate (size 13 x 15 mm^2, 0.5 mm thick) installed in a special cage assembly (Figure 4.2). This cage is installed inside the vacuum chamber, at the bottom of a motorised linear translator (called a *stick*) on the upstream end of the ALPHA-2 trap, so that it can be moved in and out of the position in front of the trap's axis. The ablation laser enters the vacuum chamber from the direction perpendicular to the trap axis, reflects at 34° to the normal direction to the mirror installed inside the source assembly, and strikes the beryllium foil at 45°. The beryllium foil is in front of the ALPHA-2 trap, aligned to the radial centre so that the generated ion beam would be loaded along the z-axis of the trap. An electrode with an aperture installed in front of the beryllium foil before ions are injected into the trap helps to form a beam of ions with low transverse energy. This electrode with an aperture is called *acceleration plate* and is connected to the negative voltage. The beryllium foil can also be biased to the positive voltage in a similar way, this plate is referred to as a *source* or a *target*. Both *acceleration plate* and *source* are electrically isolated from each other and from the rest of the cage assembly. The electric field generated between the *source* and *acceleration plate* guides positive ions from the beryllium foil to the aperture and as well repels negative ions (like electrons) to prevent them from being sent into the trap. During the 2019 experimental run, we used voltages +25 V on the source and −10 V on the acceleration plate. Although in 2022 we observed that using +10 V on the source and 0 V on the acceleration plate gave better results with loading Be^+ into the ALPHA-2 trap.

The position of the aperture on the *acceleration plate* defines the direction of velocity of an ion beam injected into the ALPHA-2 trap (to be more precise, it is about how the initial velocity of the ions aligns with the z-axis of the trap). Good alignment of the beryllium ion bunch with the z-axis of the trap is essential for efficient trapping. The cage with a beryllium source is installed at the bottom of the *stick* inside the upstream *Atom Trap* (*US AT*) vacuum chamber. The stick can be inclined from the vertical position in every direction to move within a cone-like volume (the pivot point is the top of the cross-shaped vacuum chamber). The possible movement is limited by the walls of the vacuum chamber. The *US AT stick* must be able to translate freely in between each instrument (beryllium source, electron source, MCP detector, laser mirror, aperture to transport antiproton bunch to the ALPHA-2 trap). The structure of the cage is small and compact, so it does not interfere with the walls of the vacuum chamber, but other instruments protrude significantly from the main body of the *stick*. The biggest instruments, a laser mirror and a MCP detector, are the most at risk of damage, because they are fragile instruments. The risk of hooking the MCP assembly into the wall is even higher after the upgrade of adding electrostatic shielding plates in front of the high-voltage tabs (more details in Section 6.5.5 of Jack Jones' Ph.D. thesis [131]). Correct alignment of the beryllium source is one of the most difficult tasks, since after translation of the *stick* the electron source must also remain aligned with the trap axis. Both the source of particles were designed to have apertures aligned with the vertical axis of the *stick* translation, but in practise they did not happen to be aligned so well. Good alignment is defined by a high trapping rate in the Penning trap. For given species and Penning trap configuration, trapping is provided up to a finite radius. Plasma caught off-axis will produce Helmholtz instabilities causing a radial transport of particles, leading to losses. Additionally, for the antihydrogen generation study [128], which must happen with neutral trap magnets energised, the ions trapped at the high radii will be heated by the octupole field (see J. Jones Ph.D. thesis [131], Section 8.2.1). Particles loaded to the trap follow lines of the magnetic field, so what actually matters is the alignment of the particles sources to the magnetic field apertures. In practise, the alignment of the *stick* must be a compromise between the best loading and trapping of beryllium ions and electrons. Electrons are lighter and more perturbed by magnetic field imperfections, and they are also crucial for antihydrogen formation, so good alignment of the electron source is a priority.

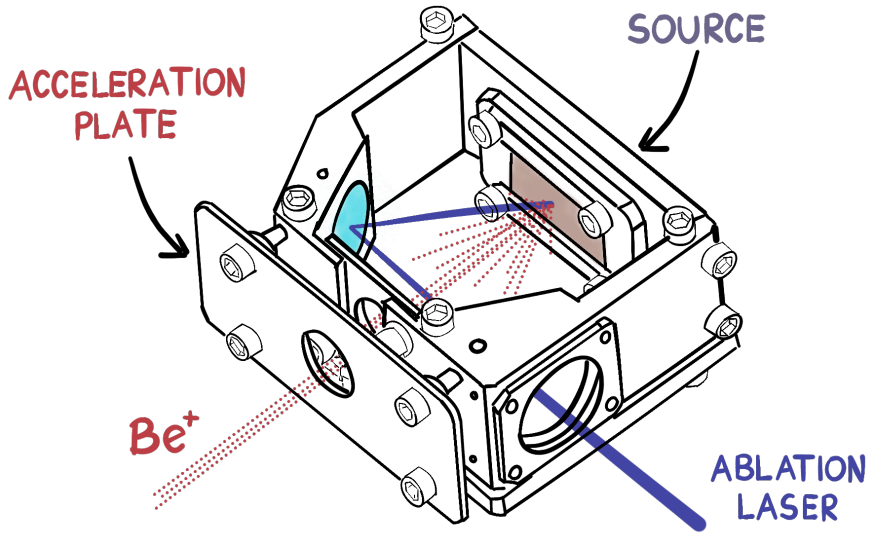

Figure 4.2 – Schematic of the cage assembly for the beryllium source.

4.0.3 355nm pulsed laser

The laser used for the ablation of beryllium ions is *Quantel Ultra 20*, a 1064 nm Nd:YAG pulsed laser with third harmonic generation stage to give 355 nm light [198]. The 355 nm laser source was chosen (instead of other popular 532 nm ablation laser), since it photoionises a significant fraction of ablated beryllium ions, so there is no need to implement additional ionisation laser. The ablation laser outputs 6 ns pulses of 2 mJ. This is too much energy per pulse for our application, so we reduce laser power by using a half-waveplate and a *polarising beam splitter* (*PBS*) cube. The *PBS* filters out one of the polarisations and the half-waveplate rotates the polarisation of the incoming laser beam, so it allows us to modulate the fraction of light that matches the polarisation transmitted through the *PBS*. The shot-to-shot variation of the pulse energy is around 10%. To achieve fluencies in the beryllium ablation range and to be able to easily tune between $2 - 5$ J/cm^2, the optics of a 355 nm laser was designed to have $\sim 20\mu$m laser spot size at the beryllium target. The *Near Field Beam Diameter* of the *Quantel* laser beam is 1 mm and has a divergence of 1 mrad.

Q-switched laser operation

Quantel Ultra 20 is a lamp-pumped laser, which means it uses a *flashlamp* for optical pumping, which is a typical design for generating higher-energy pulses of light. *Flashlamp* is a gas discharge lamp in a long glass tube, which emits light that is used to pump the gain

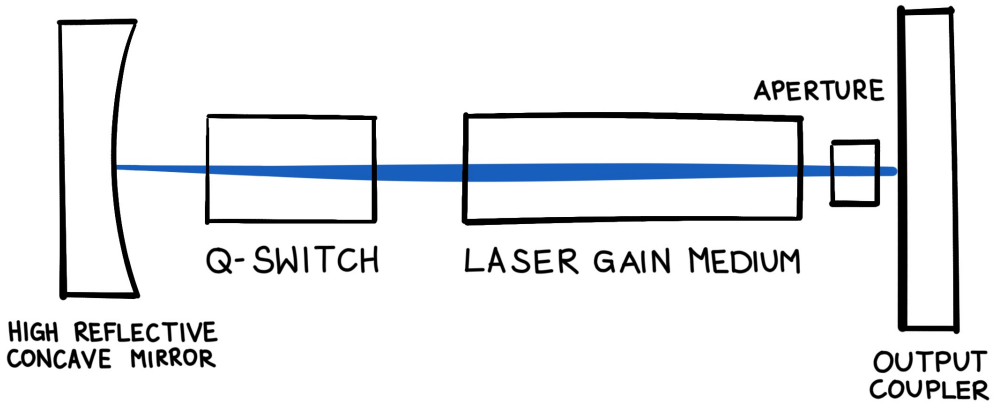

Figure 4.3 – Schematic diagram of Q-switched laser cavity. Figure adapted from Ref. [199].

medium of the laser. The *flashlamp* fires with a repetition rate 20 Hz, so every 50 ms the population inversion in the gain medium is prepared, ready to output the laser pulse. To generate the light output from the resonator cavity, the *Q-switching* technique is used [199]. *Q-switching* method relies on modulating the losses inside the laser cavity, so changing the *quality factor* (*Q factor*) of the laser resonator. *Q-switch* is an active optical modulator (like our *Quantel Ultra 20* laser) or passive saturable absorber inside the resonator that can attenuate (reduce) the light from returning to the gain medium, so increasing the losses and decreasing the *Q factor* of the resonator (schematic design of the *Q-switched* laser on Figure 4.3). *Flashlamp* is pumping the gain medium to create a population inversion, increasing the energy stored in gain medium. When the added energy compensates for losses from spontaneous emission and other sources, then the medium reaches saturation level. At the beginning the resonator losses are kept at a high level above the gain of the laser medium, which causes that there is not enough light building in the resonator to cause a lasing action. Next, the resonator losses are suddenly reduced to the value way below the gain medium by putting the Q-switch into its transparent state, which causes light feedback to the gain medium and laser power to promptly build up in the resonator. This initialises optical amplification by stimulated emission, which is the start of laser action.

Due to large amounts of energy stored in the gain medium, the intensity of light inside the resonator builds up very quickly, but it also gets released very rapidly, which results in outputting a short laser pulse (nanoseconds long) with high peak intensity. The schematic diagram of this process is presented in Figure 4.4, which presents a repetition of the *flashlamp* cycle when *Q-switch* is triggered.

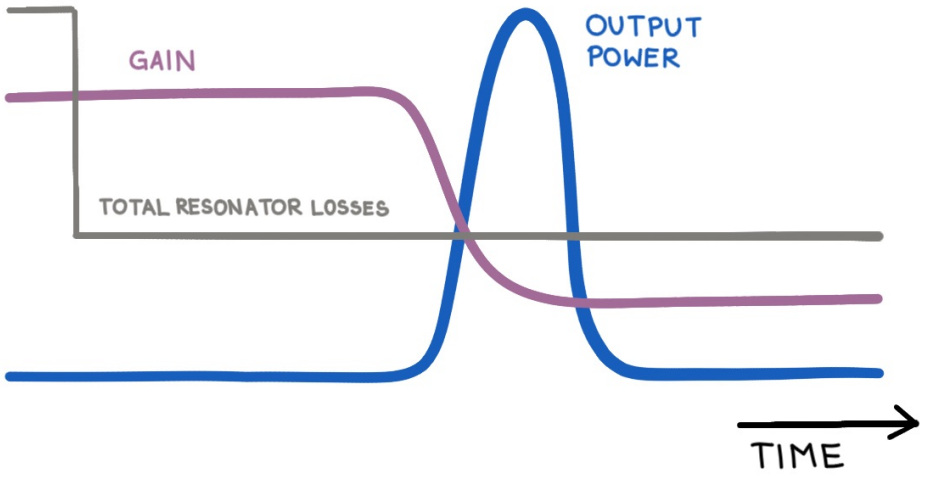

Figure 4.4 – Diagram showing the relationship between output power of the laser and a gain in the Q-Switching method. Figure adapted from [199].

The *Quantel Ultra 20* could be operated in continues pulse mode, when the actions from the Figure 4.4 leading to laser pulse emission repeat. This is useful for laser alignment, but for beryllium ablation, we need to generate a laser pulse on request with a microsecond level of control to trigger the *gate* electrode in the ALPHA-2 Penning trap at the correct moment to catch Be^+. We also want to send only as many laser pulses as desired number of ablation shots. For this we use single pulse request mode, in which the flashlamp remains operating at a standard rate of 20 Hz, but *Q-switch* is triggered to output a laser pulse only upon the request from the *Beryllium Control System*. The *Quantel*'s electronics unit *ICE450* has two inputs for the *flashlamp* and *Q-switch* triggers and two outputs to signal that each of the two (*flashlamp* and *Q-switch*) has been fired. When the ablation pulse is requested from the *Sequencer*, the *FPGA* level code of *Beryllium Control System* waits for the *Flashlamp Output* signal, then waits a constant time (called *Q-switch Delay*) before sending a trigger to fire the *Q-switch* (*Q-switch Input*) and gets the laser's acknowledgement that the ablation pulse has been sent (*Q-switch Output*). The *Q-switch Output* is used to trigger the Faraday Cup signal of the beryllium *source* to record the estimated number of ablated ions.The *Q-switch Delay* time defines the pulse energy and width. In our experiment it is set to 150 μs to give the maximum pulse energy [1]. We considered an option of adjusting *Q-switch Delay* instead of a half-wavelength plate in front of *PBS* to change the ablation pulse energy without going to the laser lab every time, but the shot-to-shot variation of energy was greater (Figure 4.5).

[1] In fact in the *FPGA* code sets the *Q-switch Delay* to 133 μs that account for electronic delay.

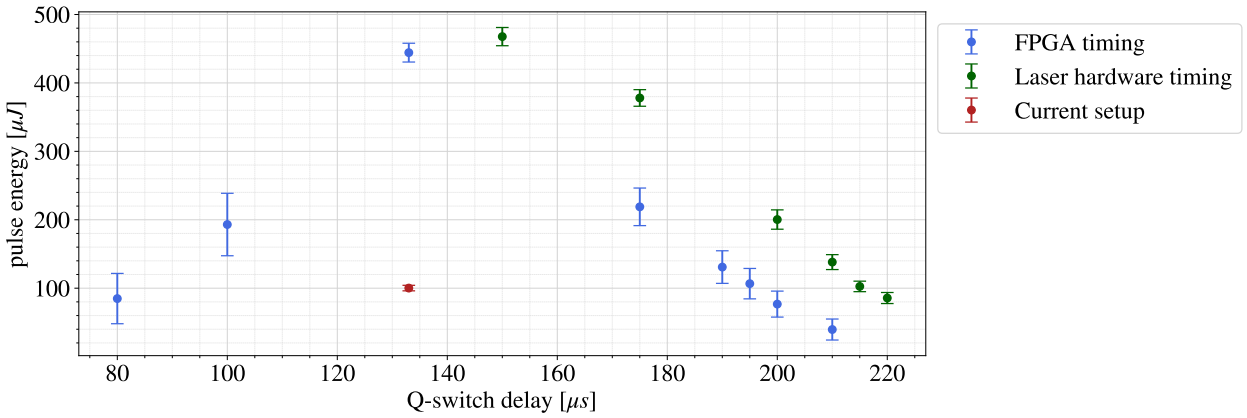

Figure 4.5 – Each data point is 10 pulses of the laser. Error bars are standard deviations. For the blue points, the *Q-switch* delay was varied in the *FPGA* software and the *FPGA* controlled the timing. For green points, the delay was changed with the laser's control unit and the laser handled the timing. The red point is the setup used in the experiment.

Ablation laser delivery to the beryllium source

The 355 nm laser propagates in a free space from the laser lab to the ALPHA-2 trap through roughly a 5 m long periscope. The ablation laser beam is collimated using a telescope (two spherical lenses), installed just after *PBS* and before a periscope, to send it to the experimental zone without the beam increasing in size significantly. Right in front of the vacuum window on the *US AT* chamber there is a focusing lens $f = 25$, which is aligned to a 25 cm optical path to the beryllium foil (accounting for the laser reflecting off of the mirror inside the beryllium source cage). The focusing lens is installed on a translation stage with a micrometre screw, allowing for motion along the laser propagation direction to move the focal point of the lens. Alignment of the focal point of the lens must be done very precisely, because even a minimal change of the beam waist position significantly changes the beam size at the beryllium target. This changes the effective fluence, so the number of ablated ions changes drastically. To change the fluence in a controllable manner, it is easier to change the laser pulses energy rather than the beam size at the beryllium foil.

Advice: Avoiding damage to the mirror with ablation laser

One should be careful not to focus too much power on the mirror inside the vacuum chamber, which could destroy the surface of the mirror. Start the alignment of the ablation laser with rather lower pulse energies.

To align the laser waist on the beryllium foil, we perform a rough alignment based on the estimated distances, and then walk the beam and move the focusing lens while looking at the signal on the oscilloscope connected directly to the beryllium plate (*source* electrode). Beryllium *source* acts like an inverse Faraday Cup: it shows the amount of electrical charge leaving the metal plate when the laser pulse strikes the surface. We fine-tune the ablation laser alignment to achieve the desired fluence: low enough to not generate multiply charged ions, but also high enough to stay above the ablation threshold for many ablations shots. The ion yield does not remain stable; after some time, it always eventually dropped down to zero and the position of the ablation laser had to be realigned. Usually it took tens to a few hundreds of ablation shots for the Be^+ yield to start to decrease. The example of around 200 consecutive ablation shots is shown in Figure 4.6.

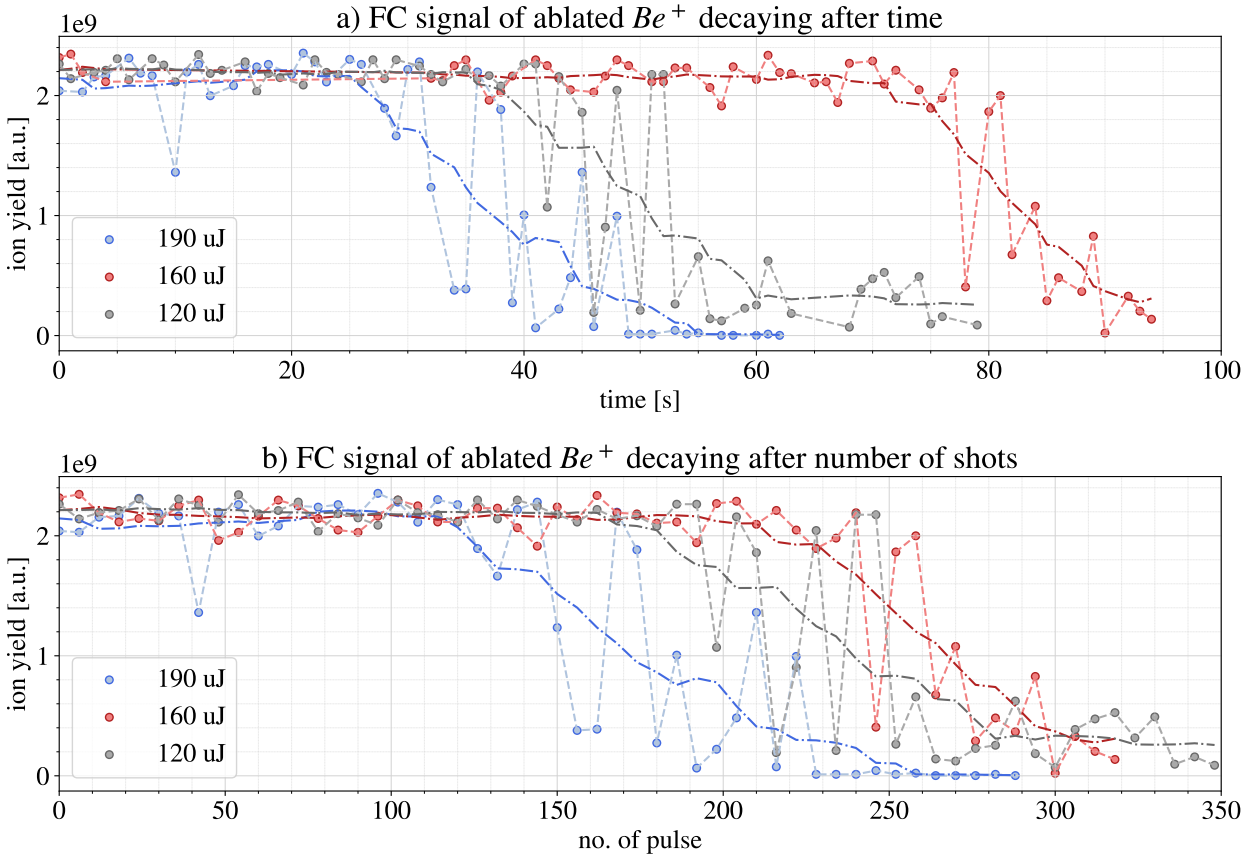

Figure 4.6 – The ion yield is decreasing after executing too many ablation shots (no change in the alignment). Brighter dashed lines connect the consecutive shots. Darker dashed lines connect the moving average values calculated for 11 data points. Data points are the approximated number of charges leaving *beryllium source*, are obtained as a fit to the Faraday Cup signal. The numbers presented on the vertical axis are the approximated number of charges leaving *beryllium source*, which are obtained as a simplest exponential fit to the Faraday Cup signal, and this fitting routine has never been optimised.

This was a single data set taken, one run for each laser pulse energy, and it is not conclusive at all how the pulse energy is related to the number of shots that can be executed before the ablation drops. The observed mixed ordering might be caused by other factors, not just pulse energy. This has not been studied in a controlled manner. Other factors that influence these results are the initial surface state, the beam waist of the ablation laser, and the pulse energy.What we get from this study is that for a given alignment of the ablation, we get 100-150 ablation shots before having to align again. We never studied in great detail how much the number of laser pulses and time it took since the last realignment of the ablation laser were related to number of ablated ions. In fact, we spent a significant fraction of the experimental time realigning the ablation laser. We found that in most cases, when the ablation laser was initially *well* aligned, in order to recover the ablation process that occurred, it was enough to gently poke the position of the final mirror before the focusing lens in the random direction or move the beryllium source position (by translating the *stick* up or down). We observed that, in fact, it was enough to move the *stick* in any direction and then come back to the initial position for the ablation signal to return. We already know that there is a tiny hysteresis of the position after translation of the *sticks*, due to the inaccurate step size of the stepper motor.

A very small offset of the laser spot at the beryllium target can already recover the ablation signal, so we drew a hypothesis that after some number of ablation pulses the surface of the beryllium source gets locally damaged. The position of the stick can end up being displaced by a submillimeter distance after returning to the same position according to the *stick's* controller. We observed that offset of the laser beam position at the beryllium source on this scale brings back good ion yield. Of course, the real offset of the laser spot at the beryllium target might be bigger than the *stick* position offset, since by translating the *stick* we move all the source assembly cage, including the beryllium plate as well as the last 45° mirror. If the angle of incidence of the laser with respect to the mirror surface changes, the position of the laser beam at the beryllium plate could be shifted more than the value of the *stick* position offset. In fact, the beam spot size could change slightly, but the fluence change in this case should not be higher than the fluence change due to the shot-to-shot variation of the pulse energy, which is at least 10%. We have not investigated the surface of the beryllium plate under a microscope to see how it looks after many months of ablation.

4.0.4 Loading Be^+ into ALPHA-2 trap

Initially we believed that the shot-to-shot variation of the number of generated beryllium ions came only from random fluctuations of the ablation process itself, since we measured fairly stable pulse energies (±5% in Section 6.2.1 of J.M.Jones' thesis [131]) for given position of a half-waveplate [2]. Measurements with a new pulse energy meter (Pyroelectric Energy Sensor *ES111C* by *Thorlabs*) showed that the shot-to-shot variation of the pulse energy is actually greater, at least 10%. So the contribution of fluence fluctuation between consecutive laser pulses might be a more significant contributor to the observed variation of the number of ablated ions. Since we do not have the method to measure the energy of exactly the same pulse that is used for the ablation pulse, we could not study the correlation between fluctuations in the pulse energy and the precise number of ablated ions. Practically for the laser ablation of beryllium ions, we were never trying to extract the exact number of ablated ions, we usually only care about the order of magnitude of the Faraday Cup signal of *beryllium source*.

In the context of this work, we developed a method to characterise the beryllium samples before the laser cooling and other manipulations (or at the desired step of the sequence), by splitting the sample into two equal parts and imaging half on the MCP detector at the beginning of each sequence. We internally refer to this method as a *Half-Dump*. By doing so, we could at least compare the number of ions and radial profile of the sample between different experimental sequences, but the properties of the samples still varied between the sequences, making it very difficult to perform a proper systematic study.

Advice: Alignment of the ablation laser on the source

The easiest way to perform the alignment of the ablation laser is to run the pulses in the continuous trigger mode while walking the laser beam. Since the ion yield decreases after some amount of ablation shots, the laser beam should be blocked immediately after a good ablation signal is observed. Any further fine tuning should be done in single laser pulse request mode, otherwise the performed alignment might become obsolete in a few seconds.

[2] We were using old Pulse Energy Sensor from *EnergyMax-RS* series by *COHERENT*

Advice: Periscope for delivering laser beams on long distances

1. The long pipes used to cover the laser beam path between the periscope's mirrors should be made (or coated) with a material that does not reflect the wavelength of the laser. Otherwise, during the alignment of the periscope, the beam reflected off of the pipe's wall could be confused with the actual beam propagating straight through.
2. It is useful to be able to remove the long pipes covering the laser beam (at least the long vertical parts) to see laser beam movement while walking it with the mirrors.
3. A small change in the alignment before and inside the periscope can cause a big misalignment of the final beam position, so it might be worth considering automatised opto-mechanics to correct the output beam position (since the beam is not continuous, traditional active beam stabilisation system would not work).

4.0.5 Beryllium ions detection

Beryllium ions are detected using standard plasma methods used in ALPHA: MCP and Faraday Cup detectors (discussed in Section 2.3) and by photon emitted in the laser cooling process (see Section 5.1.3). A *Hamamatsu* photon counter is installed outside of the vacuum chamber, about 2 metres downstream of the centre of the ALPHA-2 trap (middle of the electrode $E14$) and tilted at an angle of 2.4° from the z axis. The photon counter is connected to the *C8855-01* counting unit and controlled by *LabView* software provided by *Hamamatsu*. It operates in trigger mode once when the data acquisition signal is sent to the counting unit. Photon counts are acquired in the specified time window, called a *gate time*, the shortest time it can be set to is 50 μs.

Chapter 5

Beryllium ions laser cooling

5.1 $^9Be^+$ energy structure

$^9Be^+$ is a lithium-like atom with 2 electrons in the closed shell of $1s$ and one valence electron on $2s\ ^2S_{1/2}$ orbital in the ground state. It is an S-state, so a total angular momentum of that electron ($J = L + S$) is equal to its spin $J = S = 1/2$. The first excited state is $2p\ ^2P$ with electronic total angular momentum $J = 3/2$. A spin-orbit interaction causes splitting of the excited $2P$ state into two manifolds of a fine structure: $^2P_{1/2}$ and $^2P_{3/2}$ separated by energy (in units of frequency) 197 GHz [200, 203].

The nucleus consisting of 4 protons and 5 neutrons has a nuclear spin of $I = 3/2$, which interacts with the total electronic angular momentum and introduces a hyperfine splitting to the energy level structure. The hyperfine splitting for the ground state $^2S_{1/2}$ equals approximately $A_{hfs}(^2S_{1/2}) = 625$ MHz [132] and for the excited state $^2P_{1/2}$ energy splittings are $A_{hfs}(^2P_{1/2}) = 118$ MHz [201, 202] The standard hyperfine constant (magnetic dipole) of the $^2P_{3/2}$ excited state is around $A_{hfs}(^2P_{3/2}) = 1$ MHz and there is also an electric quadruple contribution of around $B_{hfs}(^2P_{3/2}) = 2$ MHz [203, 204], but those splittings are small comparing to the hyperfine splitting of the ground state, so they can be ignored in our case. In the presence of a magnetic field the degeneracy of the energy levels is lifted and we observe a splitting of all the hyperfine levels due to the Zeeman effect. For the ground state of beryllium ion, the Zeeman splitting has a significant contribution, and it has to be accounted for to evaluate the transition energies properly. For the excited state, we can safely neglected the Zeeman splitting in our application of laser cooling.

5.1.1 Ground state $^2S_{1/2}$

For the ground state, we consider the hyperfine interaction between electronic angular momentum $\bar{J}$ and nuclear angular momentum $\bar{I}$ as well as the interaction of both angular momenta, $\bar{J}$ and $\bar{I}$, with the external magnetic field $\bar{B}$ (electronic and nuclear Zeeman interaction). In the low magnetic field the coupling between electronic angular momentum $\bar{J}$ and nuclear angular momentum $\bar{I}$ is stronger than coupling of each of them to the magnetic field and energy levels are well described by the Zeeman effect. The interaction can be viewed as a total angular momentum vector $\bar{F} = \bar{J} + \bar{I}$ interacting with the *B-field*. This can be visualised as a vector $\bar{F}$ precessing around axis in the direction of the magnetic field. In the situation of a weak magnetic field, quantum numbers F and m_F are a good basis to represent the Hamiltonian of the interaction (so-called *coupled representation*: $|J, I, F, m_F\rangle$). The ground state splits into two manifolds according to the total angular momentum: $F = 1$ with 3 energy levels and $F = 2$ with 5 levels.

In a strong magnetic field, the coupling of spin and orbital angular momentum to the magnetic field is stronger than the interaction between them, and m_F and F are no longer good quantum numbers. Both angular momenta, $\bar{J}$ and $\bar{I}$, are precessing around the magnetic field direction independently and we call it the Paschen-Back effect. If we want to describe the energy levels in high magnetic field the representation of $|J, I, m_J, m_I\rangle$ (*uncoupled representation*) is more suitable to be used. For the fields $B > 0.1T$, the energy splitting induced by the strong magnetic field very quickly overcomes the hyperfine splitting structure and instead of two manifolds determined by the total angular momentum of the atom/ion $F = 1$ (3 levels) and $F = 2$ (5 levels), we are getting 2 manifolds defined by the orientation of the spin in the magnetic field: $m_J = 1/2$ and $m_J = -1/2$ with 4 energy levels each.

^{9}Be$^+$ ground states interaction Hamiltonian

A simple Hamiltonian defining energy levels of the ground $\mathcal{H}[2S_{1/2}]$ state of $9Be^+$, includes the magnetic dipole hyperfine interaction (first term), electronic Zeeman interaction (second term), and nuclear Zeeman interaction (third term)[1]:

$$\mathcal{H}[2S_{1/2}] = hA_{hfs}\bar{J}\cdot\bar{I} + g_J\mu_B\bar{J}\ \cdot\bar{B} + g'_I\mu_B\ \bar{I}\cdot\bar{B} \tag{5.1.1}$$

[1]Electric quadrupole moment of the nucleus is neglected

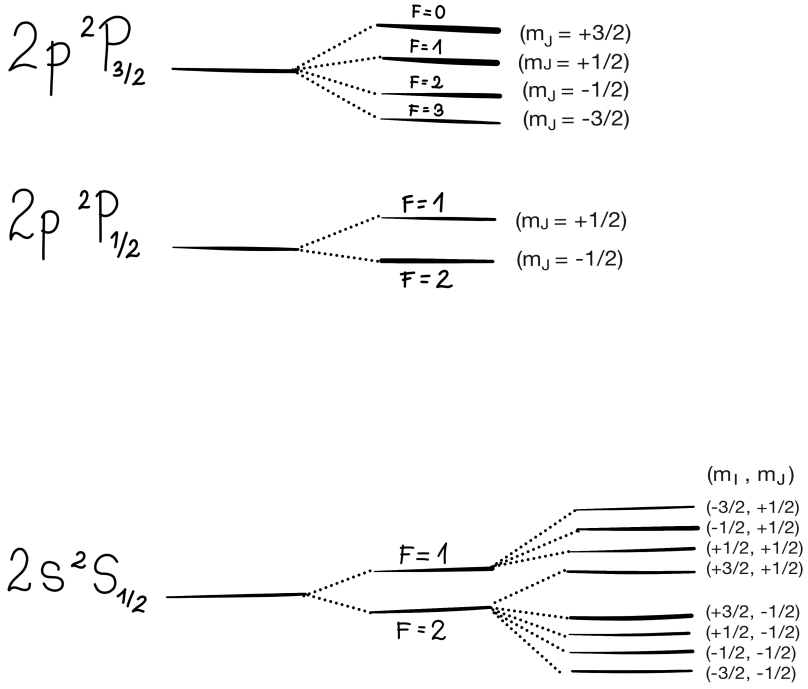

Figure 5.1 – Energy levels structure of Be^+ in a high magnetic field. [132]

where A_{hfs} is the magnetic dipole hyperfine constant value for the $2S_{1/2}$ state in $9Be^+$ (which relates to the magnitude of the hyperfine splitting in $B = 0\ T$), μ_B is the Bohr magnetron and the *g-factors* are defined [2]

$$g_J = -\frac{\mu_J}{J\mu_B} \tag{5.1.2}$$

$$g'_I = -\frac{\mu_I}{I\mu_B} \tag{5.1.3}$$

The hyperfine splitting term is diagonal in the representation $|J, I, F, m_F\rangle$, which means that states expressed as $|J, I, F, m_F\rangle$ (or $|F, m_F\rangle$ for short) are the eigenstates of the hyperfine interaction. Two other terms are diagonal in $|J, I, m_J, m_I\rangle$ ($\equiv |m_J, m_I\rangle$) representation, so the eigenstates of the Zeeman interaction are described on the basis of $|m_J, m_I\rangle$. This means that one or more terms need to be converted to the other representation in order to calculate the energy levels. There is an analytical solution to the Hamiltonian for a specific case of $J = 1/2$, called *Breit-Rabi formula*, that can be used to calculate the energy levels for states with spherically symmetric charge distribution.

[2] This g'_I is different from $g_I = \mu_I/(I\mu_N)$ with a nuclear magnetron μ_N.

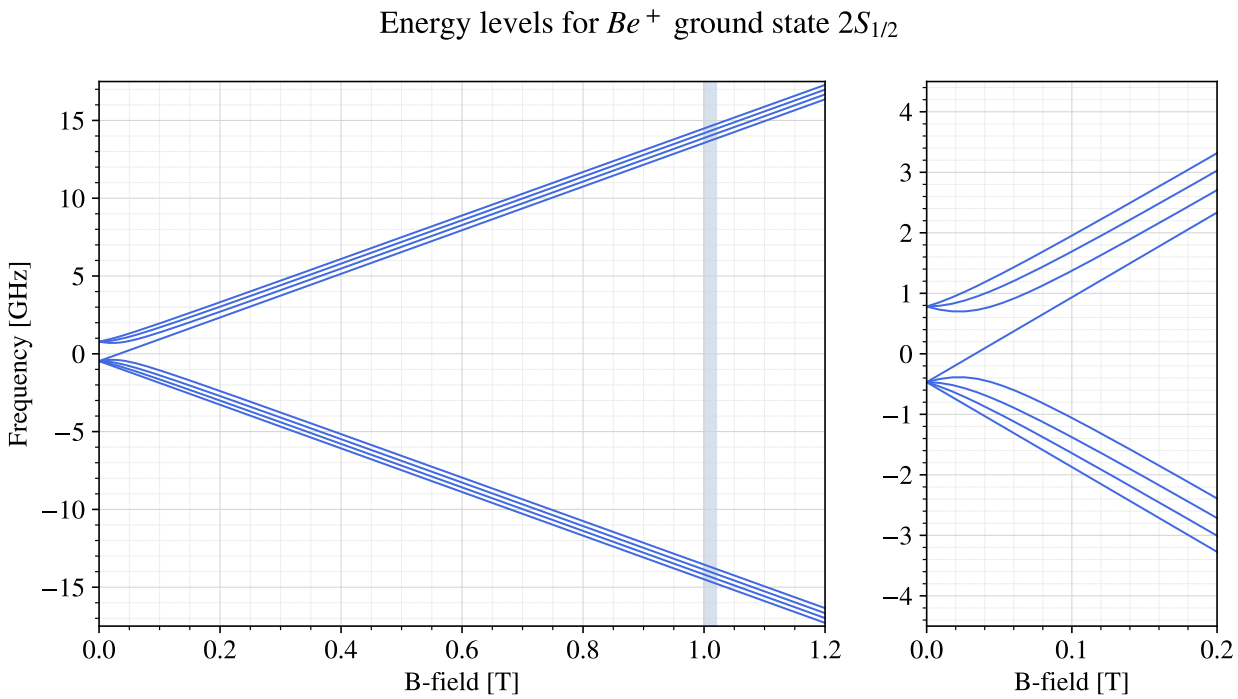

Figure 5.2 – Energy levels in $^9Be^+$. Shaded region on the left plot represents the operational range of magnetic fields of *Carlsberg magnet* (external Penning trap solenoid), which is usually $1 - 1.02\ T$.

Breit-Rabi formula

For the states of $J = 1/2$, for which the electronic charge distribution is spherically symmetric (because $L = 0$) and its interaction with the electric quadrupole moment of the nucleus can be neglected (e.g. the ground state $2S_{1/2}$ of $^9Be^+$), we can use the Breit-Rabi equation to calculate the energies as a function of the magnetic field strength [205]. The energy levels of the ground state $^2S_{1/2}$ ($L = 0$) of Be^+ for $F = I \pm 1/2$ are described by the Breit-Rabi formula:

$$E(F, m_F) = hA_{hfs}\left(-\frac{1}{4} + \frac{g'_I m_F \mu_B B}{hA_{hfs}} \pm \frac{2I+1}{4}\sqrt{1 + \frac{4m_F}{2I+1}X + X^2}\right) \tag{5.1.4}$$

and for special case $F = I + 1/2$, $m_F = \pm(I + 1/2)$:

$$E(F, m_F) = hA_{hfs}\left[\frac{I}{2} \pm \left(\frac{g_J}{2} + Ig'_I\right)\frac{\mu_B B}{hA_{hfs}}\right] \tag{5.1.5}$$

where

$$X \equiv \frac{\mu_B B(g_J - g'_I)}{(I + 1/2)hA_{hfs}} \tag{5.1.6}$$

The values of parameters A_{hfs} and g'_I are evaluated in the *Reference* [132] and remaining constants: h, μ_B and g_J are taken from the *CODATA* [7, 206].

Parameter	Value	Source
A_0	$-625\ 008\ 837.044(12)\ Hz$	*Shiga et al.* [132]
k	$2.63(18) \cdot 10^{-11}\ T^{-2}$	*Shiga et al.* [132]
g'_I/g_J	$2.134\ 779\ 852\ 0(23) \cdot 10^4$	*Shiga et al.* [132]
h	$6.62607015 \cdot 10^{-34}\ J \cdot s$	*CODATA 2006* [206]
μ_B	$9.2740100783(28) \cdot 10^{-24}\ J/T$	*CODATA 2006* [206]
g_J	2.00226239(31)	*CODATA 2006* [206]

Table 5.1 – Numeric values of the parameters used for calculating the energy levels of the ground state $2S_{1/2}$ $^9Be^+$ from the Breit-Rabi equation in the Ref. [132] (assuming they used *CODATA 2006* values available at that time [4]).

Diamagnetic shift in Be^+

As reported by *Shiga, Itano and Bollinger* [132], hyperfine structure of ground state in $^9Be^+$ is more complicated: the hyperfine interaction term between electronic and nuclear angular momenta $hA_{hfs}\bar{J} \cdot \bar{I}$ in fact has a small dependence on the magnetic field strength due to so-called diamagnetic shift. The hyperfine constant A depends on the magnetic field strength, which means that it is not a constant. Assuming the quadratic field dependence [207] the hyperfine constant takes the form:

$$A_{hfs}(B) = A_0(1 + k \cdot B^2) \tag{5.1.7}$$

where A_0 a hyperfine constant in zero-field $B = 0$ and k is a diamagnetic shift coefficient. *Shiga et al.* [132] have measured the electron spin-flip f_e and three nuclear spin-flip frequencies (f_1, f_2, f_3) in a high magnetic field of 4.4609 T and combined these results with previously measured transitions in a lower magnetic field [3] to obtain values of A_0, k and $\gamma = g'_I/g_J$, which are given in Table 5.1.

5.1.2 Excited state $^2P_{3/2}$

The excited energy levels ^2P are calculated based on the work performed by *Bollinger, Wells, Wineland and Itano* [201]. The main interactions of the excited states $\mathcal{H}[2P]$ are

- $\mathcal{H}_{fs}$:= the coupling between electron spin $\bar{S}$ and orbital angular momentum $\bar{L}$ (fine-structure interaction);

[3] *Table II.* in *Ref.* [132]

[4] Ref. [132] was published in 2011, but *CODATA 2010* was published in 2012.

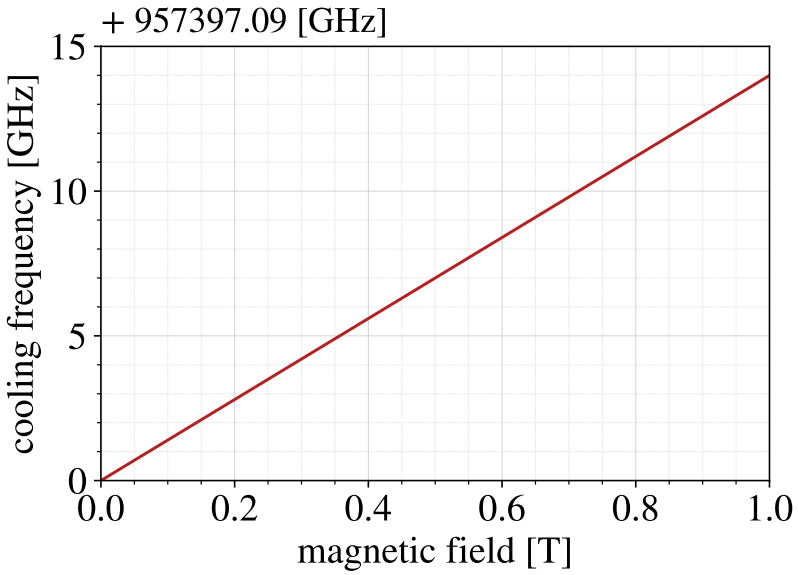

Figure 5.3 – Laser cooling transition in $^9Be^+$, Equation 5.1.9, as a function of magnetic field.

- $\mathcal{H}_{Zn}$:= interaction of external magnetic field $\bar{B}$ with nuclear magnetic moment $\bar{I}$ (nuclear Zeeman effect);

- $\mathcal{H}_{Ze}$:= interaction of external magnetic field $\bar{B}$ with total electron moments $\bar{J}$ (electronic Zeeman effect);

- neglect the relativistic, diamagnetic, and finite nuclear mass correction of the $\mathcal{H}_{Ze}$ $[\mathcal{H}'_{Ze}]$;

- neglect coupling between total electronic spin $\bar{J}$ and nuclear spin $\bar{I}$ (hyperfine structure interaction) $[\mathcal{H}_{hfs} = \mathcal{H}_{hfsm} + \mathcal{H}_Q$ (magnetic dipole interaction and electric quadrupole interaction)]

The Hamiltonian of the excited energy levels $2P$ in the $^9Be^+$ is

$$\begin{aligned}\mathcal{H}[2P] &= \mathcal{H}_{fs} + \mathcal{H}_{Zn} + \mathcal{H}_{Ze} + \mathcal{H}'_{Ze} + \mathcal{H}_{hfs} \approx \mathcal{H}_{fs} + \mathcal{H}_{Zn} + \mathcal{H}_{Ze} \\ &= \frac{2}{3}\Delta E \bar{L}\cdot\bar{S} - g_I\mu_N \bar{I}\cdot\bar{B} + (g_L\bar{L}\cdot\bar{B} + g_S\bar{S}\cdot\bar{B})\mu_B\end{aligned} \tag{5.1.8}$$

The approximation of g-factors being a pure angular orbital momentum $g_L = 1$ and g_S a free-electron g-factor were used. The calculations of the laser cooling frequency, presented in Figure 5.3, were performed by Francis Robicheaux.

5.1.3 Cooling transition for ^{9}Be$^+$

To reduce a kinetic energy of beryllium ions we use the simplest laser-cooling scheme, which is a Doppler cooling. Laser cooling requires the existence of so-called *cycling transition*, which means that the atom after transitioning to the excited state decays back to the initial ground state and photon absorption can occur again, and atoms undergo multiple scattering events. For $^9Be^+$ there is a cooling transition $2s\ ^2S_{1/2} \rightarrow\ 2p\ ^2P_{3/2}$ at 313 nm. We use the specific transition

$$^2S_{1/2}(m_J = +1/2, m_I = +3/2) \rightarrow\ ^2P_{3/2}(m_J = +3/2, m_I = +3/2) \tag{5.1.9}$$

driven by σ^+ polarisation laser. This laser cooling transition has a linewidth of 19.6 MHz, which corresponds to a lifetime of 8.1 ns [208].

Laser cooling is a cycling-transition meaning that most of the ions decay back to the original state, but in fact some ions do decay to the ground state of the opposite spin orientation, just with significantly smaller probability. An ion in the state $^2S_{1/2}(m_J = -1/2, m_I = +3/2)$ no longer interacts with the laser beam tuned to the cooling transition, so the ions would slowly accumulate in the *dark* state, reducing the efficiency of the laser cooling. Additional laser beam tuned to the transition

$$^2S_{1/2}(m_J = -1/2, m_I = +3/2) \rightarrow\ ^2P_{3/2}(m_J = +1/2, m_I = +3/2) \tag{5.1.10}$$

to bring ions from the *dark* state to the excited state from which they will in majority decay back to the *bright* state. The rate of repumping from the *dark* states to the *bright* states depends on:

1. Transition properties: the natural linewidth (decay rate) and saturation intensity of the transition.
2. Repump laser intensity: the intensity of the off-resonant repump laser.
3. Detuning: the frequency difference between the repump laser and the atomic resonance frequency.

Additionally, the efficiency of the laser-cooling process is reduced by the fact that there are sources of heating acting on the plasma in a Penning trap.

5.2 Laser system for cooling Be^+

5.2.1 313nm cooling laser

TA-FHG pro Toptica laser

To generate 313nm radiation for Doppler cooling Be^+ we use a frequency-quadrupled diode laser from *Toptica* [209]. It is a *TA-FHG pro* system, which converts 1252 nm into 313 nm using two stages of resonant frequency doubling (2x $SHG = FHG$). The initial *IR* source is a tunable semiconductor diode laser (*DL*) with a tapered amplifier (*TA*) [210] to increase the intensity of *IR* light. The frequency output of the DL can be controlled in three ways:

- by an electrical current flowing through a diode (so-called *"diode current"*)
- by a position of the grating installed in the external cavity of the DL; this change is made by changing voltage applied to the piezo actuator installed under the diffraction grating (so-called *"piezo voltage"*); this provides the widest frequency scan range and is a standard method to tune the laser frequency in the system like this
- by a temperature of the DL; this is very slow and it serves more like the *repair* adjustment

There are two optical isolators (one right after DL casing, second right after TA) to prevent the diode and the amplifier from damage due to back-reflected light of a high power. Next there is an SHG stage, which is a nonlinear doubling frequency-crystal, converting 1256 nm into 626 nm laser beam, installed inside a bow-tie cavity. The crystal type used in this laser is a manufacturer trade secret, and they did not want to tell us the material they used. A popular crystal for second harmonic generation is Beta Barium Borate (BBO). Before SHG cavity there is a mode matching optics. The SHG cavity consists of 4 mirrors (Figure 5.4) and the precise alignment of all of them is crucial for building up the power inside the cavity:

M1 input cavity mirror; it also serves as an output mirror for light leaking from the cavity to measure a power building up inside

M2 mirror installed on two piezo actuators (fast and slow) to scan the cavity length

M3 mirror that directs the laser beam onto the doubling crystal and

M4 output cavity mirror, this mirror has to have lower reflectivity than M2 and M3

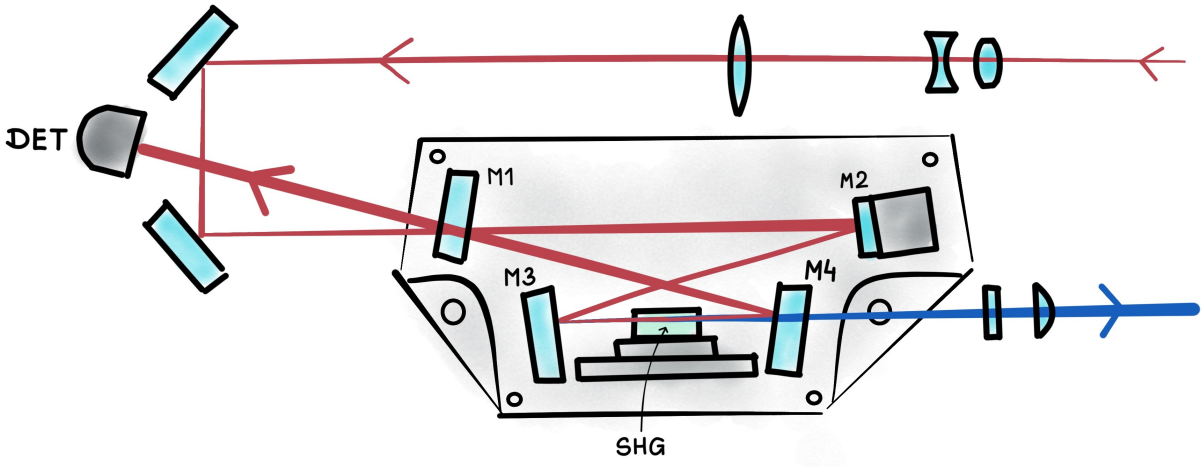

Figure 5.4 – Schematic diagram of the SHG cavity used in the *TA-FHG pro* laser by *Toptica*. The cavity is in the *bow-tie* configuration, using 4 mirrors. Figure adapted from the laser operational manual.

The doubling crystal can be tilted inside the cavity to increase the output of SHG beam. The efficiency of SHG is improved by temperature control of the SHG crystal. The SHG cavity must be kept sealed to prevent nonlinear crystal degradation due to moisture in the air (bags with hygroscopic beads are put inside) and to keep the cavity's mirrors clean (the process of cavity alignment is performed in a clean room). The photodiode detector installed behind the SHG cavity (*DET* on Fig.5.4) is detecting the light leaking out of the cavity. It is used to measure the laser power built inside the SHG cavity, which is a signal used to frequency lock the cavity. Frequency mode lockup will be discussed in Section 5.2.4.

Right on the output of the SHG we have beam shaping optics for one of the axis. After that the frequency doubling system (mode matching optics, SHG cavity, photodiode, and the output beam shaping optics) repeats to convert 626 nm into 313 nm. All of that is enclosed in the chassis that can be opened if any of the internal optics needs to be tuned. The standard internal alignment procedure should involve only steering pairs of mirrors that couple into: TA, SHG cavity, and FHG cavity. Power at each stage can be measured by flipping a prism, installed on the longer wall of the chassis, to deflect the beam path into the aperture in the chassis that sends the beam outside of the box. A dedicated detector (*IR* or *UV* photodiode) or a universal one (*thermal head*), placed in front of the aperture, can be used to measure power at each stage of the laser and this should be compared with a specification sheet (or service sheet) during any laser maintenance to diagnose the source of laser power losses.

In our lab we have two 313nm *TA-FHG pro* lasers from Toptica. The old 313nm laser was bought in 2013. In 2021 we purchased a new Toptica 313nm laser that could deliver higher power and had higher level of automated control. For the beryllium experiment performed in 2019 we used the old 313 nm laser. For the electron spin flip in the Be^+ data collected in 2022, we used a new laser.

The old laser outputs at most 35 mW of 313nm light, which after passing through the rest of external optical components gave around 8 mW injected through a glass window to the ALPHA-2 trap. The new 313 nm laser provides us with 800 mW. We initially did not need that much power and we were concerned about running too high power through the AOM, since the damage threshold for the device was not known. The power of the new laser was reduced by lowering the TA current to obtain a $\sim$ 200 mW output laser power of 313nm.

The old laser had to be manually re-aligned, and it could be controlled by analogue signals applied to the diode current or voltage applied to the piezo actuator under diffraction grating on the DL's external cavity (called later *piezo voltage*). The new 313 nm laser has a *Auto Align* system for automatic re-alignment of the steering mirrors that couple the laser beam into the TA and both doubling cavities (SHG & FHG) and it can be entirely controlled over a network by using *DLC pro* software [211]. It means that all the parameters, like diode current, piezo voltage, temperatures of DL, SHG and FHG, TA current and many others, that required turning knobs in the old Toptica laser, in the new laser can be controlled remotely. More details about frequency control will be presented in the next section 5.2.4.

Both lasers have implemented a *Feed-Forward* control, which adjusts the *diode current* by pre-set correction factor whenever the *piezo voltage* is changed. This increases the range of frequencies between which the laser can be changed in the continuous way (*Mode-Hop-Free tuning range*), which will be discussed in more detail in Section 5.2.4. The *Mode-Hop-Free* (*MHF*) tuning range of the new laser is around 120 GHz at 313 nm. According to the specification, the *MHF* tuning range for the old laser is 20 GHz. Since during the 2019 experimental run the old laser was controlled by changing the DL current (instead of controlling voltage of the piezo), our operational mode-hop-free range was only around 2.3 GHz. This was a limitation for our laser cooling measurements in 2019, because we could not start the frequency chirp further than this detuning. Later we upgraded the control system to tune the voltage applied to the piezoactuator instead of current of the diode.

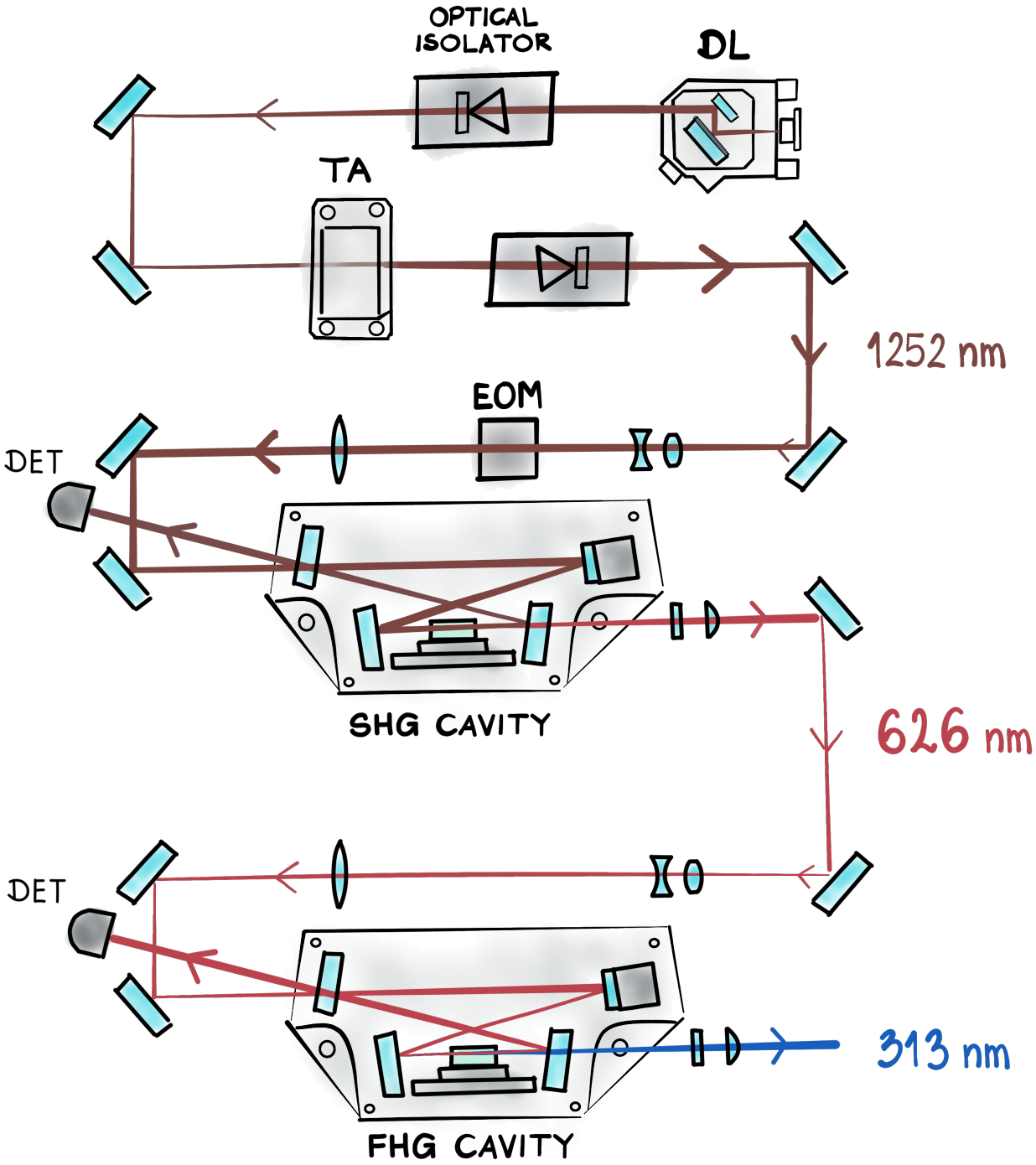

Figure 5.5 – A diagram of the *TA-FHG pro* laser system by Toptica. The diode laser (*DL*) produces a 1252nm laser. The intensity of this light is increased by tapered amplifier (*TA*. There is an electro-optic modulator to generate sideband frequency for the *PDH* locking scheme (discussed in Section 5.2.4). The first frequency-doubling cavity (*SHG*) generates light of 626nm and second (*FHG*) produces 313nm light used for laser-cooling Be^+. Figure adapted from the laser operational manual.

Advice: Polarising Beam Splitter cube at 313 nm

PBS cube keeps burning over time at the interface of the two glass pieces. Laser beam power $30 - 40$ mW, beam size ~ 1 mm.

Originally we were considering various setups using both old and a new 313 nm laser after the upgrade (they will be discussed in Section 7.2. on future prospects), but we came across various technical problems with the old 313 nm laser (misalignment of the doubling cavity and broken piezo actuator, broken steering mechanism of the cavity's incoupling mirror) and it had to be sent to Toptica for maintenance service. For the entire 2022 we used the new 313 nm laser, running with 200 mW power output, which was split into two beams to create two paths: *on-axis* and *off-axis* of the ALPHA-2 Penning trap (details on the laser beam preparation in the next Subsection 5.2.2 and more about physics motivations for having two beams and achieved performance in Section 5.3).

5.2.2 Laser delivery to the trap

The optical system that was used for the 2019 run (demonstration of sympathetic cooling of positrons with laser-cooled Be^+) was built earlier by Daniel Maxwell and Jack Jones. The upgrades introduced later to the laser system were done by myself with the help of Kurt Thompson, Maria Gomes Gonçalves and Steven Armstrong Jones. The upgrades described in this section were the main part of my postgraduate study at ALPHA.

313 nm laser on the optical table

All the lasers are located in a separate room called *laser lab*, from where they need to be transported to the *ALPHA-2* trap located in *experimental zone*. Lasers need to be transported to ALPHA-2 through the opening in the wall. The total distance from the laser box to the ALPHA-2 vacuum window is roughly 10 m. Most of the optics installed on the table serves the purpose of shaping the beam profile, to deliver a desired beam size at the position of beryllium ions in the trap. The only active component installed on the beam path is an accousto-optic modulator (*AOM*) that allows for sweeping a laser frequency in the range of a few tens of MHz. The device used for that was *AOM 3200-1210* by *Gooch & Housego* (*G&H*). More details about AOM are provided in Section 5.2.4.

The beam sizes of both 313nm lasers (new and old *TA-FHG pro*) are similar, approximately $d_x = 1.7mm$ and $d_y = 1.3mm$ of Gaussian diameter. Since the beam profile coming out of the Toptica laser is elliptical, it needs to be corrected using a pair of cylindrical lenses (*cylindrical telescope*). The first cylindrical lens is $f_1 = 200$ and the second $f_2 = 150$, installed 35 cm away to reduce the size of the X-axis to the same as the Y-axis following:

$$d_x \cdot \frac{f_1}{f_2} = d_y \tag{5.2.1}$$

The 313 nm laser radiation was delivered to the ALPHA experimental zone through a periscope during 2019 *experimental run* and by optical fibres since 2022, which will be discussed in the next subsection 5.2.3. There is a small optical table installed on the upstream side of the ALPHA-2 trap to align the lasers into the vacuum chamber.

Off-axis cooling laser

There are 4 dedicated laser ports on each, upstream and downstream, side of the ALPHA-2 trap, which makes 4 possible laser paths connecting the US and DS ports diagonally. Lasers enter the trap through special laser windows. Each laser path is tilted from the z-axis of the trap by an angle 2.4°; it passes through a radial centre r = 0 at electrode E14. Two of these laser paths have an internally built-in enhancement cavity for 243 nm laser (one used for the $1S - 2S$ measurement and one spare), one path is used for Ly-α laser and the last path was left free, so we could use this one to install 313 nm laser for laser cooling Be^+. The centre of the ALPHA-2 trap (electrode *E14* where the laser cooling process and the antihydrogen synthesis occurs [5]) is at 135 cm away from the US window port, so laser's entrance to the vacuum chamber. Since this laser path was easily accessible without any hardware modification to the ALPHA-2 trap, it was used in the *beryllium experiment* from the beginning. This laser beam is called *off-axis laser*. Even though the tilt angle is small and the laser path is nearly parallel to the axis of the Penning trap at the position of the central electrodes, it has significant radial offset from the radial centre in the Recatching Trap (Be^+ loading and preparation) and in the *positron end* (mirror reflection of the RCT trap on the DS side to catch and prepare positrons).

[5] Beryllium ions are held in the double well *E14E15*, because these two electrodes used to get internally shorted during cool-down and warm-up cycles, so now all electrode potentials are programmed to assume electrical connection between the two and apply the same voltage to electrodes *E14* and *E15*.

Most importantly, cooling laser does not overlap with beryllium ions under segmented electrodes (Rotating Walls electrodes *E3* and *E25*), which does not allow to cool and compress ions at the same time (about the plasma compression using Rotation Wall method read 2.4.2). The motivation for simultaneous compression and cooling is to shorten the beryllium preparation time for sympathetic cooling of the positrons (details in Section 5.3). Additionally, overlapping laser with ions is a condition for *beryllium magnetometry* which relies on detecting the fluorescence signal induced by interaction of Be^+ with the 313 nm laser (see Chapter 6). If we could detect the electron spin-flip in Be^+ at different axial positions, the precise value of the magnetic field along the z-axis of ALPHA-2 could be extracted [6].

On-axis cooling laser

For the reasons mentioned at the end of the previous paragraph, in 2020 we started working on implementing a new laser path that would align with the z-axis of the ALPHA-2 trap. This required hardware modifications to introduce laser mirrors on the *sticks* on both sides (upstream and downstream) of the ALPHA-2 trap. The idea was to inject the 313 nm laser via *inspection window* on the side of the US AT stick chamber, perpendicular to the z-axis of the trap (approaching from the *laser lab* side of the ALPHA-2 trap. Next the laser gets deflected from the mirror inside the vacuum chamber by 90° to overlap with z-axis of the Penning trap, passes through the trap, reflects off of the mirror installed on the DS AT stick at 90° again and gets ejected through same type of *inspection window* on the downstream stick chamber. A special type of mirrors were installed on stick, with a coating that reflects 313 nm, 243 nm (antihydrogen's spectroscopy) and 532 nm (green pointing laser) manufactured by *LASEROPTIK GmbH*. The *vacuum mirror* had to be mounted on an existing *stick* body, the surface of which was already nearly entirely occupied by other instruments (detectors and particles sources). On the upstream side we could have used a space where optical fibre for collecting fluorescence signal was installed before [7]. The *vacuum mirror* installed on the Upstream AT stick was rectangular of dimensions of $2.5 - 3.5$ cm.

[6] Of course assuming that we can detect fluorescence for all these positions. Currently with a photon counter installed outside of the trap, on the downstream laser port can see the fluorescence signal in the Atom Trap's thin electrodes (E8-E20), but it disappears when we move ions to Recatching and Positron end of the trap.

[7] There was a hope to collect photons from Be^+ decay, emitted on axis towards a *stick*. This was disproved to work before I joined the experiment in 2019, no fluorescence signal was detected.

Initially, in early 2020, we installed a small circular mirror of around 2 cm diameter [8] on the downstream AT stick. It turned out to be very difficult to align the *on-axis laser* through the trap with such a small mirror. (*Stick* can tilt inside the vacuum chamber so that the mirror is displaced from the designed position). In 2021 we added the rectangular mirror (similar to the one on upstream end) on the downstream stick. This has been installed on the back of that MCP, which is facing the Positron Accumulator. Together with adding mirrors on the ALPHA-2 trap *sticks*, the modifications to the MCP detector were performed to shield electrostatic fields coming from high voltage tabs (see the discussion of the problem in Section 6.5.5 of Jack Jones' Ph.D. thesis [131]). We benefited from the fact that in 2021 the Catching Trap was rolled out of the beamline path to undergo an upgrade of the antiproton beam degrader and vacuum system, so we could have inspected the alignment of both US and DS *sticks*.

The surfaces of the mirrors lie in $x \pm z = 0$ planes [9]. Despite the fact that the positions of both mirrors are well aligned to the axis of the trap, they may still be tilted out of the desired plane [10]. If the incident laser beam is parallel to the x-axis, even a small tilt of the upstream mirror can cause a misalignment of the *on-axis laser*. A tilt of the downstream mirror does not influence the alignment of *on-axis laser*, but it changes the path of the laser beam leaving the chamber via downstream *inspection port*. The extraction of the laser beam from the ALPHA-2 trap at the downstream end is our best diagnostics to determine whether *on-axis laser* passes through the trap without any obstacles.

Advice: Alignment of a laser through a big trap with small apertures
The method we use for aligning the 313 nm laser through the ALPHA-2 trap is to send a laser pointer beam from the downstream end (the laser pointer is installed directly in front of the downstream *inspection port*), such as it goes out on the vacuum chamber through the upstream *inspection port* and reflects on the steering mirrors for 313 nm. Then we can walk the 313 nm beam to overlap with the laser pointer beam at the two most distance points available on the upstream optical mini-table.

[8] The small size of the downstream mirror was due to the space limitation between instruments already installed on the stick.
[9] Coordinate system: x is a horizontal direction, y is vertical and both are perpendicular to z which is the axis of the trap
[10] For this reason, it might be worth to consider designing vacuum mirrors installed on piezoelectric actuators.

Advice: Alignment of a two distant points to the trap axis

We had to align two mirrors installed on both sides of the ALPHA-2 Penning trap, separated by $\sim$ 3 m, where the designed aperture was around 12 mm in diameter, while the laser beam is around 2.5 mm. The real aperture was even smaller due to misalignments of the internal components of the trap. The aim was to make a clear path for the laser beam to propagate through the trap along the z-axis. When the apparatus installed in front of the trap can be removed (or in the alternative design does not exist at all), the easy way to align two distant mirrors inside the vacuum chamber was to look directly through the trap, along the z-axis. We looked downstream via a vacuum widow installed temporarily on the upstream flange of the US AT stick chamber, and we used for that a mirror camera with a telephoto lens, the focal length of which can be adjusted between positions of both sticks. The position of the camera was fixed on a tripod and aligned to the radial centre of the trap ($r = 0$) as much as possible (even a small offset can distort the perception of angles).

The waist diameter of the beam at the position of the ions is around 2.5 mm, the beryllium ions cloud around 1 mm radius and the total aperture size along the z axis of the ALPHA-2 trap is around 12 mm. This means that there is still quite a lot of space for the laser beam to pass through the trap without clipping on mechanical apertures but missing the ions. For this reason, a system for precision beam positioning was needed for *on-axis laser*. The fibre output and a collimating telescope were installed on a double-axis translation stage to scan in the y-z plane. Initially, each translation stage was adjusted with a manual micrometre screw, later the manual micrometre screws were replaced by *Travel DC Servo Motor Actuator* (*Z812 Thorlabs*). First attempts to align *on-axis laser* manually with a micrometre screw showed that it is really difficult to overlap the laser beam with ions.

During the early 2022 mini-run, we did study the laser cooling as a function of the *on-axis laser* beam position. We held the Be^+ sample in the trap and moved the beam position with a micrometre screw, while looking at the number of photons counted by a detector installed on the downstream *off-axis* laser port. The background level of the photon counter signal was significantly higher than for the *off-axis laser* ($\sim 10\times$, but the background photon count for the *on-axis* laser highly depends on the alignment through the trap) and increasing

the photon counter signal more likely means increasing a scattered light rather than actual fluorescence signal. There were a few good data points taken, but unfortunately scanning the *on-axis laser* position in one way and returning to the original would not give the same fluorescence signal. It cannot be ruled out that the signal goes down as a result of losing ions, but we rather suspect that it was due to possible shift of all of the assembly mount when touching the micrometre screw to change its position.

Later the *Servo Motor Actuators* were installed and the fluorescence signal detected by the photon counter, which is a measure of beryllium laser cooling, was very well reproducible. Laser cooling as a function of *on-axis laser* beam position was not systematically studied with *Servo Motor Actuators*, since it just happened to be initially aligned with the position that gave really nice and efficient cooling. We preferred to rather focus on using the limited time we had for *beryllium experiment* to study laser-cooling mechanism. More details of this work are provided in Section 5.3.

2019 Setup: A single beam of 313 nm laser was sent to the trap over a periscope ($\sim$ 5m long), which accounts to total beam path of 8.2 m in the air up to the laser input port in Atom Trap. This laser beam enters the trap through a glass window port and is tilted from the trap axis by an angle 2.4°; it passes through a radial centre $r = 0$ at electrode *E14*. This laser beam is called a *off-axis* laser. The angle between the laser beam and Penning trap z-axis is very small, so it was believed that only the axial motion gets cooled, and cooling of the radial motions occurs through collisions between ions [131].

This laser beam was shaped with a pair of cylindrical lenses (*cylindrical telescope*) to correct the flattening of the beam produced by the *TA-FHG pro* laser from *Toptica*. The beam diameter at the centre of the *AT* was approximately 2.5mm (measurement done without the AOM in place, the AOM's optics is designed to output a beam of the same size as the input beam). The AOM in the laser setup was installed in the double-pass configuration, which means that the frequency offset was added twice (details in Section 5.2.4). In reality, as it was discovered after the 2019 run, the AOM was never aligned to output the beam with doubled frequency offset, it was adding a frequency offset only once. The power used for the off-axis laser injected through the vacuum window was $\sim$ 8 mW.

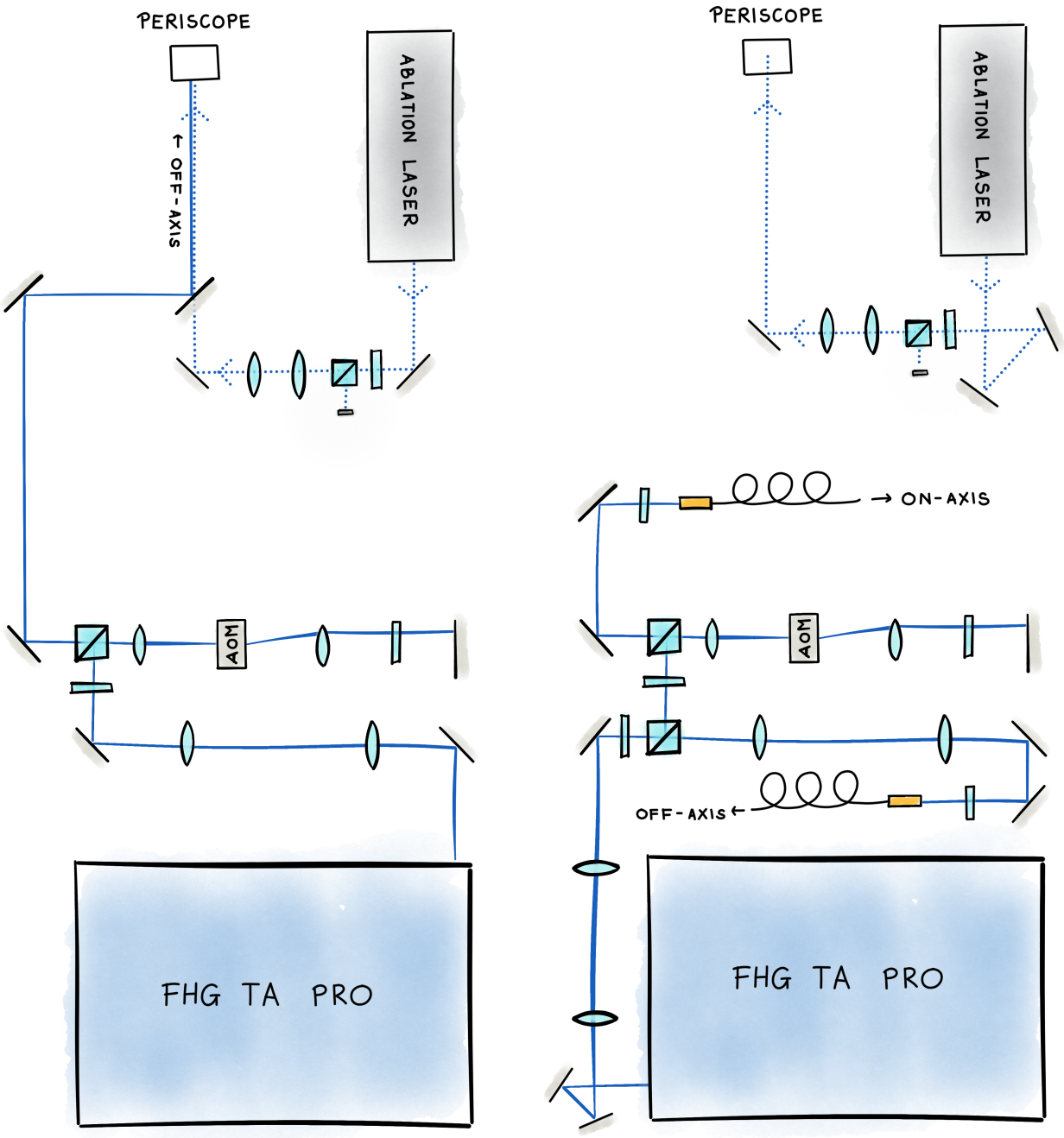

Figure 5.6 – Laser lab setup in 2019 (left) and 2022 (right).

2022 Setup: The main upgrades for the 313 laser setup were:

1. second beam was added to the trap that overlaps with the z-axis of the trap,
2. old *Toptica* laser was replaced with the newer version of higher power (up to 800 mW),
3. photonic fibres were introduced to deliver the 313 nm laser to the ALPHA-2 trap,
4. AOM driver was replaced with a new one with a wider range of RF output: 140-280 MHz (*G&H AODR 1210FM-3 2.0W*) instead of 180-220 MHz (*G&H AODR 1200AF-AEF0-2.5*).

Around 200 mW is divided in half nearly equally by *Polarising Beam Splitter* into two beams: *off-axis* and *on-axis*. There is a half-wave plate before *PBS* to give the possibility of changing the power distribution between two beams. The *AOM* is installed in the *on-axis* beam (most of the power was usually directed to the *on-axis* beam due to losses through the *AOM*). There is a common cylindrical telescope before *PBS* to change the elliptical beam shape to circular and two independent spherical telescopes to reduce the beam size from 1.3 mm to around 1 mm to achieve the best coupling to the fibres. Each of the beams is delivered to the *zone* through its own optical fibre. The fibres are connected to a special collimator and there is a half-wave plate in front of each of the fibres. We aimed to have at least 8-10 mW available as the output of each fibre.

313 nm laser beam position detector

We share an optical table in *laser lab* with the 243 nm laser for antihydrogen spectroscopy. The optical mini-table on the ALPHA-2 upstream end is not mechanically decoupled from the trap. That makes it more likely for our lasers (cooling and ablation lasers) to get misaligned or move during the experiment. We spent a significant fraction of our time realigning the lasers all over again. We have considered a beam stabilisation system with piezoelectric actuators to stabilise the beam path as it propagates along the periscope and through the AT trap. We have tested this concept in 2020, using hardware borrowed from the $\bar{H}$ spectroscopy setup, but at the end we decided to move towards testing the concept with laser delivery through the fibres. We purchased beam position detectors from Thorlabs (*Segmented Quadrant Thermal Sensor S440C*) to monitor both 313 nm lasers on the output from the ALPHA-2 trap. The equivalent window ports are installed on the downstream side of the trap:

larger perpendicular *inspection port* [11] for the *on-axis* beam and 1 of 4 small laser-dedicated ports for the *off-axis* beam (the one diagonally opposite to the window through which the *off-axis* laser was injected). The idea was to record the position of both laser beams to monitor whether the laser position drifts during the measurements. The Thermal Sensors from Thorlabs were chosen due to their operation range for laser powers and the option to switch between measuring laser position and power. The power of 313 nm laser sent to the trap is usually a few milliwatts, which is within an operational range of the sensor (0.5 mW - 5 W), but it would not reliably detect powers below 5-10 mW. The power used in 2022 experimental mini-runs was usually 8-10 mW.

5.2.3 UV fibres

All lasers and most optics are placed in a separate room (*laser lab*) from the ALPHA experimental area due to safety requirements [12] and stability of the operation of the lasers. There is a optical mini-table on the upstream end of the ALPHA-2 Penning trap where all the lasers (*beryllium experiment*: 313 nm cooling laser and 355 nm ablation laser, 243 nm laser for antihydrogen spectroscopy and *Ly-*α 121.6nm for laser cooling of antihydrogen) are injected to the ALPHA-2 trap. The optical mini-table, vacuum chambers with windows, so basically all the upstream part of the beamline, are enclosed in the light-shielding box with removable panels to work on aligning the laser through the Penning trap. The distance from the optical table in the *laser lab* and optical mini-table in the *zone* is roughly 8m (the beam path must bend upward and travel above people's heads to allow passage between the *laser lab*'s wall and the ALPHA-2 trap). The laser beam must be transported from the *laser lab* to the ALPHA-2 trap in such a way that all stray and reflected light is covered up, so people working in the experimental zone do not need to wear protective googles.

Advice: Thermal position sensor S440C from Thorlabs

This sensor was meant to work for laser powers $\geq$ 0.5 mW, but it did not detect reliably the beams of a few milliwatts, and probably could be trusted only above 10 mW.

[11] It is an inspection window that is installed on every cross-chamber that contains a motorised *stick* with detectors and particle sources, to see the position of the instruments inside the vacuum chamber and safely install and align the *stick*.

[12] It is about safety of people non-authorise to work with lasers and safety of the laser system itself.

In the original design, which was used during the 2019 *beryllium experiment* (demonstration of sympathetic cooling of positrons [1]), both 313 nm and 355 nm lasers were delivered to the experimental area over a periscope. We struggled to deliver a clean and well collimated beam over the periscope. Furthermore, having such a long optical path (around 10 m in total) was more prone to misalignment in the *laser lab* causing a possible offset of the laser beam inside the ALPHA-2 trap. We did investigate using an active beam stabilisation system for the 313 nm laser with mirrors installed on piezoactuators with PID controller based on the photodiode readout of the beam position. In early 2020 we borrowed hardware from the experimental setup of the $\bar{H}$ spectroscopy experiment to test this concept, which gave satisfactory results in terms of stability, but, of course, it did not improve the beam shaping in the trap. Adding piezo-actuated mirrors and detectors took more space on the optical mini-table in front of the ALPHA-2 trap. Since we planned to introduce an *on-axis* 313 nm laser beam and we still had to keep enough space for the 243 nm laser setup, this caused a limitation to implement the beam stabilisation system. There was simply not enough space to have beam stabilisation hardware for two laser beams. Finally, since exactly the same mirrors inside the periscope were used to reflect 313 nm and 355 nm lasers, it meant that the two light beams were coupled and had to be steered together from the *laser lab* to the *experimental zone*. The laser alignments would become even more difficult in the case of two independent 313 nm laser beams that would have to travel together in the same periscope. Separation of the delivery paths for each laser would allow to independently steer and re-align each beam if needed.

We have been encouraged by work of other groups using photonic crystal fibres to deliver 313 nm light, so we decided to upgrade the laser system to replace the periscope. Fibres for *UV* are not commercially available and need to be custom made, usually by the research groups themselves. Over time the *UV* radiation damages the glass material in standard photonic fibres due to a process called *UV solarisation*. *UV solarisation* is a chemical process that involves the formation of colour centres in the silica of the fibre glass, causing an increase in the opacity of the fibre [212, 213]. The way to prevent fibre damage is to perform the *hydrogen-loading* procedure [214, 215]. This is done by diffusing hydrogen gas into the fibre structure under higher pressure and increased temperature and then exposing the fibre to *UV* radiation (called *curing*) to bound hydrogen inside the glass structure.

The first investigation steps to introduce optical fibres to the 313nm system were done by Daniel Maxwell and Jack Jones. Later I took over and it was one of the major projects I worked on during my PhD programme. I got the help of Kurt Thompson and Maria Gomes Goncalves to prepare the fibres and especially to bring them to the *experimental zone* and align the output through the ALPHA-2 trap. I need to acknowledge here the advice and guidance of Celeste Carruth Torkzaban who shared with us her experience of working on 313 nm optical fibres Trapped Ion Quantum Information Group at ETH and hosted me and Jack in their laboratory in Zurich. It seems like there is a big interest of the community in the preparation of *hydrogen-loaded* fibres for 313 nm laser application, so this motivated me to describe our experience *UV* photonic crystal fibres in great detail. We used jacketed fibres (fibre glass covered with PVC protection, like commercial telecommunication fibres), unlike all other people from the ion trapping experiments I have met so far, who are using bare fibres. We seemed to struggle much more to maintain stable transmission through the jacketed fibres than people who are using bare fibres. We observed a huge sensitivity of the transmission to the fibre's shape, orientation in space, and the tensions applied (mostly applying the tension on the input end was necessary). This was even the case for bends with a greater bending radius than the critical radius of around 5cm.

UV optical fibres hydrogen-loading

To prepare the *UV*-resistant photonic crystal fibres we followed the procedure described by *Marciniak et al.* [215]:

1. place the fibre in the chamber with high pressure hydrogen gas and increased temperature ($\geq 60^\circ$ C) and hold for few hours
2. if the fibre needs to be transported, place it in a *cold box* ($< 0^\circ C$) until the fibre can be cured with *UV* light
3. set the nitrogen gas flow through the fibre collimators to avoid particles deposition on the fibre's interface
4. cure the fibre, so expose the fibre to the *UV* radiation over full length of the fibre for several hours
5. in case if the fibre has PVC jacketing, stretch the fibre for couple of days

We do not have the capabilities of *hydrogen-loading* the fibres ourselves, so we (as most research groups) had to use the service of external companies. Initially in 2019 we have tried to use *17M LMA-PM-10-UV-FUD* from *NKT Photonics* and we sent it to *O/E Land Inc.* in Canada for *hydrogen-loading*, but this fibre broke before we started curing it. We found a fracture of the fibre glass and our suspicion was that the fibre was manipulated while still being cold and fragile. We have no evidence whether the damage was our fault or not, but we got overly paranoid while handling the fibres later. The next time we took the fibres out of *cold box*, we left them untouched on the table to warm up to the (hopefully[13]) room temperature. It should be remembered not to leave the fibres outside the *cold box* for too long and to cure as soon as possible, since the hydrogen diffuses out of the fibre glass over time at room temperature. Ref. [215] states that curing should begin within 24 h.

We had two more successful rounds of hydrogenating fibres, each time with two *10M LMA-PM-10*[14] from *NKT Photonics*: in 2020 (name the fibres *1A* and *1B*) and in 2021 (*2A* and *2B*). This time for *hydrogen-loading* we used a company in France called *iXblue*. Fibre *1A* has been cured with 100 mW input power for 1 day and fibre *1A* with 20 mW for 3 days. We used the nitrogen gas (GN_2) to purge the fibre collimator with the flow rate 30 sL/hr (although at that point the special fittings for connecting the gas inlet to the fibre collimator did not arrive yet, so we just taped the gas hoses to the collimator, which meant the nitrogen gas flow rate might have been lower due to possible leaks on that *"seal"*).

In the second series of *hydrogen-loading* and curing (fibres *2A* and *2B*) we already got proper fittings for purging the collimators with GN_2 [15], but we came across other problems related to the *cold box* warming up to quickly while at the same time the piezo actuator in the *FHG* cavity of the old laser happened to break . Additionally the fibre *2B* was accidentally left for entire day in the room temperature before curing. We did not know how fast the hydrogen was diffusing out of the fibre, but *Marciniak et al.* [215] suggest that the *UV*-curing process should start within 24 hours after removing the fibres from the *cold box*. The fibres were placed in the freezer in the hope of preventing further loss of hydrogen until we could start the curing process.

[13] since we have no way of measuring the internal temperature of the fibre's glass.

[14] Later on *LMA-PM-10-UV* fibres were not available in stock, so we had a choice of polarisation maintaining *PMA* non-UV fibres or *UV*, but not maintaining the polarisation.

[15] The collimator is installed in the unthreaded adapter *AD12NT* from *Thorlabs* with a hose barb.

The fibre *2A* was cured for 50 h with an input power of 4.0-2.5 mW. The last fibre *2B* was cured for more than 80h, the input power was in the range of 5-3 mW. During curing the fibre *2B*, the laser kept falling out of lock due to a broken piezo actuator in the *FHG* cavity, so the *UV* light kept pulsing for some time until the cavity lock was readjusted. This was repeated until the piezo actuator died completely [16]. During the whole curing process we controlled the output power. We have observed that the output power would always gradually decrease over time. This could be corrected by moving the fibre around and pulling on its input end (the fibre was loosely spooled, with both ends extended on the optical table). This was most likely due to the plastic deformation of the jacketing decreasing the transmission. We think that this deformation was introduced during hydrogen loading in an increased temperature of the pressure chamber. For this reason, the authors of Ref. [215] suggest stretching the fibres to "mitigate plastic memory which can destabilise transmission and even inhibit appropriate curing". Stretching procedure will be described in the next subsection.

Advice: Unstable transmission of *hydrogen-loaded LMA-PM-10* (NKT Photonics) jacketed fibres, even after stretching

The transmission of light through the fibre after *hydrogen-loading* process is very sensitive to the shape and orientation of the fibre in the space and the tensions applied to the fibre. If you can, it is better to avoid using fibres with plastic jacketing. As these jackets mould the fibre into a very specific shape that significantly reduces the transmission, sometimes stopping transmission entirely. If using a version of jacketed fibre is necessary, both input and output ends should be tensioned, and the fibre should be clamped to the table (or other mechanically rigid structure) immediately outside the metal conduit. The fibre will have to be manoeuvred around along its entire length to find an orientation in space that provides the highest possible transmission. It might help fix the fibre at various points along its length. The mechanical state of the fibre with highest transmission possible possibly will not remain stable, we have seen the highest transmission signal to decay very quickly, probably due to the fibre deforming back. Aiming for the most stable transmission level might be more desirable.

[16] In our case there was a temporary solution to maintain the cavity lock, but we have learnt about the trick right after finishing the fibre's curing process. This is described in the *Advice* box in the subsection 5.2.1: *TA-FHG pro Toptica system*.

In the end, after *hydrogen-loading* and the curing procedure, there was no noticeable difference in the performance of the fibres of the first (1A & 1B) and second (2A & 2B) series. Transmissions through the fibres before and after *hydrogen-loading* did not change in an observable way. Since the main transmission loss comes from the shape of the fibres and the applied tensions (more details in Section 5.2.3), we were unable to quantify whether there is any degradation of the fibre after longer periods of *UV* light exposure. After running the experiment for a few weeks [17] with transmission around 10-15%, we were always able to recover the transmission to this level by moving the fibre around. During the actual *beryllium* experimental *mini-runs* in 2022, we did not purge the collimators due to concerns of overloading the air in *laser lab* with nitrogen gas.

Stretching optical fibres

We performed the procedure of stretching the fibres to mitigate plastic memory of the PVC jacketing that introduces undesired bends and stresses to the fibre structure, which decreases or completely stops the transmission of the *UV* light. In the Ref. [215] *Marciniak et al.* say that they stretched the fibre before and during *hydrogen-loading* (they had 1 m long fibre). We did not have a good way to stretch the 10 m long fibre while curing. We also did not stretch the fibres before curing because we were afraid that if something goes wrong with our laser or incoupling of the light to the fibre, we would lose the time during which the hydrogen is diffusing out of the fibre after taking it out of the *cold box* (we assumed that stretching the fibre while it is still cold is not a good idea).

The first pair of fibres ($1A$ & $1B$) in 2020 was stretched on the floor using two pulleys, made of a standard fibre spool, to save space (there was no safe place to stretch the 10 m long fibre). One end of the fibre was connected to the adapter installed in a fixed position on the floor and the other end was attached to the translation stage to controllably apply the tension (Figure 5.7.a). For tensioning the second fibre $1B$ we used a force meter (*Sauter FK-50 dynamometer*). We started with 6 N [18], but the force kept gradually decreasing. On the 4^{th} day it reached 3 N, then we increased it back to 6 N and continued to be stretched for 10 more days. The $1A$ fibre was stretched for 12 days. There was no force meter installed on that fibre, but comparing the tension with another fibre, the applied force was $\sim 3-6$ N.

[17] Laser is not on all the time, we open shutters only when we actually want expose ions to the 313 nm radiation.
[18] It was an arbitrary choice of the force made by looking at the fibre's tension.

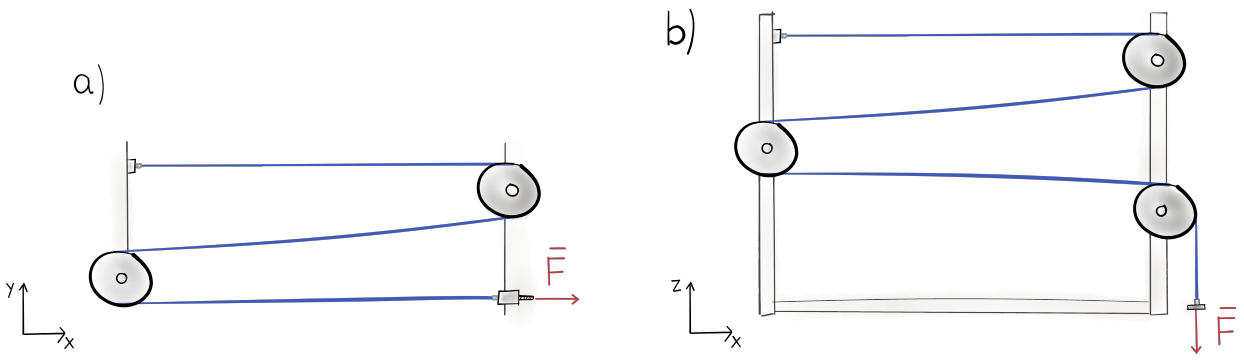

Figure 5.7 – a) Setup of pulleys for stretching the first series of fibres ($1A$&$1B$) in 2020. Pulleys were installed on the floor and tension was applied with moving a micrometer screw. b) Setup of pulleys for stretching the second series of fibres ($2A$&$2B$) in 2021. Pulleys were installed on on the stand and a weight was attached to one end of the fibre to apply a tension.

The transmission through the fibres after stretching improved in stability and was around $40 - 50\%$. After stretching, the fibre $1A$ was stored in the box, with a bend radius similar to or slightly smaller than the bend radius in the package delivered by *NKT Photonics* (15 cm). After about two weeks (the time to stretch the fibre $1B$) we tested the transmission through the fibre $1A$ and observed that the stability of the transmission level achieved during the stretching process was gone and the fibre behaved like before the stretching process. We stretched the fibre $1A$ once again for 12 days with force in the rage of 4.5-5.6 N. After that we achieved transmission around $35 - 45\%$. The two fibres have been stored in the original box fairly loosely (≥ 15 *cm* bending radius).

The second series of fibres ($2A$ & $2B$) was stretched on a vertical frame with 3 pulleys, where a tension was applied by hanging a weight at one end of the fibre while the connector at the other end was attached to the top of the frame (Figure 5.7.b). The weight was made from the circular optics size adapter attached to the fibre connector, which weight must have been below 0.5 kg, so the tension applied to the fibre was significantly lower this time (the force meter was not used this time). The setup build allowed us to stretch both fibres at the same time. The bending radius on the pulleys was 6.7 *cm* (comparable to the pulley of the horizontal setup). After 10 days, the fibres were swapped *"upside down"* and continued to be stretched for another 6 days. Fibres $2A$&$2B$ were meant to be installed in the laser system around 2 months after stretching and at this time the transmission performance was comparable to the one before the stretching process. They were stretched in the vertical

setup once again for a few days, just before *beryllium mini-run*, but this did not improve performance. We installed the fibres $2A$ & $2B$ (one for *off-axis* and the other for the *on-axis* laser) between the laser lab and the experimental zone. We struggled a lot to keep a stable transmission at the level of 10-15%. At this point fibres $1A$ & $1B$ performed similarly.

The transmission of light through the fibre after the *hydrogen-loading* process is very sensitive to the orientation of the fibre in space and the tensions applied to the fibre. What mattered the most for good transmission through the fibre was a tension applied to the fibre on the input end (the fibre's connector was clamped at the optical table and the fibre on that end was tensioned using a custom-made 3D-printed clamp. Transmission was also significantly reduced when any bend was applied to the fibre in its first 30-50 cm from the input side, even if the radius of bend was greater than critical bend radius [19].

At each end of the fibre, behind the connector, the fibre is reinforced with a metal conduit of around 25 cm in length, which is meant to secure the fibre. The first series of fibres from 2020 (*1A&1B*) had a fairly flexible metal conduit, which would slightly bend following the direction of bend of the following part of the fibre. The second series of fibres from 2021 (*2A&2B*) had a very stiff metal conduit that would not follow the bend of the further part of the fibre. This was causing that bend created at the end of the conduit would be significant if the fibre was pulled up to be transported overheads to the experimental zone (fibres were transported inside the same periscope that was used previously for free-space laser propagation). The fibre is glued to the metal conduit at the ends. One of the fibres from the second round was glued poorly enough to go out of the conduit with a bend already. For this reason, special 3D printed clamps were designed to fix the fibre after the end of the metal conduit and straightened first foot of the fibre's length. A clamp is installed on the optical table to fix the input end of the fibre. The final length of the fibre just before the output connector also had to be at least straightened (same min. last 30-40 cm) and secured in a *good* position, which we did not predict initially, so we did not design any clamp for the output end. Fibre's output end is not attached to the optical mini-table at the ALPHA-2 trap, it just approached from the above of the laser shielding box (roughly the height of the top of ALPHA-2 solenoid magnet). There was no good point on the mechanical structure in the near proximity to clamp and straighten the fibre, so its output position was not well fixed.

[19] It is know phenomena that too big bends cause a light leaking out of the fibre through the cladding.

We spent a lot of time manipulating the fibres to get decent stable transmission of around $10 - 20\%$ (we did not aim for highest possible transmission, because this was falling down within minutes time scale) and even despite attaching the fibre to the frame and mechanical structures around, we had to correct the fibre's position nearly every day.

Coupling light in and out of the fibres

The 313 nm laser beam needs to be coupled from a free space into the fibre. The best input coupling is provided if the beam size at the fibre faced is equal to the mode-field diameter (*MFD*), so the radial size for which the light intensity falls to $1/e^2$ of the peak value, for the beam propagating inside the fibre. The core diameter of the *LMA-PM-10* fibre is 10.1 ± 0.5 μm and *MFD* is 8.4 ± 1.0 μm at 532 nm wavelength. From our 0.9 ± 0.1 mm roughly collimated beam [20] we want to focus the laser beam to ~ 9 μm to couple it into the *LMA-PM-10* fibre. For that we used the fibre collimator *60FC-4-S24-49-XV* by *Schäfter + Kirchhoff GmbH* with a bore hole for flushing purposes [216] (N_2 gas purging to avoid dust deposition on the fibre's facet). The fibre coupler has a plano-convex lens $f = 24$mm installed on the cylinder threaded from the outside, which sits inside the cylinder of the main body of the collimator. The threading can be accessed with a special tool ("eccentric key") through a hole in the outer body to shift the lens along the axis of laser propagation. The problem is that, after aligning the lens to a good axial position, a small stud is screwed in to fix the position of the inner cylinder holding the lens. The stud is meant to clamp the cylinder in the stable position, but in practice the stud pushes the lens out of the previously aligned position and introduces a tilt of the inner cylinder. The method to deal with this problem is described in the *Advice* section. Since a good input coupling to the fibre was found, we did not have to realign the coupling nearly at all (for the fibre winded in the spool in its *"natural"* orientation). If the fibre was unplugged and plugged back to the collimator very gently, the transmission would usually remain, and a small beam walking was sufficient to achieve the best possible coupling. To find the initial alignment to couple the laser into a fibre, we send a backward propagating laser beam from another end of the fibre [21] to align the input beam path with the outgoing beam of the backwards propagating laser.

[20] Initial eliptical laser beam produced by *TA-FHG pro* laser by *Toptica* of around 1.7×1.3 mm gets reshaped by cylindrical and spherical telescopes to the circular beam of size 0.9 mm.

[21] Using the *FibreDock* output of the 626 nm on the *Toptica* laser or green pointer laser with a special collimator setup.

To find the best alignment of the fibre collimators, we follow the procedure:

1. Install input of the fibre with the *collimator 1* in front of the circular, collimated 313 nm beam, with at least two steering mirrors right in front of the fibre's input
2. Connect output of the fibre to the 626 nm fibre interface on the *TA-FHG pro* laser (*fibre dock*), which normally is used to send a reference signal to the wavemeter [22]
3. Align 313 nm beam to overlap with the red laser leaving through the *input end* on the longest path available (at least $\sim 30 - 40$cm; the longer overlap distance, the easier it will be to find initial coupling), the centres of two beams need to be really well aligned to give a minimal transmission through the fibre
4. Disconnect output end of the fibre from the *fibre dock* and install it on the table in front of the power meter (at the beginning it might be actually easier to detect transmitted light by eye on the piece of paper)
5. The output end can be installed already with the other fibre *collimator 2*, that we will be aligning later
6. Walk the 313 nm beam to enhance the transmission signal until decent transmission is found (eventually moving the lens inside the *collimator 1* could also help, but this way it is very easy to entirely lose the coupling); what we considered a decent transmission at this stage was around 10%
7. Remember to scan the angle of the half-waveplate installed in front of the coupler
8. If step no. 5 has not been done yet, it should happen now
9. Align the *collimator 2* installed on the output end of the fibre to give a beam profile that is the most similar to the profile of the input beam (it is the easiest to make nearly collimated beam on the input and aim for similar at the output)
10. *Collimator 2* that was installed on the output end should be now better aligned than than *collimator 1* on the input and they could be swapped to get better input coupling (repeat steps 1-7)
11. Step 9 could be repeated to find the best alignment for *collimator 1*

[22] Very little of red light is needed, so the coupler on the *fibre dock* was always misaligned and the aperture was barely open

Advice: Coupling free-space propagating beam into the fibre by using backwards propagating light

Use 626 nm red light connected to the *FibreDock* of *Toptica* laser to send it backward through the fibre. The 313nm laser can be steered using mirrors installed before fibre input collimator to overlap with the red laser beam. They should overlap at a distance of at least tens of centimetres. If the centres of the two beams overlap very well along all the path, the a tiny amount of 313 nm light should already be transmitted through the fibre. Be careful which of the red beams is *real*, because 626 nm can also reflect from the back of the mirror and create additional beam spot.

Polarisation of the light

LMA-PM-10 is a single-mode fibre, which allows propagating only a fundamental mode of light. The *PM* stands for polarisation-maintaining [217], which means that the polarisation of the laser light inside the fibre should be preserved throughout the length. The linear polarisation is maintained along a specific axis of the fibre, so the polarisation of the input light should match that axis for a maximum transmission through the fibre. This is achieved by placing a half-waveplate in front of the fibre's input collimator. The half-waveplate can be rotated around the laser propagation axis to choose an azimuthal position that provides the best input polarisation matching and the highest transmission. The beam coming out of the fibre has a specific linear polarisation. For our $^9Be^+$ laser-cooling transition $^2S_{1/2}(m_J = +1/2, m_I = +3/2) \rightarrow {}^2P_{3/2}(m_J = +3/2, m_I = +3/2)$ circular polarisation σ^+ is needed. To convert a linear polarisation of light coming out of the fibre into a circular polarisation, we use a quarter-waveplate installed right behind the output collimator. To obtain correct direction of the circular polarisation we change the azimuthal angle of the quarter-wave plate around the laser propagation axis and look at the intensity fluorescence signal that is directly related to the laser-cooling transition rate [23]. Despite the fact that the output connector of the fibre was fixed in one specific azimuthal position, we observed the output polarisation changing. The quarter-wave plate had to be rotated between our beryllium experimental mini-runs in 2022.

[23] Previously it was done by looking at final beryllium ions temperature measured with plasma Temperature Diagnostics method (Figure 6.16 in Jack Jones' PhD thesis [131].

Advice: LMA-PL-10 fibres for 243 nm

We also tried using the same *LMA-PL-10* fibre from *NKT Photonics* (it is not a *UV* dedicated fibre) for the 243 nm laser, but we did not see any transmission of this wavelength.

Future prospects: bare fibres

After installing the fibres in final location, between the *laser lab* and the ALPHA-2 trap, the transmission stability performed very poorly. Fibres were installed inside a periscope used previously for free-space delivery of the laser, and fixed in a few points along the way, but not tensioned along the way. The fibre's orientation in space, bends, and tensions along all the length were constantly changing. We had to move the fibre around almost every day to recover a decent transmission level ($10 - 20\%$). From discussions with people working in the Trapped Ion Quantum Information Group at ETH Zurich and other people in the trapped ion community working with 313 nm lasers, we know that the bare fibres (without PVC jacketing) did not cause as many problems with keeping a stable transmission. We did not meet anybody who used jacketed fibres like ours. We based our fibre preparation procedure on the work performed by *Marciniak et al.* [215] [24], who did not report problems with transmission stability over time after performing the stretching procedure, which we experienced. The problems with stable transmission through the fibre seem to be related to the tension, bends, and twists applied to the fibre that keep changing even if the fibre remains untouched. This effect was meant to be reduced by stretching the fibres. Our impression was that the stretching procedure relaxes the fibre's jacketing only temporarily, and after some time (days/weeks, especially if stored away in the bundled form) it comes back to its initial properties, when the transmission is ultra-sensitive to the orientation in space and tension applied. The transmission could change from not detectable output signal below a few μW to hundreds of μW just by manipulating the fibre along its length. As mentioned previously, the main enhancement came from applying a tension to the fibre at the input connector and removing bends on the first 30-40 cm of the length. The reference [215] did not mention these problems in the case of the jacketed fibres, so we did not expect it would require correcting the fibre's position all over again.

[24] With a difference that we stretched the fibres after curing, while they did that before and during the curing.

Advice: Fiber Collimator 60FC by Schäfter + Kirchhoff GmbH
After releasing the small stud that holds the cylinder with the lens inside the main body, the lens can move off axis by a tiny angle. If the stud is released entirely when moving the lens tube, after an attempt to tighten the stud after finding the best focus, the stud will offset the lens out of its best position, often resulting in a completely loss of the coupling into the fibre. Following the method described in *Schäfter*'s manual and holding the lens tube with an eccentric key did not work. The method I found working best was to tighten the stud as strongly as possible to still be able to slide the lens and then use some very small tool to push the lens tube by pressing on the groove in desired direction instead of using eccentric key. Using other small tools (like a tiny flat screwdriver) gave me more control over the offset of the lens than using the eccentric key. After doing that, I did not tighten the stud anymore.

5.2.4 Frequency control

The *TA-FHG pro* system by *Toptica* is a tunable ($\sim$ 1 nm) diode laser (*DL pro*) of very narrow linewidth [25], with two Second Harmonic Generation ($2 \times SHG = FHG$) cavities to obtain 313 nm light. *DL pro* are single-mode operating lasers thanks to active stabilisation methods implemented. The frequency of the laser can be scanned continuously (so-called *Mode-Hop-Free* tuning) thanks to External Cavity design. The laser frequency is stabilised to an additional external reference using a precision wavelength meter (*WLM*, also called a wavemeter). The frequency readout from the wavemeter serves as a feedback to the PID controller that executes the far-frequency scan during the initial laser cooling of beryllium ions (up to 15 GHz in our experiment). Smaller and more precise frequency sweeps (tens-hundreds of MHz) are performed by the *Acusto-Optic Modulator* (*AOM*). Another benefit of the acusto-optic modulation is the fact that the *AOM* device can act as a fast switch (< 50 μs) to turn on and off the cooling laser beam. In this Section we will discuss the design features of the *TA-FHG pro* and our frequency control setup for the 313 nm laser.

[25] Linewidth < 500 kHz according to information provided on *Toptica* website.

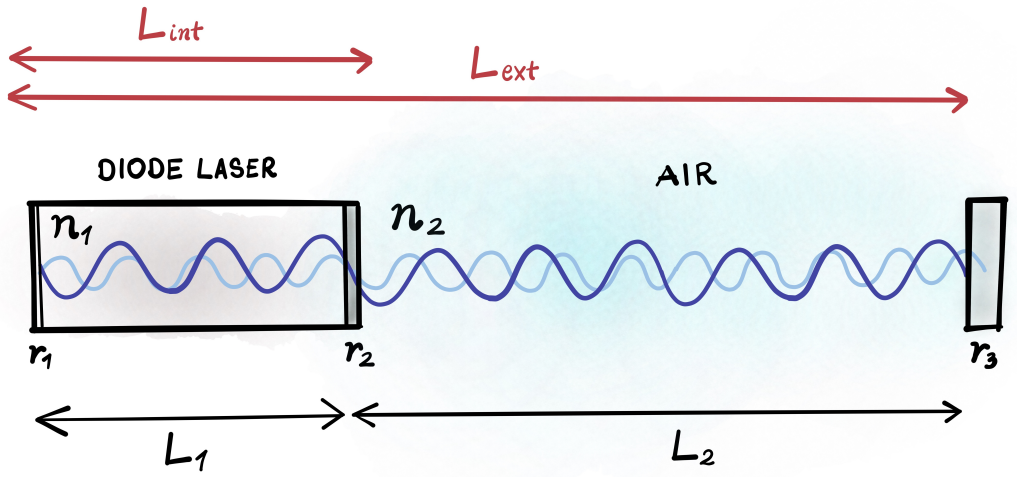

Figure 5.8 – Schematic diagram of an external cavity design used for the *Toptica* diode laser (*ECDL*). This design allows for narrow wavelength and single mode operation of the laser.

Extended Cavity Diode Laser: narrow & tunable frequency

The diode lasers are made from semiconductor p-n junctions, in which the recombination of electrons and holes generates photons. Surfaces of the p-n junction act as an optical resonator to amplify the light emitted from the energy band gap. The emission spectrum of the laser diode's *gain medium* is still broad for the precision atomic physics applications, but narrower linewidth can be achieved by applying the *Extended Cavity* (or *External Cavity*) design concept [218]. The diode with a built-in resonator (*internal cavity*) is installed before another external reflective element that creates *extended/external cavity* (*ECDL*) (Figure 5.8). If the output facet of the diode laser has low reflectivity ($r_2 \ll 1$), due to anti-reflective coating, the external reflector and the rear mirror of the laser diode would form the *ECDL*.

The frequencies allowed inside an optical cavity (*cavity modes*) are determined by the cavity length L and the refractive index n of the medium between the two cavity mirrors, and those frequency modes are separated from each other by a frequency equal to the fundamental cavity mode. The spacing between axial modes of the cavity is a *free spectral range* (*FSR*):

$$\Delta f_{FSR} \equiv \frac{c}{2nL} \tag{5.2.2}$$

The mode spacing of the internal cavity will be defined:

$$\Delta f_{int} = \frac{c}{2n_1 L_1} \tag{5.2.3}$$

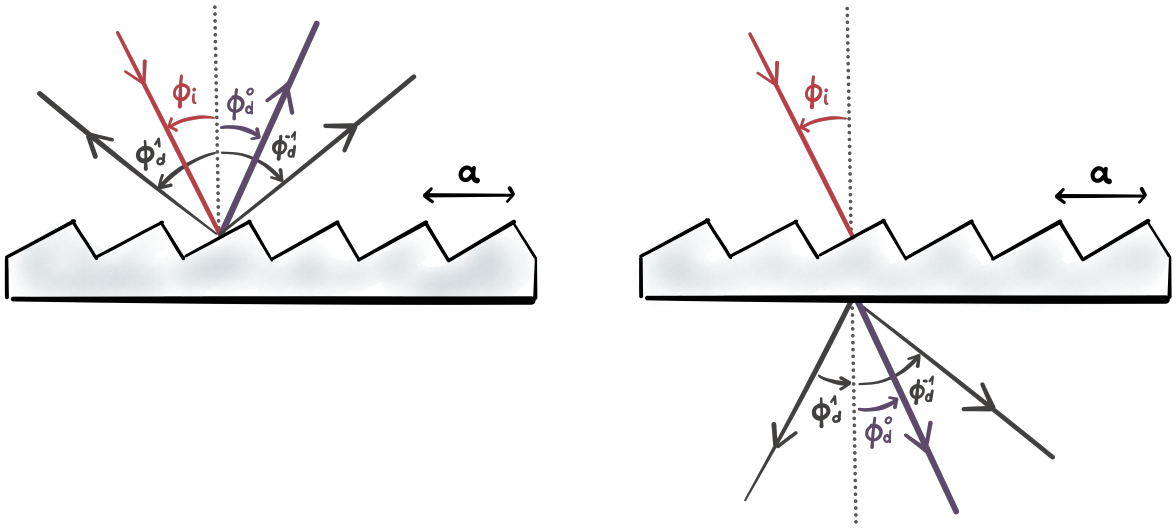

Figure 5.9 – Diffraction gratings, where diffraction modes are generated by refraction (left) and transmission (right). Figure adapted from Ref. [219].

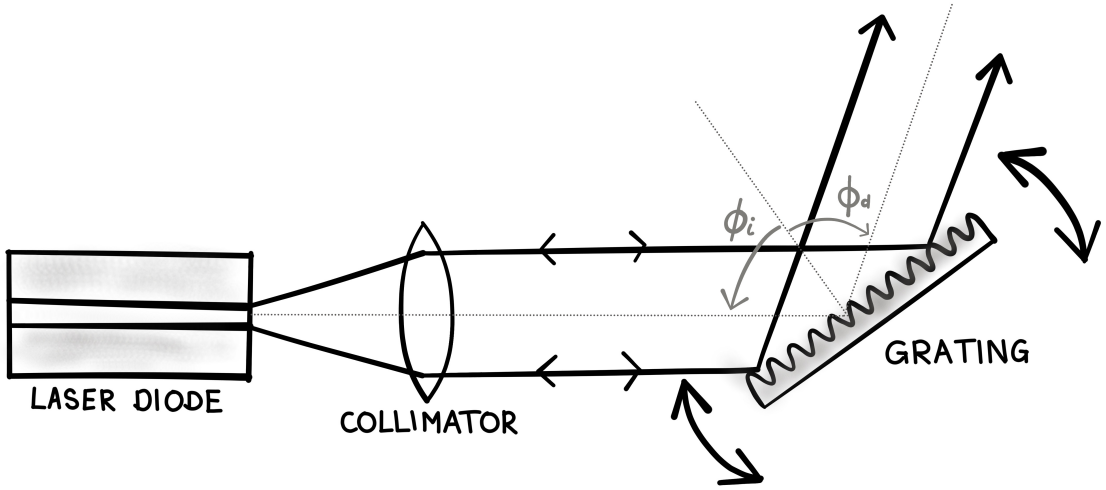

Figure 5.10 – Littrow configuration of External cavity diode laser (*ECDL*).

For the external cavity, formed by rear reflective surface of the internal cavity and the external tunable reflector:

$$\Delta f_{ext} = \frac{c}{2n_1L_1 + 2n_2L_2} \tag{5.2.4}$$

The external cavity would be longer than internal cavity $L_1 < L_2$ and the refractive index of the air smaller than the refractive index of the laser gain medium $n_2 < n_1$. In this case, the mode spacing of the external cavity will be smaller than that of the internal cavity $\Delta f_{ext} < \Delta f_{int}$. Only those frequencies that are simultaneously modes of the internal and external cavity and fulfil the condition

$$m_{int}\Delta f_{int} = m_{ext}\Delta f_{ext} \tag{5.2.5}$$

where m_{int} and m_{ext} are the modes numbers of the internal and external cavities. The linewidth of the external cavity modes is significantly narrower than the width of the internal cavity modes. The optimal design would set the external modes spacing high enough with respect to the internal cavity frequency spectrum linewidth, such that only a few (ideally only one) of external modes could overlap with a single internal mode and satisfy the condition in Eq. 5.2.5. Thanks to introducing the external cavity, narrower line width with higher modes spacing can be achieved, but we still have multiple frequency modes that can be enhanced in the *ECDL*. The single-mode operation is achieved by introducing the diffraction grating to the system; in order to select only one internal cavity mode that is sent back to the gain medium to generate optical feedback, this way we can choose only one wavelength to be output from the system.

The diffraction grating is at the same time the reflector for the external cavity, which is placed a few centimetres away from the diode laser. There are two principle designs of the *ECDL* with a diffraction grating: Littrow configuration and Littman-Metcalf (grazing-incidence) configuration. In our laser the *ECDL* in Littrow configuration is used [220].

The light of a wavelength λ striking the grating at the angle of incidence ϕ_i to the normal will diffract at the angle ϕ_d, the grating equation will be:

$$m\lambda = a(sin\ \phi_i + sin\ \phi_d) \tag{5.2.6}$$

where $m \in \mathbb{Z}$ is the diffraction order, a is the grove spacing on the diffraction grating. In the Littrow configuration, incident and diffracted angle is equal to *Littrow angle* $\theta = \phi_i = \phi_d$.

Then Equation 5.2.6 becomes

$$m\lambda = 2a\ sin\ \theta \tag{5.2.7}$$

Usually the first order of diffracted beam ($m = 1$) is reflected back to the internal cavity of the laser diode. The frequency f_g that satisfies the grating angle criterion

$$f_g = \frac{c}{2a\ sin\theta} \tag{5.2.8}$$

gets reflected back to the *ECDL*. The laser beam size is significantly bigger than the grove spacing, so many groove lines will diffract the laser light. The diffraction grating is tilted with respect to the incoming beam, so the effective length of the external cavity is slightly different for each grating line, leading to the broadening of the frequencies that are building in the external cavity. The linewidth Δf_g depends on the number of grating lines N on which the laser beam was diffracting off (the smaller the size of the laser beam and the fewer grating lines have been illuminated, the smaller the linewidth Δf_g will be)

$$\frac{\Delta f_g}{f_g} = \frac{1}{N} \tag{5.2.9}$$

The output laser frequencies are those that satisfy the grating angle criterion and the criteria for constructive interference in the internal and external cavity

$$f = f_g = f_{ext} = f_{int} \tag{5.2.10}$$

There is a mode competition between all possible laser output and the selected output mode is the one with the largest overall gain (Figure 5.11).

The frequency of the output mode can be tuned by turning the grating around the pivoting point and changing the diffraction angle, resulting in a change in the frequency that satisfies the condition 5.2.8. Frequency shift *df* introduced by turning the grating by angle $d\theta$ (deriving Eq. 5.2.7 for $m = 1$)

$$\frac{df}{d\theta} = -\frac{2ac\ cos\theta}{\lambda^2} \tag{5.2.11}$$

Changing the angle of the diffraction grating alone will shift the *grating profile*, which changes the external mode that is winning the modes competition, but that change occurs in discrete jumps when the f_{ext} and f_g get separated by more that half of *free spectral range*:

$$|f_{ext} - f_g| \geq \frac{1}{2}\frac{c}{2L_{ext}} \tag{5.2.12}$$

The change of the mode that is matching the cavity length is called a *mode-hopping*. To achieve a continuous frequency sweep, the *external modes* must shift simultaneously with the *grating profile* in such a way that the number of modes in the cavity is preserved. This is done by changing the length of the external cavity while at the same time rotating the diffraction grating. The change in length ∂L_{ext} causes a shift of the frequency ∂f:

$$\frac{\partial L_{ext}}{\partial f} = -\frac{L_{ext}}{f} \tag{5.2.13}$$

Synchronising the rotation of the diffraction grating and change the cavity length can be achieved by adjusting the grating angle around the pivoting point which lies in front of the back mirror of the laser diode (which is the rear facet of the diode). Rotation happens by applying a voltage to the piezoelectric transducer (*PZT*, often called a piezoactuator or *piezo* for short) that expands to push the lever arm on which the diffraction grating is installed.

While *external modes* are shifting in the frequency space, they are also moving with respect to the *internal modes* structure, and similarly whenever frequency changes by around half of the external mode spacing, the *mode-hop* will occur (scale of a few GHz). To provide a *mode-hop-free* (*MHF*) operation, *internal modes* also need to be changed together with *external modes* and *grating profile*. The length of the internal cavity L_1 is predetermined by the size of the semiconductor gain medium, but its change can be tuned by the injection current to the laser diode. Changing the current value through *DL* the refractive index of the medium n_1 is modulated [221] and temperature modulation [222] (lasers like *TA-FHG pro* also have independent temperature control for *DL*). Modulating the current running through the diode laser (*diode current*) in correlation with the voltage applied to the piezoelectric actuator that moves the diffraction grating (*piezo voltage*) can give a pretty wide (tens of GHz) *mode-hop-free* frequency tuning range, while maintaining the single-mode operation of the narrow frequency linewidth output of the laser system. The correlated change of *diode current* and *piezo voltage* in the *TA-FHG pro* laser is implemented under the function of the *feed-forward* control. Whenever *piezo voltage* is changed, *diode current* also changes by a value of a pre-defined correction factor.

The *TA-FHG pro* laser from *Toptica* has two analogue control inputs: for the *diode current* and *piezo voltage*. Applying external voltage offset to the *piezo voltage* gives a wider frequency range than controlling a *diode current*, so this is a proper way to implement a frequency scan for this type of laser.

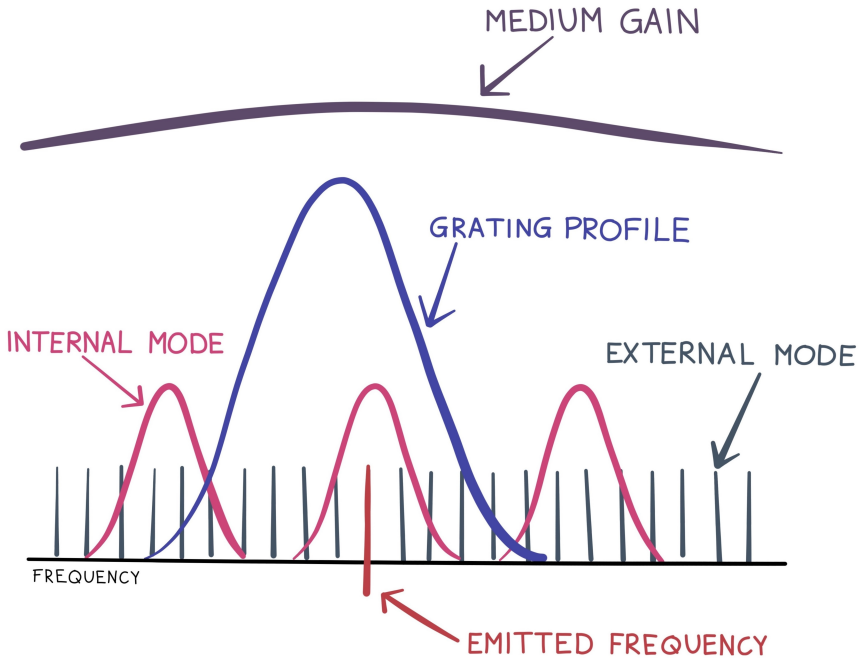

Figure 5.11 – Mode lock of the *Toptica DL pro* laser, it shows which mode of the cavity are locked. Figure adapted from the laser operational manual.

The technology of *External Cavity Diode Lasers* allows us to achieve narrow-line laser source of a wide *mode-hop-free* tuning range of frequencies, that can be controllably chosen by adjusting the input parameters: laser diode current, voltage applied to the piezoactuator that moves the diffraction grating of the external cavity and the temperature controller of the laser diode. The exact wavelength emitted by the *DL pro* module (diode laser with external cavity) can change over time due to fluctuations of the current driving the laser diode, acoustic vibrations, or changes in the surrounding air pressure and temperature (Figure 5.12). For the timescales of experimental sequences lasting minutes to hours [26] and the *experimental run* campaigns lasting even months [27] we want maintain stable frequency of 313 nm cooling laser. The stability of the 313 nm frequency depends on the stability of 1252 nm emitted from the *DL pro* module) and stability of both doubling cavities *SHG* and *FHG*. This can be achieved by active control of input parameters to the diode laser and to the *SHG* and *FHG* cavities based on the feedback signal of the present frequency measurement. Frequency measurement for the feedback controller might be direct by comparison with a reference frequency source or indirect by measuring changing intensity of light inside a reference cavity).

[26] Laser-cooling of Be^+ plasma in ALPHA-2 takes few minutes. We operate the laser nearly continuously during 8h long shift.
[27] Like *beryllium experiment run* in 2019 when we demonstrated sympathetic cooling of positrons [1].

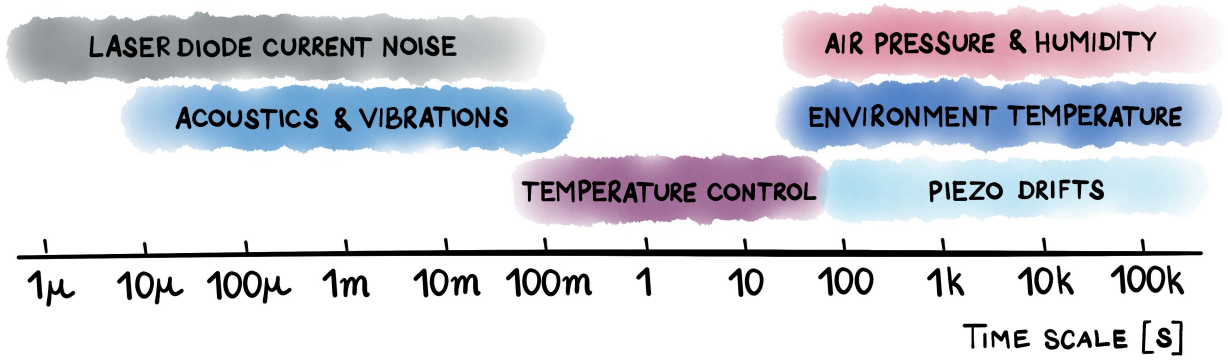

Figure 5.12 – Time scales of various sources of laser's frequency drift. Figure adapted from [223]

In our setup for 313 nm laser we use direct frequency readout of the SHG (626 nm) provided by a *Wavelength Meter* (commonly called a *wavemeter*) with a PID controller to generate analogue input signal for the *DL*: *diode current* and *piezo voltage*, which allows for long-term stabilisation of laser frequency up to the level of ~ 20 MHz, as well as controllable frequency sweep for laser cooling of Be^+ (more details of the setup in the Subsection 5.2.4: *Wavemeter: Frequency measurements and stabilisation*). To maintain their stable, single-mode operation of both frequency doubling cavities in *TA-FHG pro* lasers, *Toptica* implemented *cavity mode-locking* solution based on the *Pound-Drever-Hall technique* (*PDH*) [224], which uses the intensity of the light reflected from the doubling cavity to generate a modulation of the voltage applied to the piezoactuator holding one of the mirrors inside each of the cavities (technically, each doubling cavity has two piezoactuators: *Piezo 1* and *Piezo 2*). More details of the *PDH* technique and doubling cavity *mode-locking* will be described in the following Subsection 5.2.4: *Pound–Drever–Hall technique: frequency mode locking*. The overview of the *Toptica*'s locking solutions can be found on their website: [225, 226].

Pound–Drever–Hall technique: frequency mode locking

Fabry-Pérot cavity [227, 228] is used as a frequency reference for measuring laser frequency, due to the fact that Fabry-Pérot cavity transmits through only the frequencies of light that are integer multiplicity of its free-spectral-range (Eq. 5.2.2):

$$f_L = n \times \Delta f_{FSR}, \qquad n \in \mathbb{Z} \tag{5.2.14}$$

Fabry-Pérot cavity acts as a frequency filter by reflecting back all other frequencies.

The spectrum of reflected light would have dips at frequencies separated by Δf_{FSR}, which are the modes of the cavity. We could look at the intensity of the light reflected (or transmitted) from the cavity and from that we can deduce whether the laser frequency f_L is in resonance with the cavity. The frequency of the laser could be tuned to match the cavity of length L or oppositely, the cavity length L can be tuned by a piezoactuator, installed beneath one of the mirrors, to give a maximum light transmission condition. Whenever the photodetector sees the intensity of light change, the correction voltage could be applied to the piezoactuator to change the length of the cavity. If we look at the signal reflected back from the cavity, starting from the minimum intensity, whenever the intensity of reflected light increases, we could expect that the laser frequency is moving away from the resonance with the cavity (this of course assumes that the total intensity of the light source is stable, which is the main flaw of this simple method). But looking at reflected light intensity alone is not enough to tell whether it moved toward lower or higher frequencies, since the signal is symmetric around the resonance. Possible solutions to overcome this problem:

1. move away from the resonance by a small step of frequency, such as there is still enough light transmitted through the cavity (e.g. half of the intensity); for known direction of that step we can get information about the direction of the frequency drift that we want to compensate for. This method is called *side-of-fringe locking*.
2. get information about direction of the frequency drift by looking at the derivative of the intensity, which is an asymmetric function of frequency: below resonance the derivative of the reflected light intensity is negative and above it is positive. This is called *top-of-fringe locking*

In order to obtain the derivative of the intensity signal, the frequency should be varied slightly over small frequency range to see how the intensity of reflected laser light changes. By applying a sine-wave modulation to the laser's frequency, the signal reflected back by the cavity will also vary like a sinusoidally in phase with the modulation signal. Depending on the sign of the derivative, the correction signal can be applied to tune the laser frequency to be back in resonance with the Fabry-Pérot cavity. The correction signal can be sent to the laser source to lock the laser to the cavity or input to the cavity by shifting one of the mirrors to lock the cavity to the laser. This is the basic idea behind the Pound-Drever-Hall phase and frequency stabilisation technique.

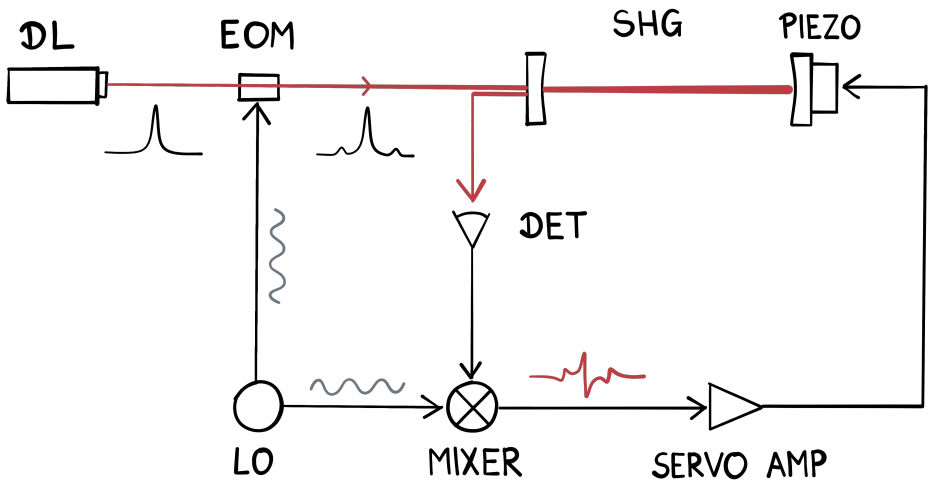

Figure 5.13 – PHD setup diagram. The carrier frequency generated by the diode laser (*DL*) is overlapped with the frequency sidebands generated by the electro-optic modulator (*EOM*) and the frequency of those sidebands is modulated by the local oscillator (*LO*). Both frequencies are sent to the reference cavity (in our case it is the *SHG* cavity). The light reflected of the cavity is measured by the detector (*DET*) and the resulting signal is mixed with the modulation signal to generate the *error signal*. Based on the *error signal*, the the servo amplifier adjust the voltage applied to the piezoelectric actuator (*PIEZO*), which controls the length of the cavity.

Pound-Drever-Hall technique was created for the gravitational wave interferometry experiment [229] by R.W.P. Drever and J.L.Hall in 1983 [224] and it was based on a technique developed for microwave oscillators by R.V. Pound in 1946 [230]. The technique involves placing an electro-optic modulator (*EOM* device, like a Pockels cell) between the laser source and the reference cavity. The *EOM* gets the input modulation signal from *local oscillator* (*LO*), which creates two symmetric *sidebands* of the laser frequency that are sent together with the original laser frequency (*carrier*) to the reference cavity. The signal of light intensity reflected from the cavity is mixed with the modulation signal applied to *EOM*, the mixed signal goes through a low-pass filter to generate *error signal* (Figure 5.14). Based on the *error signal* a feedback control signal is created. A good explanation on the PDH technique can be found in References [231, 232] by Eric D. Black from the LIGO project.

In our case, we lock the doubling-cavities (*SHG & FHG*) to the frequency of light entering the cavity. The idea is that whenever we sweep the frequency of 1252 nm using a *wavemeter*, the output frequency mode generated by the *DL* becomes mismatched from the *SHG* cavity. To avoid *mode-hopping* and maintain a continuous single-mode output of *SHG*, its length has to be readjusted by acting on the piezo actuator installed beneath the *M2* mirror in Fig.5.4.

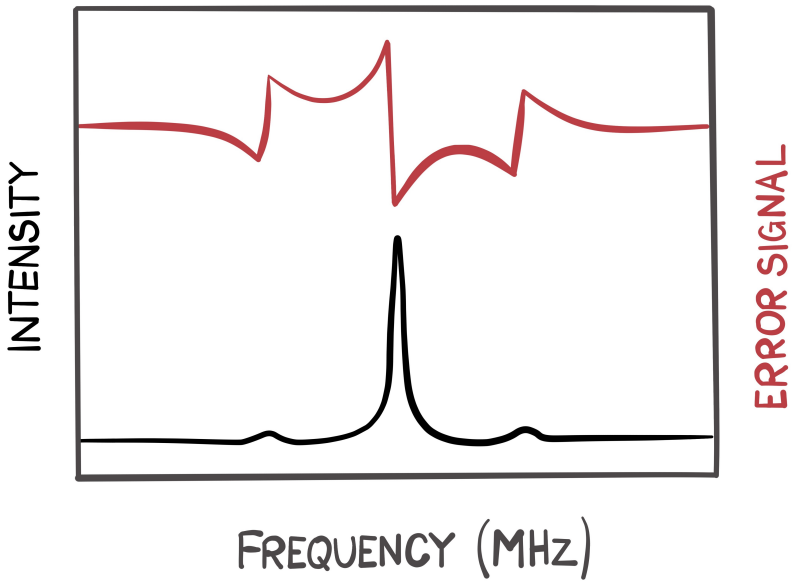

Figure 5.14 – Laser intensity transmitted through a cavity and an error signal used for the *Pound-Drever-Hall* laser locking technique.

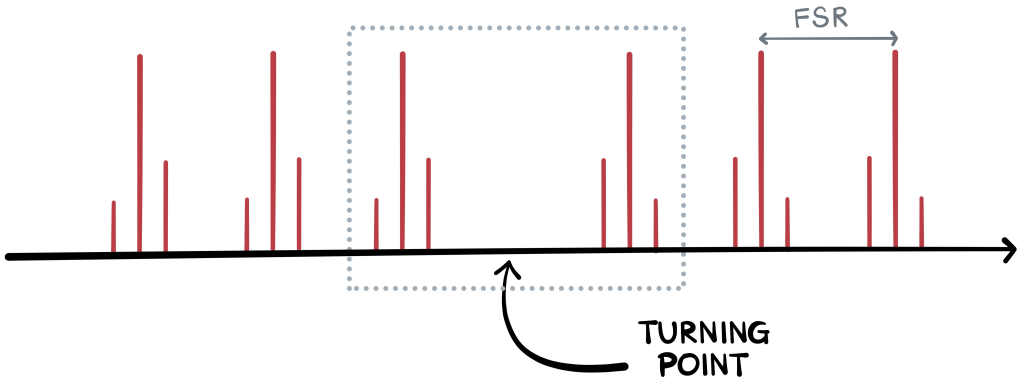

Figure 5.15 – Frequency modes present in the doubling cavity in the *scanning mode*. Example of the signal around the turning point of the scan (in grey dotted frame) shows that by having only two modes on display might cause confusion in determining the *free-spectral-range* (especially if the sidebands are very weak, which is s desired state). It is recommended to always display 3 modes on the oscilloscope.

Advice: Broken *fast* piezo actuator in the *SHG* cavity of the *TA-FHG pro Toptica laser*

If the *Piezo 1* (*big*, slow acting piezoactuator connected to the *PID 110* module) breaks, which can be determined by low resistance (the resistance of properly operating piezoactuator should be 1 $M\Omega$), the other piezoactuator (*small*, fast-acting *Piezo 2* connected to the *FALC 110* module) can be used instead. It is enough to swap the BNC cables on the back of the *TA-FHG pro* box between the two channels of the same doubling cavity. It should be possible to find and catch a lock just with that one small piezo driven by the controller in the *PID 110* module dedicated to the *slow* piezoactuator. Although the range of the drift compensation is going to be limited. It is good as a temporary solution; however, the piezoactuator will eventually have to be replaced for a proper cavity lock and to maintain long-term stability.

A photodetector to measure the light reflected back from the cavity (sometimes also called a light leaking from the cavity) is installed behind the input mirror *M1*. The light intensity measurement is sent to the *PDD 110* module on the *DLC pro* controller of the old laser. The *PDD 110* generates the *PDH error signal* that is sent to the PID controller to adjust the piezo actuator inside the cavity. Technically there are two piezoactuators installed on the same mirror to achieve a wider *mode-hop-free* tuning range. *Piezo 1* is bigger and connected to the *PID 110* module, which provides the standard response. *Piezo 2* is a smaller piezoactuator connected to the *FALC 110* (*Fast Analog Linewidth Control*) module (15 ns signal delay) giving a locking bandwidth of ~ 10 MHz according to *Toptica*. The same setup repeats for the *FHG* cavity, which is stabilised to the 626 nm output mode from the *SHG* cavity in the same way.

Wavemeter: Frequency measurements and stabilisation

To extract the absolute frequency of the *TA-FHG pro* laser, we use a *Wavelength Meter* (*WLM*), commonly referred to as a *wavemeter*. Wavemeter is a device that uses an interferometer to measure the laser frequency with respect to other well-known and stable frequency reference. A Fizeau interferometer is used to generate an interference pattern between the measured laser and a reference laser. The laser used for the reference in our case is a *He-Ne*.

We use a Wavelength Meter by *High Finesse* from *WS* series, model *HF-MC4-SM460*, 460 nm version with 4 channel switch. Switch has 4 fibre inputs for different lasers and single fibre output capable of transmitting all the wavelengths to the wavemeter. So the switch itself and the fibres are the limitation for the wavelengths of the laser that could be measured. Its operational range of wavelengths according to specifications is 450-600 nm, but *Ly-α team* uses it for 730 nm laser measurement and achieves sufficient transmission through the switch. Lasers connected to the wavemeter via the switch must be within the operational range, so for *beryllium experiment* and *antihydrogen spectroscopy* the laser wavelengths from *SHG* stage are coupled to the fibre via *Fibre Dock* on the *Toptica* laser. Inputs to the switch are:

1. 486 nm 1S-2S spectroscopy
2. 730 nm Ly-α [28]
3. 626 nm beryllium laser-cooling
4. 633 nm *He-Ne* calibration laser

A reference *He-Ne* laser is calibrated to the *ULE* cavity every some time. Wavemeter measurements combined with feed-back loop controller can be used to stabilise the laser frequency, as well as to perform controllable long-range frequency sweeps [29]. The wavemeter is connected to the computer to display the interference pattern and the current measured frequency in the software *Wavelength Metre WS*. There is a solution for frequency stabilisation and sweep implemented in the software, which runs the PID feedback controller and determines an analogue control voltage that is output from the *PCI* card installed in *Wavemeter PC*. This signal from the wavemeter can be sent to the laser diode to actively update the frequency. During 2019 *beryllium experiment run*, when we demonstrated sympathetic cooling of the positron with laser-cooled Be^+ [1], wavemeter control signal was connected to the *diode current* input of the old *Toptica* laser controller [30]. This was not the best design, since it allowed to sweep the 313nm laser frequency only by around 2.5 GHz without *mode-hops* to occur. Changing the *piezo voltage* gives a significantly wider *mode-hop-free* tuning range 20 MHz for the old laser and 100 MHz for the new *Toptica* laser. The wavemeter control output could be connected directly to *piezo voltage* and due to the *Feed-Forward* solution from *Toptica*, the *diode current* is adjusted together with the change of *piezo voltage*.

[28] The wavemeter from *High Finesse* works for 730 nm, even though this wavelength is beyond the manufacturer's specification.
[29] Up to 100 GHz for the new *Toptica* laser, the available frequency range depends on the design of the laser, not the wavemeter
[30] The signal applied to the input terminal is a voltage, that gets converted to current by internal electronics.

The frequency sweep by the wavemeter controller was requested via the *LabView* interface that was communicating over the network with the *CompactRIO* that runs the master *Beryllium Control Software VI* on *FPGA*. This master *VI* was sending the sweep start and final frequency and the sweep rate to *LabView VI* running on *Wavemeter PC* to update the sweep parameters and trigger sweep execution. The frequency sweep used in 2019 was not the ideal linear ramp from current frequency to the final setpoint; the setpoint was updated in steps. The main concern of the 313 nm laser frequency sweep was to avoid overshooting the final setpoint frequency, because if we would like to approach very close to the resonance frequency of the laser cooling transition, accidentally moving the frequency to the blue-detuned will heat the ions. The PID control by wavemeter worked well, but the problem was that we had only one wavemeter output signal available (*PCI* card had two outputs, one used already by *Ly-*α laser), while we were planning to add a new *Toptica* laser to the system. Having two 626 nm inputs would already require upgrading the switch to the version with more input channels, but an additional voltage control output channel would still be needed. *High Finesse* offered us a solution with upgrade *PCI* card, but at the end it was decided to go with the budget solution of a postdoc designing a PID controller for the new laser. In the meantime, the old laser broke and had to be sent to *Toptica* for repair, so in 2022 we were left with only one laser that had to be connected to the wavemeter. The new *TA-FHG pro* laser runs on an internal *FPGA* and has a *DLC pro* software interface that can be run on a computer. All operational parameters can be controlled directly from *DLC pro* software or via commands sent to the laser control system by a program written in one of the common programming languages. In our case, we used *LabView* since this is how the rest of the ALPHA experiment is controlled. There is a command that lets the user update *piezo voltage*, and the updated value of the voltage applied to the piezoactuator inside the laser diode could be sent over a network from different computers or *compactRIO*. The new PID controller for sweeping the frequency of the 313 nm laser was written by Steven Jones. This PID control runs on the master *Beryllium Control Software VI* on *compactRIO* and it receives the current value of the laser frequency from the *Wavemeter PC* over the network. A ramp for the frequency sweep is defined in the *Beryllium Control Software VI* running a *FPGA* code and executed by a trigger in the *Laser sequencer* [31].

[31] New *FPGA*-running program to execute laser-related actions (opening/closing shutters, switching and sweeping the laser, photon counter, etc.) in a manner similar to the main ALPHA *Sequencer* software (main control system for the experiment)

AOM: Frequency scans and laser switcher

Devices based on the acousto-optic effect are commonly used to modulate the frequency of light. Acousto-optical devices use a sound wave to generate additional sidebands of laser frequency that are shifted by an integer multiple of frequency of the sound wave. A detailed introduction to the acousto-optic effect can be found in *Fundamentals of Photonics* by Saleh & Teich [233] and in Ref. [234, 235]. The principle of operation is that the acoustic wave travelling through the crystal with a velocity v_{ac} induces vibrations of atoms/molecules, which locally changes the optical polarasibility and modulates the refractive index of the crystal. The refractive index in the crystal changes periodically (period of the wavelength of sound $\Lambda_{ac} = 2\pi v_{ac}/\Omega_{ac}$) and it varies in time as the sound wave propagates. The laser passes through a crystal perpendicularly to the acoustic wave and it reflects off of planes created by varied refractive index (planes separated by Λ). Since the timescale of the laser field oscillation is orders of magnitude smaller than for the acoustic wave, during a single oscillation of the optical wave ($T = 2\pi/\omega = \lambda/c$), the refractive index is basically constant. The reflection occurs if the laser beam approaches with the angle θ_i to the normal of the direction of the sound wave propagation, which satisfies a Bragg condition:

$$sin\ \theta_i = \frac{\lambda}{2\Lambda_{ac}} \tag{5.2.15}$$

This condition gives constructive interference between light waves reflected off the different planes of that quasi-constant refraction index. The output light wave is reflected from the plain moving with velocity v_{ac} and the angular frequency is Doppler-shifted

$$\omega_r = \omega \left(1 \pm \frac{2v_{ac}sin\theta}{c}\right) \tag{5.2.16}$$

where $v_{ac}sin\theta$ is a velocity component of the sound wave in the direction of propagating light and $\theta = \theta_i + \theta_d$ is the angle between the diffraction peaks and $\theta = 2\theta_i$ for isotropic crystals. Bragg diffraction produces light of angular frequency shifted from the laser light by the frequency of the sound wave:

$$\omega_r = \omega \pm \Omega_{ac} \tag{5.2.17}$$

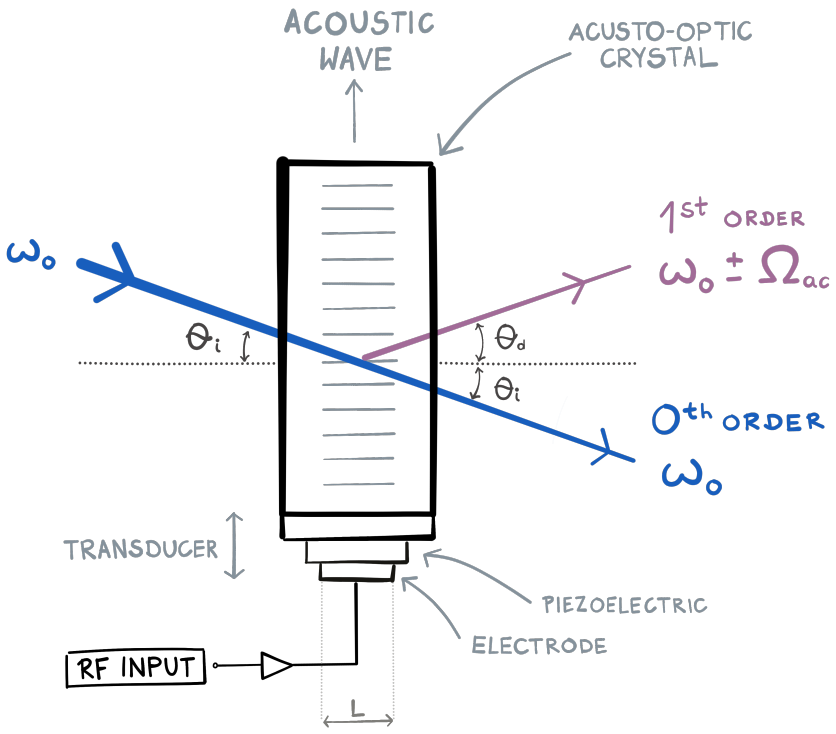

Figure 5.16 – The principle of AOM operation. The acoustic wave is generated by applying a RF signal to the piezoelectric actuator installed on the side of the AOM. Laser entering AOM crystal scatter on the acoustic wave which causes generation of the frequency shifted sidebands. Figure adapted from [235].

The angle of the diffracted beam depends on the frequency of the acoustic wave, which means that changing the frequency Ω_{ac} varies the direction of the outgoing sidebands. In the practical application of the laser setup, this is undesired, since it might change the laser beam position in the experimental volume during the frequency sweep. The solution to overcome the movement of the sideband beam is to use the AOM in a *double-pass configuration* [236]. This means that the first sideband, generated after passing the AOM first time, is reflected back through the AOM and the first sideband of the second pass (double-shifted frequency $\omega_r' = \omega + 2\Omega_{ac}$) is sent further out. In this configuration, the beam position shift is meant to cancel after double-pass thanks to alignment through the optics, and the beam pointing of the outcoming beam maintains stable position.

Advice: AOM 3200-1210 Gooch & Housego

The AOM crystal works only for one light polarisation (perpendicular to the mounting plate). Standard double-pass configuration would not work, the incoming and outcoming beams must be offset vertically, for example, using a prism.

Standard double-pass AOM setup includes a quater waveplate to change the polarisation of the laser (from one linear polarisation to the opposite) and a polarising beam splitter to separate spatially incoming and outcoming laser beams of different polarisations (Figure 5.17). This is how AOM double-pass for 972 nm light (diode laser wavelength that is doubled in frequency twice to obtain 243 nm laser source) in *1S-2S* laser setup was built, so the same configuration was design for 313 nm laser in 2019. As we did not know at that point, the AOM crystals for *UV* light operate only for one polarisation (perpendicular to the mounting plane). That means that in the setup presented in Fig. 5.17, the 1^{st} order sideband entering the AOM after passing the quater-waveplate twice has wrong polarisation for the 2^{nd} sideband generation to occur. Since the only light transmitted through this set-up was the sideband of 1^{st} order, that means that for the entire 2019 experimental run, when we performed the experiment of sympathetic cooling of positrons with Be^+ [1], we were using a single shifted frequency $\omega + \Omega_{ac}$ instead of the desired double shifted $\omega + 2\Omega_{ac}$.

This was hard to realise in the experiment since, due to the unknown heating mechanism acting on trapped Be^+, the laser cooling rate was different from that theoretically predicted. The double-pass AOM setup was corrected in the setup prepared for the 2022 experimental mini-run, by removing the quater-waveplate and beam splitter and introducing a *Retroreflecting Hollow Roof Prism Mirror* [32] to vertically separate the incoming and outcoming beams (Figure 5.18 shows the top view and Figure 5.18 shows the side view). This idea comes from the work of the Trapped Ion Quantum Information Group at ETH [237].

The acoustic wave is generated by a piezoelectric transducer by applying a radio frequency (*RF*) signal to the electrode (schematic in Figure 5.16). The acoustic wave is generated by a *RF* driver. The AOM driver used in 2019 was *1200AF-AEF0-2.5* by *Gooch & Housego* which gave a 180-220 MHz signal and got upgraded to *1210FM-3-2.0W* (140-280 MHz) for 2022 measurements that after properly implemented double-pass configuration was capable of shifting the laser frequency by 280-560 MHz.

Advice: Do not operate the RF driver if the output is not connected
If the output of the RF driver is not connected to the AOM, the generated signal might be reflected back, due to the impedance mismatch, causing damage to the device.

[32] *HRS1015-F01* by Thorlabs.

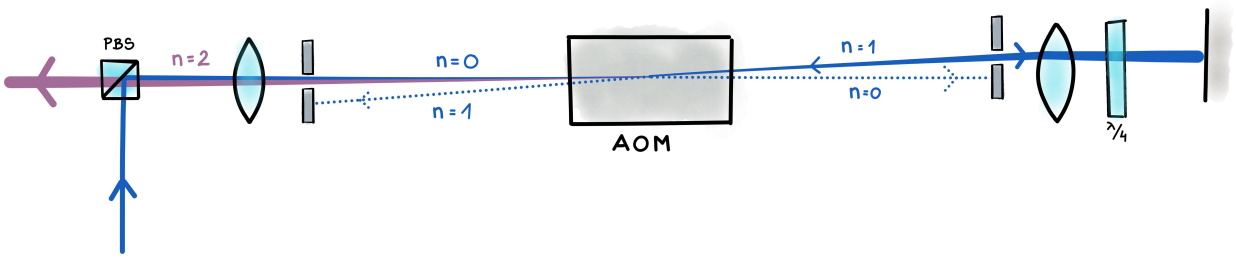

Figure 5.17 – Simple double pass AOM setup used in 2019, top view. The laser light of linear polarisation passes twice by a quarter waveplate and the polarisation is rotated by $\pi/2$. This setup works with the AOM crystal for the 972 nm (diode laser source for the *1S-2S* transition), but not with the crystal for the 313 nm laser, which can transmit only one polarisation (perpendicular to the mounting plate). This meant that in experiment in 2019, the $n = 1$ diffraction mode was extracted instead of $n = 2$.

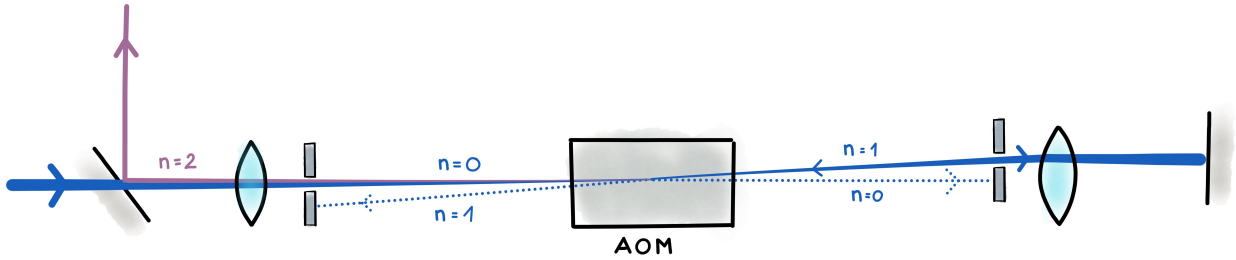

Figure 5.18 – Double pass AOM setup used for 313 nm laser in 2022, top view. Laser light of the same linear polarisation passes twice through the AOM crystal, but the incoming and outgoing beam are vertically separated (as shown on the Fig. 5.19) to extract the $n = 2$ diffraction mode through a different path than incoming laser beam.

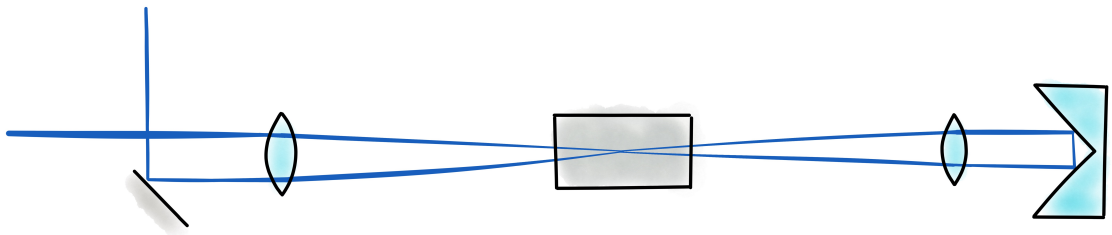

Figure 5.19 – Double pass AOM setup used for 313 nm laser in 2022, side view. The AOM crystal for UV works only for one polarisation (perpendicular to the mounting plane), so incoming and outgoing beams must be vertically separated to extract the output beam from the AOM arm. The outgoing beam reflected by the mirror on the left continues propagating into a page.

The 313 nm laser beam had to be coupled into a fibre to be transported to ALPHA-2 trap, which was a limitation to how far the laser frequency can be scanned using the AOM. Despite the fact that the double-pass configuration is meant to mitigate the beam position shifts, in practice it is very difficult to align the sideband beam to follow exactly the original incoming beam. The core of the fibre has only 10 μm, so movement of the laser beam even by a few micrometres can cause significant power losses. For our best AOM alignment we measured the transmission through the fibre and decided to use the frequency range for which power stays above 50% of the maximum power available at the central AOM frequency. The power of the sideband peak can be modulated by changing the amplitude of the *RF* signal applied to the AOM's input (input called *Analog RF Modulation/Level Control*). The input voltage of *AOM modulation* can be adjusted in the range of 0-1V, which corresponds to the power range of 0-2W for the new driver (2.5W for the old driver). Setting *AOM modulation* to 0V completely stops the generation of sidebands and since the original unshifted laser beam is blocked by physical apertures, this effectively stops the laser beam going to the ALPHA-2 trap. We use the AOM as the switcher for the 313 nm laser beam. The time to ramp up the input of the *RF* signal from 0 to the maximum level takes $\leq 20\mu$s. For comparison, the time it takes to open a mechanical shutter is around 10 ms. This is important for the Be^+ electron spin flip measurement (Section 6.2), when time for turning on/off the 313 nm laser needs to be very short in order to properly detect a level of a dip in the fluorescence signal, which is a measure of how many beryllium ions underwent the electron spin-flip after microwave pulse was sent to the ALPHA-2 trap.

5.3 Beryllium laser cooling in ALPHA-2

Be^+ are produced in all possible electronic states and then decay to all possible ground states, so they need to be optically pumped into our desired $2S_{1/2}(m_J = +1/2, m_I = +3/2)$. An initial period of 313 nm laser exposure is needed to bring most of the Be^+ this state; after optical pumping only 1 in 17 of the Be^+ ends up in a different state ground state [238]. To pump ions the most efficiently, the initial detuning of the laser should correspond to the average velocity of ions loaded to the Penning trap. The temperature of ions is reduced from the temperature of 15.000 K (baseline without laser cooling) to below 1 K in a few minutes.

In our experiment, the initial cooling phase takes more time than in typical experiments with trapped ions or atoms ($\sim$ ms timescale), because we have $10^5 - 10^6$ ions with significantly wider velocity spread (ions are loaded at $\sim$ 10 eV). In the original experiment of sympathetic cooling of positrons [1,131], we had only one 313 nm laser beam, which was introduced via a special optical port on the upstream end of the ALPHA-2 trap. The injection port is tilted from the centre of the Penning trap at an angle of 2.4°, therefore the name *off-axis laser*. For the central electrodes, the laser beam is nearly parallel to the z-axis of the Penning trap, but the further away from the central electrode $E14$, the larger the radial offset between the laser beam path and the centre of the cylindrical electrode. The consequence of this is that for the plasma of $\sim$ mm size, there is no overlap between laser and ions outside of the thin trap (electrodes $E8 - E20$) and laser cooling can only occur in the middle of the ALPHA-2 trap. Efficient cooling also requires a small radial size of the plasma [33]and efficient mixing between axial and radial motions. Mixing the axial and radial energy could be achieved by laser cooling ions under *Rotating Wall* at frequency driving the radial compression of ions – *RW* compression increases the energy of the magnetron motion, by decreasing the radius of the magnetron motion. In principle, heating by *RW* compression can be compensated by laser cooling. This was not possible to achieve for the *off-axis laser*, because at the positions of both Rotating Walls (electrodes $E3$ and $E25$) it does not overlap with Be^+.

In the original work performed in 2019, we managed to achieve sympathetic cooling of positrons to temperatures $\sim$ 7 K, we had to cool down Be^+ by a series of subsequent periods of laser cooling in central electrodes, transfers to *RW*, compression under *RW* and repeated laser coolings. This method was sufficient for demonstration of sympathetic cooling of positrons with laser-cooled beryllium ions, but Be^+ preparation was long (total cycle with positrons cooling was around 10 min) and for numbers of positrons required for antihydrogen synthesis, the compression was not possible to be performed with the $\bar{H}$ trapping magnets energised [34]. For these reasons our procedure for laser cooling of beryllium ions was incompatible with the standard antihydrogen production sequence. We decided to introduce an additional 313nm laser beam, which would overlap with beryllium ion plasma at the position of both Rotating Walls, so it would propagate exactly along central axis of the Penning trap, so *on-axis laser*.

[33]Ideally significantly smaller than the laser radial beam profile, to not vary too much the laser intensity across all the plasma.

[34]The octupole magnet produces significant magnetic field for non-zero radial positions, causing heating of ion plasmas, which held in the Penning trap. Ion plasma must be small in radius, when magnetic trap for $\bar{H}$ is energised.

The *on-axis* cooling laser was introduced by splitting the beam generated by the new *Toptica* laser (providing up to 800 mW) and delivering both beams via the optical fibres to the experimental area. The *on-axis* beam is injected through a large optical port in the upstream AT stick chamber at the 90° angle from the z-axis and it reflects from the special rectangular mirror installed at the stick (at the 45° angle of incidence) to pass through the trap exactly in the middle of each cylindrical electrode. On the downstream AT stick there is the same mirror to eject the beam at 90° via similar port on the side of the DS AT chamber. The mirrors are 2.5 × 3.5 cm and they have coating that reflects 313 nm, 243 nm and 532 nm (green pointer laser that helps with the alignment). Mirrors for the *on-axis laser* must be installed on the sticks, such as they can be moved away from the axis to inject and eject particles from the trap, therefore they were integrated onto the stick.

In our measurement in 2022, both *on-axis* and *off-axis* beams originated from the same laser source and were offset from each other by a value of 400 MHz with the Acousto-Optical Modulator (AOM), whose frequency could not be tuned by much to not loose coupling to the fibre. At the moment of beryllium spin-flip measurement, the old 313 nm laser, which was used in the previous experiment, was not operational. Now that the laser is repaired, it could be integrated to the experiment. The advantage of two independent laser sources is that we could have two different frequencies. That would allow to have separate laser-cooling and a probe laser for various applications:

i. To characterise the lineshape of the cooling transition $^2S_{1/2} \rightarrow \ ^2P_{3/2}$ as a method of measuring ions temperature.

ii. To introduce a repumping laser to the system.

iii. To laser-cool and detect Be+ ions at two different magnetic fields at the same time (for example, 1T in trapping volume and 3 T under *Rotating Wall*)

Chapter 6

Magnetometry with Be^+

There are two aspects of magnetic field measurements in ALPHA experiment:

1. the absolute magnetic field generated by superconducting magnets, that determines the Zeeman splitting of energy levels and the magnetic force experienced by atoms;
2. the strength of the magnetic field that drives the transition, relevant for the positron spin-flip in the antihydrogen, which is induced by the microwave radiation.

Measurements of the absolute magnetic field inside the trap [1] are important for every type of antihydrogen experiment performed by ALPHA: for *1S-2S* spectroscopy, positron spin-flip (hyperfine spectroscopy), laser cooling to determine the energy levels splitting and it is crucial for antihydrogen's gravity measurement to distinguish the gravitational acceleration $\bar{g}$ from the acceleration caused by the magnetic field $\bar{a}_B$ [2]. For all the previous ALPHA work, the absolute magnetic field value was obtained with an *Electron Cyclotron Resonance* (*ECR*) technique [162,239], which relies on measuring the cyclotron frequency of the electron plasma in a Penning trap (more details in the next Section 6.1.1). So far, the main limitations of the *ECR* method were that it works for the high and flat (non-gradient) fields and measures the *B-field* only on the axis of the Penning trap (plasmas are confined at radial positions $r \simeq 0$). The *ECR* technique is under continuous development and significant progress has been made to address these issues. An alternative technique for measuring magnetic field inside the ALPHA trap would first of all serve as a cross-validation of our present magnetometry method.

[1] In context of antihydrogen experiments we usually refer to the magnetic field of the Ioffe-Pritchard trap for neutral atoms. Knowledge of the magnetic field of the Penning trap is useful for developing methods of charged plasma manipulation etc.

[2] We the symbols related to antimatter with a bar at the top, so it is also common to use a bar above the symbols of physical variables to denote that they are referred to antimatter systems, E.g. antimatter's gravitational acceleration $\bar{g}$.

The beryllium ion source and diagnostic tools dedicated to it already existed in the ALPHA-2 trap for the previous work on sympathetic cooling of positrons[3]. The promising aspect of *beryllium magnetometry* is non destructive diagnostics via emitted fluorescence light and the prospects of improving the precision of the measurement. With an improved detection scheme for Be^+ (photon counters installed inside the Penning trap), significantly smaller samples of ions and possibly even single ions could be used, increasing the spatial resolution of the magnetic field measurement.

Another aspect of magnetometry is to measure the intensity of the magnetic field component of the microwaves used inside the ALPHA-2 trap. This is important for the hyperfine spectroscopy of antihydrogen. The hyperfine structure in the antihydrogen is measured by a microwave-induced positron spin-flip, which is a magnetic dipole transition caused by an oscillating magnetic field. Knowledge of the magnetic field component of the microwaves is crucial for evaluation of the hyperfine transitions. The microwave power was estimated based on the calculation of the freely propagating wave, but we already empirically know that microwaves inside the ALPHA-2 trap do not propagate in the same way as in free space and the intensity of the microwave radiation changes depending on the axial position in the Penning trap [35]. The amplitude of the magnetic field component of the microwaves could be estimated by using electron spin-flip transition of Be^+ in the Rabi-style experiment (more details are given in Section 6.2.2.

6.1 Current magnetometry methods in ALPHA

The main technique used in ALPHA for magnetometry is the *Electron Cyclotron Resonance* (*ECR*) technique, which will be presented in this section. The *ECR* is the method to probe the magnetic field inside the Penning trap *in situ* using an electron plasma. Additionally, the magnetic field is monitored during the experiments with online *Hall probes* installed outside of the trap. The magnetic field generated by external solenoid magnets of the Penning traps can be characterised offline with *Nuclear Magnetic Resonance* (*NMR*) technique. More information about the *Hall probes* and *NMR* method can be found in the Ph.D. thesis of Nathan Evetts [240], which focuses on the development of *NMR* probes for low temperatures to possibly use them as online monitors in the ALPHA Experiment.

[3]MCP and Faraday Cup are the same as used for antiprotons, positrons and electrons.

6.1.1 Electron Cyclotron Resonance technique

The cyclotron frequency of a given particle is constant in a static magnetic field; therefore, this frequency is used to characterise the magnetic field inside a Penning trap. The cyclotron frequency for electrons within a magnetic field of around 1T lies in the microwave regime:

$$f_{ECR} = \frac{qB}{2\pi m} \approx 28\ GHz \cdot B\ [T] \tag{6.1.1}$$

The cyclotron frequency of an electron plasma can be determined by inducing a heating of the plasma by microwave radiation and then measuring the change in plasma temperature either passively or destructively in a method called *Electron Cyclotron Resonance*. This method samples the radially-central ($r = 0$) magnetic field strength of Penning traps. The earliest ECR method used by ALPHA was a passive measurement. That method involved observing the heating of an electron plasma by measuring the temperature sensitive frequency of the quadrupole mode of an oscillating plasma, as this oscillation generates image currents on electrode surfaces [239]. The induced quadrupole mode frequency shift is correlated with the injected microwave frequency to obtain the ECR resonance. This method required that the electron plasma be physically large, with radii of 0.1 cm and length 4 cm, such that the image currents can be measured. One problem with this method is that the larger volume occupied by the plasma induces broadening of the ECR resonance due to magnetic field inhomogeneities. A microwave frequency sweep to obtain an ECR resonance takes 10 minutes. Recently, an improved method was introduced that uses small electron plasma samples, called scoops, ($\sim$ 1500 electrons) extracted from a trapped electron reservoir (24 million). This method called *Reservoir ECR* was developed by Eric Hunter [162, 241]. The temperature of the electron plasma is measured with the *Temperature Diagnostic* technique 2.3.3. $60 - 120$ scoops can be extracted from the reservoir. Each scoop is interrogated with a different microwave frequency to obtain the ECR resonance. Small scoops of electron plasma allow for faster scan of microwave frequencies (around 2 minutes) and since scoops are smaller than previously used electron plasma they probe smaller volume of the magnetic field inside the trap. *Temperature Diagnostic* technique, using *SiPM* detectors [160], is more sensitive than modes diagnostics, which results in increased precision of the *ECR* frequency measurement, which allows to resolve peaks of the *ECR* frequency and other plasma modes.

The ECR measurement produces multiple resonance peaks: the ECR resonance and various sidebands resulting from the axial and magnetron dynamics of the electron plasma. The ECR resonance peak is identified as one that does not change its frequency when the axial frequency is modified by varying the shape of the trapping well.

Electrons used in ALPHA for ECR measurements are produced on demand by an *electron-gun* instrument installed on a stick. All sticks neighbouring the ALPHA Penning traps include an *electron-gun*. The same microwave hardware used for the hyperfine spectroscopy of antihydrogen is used for exciting the cyclotron motion of the electron plasma as the *ECR* frequency is close to the frequency of the positron spin-flip in $\bar{H}$). Microwaves at frequencies between 26 and 30 GHz and powers up to 20 dBm are generated by an *Agilent HP 8673D* synthesiser [4] and sent to the ALPHA-2 trap via a waveguide ended with a microwave horn. The microwaves propagate inside cylindrical electrodes of radius 2.25 cm (central electrodes that overlap with the magnetic minimum trap where the antihydrogen is confined), which is comparable to the size of the microwave wavelength ($\sim$ 1 cm). There are gaps between electrodes, the radius of the electrodes differs between normal (*RCT* and *POS*) and thin (*ATM*) traps and there are many physical apertures inside the vacuum chamber that restrict the free-wave propagation of the microwaves. The electrode geometry acts as a microwave cavity, modifies the freely propagating microwaves and creates some not-well-known standing waves, which cause the power of the microwaves to vary depending on the position inside the trap. The standing-wave pattern is highly sensitive to the microwave frequency, so that the microwave power at a given position is frequency dependent. This effect was studied using a set of replica electrodes and simulations [243]. Heating of an electron plasma induced by microwaves is proportional to the intensity of the electric field component of the microwaves, so the electrons' temperature measured in *ECR* experiments was used to extract information about the intensity of the electric field component of microwaves inside the ALPHA-2 trap. Although the pattern of the magnetic field wave generated inside the trap can be different from the electric field component of the wave [5], which is important for measuring $\bar{H}$ positron spin flip. The polarisation of microwaves is also mixed inside of the trap.

[4] The relative accuracy of the microwave synthesiser *Agilent 8257D PSG* is 10^{-7}, and resolution 10 mHz.

[5] The electrodes are made of a good electrical conductor (aluminium with gold plated surfaces), which makes electric field lines to terminate at the electrodes surfaces. Electrodes, as well as all other components of the ALPHA-2 trap, are made from material with low magnetic content, so the magnetic field is slightly distorted but does not terminate at the boundary of electrode surfaces.

ECR measurements for the $\bar{H}$ hyperfine spectroscopy

The positron spin-flip in the ground state of $\bar{H}$ $(1S)$ is a method to investigate the hyperfine interaction in the $\bar{H}$ atom. The basic idea of the measurement is that $\bar{H}$ atoms are trapped in the ALPHA magnetic trap only in 2 out of 4 hyperfine states (so-called *low field seeking states*, with an electron spin anti-aligned with the magnetic field $|\downarrow\rangle$, referred as $|c\rangle$ and $|d\rangle$ states in *Ref.* [35]) and they are irradiated with microwaves. If the frequency of microwaves matches the energy difference between $|\downarrow\rangle$ and a corresponding *high field seeking state* $|\uparrow\rangle$ of the same antiprotons spin state (referred to as $|a\rangle$ and $|b\rangle$ states), the transition to the $|\uparrow\rangle$ state (transitions $|c\rangle \rightarrow |b\rangle$ and $|d\rangle \rightarrow |a\rangle$) can occur and those $\bar{H}$ atoms that changed the positron spin state are ejected from the magnetic trap (more details in *Section* 1.2.2). The main factor that determines the frequency of the hyperfine transition is the strength of the external magnetic field due to the Zeeman effect. We operate in the high-field regime, where both of the positron spin-flip transitions increase with increasing external magnetic field. Both positron spin-flip transitions are offset in frequency by a value of $1,420.4 \pm 0.5$ MHz. The positron spin-flip is induced by the microwave pulse and the probability of the transition depends on the intensity of the microwave field, frequency detuning from the resonance of the transition and duration of the microwave pulse (the same as for the electron spin-flip, see Eq. 3.1.5).

ECR measurement vs beryllium magnetometry

The *ECR* method in ALPHA Experiment has some limitations:

(a) it is a destructive method that requires loading new electron sample for every probed microwave frequency

(b) *ECR* works well in flat magnetic field, but does not work in the high gradient fields (work ongoing, first measurements under Mirror Coils)

(c) it works for static, but not for changing magnetic fields, which would be desired for ALPHA-g measurement

(d) ECR is a good method for high magnetic field, but not for low fields

The possibility of using electron spin-flip in $^9Be^+$ induced by an oscillating magnetic field opens a new endeavour for the precise magnetometry in the ALPHA Experiment.

First of all, the intensity of the magnetic field component of microwave radiation inside the ALPHA-2 could be investigated with Be^+. The benefit of using beryllium ions over an electron plasma is that it is a non-destructive detection method. The probability of the transition is measured by the change in fluorescence level, and a single sample of Be^+ can be used even for multiple microwave frequency sweeps. Currently, this measurement technique has some limitations; the main problem being the limited axial range in which fluorescence can be detected with a photon counter placed outside of the trap. With an upgraded fluorescence detection system, such as photon detectors are placed inside the trap in the vicinity of beryllium ions increasing the detection solid angle drastically, even single ions could be detected, which would greatly improve the precision, by removing collective effects and by probing significantly smaller volume within the trap, which could possibly allow applying beryllium magnetometry to do the measurement in the magnetic field gradient. Similar measurement time scales as the *ECR* technique could be achieved for the current photon detection system (if the repumping laser would be introduced) and possibly even $\sim$ sec for the photon detectors installed inside the trap.

6.2 $^9Be^+$ electron spin flip measurement

6.2.1 Idea for using beryllium for magnetometry

In our case of electron spin-flip in $^9Be^+$, we are interested in one of the hyperfine transitions in the ground state $^2S_{1/2}$ [6]

$$|\uparrow,\Uparrow\rangle : \ ^2S_{1/2}(m_J = +1/2, m_I = +3/2) \longrightarrow |\downarrow,\Uparrow\rangle : \ ^2S_{1/2}(m_J = -1/2, m_I = +3/2).$$

Ions in the $|\uparrow,\Uparrow\rangle$ state, denoted as $|\uparrow\rangle$ for short, can be detected by fluorescence of light, which is emitted from Be^+ ions while they decay from the excited state back to ground state during the cycle of laser-cooling transitions

$$^2S_{1/2}(m_J = +1/2, m_I = +3/2) \longleftrightarrow \ ^2P_{3/2}(m_J = +3/2, m_I = +3/2),$$

therefore the $|\uparrow\rangle$ is refereed as a *bright state*. The $|\downarrow,\Uparrow\rangle$, denoted as $|\downarrow\rangle$, is not part of this laser-cooling cycling transition and does not emit light, so it is called a *dark state*.

[6] In general electron spin-flip transition is any transition that changes m_J from $+1/2$ to $-1/2$. We have chosen the hyperfine transition such as it uses the ground state of the *cooling transition* that we typically use in our experiment.

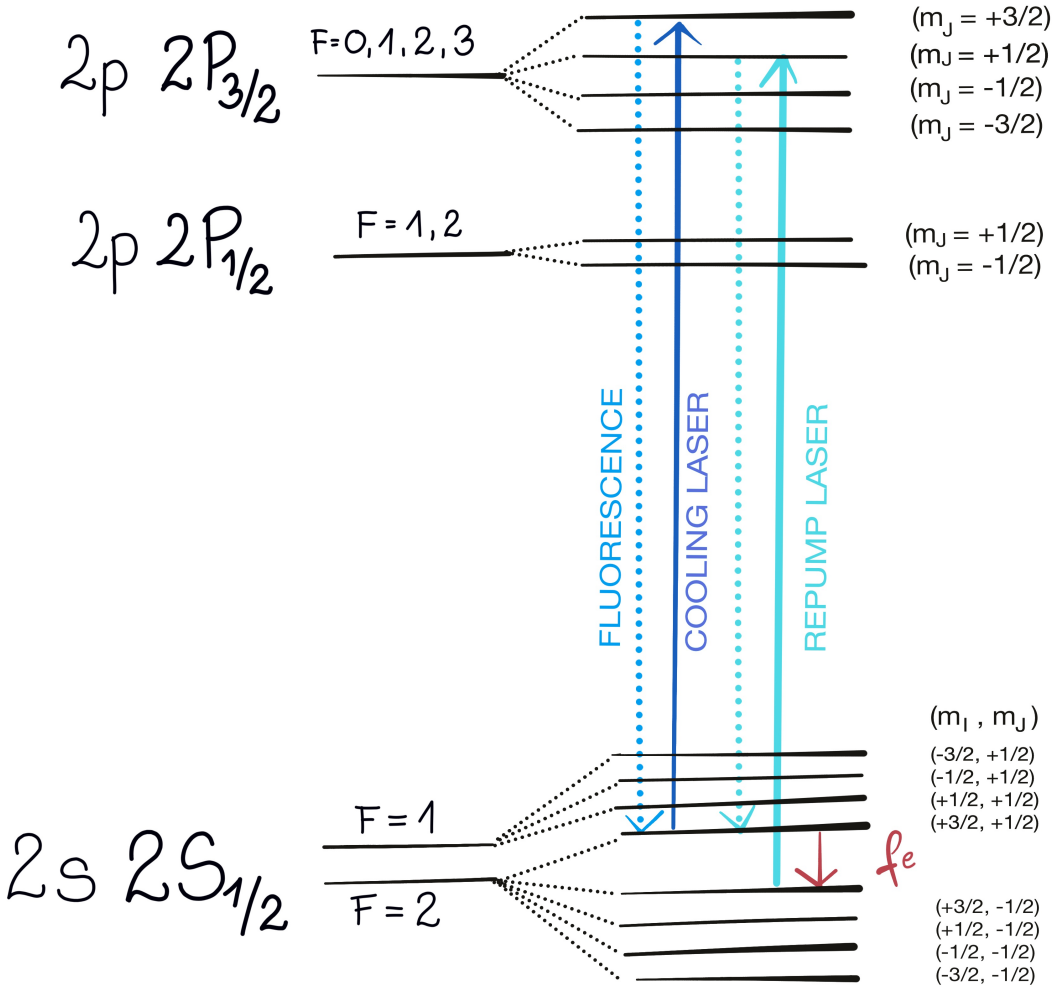

Figure 6.1 – Energy levels structure of Be^+. The transitions relevant to the laser-cooling process and electron spin flip transition in the ground state are marked. In our experiment we did not have a separate repump laser, we relied on the fact that the cooling laser off-resonantly repumps the ions from the $m_J = -1/2$ to the $m_J = 1/2$ state.

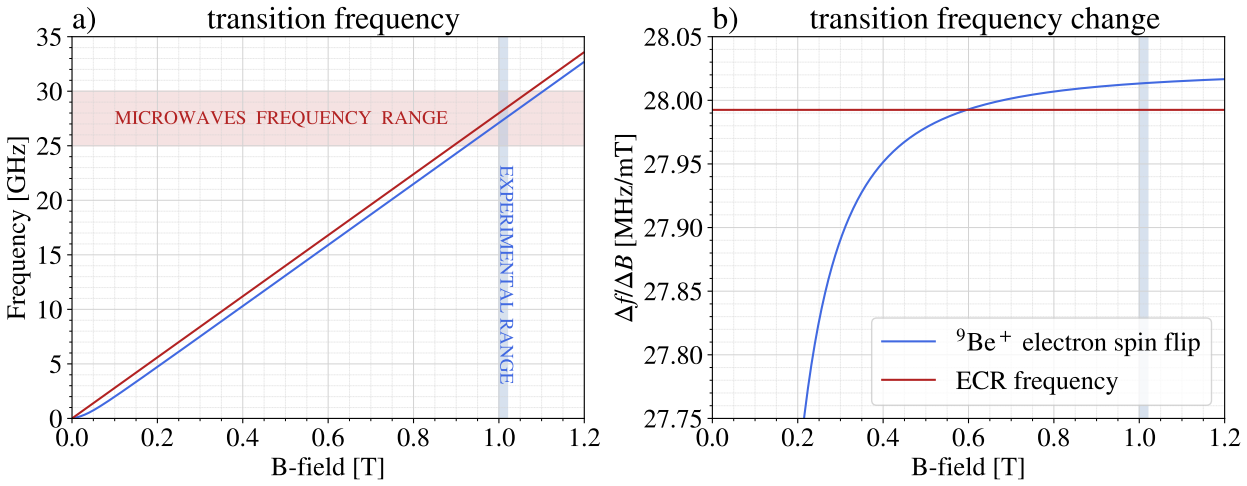

Figure 6.2 – (a) Frequency of the electron spin-flip in Be$^+$ and frequency of the *ECR*. (b) Frequency change for the electron spin-flip of Be$^+$ and *ECR* as a function of the magnetic field. The blue shaded region is the range of magnetic fields that ALPHA-2 usually operates at. The red shaded region is the microwave frequency operational range in the ALPHA-2 trap [244].

The frequency of the electron spin-flip transition f_e depends on the strength of the external magnetic field, as shown in Figure 6.2. Based on the frequency calculations in Section 5.1.1 of this electron spin-flip transition at standard magnetic field in the ALPHA-2 trap $B \simeq 1.02\ T$ is around 27.6 GHz.

We can detect whether microwaves interact with $^9Be^+$ and cause the electron spin-flip transition by looking at the fluorescence of the cooling transition. Ions that go into the *dark state* do not fluorescence until they are repumped back into the *bright state*. If we send the microwave pulse at frequency f_i near the resonance f_e while shining the 313 nm laser at the ions we will see a characteristic dip in the fluorescence signal (example of the spin-flip signal in Figure 6.5). The depth of the fluorescence signal drop corresponds to the fraction of ions for which the electron changed the spin state. Since during the laser cooling experiment we rely on the laser off-resonantly repumping Be$^+$, the ions will come back to the $|\uparrow\rangle$ state a few seconds after the microwave pulse has been applied. In fact, this was the first time we had measured directly the repump rate of beryllium ions inside *ALPHA-2 Atom Trap*.

Electron spin-flip measurement in ^{9}Be$^+$ could address both aspects of magnetic field measurement in the ALPHA Experiment mentioned in the Introduction Section 6.1. Measurement of the electron spin-flip frequency f_e could inform us about the strength of the external magnetic field inside the ALPHA trap similarly to the *ECR* technique, which would

first serve as cross-calibration our current magnetometry and next it could push our magnetic field measurements methods further towards increased precision and simpler protocols. Beryllium magnetometry is based on reading an atomic transition via fluorescence, which is a non destructive method. This would allow to measure full transition lineshape or even many of them with the same sample of ions, unlike ECR, which requires loading a new electron plasma to probe each microwave frequency. In order to make this measurement a reliable and robust magnetometry technique, we would have to prepare Be^+ samples that are reproducible in size and number of ions, similar to the electron scoops in the ECR method. Since the beryllium ion plasmas produced from the laser ablation can differ significantly in size, we might also want to use SDREVC method on Be^+ (when developed), as in the case of electron reservoirs. The SDREVC requires turning on the internal superconducting magnets [7], which changes the overall magnetic field in the ALPHA-2 trap. So far only the measurements in the flat field of the *Carlsberg magnet* only were made. In fact the final goal is to develop this method to work with the internal magnetic Ioffe-Pritchard trap for $\bar{H}$ energised, so study of the electron spin flip in Be^+ for various magnetic fields configuration must be performed. It should be noted that ramping the internal superconducting magnets up and down, induces persistent currents in the external solenoid magnet of the Penning trap, which change the initial magnetic field by a small amount. Also it is not know how ramping up the down the magnets of the transfer beamline influences the B-field of the ALPHA-2. It would be favourable to not have to change any of the magnetic fields configuration during the actual B-field measurement.

The second possible application of the electron spin-flip transition in beryllium ions could be to map the strength of microwaves inside the ALPHA-2 trap along the z-axis of the trap. We already know that the microwave field is not uniform along the entire $\bar{H}$ trapping volume, because the electrode stack of the Penning trap acts as the cavity (the microwave wavelength is around 10 cm, which is a scale comparable to the electrode size) that causes an unknown pattern of standing waves inside the trap. The amplitude of the microwave field defines the Rabi frequency Ω, which is one of the factors determining the probability of the hyperfine transition in antihydrogen. In the latest measurement [35], the approximation of free-propagating wave was used.

[7] Internal solenoids ramp to 2T on top of the 1T of the external solenoid of the Penning trap (*Carlsberg magnet* in ALPHA-2, but the same design is implemented for ALPHA-g trap), to give total 3T at the position or *Rotating Wall*.

Simulating microwave propagation inside *ALPHA-2 Atom Trap* is difficult, because it is very sensitive to the precise placement of the internal components, and we prefer to rely on the actual measurement. So far the *ECR* technique has been used to estimate the magnitude of the electric field component of microwaves at different positions of the trap by looking at the strength of the resonance signal. However, the a positron spin-flip is a magnetic dipole transition, therefore it is driven by the magnetic field component of the microwaves and this could not be measured so far. Electron spin-flip in the ground state of the beryllium ion is equivalent to the positron spin-flip measured in antihydrogen, so it could serve as a probe to characterise the amplitude of the magnetic field component inside the *Atom Trap*. This could reduce systematic errors of the ground state hyperfine measurement in the antihydrogen.

Electron spin-flip in Be^+ measurement at NIST

An inspiration for the work presented in this thesis was a Rabi measurement with beryllium ions performed by *Shiga, Itano and Bollinger* [132]. In their experiment at NIST *Shiga et al.* used a laser-cooled plasma [8] of approximately 500 beryllium ions confined in a Penning trap to measure the hyperfine transitions in the ground state of $^9Be^+$: 1 electron-spin-flip transitions and 3 nuclear-spin-flip transitions. The electron spin-flips were performed using a π-pulse of microwaves, which is the standard *Rabi method* and nuclear spin-flips were measured with a series of two $\pi/2$-pulses of radiofrequency radiation, which is a technique known as the *Ramsey method* or *Ramsey interferometry* [242]. Be^+ were prepared in the initial state $|i\rangle = {}^2S_{1/2}(m_I = +3/2, m_J = +1/2) = |\uparrow, \Uparrow\rangle$ (both electron and nuclear *spin up*) by optical pumping using a 313 nm laser tuned to the cooling transition (the same transition as in our Be^+ laser cooling experiment, see Figure 6.1)

$$^2S_{1/2}(m_I = +3/2, m_J = +1/2) \longleftrightarrow {}^2P_{3/2}(m_I = +3/2, m_J = +3/2)$$

and probed with 600 μs pulses (corresponding to a π-pulse at the resonance) of varied microwave frequencies. The ions in the $|\uparrow\rangle$ state undergo a transition to the $|\downarrow\rangle$ state with a probability dependent on the detuning of the microwave pulse with respect to the electron spin-flip resonance frequency f_e. The number of ions in the $|\uparrow\rangle$ state is measured by fluorescence, which occurs during a decay from the excited level $^2P_{3/2}(m_I = +3/2, m_J = +3/2)$.

[8] More on laser-cooling in the Sections 3.2.

The fluorescence signal decreases proportionally to the number of ions that changed an electron spin state to $|\downarrow\rangle$. In fact, the *dark state* interacts very weakly with the cooling laser, which nonresonantly drives the *dark state* into the $^2P_{3/2}(m_I = +3/2, m_J = +1/2)$ state, from which it decays to the *bright state*. This process is called *off-resonant repumping* and takes on the order of a few seconds to pump ions back into the *bright state*, and the time of the process depends on the rate of the repumping transition

$$^2S_{1/2}(m_I = +3/2, m_J = -1/2) \rightarrow \ ^2P_{3/2}(m_I = +3/2, m_J = +1/2)$$

All ions need to be repumped back into the bright state before they are exposed to the next microwave π-pulse. The time that it takes to perform the full microwaves frequency sweep is usually determined by the time to repump all the ions to initial state between each pulses [9]. The repumping process could be sped up by introducing an additional laser, which is detuned further away from the cooling transition and closer to the repumping transition, to faster populate the $^2P_{3/2}(m_I = +3/2, m_J = +1/2)$ state. This has been done in the discussed work of *Shiga et al.* by adding a dedicated *repump laser* along the z-axis of the Penning trap, which reduced the repumping time from $5s$ to < 1 ms. In the NIST experimental setup there were two cooling lasers: one on the axis of the trap to cool the axial motion and the other perpendicular to cool the radial motion of the beryllium ions.

Those ions that changed electron spin state after interaction with microwaves will no longer emit photons when exposed to the 313 nm laser, which accounts for reduction of the fluorescence signal. The fluorescence signal after the microwave pulse $\mathcal{S}_{after}(f_i)$ normalised to the signal $\mathcal{S}_{before}(f_i)$ equals the fraction of ions that remained in the $|\uparrow\rangle$ state:

$$\frac{\mathcal{S}_{after}(f_i)}{\mathcal{S}_{before}(f_i)} = \frac{|\uparrow\rangle_i}{|\uparrow\rangle_i + |\downarrow\rangle_i} = 1 - \frac{|\downarrow\rangle_i}{|\uparrow\rangle_i + |\downarrow\rangle_i} \tag{6.2.1}$$

The fraction of ions that changed the electron spin state $\mathcal{F}_{flip}$ for given microwave frequency f_i equals then

$$\mathcal{F}_{flip}(f_i) = \frac{|\downarrow\rangle_i}{|\uparrow\rangle_i + |\downarrow\rangle_i} = 1 - \frac{\mathcal{S}_{after}(f_i)}{\mathcal{S}_{before}(f_i)} \tag{6.2.2}$$

which is related to the probability of the electron spin-flip transition $\mathcal{P}_i$ for given microwave frequency f_i. In the experiment performed at NIST, signals were recorded for 0.5 s before and after the pulse and the cooling laser was off during the microwave/radiofrequency pulses.

[9] The π-pulse time is usually on the order of hundreds of microseconds (for *Shiga et al.* work 600 μs), while repumping time varies from milliseconds to seconds

The repump laser was turned on after the detection period. The cooling laser beam is at the same time the probing beam, so in fact it changes the population of ions in a *dark state* due to the off-resonant repumping, but it seems like in the experiment performed by *Shiga et al.* this has been neglected.

In the work of *Shiga et al.* the values of fractional drop of the fluorescence signal $\mathcal{F}_{flip}$ as a function of the microwave frequency f_i were fitted with the Rabi resonance curve (as in Equation 3.1.9) to obtain the resonance frequency of the electron spin-flip transition f_e in $^9Be^+$. This frequency combined with the results of the nuclear spin-flip transition measurements was used to obtain the value of the diamagnetic correction to the ground state hyperfine constant in $^9Be^+$ (see more details in Section 5.1.1).

6.2.2 Rabi measurement with Be^+ in ALPHA

We planned to perform the Rabi-type experiment, in which we look for the resonance peak at the transition frequency after sending the microwave pulse, similar to the experiment performed by *Shiga, Itano and Bollinger* [132]. Scan of different microwave pulse frequencies around the resonance frequency f_e would give us the resonance curve defined by the probability of the spin-flip transition:

$$\mathcal{P}_i = 1 - \frac{(\Omega/\pi)^2}{(f_e - f_i)^2 + (\Omega/\pi)^2}\ sin^2\big(\pi t\sqrt{(f_e - f_i)^2 + (\Omega/\pi)^2}\big) \tag{6.2.3}$$

where Ω is the Rabi frequency, t is the time of the microwave pulse and f_i is the frequency of the i^{th} pulse. Equation 6.2.3 can also be expressed as a function of the frequency detuning $\Delta_i = f_e - f_i$ from the electron spin-flip resonance. In a proper Rabi experiment, the duration of the microwave pulse should correspond to π-pulse $t_\pi = \pi/\Omega$ (see Figure 3.5).

The idea is to measure the probabilities $\mathcal{P}_i$ for various microwave pulse frequencies f_i, to get a data set that could be fitted with Equation 6.2.3, with f_e and Ω as fitting parameters. From the electron spin-flip resonance frequency f_e we could derive the strength of the static magnetic field generated by the external solenoid magnet (*Carlsberg magnet*), the internal magnets of the Ioffe-Pritchard trap [10] and also background generated by other magnets in the background, mostly ALPHA-g external solenoid (*ALPHA-g external solenoid magnet*), if present.

[10] During the development work the internal magnets are turned off, but ultimately we want to apply this technique during experiments with antihydrogen, when the *magnetic trap* for antihydrogen or internal solenoids for *SDREVC* are ramped up.

The Rabi frequency Ω is proportional to the intensity of the oscillating magnetic field generated by microwave radiation. To improve the accuracy of the fit, it would be helpful to be able to approximate the expected value of the Rabi frequency Ω, by independent measurement in which the microwave pulse time scan t_{pulse} is performed for constant microwave power to observe Rabi flopping (as in Figure 3.1), from which the Rabi frequency could be extracted. Alternatively, the microwave strength can be scanned for a constant pulse duration to find a Rabi frequency, for which this pulse becomes a π-pulse. This seems to be the most common approach to get a nicely rounded value for the pulse duration (e.g. $t_\pi = 600\mu s$ in Ref. [132] or $t_\pi = 450\mu s$ in Ref. [186]). Using a π-pulse is beneficial in maximising the probability of the on-resonance transition f_e, which in theory should correspond to changing the spin state of all Be^+ that experience a field oscillating with frequency Ω for the duration of t_π. In principle, the longer the pulse time, the more ions in the population will gain some phase offset in their Rabi oscillation due to the influence of the environment (decoherence effect), so the fraction of ions $\mathcal{F}_{flip}$ that change spin state after interaction with the microwave pulse at resonant frequency f_e would decrease. On the other hand, for very short pulses (microseconds and below), the microwave power required to perform a π-pulse would be very high, higher than practical for many experiments.

The experimental sequence of Rabi measurement with Be^+ should look as follows:

I. preparation: laser cooling of ions sample

II. fluorescence background acquisition (with ions)

III. microwave pulses and signal acquisition

   (i) record fluorescence

   (ii) turn off the 313 nm laser

   (iii) apply microwave pulse

   (iv) turn on the 313 nm laser

   (v) record fluorescence

   (vi) repump and cool

IV. * fluorescence background (with ions)

V. * laser background (no ions)

It might be helpful to measure the fluorescence background (the last two steps marked with $*$) multiple times during the frequency sweep if the fluorescence signal level is not stable. Measuring laser background with no ions, might be difficult since it is better to use the same sample for entire microwaves sweep or even for many of them in case of performing a parameter scan. Loading a new sample of Be^+ takes time, and so far the number of ions produced is not well under control. Applying a *SDREVC* method to beryllium ions could make the ion preparation process much more reproducible, but that would require even more time on sample preparation, which has the clear disadvantage of long times required to perform the full microwave frequency sweep, during which the field of *Carlsberg magnet* and the background magnetic field can drift already enough to disturb the electron transition lineshape. An alternative method to measure the laser background with fluorescence coming from beryllium ions would be to shuffle the ions to a neighbouring electrode, where they would not overlap with the laser beam anymore, which could be done within $10 - 100$ ms. If this approach is taken one should ensure to perform a potential well manipulation in such a way to not disturb the plasma properties and to not lose the ions during the shuffle. Beryllium ions are heavier than electrons, so slower steps > 10 ms might have to be used.

Challenges of the Rabi measurement in ALPHA-2

1. Determine correct timings for the experimental sequence

a. correct microwave pulse duration and power to perform a π-pulse,

b. correct time between microwave pulses to give enough time for ions to get re-pumped back to the *bright state* and cooled to initial equilibrium temperature,

c. correct time for turning off the laser to not let them heat too much when they are not laser-cooled.

The time t_{off} for which the laser is switched off must be equal to or greater than the duration of the microwave pulse $t_{\text{off}} \geq t_\pi$. The 313 nm laser induces fluorescence to detect the $|\uparrow\rangle$ states and at the same time provides cooling to the trapped beryllium ions. In the absence of the laser, ions' temperature depends on the various sources of heating inside the trap (with the cooling laser beryllium ions have temperatures of thousands of Kelvins [131]).

When ions are exposed to a red-detuned laser, initially their kinetic energy is getting reduced due to the laser-cooling effect until some equilibrium temperature is achieved when cooling by the laser is compensated by heating mechanisms acting on ions confined in the Penning trap and new equilibrium temperature is maintained, when heating in the trap and cooling force of the laser remain constant in time. This *laser-cooling equilibrium temperature* depends on laser-cooling parameters: the laser detuning and intensity of the laser per ion, as well as parameters that determine plasma temperature: ions density, trapping potential depth (electric and magnetic fields), shape of the electric well, and temperature of the cryostat. Turning off the 313 nm laser stops the cooling source, so the ions start heating. We want to switch off the cooling laser for as short as possible to avoid heating the beryllium ions sample. We also want to make sure before each new microwave frequency pulse that we have re-cooled the ions back to their initial temperature.

2. Optimise laser cooling process

Since the magnetic field of the *Carlsberg* external solenoid of the ALPHA-2 trap is decaying over time, the shortest possible time for a full microwave frequency sweep over the full electron spin-flip transition would be preferred. It is also possible that there are some short-term fluctuations of the magnetic field that have never been detected with previous techniques. The main factor determining the measurement sequence is the time between microwave pulses, when we wait for ions to be repumped back to the $|\uparrow\rangle$ state and cooled back to the initial temperature before the pulse. Both the repump rate and the cooling rate depend on the cooling-laser intensity and the spatial overlap between the ions and the laser beam. Assume that all ions are exposed to the uniform laser field and that the laser power can be adjusted to the reach transition saturation intensity I_s to drive the cooling transition at the highest rate, but the final equilibrium temperature achievable in the cooling process could still vary, depending up the strength of the heating mechanisms in the trap. For example, larger plasmas experience stronger heating, since ions radially further away from the centre of the trap are more affected by the electrical noise on the electrodes surfaces and oscillating electric field is known to be a source of heating in the plasma. Electrostatic field anomalies have also been observed on the electrodes surfaces, called *patch potentials*, that significantly contribute to the heating rate of plasmas in the Penning trap [6].

The patch potentials are expected to be generated *i.a.* by the UV laser used for the $1S2S$ spectroscopy of antihydrogen. Additionally, in the case if the magnetic trap for antihydrogen would be energised, the octupole generated magnetic field that raises for non-zero radial positions in the trap, would significantly contribute to heating the ion plasma, unless the plasma size is very small [11]. The equilibrium temperature of the Be^+ sample determines the thermal broadening of the electronic transitions linewidth, so the electron spin-flip linewidth would also be broadened for larger ion plasmas, leading to lower precision of the final result.

Another experimental parameter that should be chosen carefully is the frequency detuning of the cooling-laser. On the one hand, we wish to optimise the cooling process and increase the fluorescence signal-to-noise ratio, so close red-detuning would be desired. On the other hand, if the same laser beam is used for probing the states of Be^+, a higher laser-cooling transition rate would also mean higher off-resonant repumping of the ions into the *dark state*, and that would disturb the signal during the detection period right after the microwave pulse $\mathcal{S}_{after}$, which is needed to correctly interpret fraction of ions that changed the electron spin state for given microwave frequency. An additional problem with using a closely tuned probing laser is that it could disturb the background fluorescence signal level generated by ions in the *bright state*. The rate at which the fluorescence signal changes for changing frequency detuning is significantly higher for smaller detunings. If the cooling/probing frequency is set close to the resonance, then smaller changes of the magnetic field (caused, for example, by changes of the magnetic field generated by the external solenoid) would cause a greater change of the fluorescence signal, which could be wrongly attributed to the effect of the interaction with the microwave pulse. The problem of choosing the frequency of cooling laser could be solved by having a separate probing and cooling beams, which could be frequency tuned independently or by fast switching the frequency of the laser between probing and cooling frequencies. The probing beam could be set to low power to not change significantly the state of ions, while a higher power cooling beam could be switched on after the detection period to speed up the cooling process and reduce time needed to perform a full sweep of microwave frequencies. The reduced time of the full frequency sweep should at least limit the influence of the external solenoid magnet decay.

[11] For example in the experiment of sympathetically cooling positrons with laser-cooled Be^+ [1, 131], we had to significantly reduce the beryllium plasma size in order to efficiently cool it in the octupole's magnetic field.

Whether the probe beam should be tuned to close- or far-detuning is still a matter of compromise between getting sufficient fluorescence signal and minimising the signal change due to the possible changes of effective detuning caused by changes of the external magnetic field. It is possible to implement two laser beams, which could be frequency tuned independently, because we already have two 313 nm lasers: one is the old *Toptica* laser used in the past for the positron sympathetic cooling measurement and the second is the new laser of the same type that was used for these Be^+ electron spin-flip measurement. We did not have enough time to recommission the old *Toptica* laser to be used for this experiment. The laser could also be fast switched between cooling and probing frequencies by the *AOM*, if the frequency between them was on the order of tens of MHz.

3. Transition broadening due to changes in the magnetic field

There is another source of spatial effect on the transition line broadening due to the magnetic field inhomogeneities. For larger plasmas, the external magnetic field would be less uniform across the axial and radial extents of the plasma. This would cause the effective detuning of the cooling-laser frequency with respect to the actual resonance of the $^2S_{1/2}(+\frac{3}{2},+\frac{1}{2}) \leftrightarrow {}^2P_{3/2}(+\frac{3}{2},+\frac{3}{2})$ transition, which is a function of the magnetic field, to be different for ions at different positions inside the plasma, which is another possible source of the transition linewidth broadening. These effects due to the plasma size are in fact the same problems that the *ECR* method has to deal with. The effect of a non-uniform magnetic field across the radial position is especially apparent in the situation when the neutral Ioffe-Pritchard trap is turned on during antihydrogen experiments. The octupole magnet, one of the internal superconducting magnets, generates a magnetic field increasing radially outward to confine antihydrogen atoms. The effect of the octupole field on the Be^+ laser-cooling efficiency has been observed in the positron sympathetic cooling experiment [1], where only smaller Be^+ plasmas were cooled sufficiently (more details can be found in J.Jones' Ph.D. thesis [131], in Section. 8.2.1). Ideally, we would use the smallest sample of ions possible, but this reduces the fluorescence signal, which is proportional to the number of ions. Our current fluorescence diagnostics are limited to a very small solid angle of 2.3 μSr (assuming that the photon counter detector is well aligned to the centre of the trap, where beryllium ions are confined and that fluorescence emission is approximately uniform in all directions), resulting in a very small signal and a low signal-to-noise ratio.

All of this gives some trade-off between getting a decent fluorescence signal and narrowing the transition linewidth. The intensity of the fluorescence signal could be improved by upgrading the detection system to cover more of the solid angle, but it would require installing a photon detector inside the trap in the cryogenic volume.

An additional well-known effect is the decay of the magnetic field generated by a superconducting magnet that produces the external B-field in the Penning trap (*Carlsberg magnet*). It has previously been measured that the *ECR* frequency changes by around 1.6 kHz/min, which corresponds to 60 nT/min. This rate of the magnetic change has to be accounted for if the microwave sweep duration is on the order of minutes. This is an additional argument to reduce the time needed to collect data for single spin-flip transition lineshape.

4. Determine the number of beryllium ions in the sample

It is important to interpret the drop in fluorescence level correctly as a fraction of Be^+ for which the transitions from $|\uparrow\rangle$ to $|\downarrow\rangle$ state occurred. We must understand the relation between the photon count signal and the number of beryllium ions emitting photons. The first step is to optimise the overlap between the plasma and the laser beam to ensure that the number of ions in the trap is equal to the number of ions generating fluorescence. It would be beneficial to measure the number of Be^+ with another device (destructive measurement with a *Faraday Cup* or non-destructive plasma modes diagnostics) to calibrate the photon count rate vs. number of beryllium ions in the trap. The intensity of the laser should be uniform across the entire ion plasma, or the intensity distribution should be known to obtain the conversion factor between number of Be^+ in the trap and total number of emitted photons. From this the actual photon detection efficiency could be inferred.

The intensity of the laser beam should be stable. Otherwise, the background photon rate might increase (e.g. scattered light inside the trap), as well as the number of photons emitted by ions could change if the laser intensity is smaller than saturation intensity I_s, since the laser-cooling transition rate would change accordingly. Next, number of beryllium ions in the sample should remain constant or depletion rate should be characterised in order to extract the fluorescence signal decrease that is related to decreasing number of Be^+ in the trap. Alternatively, if the *SDREVC* technique for beryllium ions is developed and reproducible samples can be loaded into the trap, each microwave frequency could be probed if a new sample of Be^+ to avoid the ion depletion problem.

5. Changing microwave intensity problem

One of the motivations to develop the beryllium magnetometry, that relies on electron spin-flip transition in $^9Be^+$, is to characterise the intensity of the magnetic field component of the microwave field in the ALPHA traps. The electrode stack acts as a form of cavity for the microwaves, which causes that instead of freely propagating wave, some non-uniform standing wave is created. A pattern of this standing wave depends on the frequency, which means that for given position inside the trap, the intensity of the oscillating microwave field varies depending on the frequency of microwaves. The Rabi frequency Ω' would differ for different microwave frequencies, which means that using a constant pulse duration t_{pulse} during the microwave frequency sweep would cause the ions to experience a different phase shift from the π-pulse: $\Omega' t_{pulse} \neq \pi$. Therefore, a better approach would be to measure the Rabi frequency at each microwave frequency individually by probing various pulse durations t_{pulse} at the constant microwave synthesiser output power and the constant microwave frequency (or alternatively probing the microwave synthesiser output power, while maintaining constant pulse duration and frequency), in order to measure Rabi flopping similar to the oscillation shown in Figure 3.1. This measurement could be directly used to extract the intensity of the magnetic field component of the microwaves and if performed at various locations inside the Penning trap it would allow to map how the standing magnetic wave pattern looks like, which would benefit the antihydrogen positron spin-flip measurement.

6. Perform a Rabi-type experiment (laser off during microwave pulse)

In principle a measurement with any arbitrary pulse duration could be performed and the data obtained could be fitted by the function in Equation 3.1.9 with resonance frequency f_e and Rabi frequency Ω as the fitting parameters. Although in a real experiment, after multiple Rabi oscillations, the ions lose coherence, which results in damping of the Rabi oscillation (as presented in Figure 3.1), so the magnitude of the main resonance peak will decrease for each successive multiple of the π-pulse. For the case where the duration of the microwave pulse would be equal to or greater than the decoherence time, Equation 3.1.7 could be used to fit the measurement data and would require that the decoherence time τ_c be an additional parameter of the fit.

Proper Rabi-type experiment requires turning off the cooling/probing laser during the time that the ions are exposed to the microwave pulse. If we test f_e by applying microwaves during the laser exposure, the resonance will be broader and the frequency is offset from the real resonance due to the AC Stark shift (as presented by *Nakamura et al.* [186] (see the schematic of the energy level shift in Figure 3.6). Although this method is proposed as an initial quick hunt for the resonance. We can start the experiment by running *ECR* measurement in the same electrostatic potential well to get a good initial estimate of f_e. To perform a measurement of the magnetic field that achieves better precision than the *ECR* method, we would have to use the proper Rabi method.

Experimental setup

Beryllium ions obtained by pulsed laser ablation [130] were trapped in the cryogenic ALPHA-2 Penning trap, which is primarily used for the production and trapping of antihydrogen (it contains an additional set of internal superconducting magnets that allow magnetic trapping of antihydrogen). Beryllium ions are confined in this Penning trap with a magnetic field of 1 T. Beryllium ions are laser-cooled with a 313 nm laser beam of 9 mW at the input to the trap. The same laser beam, propagating with a small angle, 2.4°, with respect to the z-axis of the ALPHA-2 trap, so-called *off-axis laser* (see details in Section 5.3), was used to cool ions, induce a fluorescence signal and repump ions after the microwave pulse. The fluorescence signal was recorded with a *Hamamatsu* photon counter with a *C8855-01 counting unit*. The photon counting head was installed more than 1 meter away from the trap's centre on one of unused laser access widow ports on the downstream end of the trap, which means it is also pointing at the angle of 2.4° from the trap axis. The photon counter was usually set to count photons for 10 ms (referred to as *gate time*). To generate microwave pulses, we have used the same *Agilent 8257D PSG* microwave synthesiser that is being used for the electron cyclotron resonance and $\bar{H}$ hyperfine measurements. The relative accuracy of this microwave synthesiser is 10^{-7} and the resolution 10 mHz [245]. The operational microwave frequency range in the ALPHA-2 trap is 25-30 GHz [244]. The maximum power output of the synthesiser is 20 dBm, for our measurement we did not use any amplifier. Microwaves are delivered to the ALPHA-2 trap via a waveguide and injected on-axis of the trap through a microwave horn installed on the linear translator (*stick*).

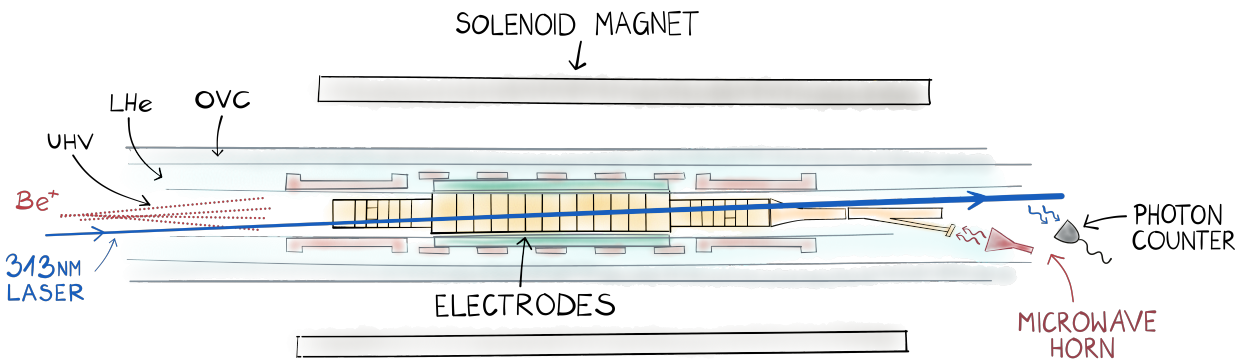

Figure 6.3 – Simplified scheme of the apparatus, where beryllium experiment was performed. A cross section of the ALPHA-2 trap (a Penning trap combined with magnetic minimum trap, same apparatus as shown in Figure 1.1) is presented. Beryllium ions are loaded from the *upstream* side and the cooling laser is passing through the trap with an angle of 2.4° from the z-axis of the trap. A microwave source and the photon counter for fluorescence detection are installed on the *downstream* end of the trap.

Preparation of the Be^+ sample

We load Be^+ sample by a pulse laser ablation from beryllium target installed inside the vacuum chamber on the upstream side of the ALPHA-2 trap (see discussion in the Chapter 4). Before probing Be^+ with microwave pulses at various frequencies, we had to cool the beryllium sample. We apply an initial long range sweep from $\Delta \simeq -15$ GHz to -920 MHz in 80 s, next a slower sweep to -70 MHz in 40 s and then a few manual steps of 10 MHz, 10 s each, to reach the final detuning around -40 MHz, which is around $2\gamma_0$. The detunings for which the chirp rate is changed were chosen by a few test cooling sweeps, during which it has been determined that we should start from detunings greater than 10 GHz. The first sweep can be fast, we chose the shortest time of the second, slower, sweep that resulted in successful cooling. The last manual sweep starts roughly around the detuning for which the fluorescence signal starts to raise rapidly. The last steps of the detuning chirp are requested manually, and the final detuning is chosen based on the observed fluorescence signal with respect to the signal level observed for the far detunings. We have done this to avoid overshooting the resonance and heating the ions, which used to happen if the frequency chirp was automated. This is because the requested detuning sweep is based on the frequency calculation using magnetic field, which has to be repeatedly updated due to the decays of magnetic field generated by the Penning trap solenoid. If the magnetic field drifted down too much since the last setpoint update, then our transition frequency calculation gives a too high value.

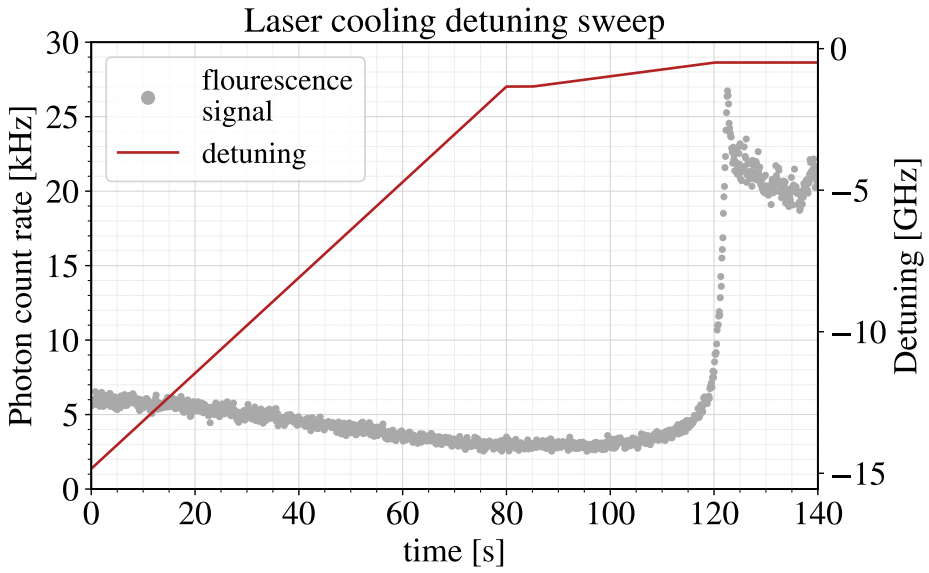

Figure 6.4 – Fluorescence signal measured during laser cooling Be^+ samples used for electron spin-flip measurement. Cooling-laser is chirped in frequency from $> 700\gamma_0$ to $\sim 2\gamma_0$.

Therefore, the laser frequency chirp can go on the blue-detuning side of the resonance. The solution would be to automate the setpoint update of the magnetic field value. The decay of the magnetic field is already known and is simple to predict. More problematic would be the prediction of shifts caused by internal superconducting magnets ramping up and down and the persistent currents induced in the main solenoid due to those changes.

The exact number of ions is not known because calibration of the MCP pictures was not possible at the time. The pictures of beryllium ion plasma were too distorted to perform a fit using a Gaussian beam profile. The ablation and trapping procedure was similar to that used for sympathetic cooling of positrons, where the number of ions measured was 0.1-0.5 million [1]. That calibration was also imperfect because of the distortions of the images caused by the electrostatic apertures of the MCP's high-voltage tabs. Calibration of the MCP signals for the Be^+ plasma was performed a few months after the electron spin-flip experiment. Using the results from the calibration performed later, we would have had around 80 millions of Be^+. This discrepancy means that we do not know the exact number of ions or even the order of magnitude. Between the measurements in 2019 and 2022, the MCP voltages were changed (front voltage changed from -100V to -300V). The camera position, determining the pixel-to-size calibration, and possibly some other settings might have been changed between the data taking and the calibration performed a few months apart.

To perform a proper calibration of the MCP for Be^+, the plasma must be small enough to fit in the sensitive region of the MCP and not get distorted on the edges. Similarly, the Be^+ plasma imaged during the experiment must have the same small, non-distorted radial profile. Reliable calibration and ion number calibration should be possible whenever a *SDREVC* technique is established for Be^+ to control the density of the ions and obtain reproducible samples. From the fluorescence signal level readout for small detuning, we could make a relative comparison of how many ions have been trapped. For each new sample, we discarded half of the ions before the laser frequency chirp to image them on the MCP detector, intending to measure the initial number of ions. This is called a *Half-Dump* measurement. After the sweep microwave pulses, the remaining ions are also dumped and imaged on the MCP. After the ejection of remaining ions, the background photon count is measured. Usually, a beryllium ion sample was used for a few frequency sweeps, each sweep lasting 10-15 minutes. The background photon count was then measured 1-2 times per hour, and the background photon count rate for the *off-axis* laser beam was measured to be 2-3 kHz. This background level is subtracted from all the photon count measurements. If the fluorescence signal level after initial cooling was lower than ~ 5 times the background photon count, the sample was discarded. In the future, it will be important to correlate the fluorescence signal with the number of ions obtained with plasma measurements techniques.

6.2.3 Electron spin-flip in Be^+ demonstration in ALPHA

In July 2022 we managed to perform a proof of concept experiment, in which we demonstrated microwave induced electron spin flip in Be^+ and we took couple of f_e transition lineshapes from which we have extracted the values of the external magnetic field on the level comparable to the *ECR* technique. The example of the observed electron spin-flip in the $^9Be^+$ signal is shown in Figure 6.5. The measurement was carried out only for 3 days due to the ongoing commissioning of the ALPHA-g experiment. Due to the limited time in which we could use the ALPHA-2 trap, we did not manage to characterise the microwaves strength and study the sources of systematic errors. The results presented here are the first trials to induce and detect electron spin-flip in Be^+. It was more a debugging phase during which we have tried to vary the microwave pulse parameters and see which settings maximise the fluorescence-dip signal.

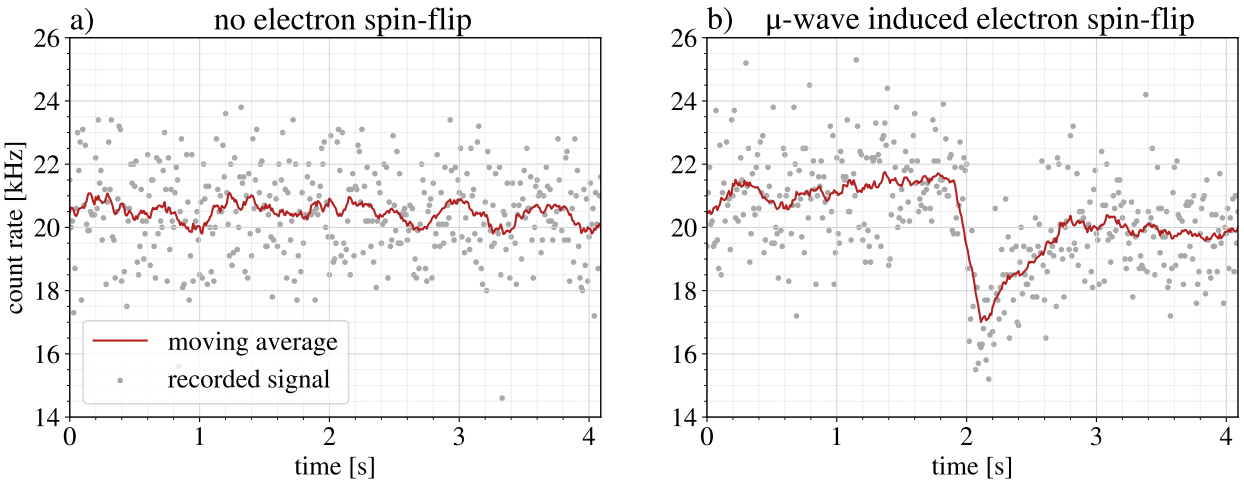

Figure 6.5 – First observation of microwave induced electron spin-lip in ^{9}Be$^+$ in ALPHA-2. Example of the signals from the same dataset (single microwave frequency sweep) for two different microwave frequencies. The microwave pulse length was 100 *ms*. The actual signal is marked with grey points, red line is the moving average over 20 datapoints. The gatetime for single datapoint acquisition is 10 ms.

The main unknown for this experiment was the duration of the microwave pulse that would correspond to the π-pulse for a given microwave power. Additionally, we could not well control the number of beryllium ions, their overlap with the 313 nm laser beam and laser's power stability (due to unstable transmission through the UV fibres discussed in Section 5.2.3). We did not study the correlation between the number of counted photons with the actual number of beryllium ions held in the trap.

The protocol of electron spin-flip experiment that we performed differed significantly from the initially planned Rabi method. We did not have enough time to find the pulse duration that corresponds to the π-pulse or even an approximate value of t_π. We performed complete microwave frequency sweeps around the expected f_e resonance using eight different lengths of the μwave pulse, shown in Figure 6.11. Pulses of 100-200 ms gave the deepest fluorescence drop corresponding to the strongest spin-flip signal. The maximum fraction of Be$^+$ that changed the electron spin state was $\leq 50\%$ for 10 ms, suggesting that the duration of the π-pulse must be shorter than this. The linewidth of the transition did not depend as much on the microwave pulse parameters, as on the time when the lineshape measurement was taken. This is shown in Figure 6.12, where lineshapes collected during different days, but for the same microwave pulse parameters ($t_{pulse} = 100$ms and power of 20dBm).

The second major difference from the Rabi method was that for most of the recorded data the cooling laser was turned on all the time while the ions were exposed to microwave pulses and we continuously measured the fluorescence of Be^+. This is expected to broaden the lineshape and offset it from the centre of the resonance due to the laser-induced AC Stark shift, as shown by *Nakamura et al.* [186]. During the last 2 hours we attempted the spin-flip measurement with no laser during the microwave pulses and got 7 transition lineshapes. The microwave pulses were 50 ms, and the laser was blocked for 100 ms by turning off using the AOM. As shown in Figure 6.13, there was no convincing evidence for lineshape narrowing between runs with the laser off and the laser on during the microwave pulse. This is most likely due to the fact that the transition lineshapes are already broadened due to the decoherence effects and other effects play a more significant role.

In our case, most of the ions are repumped within 0.5-1 s after the end of the microwave pulse. Only the very initial fluorescence signal right after the microwave pulse would correspond to the number of ions for which the electron spin-flip was induced. In fact only for the runs, in which laser was turned off during the microwave pulse, the initial signal after the microwave pulse truly corresponds to fraction of ions that went from the $|\uparrow\rangle$ to the $|\downarrow\rangle$ state. When the ions remained exposed to the laser, the off-resonant repumping continued during the microwave pulse. Therefore, the magnitude of the fluorescence signal drop is smaller than it would be if the laser was off.

To know whether this effect of repumping significantly influences the population in the $|\downarrow\rangle$ state during the microwave pulse, the repump rate and the rate at which the spin-flip transitions occur would have to be estimated. If the repump rate would be significantly smaller than the spin-flip rate, then this effect could be neglected, and the fluorescence signal drop right after the microwave pulse could be well approximated as the fraction of ions that changed the electron spin state. Information about the repump rate can be extracted by fitting the fluorescence signal after the microwave pulse ends, as it recovers to the level before the microwave pulse. During the microwave pulse, if the probe laser is on, the observed signal is decreasing at a rate that is a combination of spin-flip rate and counter acting repump rate. The repump rate obtained in the previous step could allow us to estimate the spin-flip rate during the microwave pulse.

The fluorescence signal was very noisy and global non-uniform instability of the fluorescence level was observed, which makes it more difficult to evaluate a baseline and a background signal, so I decided to use a more complicated method to extract the fraction of ions that changed the spin state $\mathcal{F}_{flip}$, by using a fit function that models the dynamics of ions changing the electron spin state between $|\uparrow\rangle$ and $|\downarrow\rangle$, which will be discussed in the next subsection.

6.2.4 Electron spin-flip data analysis

A series of fluorescence signals for multiple microwave frequencies were recorded around the expected electron spin-flip frequency. The expected resonance frequency f_e was obtained based on the *ECR* measurement of the *B-field*. The microwave frequencies were usually scanned over 1 MHz and later 500 kHz around the expected resonance in 101 equally spaced frequency steps. Each fluorescence signal started before the microwave pulse was triggered to record the signal when all ions were in the $|\uparrow\rangle$ state (*pre-pulse signal*). The microwave pulse of the duration t_{pulse} is sent to the trap and the fluorescence signal continues to recorded during the pulse (*μ-wave pulse signal*) and after until the ions get repumped back to the initial state (*repumping signal*). For most of the data that we have recorded, the cooling laser was on all the time during the microwave pulse, which means that the line broadening and offset might be expected due to the AC Stark shift as reported by *Nakamura et al.* [186]. The fluorescence signals for which the electron spin-flip occurred look like Figure 6.5 b. and 6.6. The lineshape of the electron spin-flip transition is built by extracting the probability $\mathcal{P}_i$ of the transition associated with each microwave frequency f_i. The resulting transition probability for each microwave frequency could be fitted with a function from Equation 6.2.3 to get the resonance frequency f_e. We do not know the Rabi frequency Ω and in fact the Rabi frequency can vary for each microwave pulse, as discussed on page 201. This will be ignored for now, and the centre of the lineshape will be assigned as f_e.

To obtain the spin-flip transition probability for a given microwave frequency, we need to evaluate the fraction of beryllium ions that went to the *dark state*, which is given by the fractional drop of the fluorescence signal from the initial level of $\mathcal{S}_{max}$:

$$\mathcal{F}_{flip} = \frac{\mathcal{S}_{flip}}{\mathcal{S}_{max}} \tag{6.2.4}$$

where $\mathcal{S}_{flip} = 1 - \mathcal{S}_{max}$ is the signal drop corresponding to electron spin changing the state.

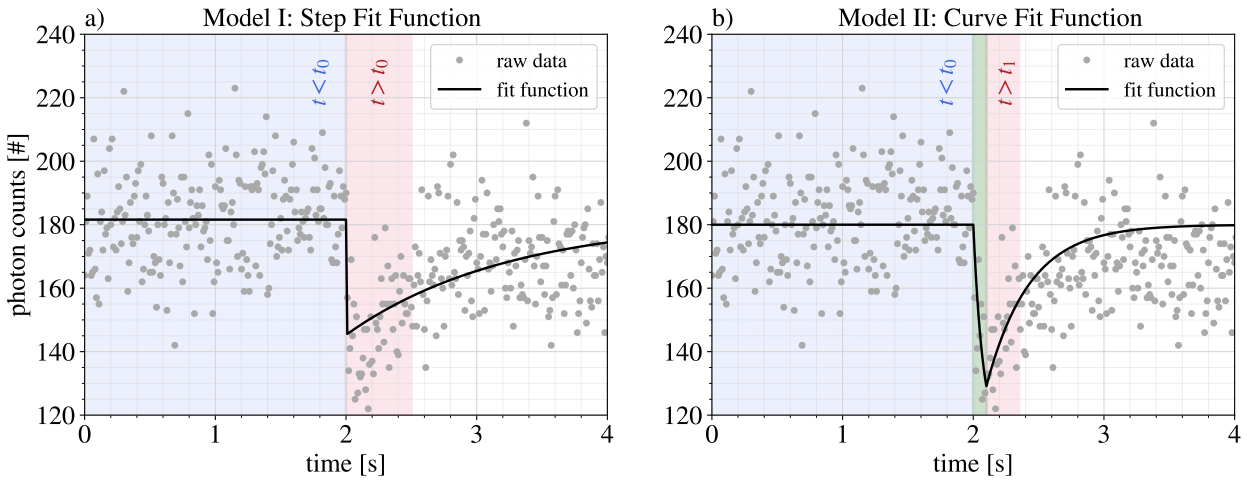

Figure 6.6 – Analysis regions for fitting the piecewise functions. The blue region is the *pre-pulse* ($t < t_0$), fitted with the average value $\mathcal{S}_{max}$. The red region is the repumping time ($t_1 < t$). The fitting range was reduced in the repumping region to the time at which half of the ions were repumped back to *bright* states or to 0.5 s, depending on which occurred first. In *Model I* repumping region is defined from the beginning of the microwave pulse $t_1 = t_0$. *Model II* uses additional region during the pulse ($t_0 < t < t_1$), marked in green. In *Model III* the fluorescence signal during the pulse is set to zero (not shown in this figure).

In a Rabi method (laser off-during μwave pulse) the $\mathcal{S}_{flip}$ would be directly related to the minimum of the fluorescence signal, right after the pulse. If the μwave pulses are sent to ions during the laser is on, *continuous method*, which is the case for most of our data collected, 58/65 of the microwave frequency sweeps, the ions that have spin-flipped are continuously repumped back to the *bright state* during the microwave exposure, so the $\mathcal{S}_{flip}$ does not reach the value that it would if the laser was off.

To extract the values of $\mathcal{S}_{flip}$ from the collected data, a fitting function was used that accounts for the dynamics of spin-flipping and repumping. The level of the initial signal changes during the full microwave frequency scan, so for each frequency a new value of $\mathcal{S}_{max}$ must be assigned. The initial hypothesis was that the sample of ions is depleting over time and $\mathcal{S}_{max}$ is steadily decreasing. This, in fact, is not true, the global change of the signal is sometimes increasing and there is no general trend. Furthermore, the recorded signal is subject to noise, so even a fluorescence signal recorded for a single microwave frequency is difficult to assign the correct value of the initial signal $\mathcal{S}_{max}$. The fluorescence usually did not recover to the same level as before the pulse, so only the initial part of the signal after the end of the pulse was used for the analysis, as shown in Figure 6.6.

Model I: spin-flips occur instantaneously (*Step Fit Function*)

The assumption of this model is that the μ-wave pulse duration is not greater than spin-flip transition time-scale:

$$t_{pulse} \lesssim \frac{1}{\kappa} \tag{6.2.5}$$

where κ is the *spin-flip rate*, so an average probability per second that a single ion changes the electron spin state from $|\uparrow\rangle$ to $|\downarrow\rangle$.

The electron spin-flip occurs instantaneously and the fluorescence signal $\mathcal{S}$ drops from $\mathcal{S}_{max}$ to $\mathcal{S}_{flip}$ in a single step at the time t_0 when the microwave pulse is triggered. In this simplest model, the only dynamic change of the signal occurs due to the repumping of the ions back to the bright state at the rate α. Since the cooling laser is turned on during the microwave pulse, the repumping process starts immediately when the μ-wave pulse starts.

The fluorescence signal before t_0 is constant and equal to the maximum signal corresponding to all ions in the bright state:

$$\mathcal{S}(t) = \mathcal{S}_{max} \tag{6.2.6}$$

After the time t_0 the signal changes as:

$$\frac{\mathrm{d}\mathcal{S}}{\mathrm{d}t} = \underbrace{+\alpha(\mathcal{S}_{\max} - \mathcal{S})}_{\substack{repumping \\ |\downarrow\rangle \to |\uparrow\rangle}} \tag{6.2.7}$$

The solution $\mathcal{S}(t)$ of this ordinary differential equation (*ODE*) has a form

$$\mathcal{S}(t) = c_0 \exp(-\alpha t) + \mathcal{S}_{max} \tag{6.2.8}$$

and the constant c_0 is obtained by applying a condition that all the ions changed the spin state immediately when the microwave pulse started

$$\mathcal{S}(t_0) = \mathcal{S}_{max} - \mathcal{S}_{flip} \tag{6.2.9}$$

which in this case gives

$$c_0 = -\mathcal{S}_{flip} \exp(\alpha t_0) = -\mathcal{P}_i \mathcal{S}_{max} \exp(\alpha t_0) \tag{6.2.10}$$

The piecewise function describing the fluorescence signal in this model looks like

$$\mathcal{S}(t) = \begin{cases} \mathcal{S}_{max} & \text{if } t < t_0 \\ \mathcal{S}_{max}\Big(1 - \mathcal{P}_i \exp\big[-\alpha(t - t_0)\big]\Big) & \text{if } t \geq t_0 \end{cases} \tag{6.2.11}$$

Model II: spin-flips occur in a finite time (*Curve Fit Function*)

For long microwave pulses (duration of multiple π-pulses) the condition 6.2.5 does not apply and the electron flips between $|\downarrow\rangle$ (*dark state*) and $|\uparrow\rangle$ (*bright state*) states multiple times. Since we do not know how our μwave pulse duration relates to the π-pulse duration for unknown microwave field intensity, instead of talking about transition probability for given microwave frequency, we will try to consider dynamics of the system and find the spin-flip rate κ to get the information about the signal drop $\mathcal{S}_{flip}$ that could occur if the laser was off. For that we will use the model that accounts for microwaves driving transition from a *bright* to *dark state*, as well as microwaves repumping the ions back to the *bright state*, both at the rate κ and laser repumping ions to the *bright state* at the rate α.

Before the μwave pulse ($t \leq t_0$) the signal is equal to $\mathcal{S}_{max}$, which is the same as the initial signal in the first model (Equation 6.2.6). The pulse ends at

$$t_1 = t_0 + t_{pulse} \tag{6.2.12}$$

During the microwave pulse the fluorescence signal changes due to simultaneous repumping with the 313 nm laser at the rate α and Rabi flopping induced by microwaves with a spin-flip rate κ:

$$\frac{\mathrm{d}\mathcal{S}}{\mathrm{d}t} = \underbrace{+\kappa\mathcal{S}}_{\substack{spin-flip\\ |\uparrow\rangle\rightarrow|\downarrow\rangle}} \underbrace{-\kappa(\mathcal{S}_{max}-\mathcal{S})}_{\substack{spin-flip\\ |\downarrow\rangle\rightarrow|\uparrow\rangle}} \underbrace{+\alpha(\mathcal{S}_{\max}-\mathcal{S})}_{\substack{repumping\\ |\downarrow\rangle\rightarrow|\uparrow\rangle}} \tag{6.2.13}$$

The general solution to this ODE has a form

$$\mathcal{S}(t) = \mathcal{S}_{max}\frac{\alpha+\kappa}{(\alpha+2\kappa)}\Big(1 + c_1 \exp\big[-(\alpha+2\kappa)t\big]\Big) \tag{6.2.14}$$

Constant c_1 is assigned by condition of continuity between boundaries of first and second region:

$$\mathcal{S}(t_0) = \mathcal{S}_{max} = \mathcal{S}_{max}\frac{\alpha+\kappa}{\alpha+2\kappa}\Big(1 + c_1 \exp\big[-(\alpha+2\kappa)t_0\big]\Big) \tag{6.2.15}$$

The constant c_1 that satisfies the condition above is equal to

$$c_1 = \frac{\kappa}{\alpha+\kappa}\exp\big[(\alpha+2\kappa)t_0\big] \tag{6.2.16}$$

which gives a solution of the signal function in the second region

$$\mathcal{S}(t) = \mathcal{S}_{max}\Big(\frac{\alpha+\kappa}{\alpha+2\kappa} + \frac{\kappa}{\alpha+2\kappa}\exp\big[-(\alpha+2\kappa)(t-t_0)\big]\Big) \tag{6.2.17}$$

At the end of the pulse ($t = t_1$) the fluorescence signal reaches value

$$\mathcal{S}(t_1) = \mathcal{S}_{max}\Big(\frac{\alpha+\kappa}{\alpha+2\kappa} + \frac{\kappa}{\alpha+2\kappa}\exp\big[-(\alpha+2\kappa)\underbrace{(t_1-t_0)}_{t_{pulse}=const}\big]\Big) \tag{6.2.18}$$

which is a constant value, equal to the lowest value $\mathcal{S}_{min}$

$$\mathcal{S}(t_1) = \mathcal{F}\cdot\mathcal{S}_{max} = \mathcal{S}_{min} \tag{6.2.19}$$

where

$$\mathcal{F} = \frac{\alpha+\kappa}{\alpha+2\kappa} + \frac{\kappa}{\alpha+2\kappa}\exp\big[-(\alpha+2\kappa)t_{pulse}\big] = 1-\mathcal{F}_{flip} \tag{6.2.20}$$

is a constant informing about what fraction of the initial signal does the minimal value correspond to. The value $\mathcal{F}_{flip}$ could be plotted against the microwave frequency to obtain the approximated lineshape of the electron spin-flip transition.

After the μwave pulse ($t \geq t_1$), the laser repumping still continues and the fluorescence signal changes in a similar way as in the second region of the first model (Equation 6.2.7). For this case the constant c_0 of general solution in a form given by Equation 6.2.8 is found by applying the continuity condition between second and third region

$$\mathcal{S}(t_1) = \mathcal{F}\cdot\mathcal{S}_{max} = c_0\exp(-\alpha t_1) + \mathcal{S}_{max} \tag{6.2.21}$$

$$c_0 = \mathcal{S}_{max}(\mathcal{F}-1)\exp(-\alpha t_1) \tag{6.2.22}$$

which gives the final piecewise function form of the expected fluorescence signal

$$\mathcal{S}(t) = \begin{cases} \mathcal{S}_{max} & \text{if } t \leq t_0 \\ \mathcal{S}_{max}\Big(\frac{\alpha+\kappa}{\alpha+2\kappa} + \frac{\kappa}{\alpha+2\kappa}\exp\big[-(\alpha+2\kappa)(t-t_0)\big]\Big) & \text{if } t_0 < t < t_1 \\ \mathcal{S}_{max}\Big(1-\mathcal{F}_{flip}\exp\big[-\alpha(t-t_1)\big]\Big) & \text{if } t_1 \leq t \end{cases} \tag{6.2.23}$$

In the absence of laser repumping ($\alpha = 0$) during the μwave pulse, as it should be performed in proper Rabi method, the signal function in Equation 6.2.17, in the second region, would look like

$$\mathcal{S}(t) = \frac{1}{2}\mathcal{S}_{max}\Big(1+\exp\big[-(\alpha+2\kappa)(t-t_0)\big]\Big) \tag{6.2.24}$$

which means that the signal approaches to half of the initial signal for longer microwave pulses. This behaviour is similar to interaction with continuous electromagnetic wave, when the population is evenly split between the lower and upper states.

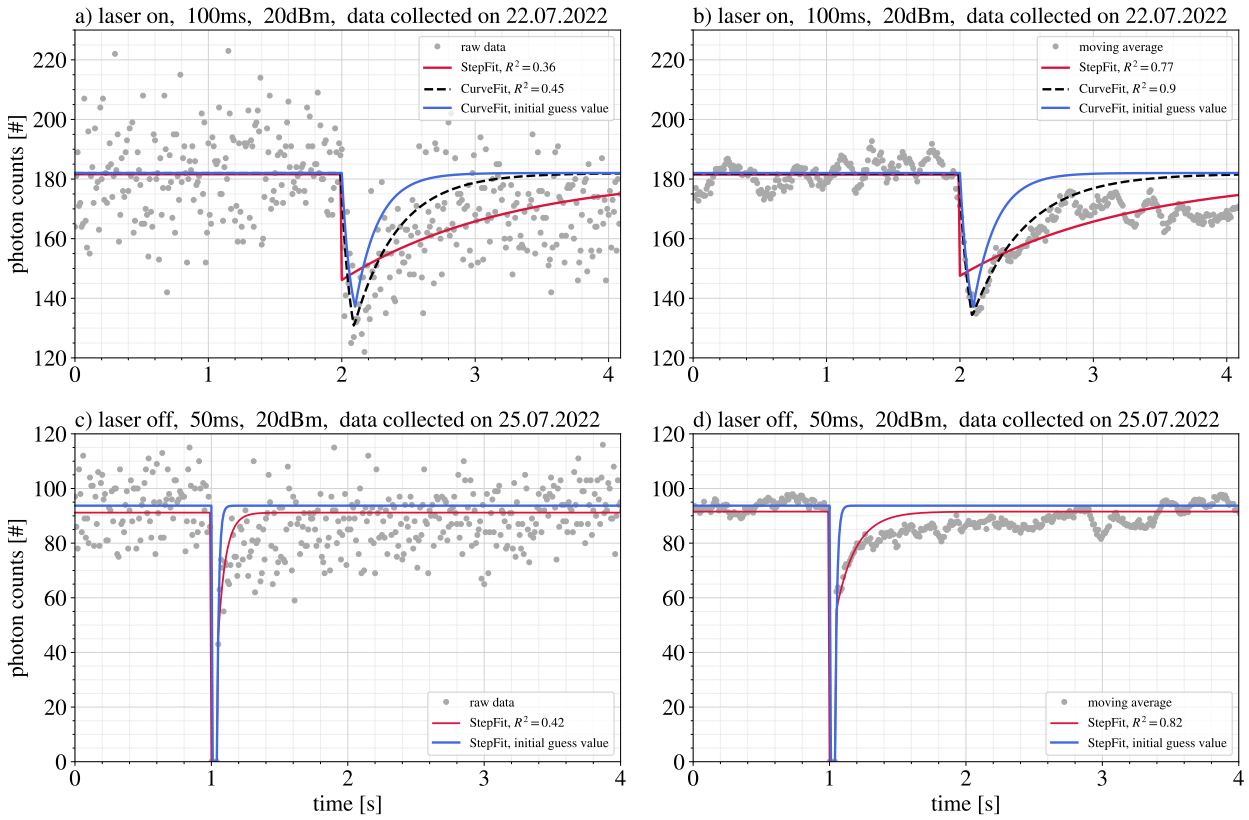

Figure 6.7 – The example of fluorescence signal fits using *Model I: Step Fit* (solid red lines) and *Model II: Curve Fit* (dashed black lines) for laser on during the microwave pulses (top row) and *Model III: Step Fit* (solid red lines) for laser off cases (bottom row). Each curve was fitted to the raw signal (left column) and the averaged signal (right column). Moving average uses 11 data points. The solid blue lines represent the initial guesses of the parameters for the fit functions.

An obvious consequence of *Model II* is that this model cannot detect spin-flip signals greater than $\frac{1}{2}$. Therefore, this model cannot be used for the Rabi method to find Ω. Although it can still be useful to find the spin-flip resonance frequency f_e, as for the fixed microwave pulse duration, the spin-flip rate κ is the greatest at f_e and decreases with increasing detuning.

Data obtained using the Rabi method could be fitted by *Model I*, where *pre-pulse signal* and *repumping signal* are disconnected to obtain the value of signal drop. If the pulse time is greater than the decoherence time (which is already assumed in *Model II*), a modified version of the signal function in the *microwave pulse* region

$$\frac{\mathrm{d}\mathcal{S}}{\mathrm{d}t} = \underbrace{+\kappa\mathcal{S}}_{\substack{spin-flip \\ |\uparrow\rangle\rightarrow|\downarrow\rangle}} \underbrace{-\kappa(\mathcal{S}_{max}-\mathcal{S})}_{\substack{spin-flip \\ |\downarrow\rangle\rightarrow|\uparrow\rangle}} \tag{6.2.25}$$

can be used to relate the spin-flip rate κ with the fractional drop F_{flip} as in Equation 6.2.20:

$$F_{flip} = \frac{1}{2} - \frac{1}{2}\exp\big(-2\kappa\ t_{pulse}\big) \tag{6.2.26}$$

F_{flip} is obtained from the boundary condition between second and third region.

Model III: no repumping during microwave pulse (*Step Fit Function*)

It is a modification of *Model I: Step Fit Function* that is used to fit the data collected in Rabi-style experiment, when the laser was switched off during the microwave pulse. The piecewise function describing the fluorescence signal in this model looks like

$$\mathcal{S}(t) = \begin{cases} \mathcal{S}_{max} & \text{if } t \le t_0 \\ 0 & t_0 < t < t_1 \\ \mathcal{S}_{max}\Big(1 - \mathcal{P}_i \exp\big[-\alpha(t-t_1)\big]\Big) & \text{if } t_1 \le t \end{cases} \tag{6.2.27}$$

Fitting fluorescence signals for individual microwave pulses

The fluorescence signal recorded for each microwave pulse were fitted with the *Step Fit Function* and signals recorded with the laser on during the pulses were additionally fitted with the *Curve Fit Function*. The fits were performed on the raw fluorescence signals, as well as using moving average (over 11 data points) of the collected signals for comparison. The fitting routing requires an initial guess of the fit function parameters, which should be correct at least to the order of magnitude. The initial guess value for the repump rate is

$$\alpha_{guess} = \frac{\ln(2)}{t_{1/2-rep}} \tag{6.2.28}$$

where $t_{1/2-rep}$ is the time when half of the population gets repumped back to bright state, assuming the after repump the signal level comes back to initial value of S_{max}. The guess value of the spin-flip rate is made on the signal drop during the microwave pulse

$$\kappa_{guess} = \frac{\mathcal{S}_{min}}{2t_{pulse}} \tag{6.2.29}$$

where $\mathcal{S}_{min}$ is the minimal signal from the moving-averaged data. For each microwave pulse the fit function was plotted together with the collected fluorescence signal, the example with one of the clearest signal *dip* is presented in Figure 6.7.

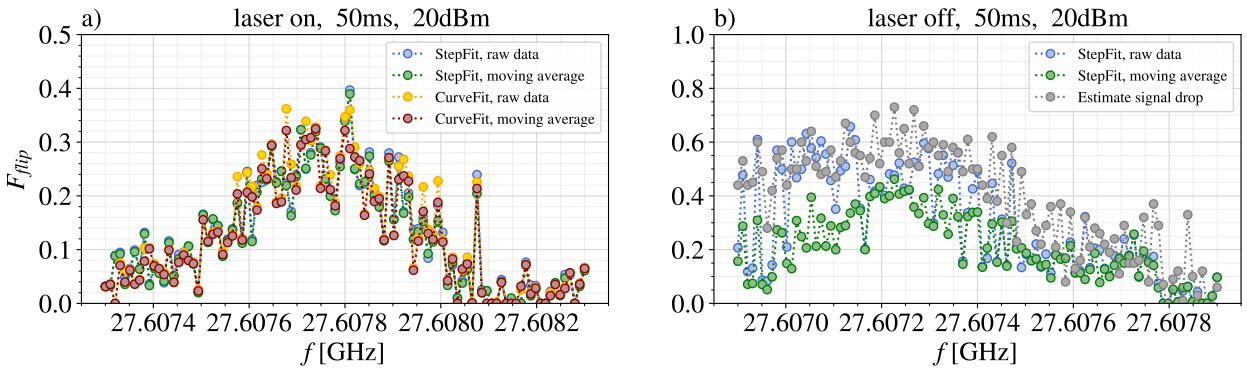

Figure 6.8 – Example of the fraction of beryllium ions that changed the spin state F_{flip} as a function of frequency of microwave pulse obtained using different functions to fit the fluorescence drop signals.

The *dips* in the fluorescence signal are more clearly visible on the *moving average* plots, but fitting is more precise with the *raw data*, because averaging smooths the sharp edge at the beginning and end of the microwave pulse. The results of all these fits for each microwave frequency sweep were plotted as a function of frequency in plots as an example presented in Figure 6.8. The *Curve Fit Function* performed significantly better than *Step Fit Function* in fitting individual fluorescence signals, but there was no qualitative difference between the two models when it comes to reconstructing the transition linewidth. Similarly, there was no significant difference between lineshapes based on *moving average* and *raw data*. For sweeps with laser off during microwave pulses *Step Fit Function* was also compared with a fraction drop value $\mathcal{F}_{flip}$ defined as a ratio of minimal signal right after the laser turns back on to the average signal collected for 1 s before the microwave pulse. This method has an obvious weakness that the information about the fractional drop is obtained from a very short time window compared to the averaged signal before the pulse. For a noisy signal, as in our case, this method will be inaccurate. For the rest of the analysis the *Curve Fit Function* applied to the raw data was used to analyse the microwave sweeps data for the laser ON and *Step Fit Function* applied to the raw data for the laser OFF. Since the fluorescence level does not recover to the initial $\mathcal{S}_{max}$ signal, a simple fitting routine usually overestimates the repump time.This has been solved by fitting only to the initial part of the signal in the third region, so after the end of the pulse t_1. The fitting region was defined up to the time needed to repump half of the ions in the dark state or 0.5s in the case if this repump level of $\frac{1}{2}$ is not reached within this time. Using this constraint, most of the signals were fitted well in region II during the microwave pulse and in that new limited region III right after the pulse.

Except for short-term fluctuations, the fluorescence signal level is drifting over time. The rate of that drift is not constant, neither is the direction. The fluorescence signal globally decreases over a long time (tens of minutes), but locally it was also observed to increase. The long-term decrease could be caused by the loss of beryllium ions over time. The increase in fluorescence signal could be caused by fluctuation in the power of the laser that probes the states of Be^+. Laser power was not stabilised nor measured online. In the next attempt of this experiment, it needed to correlate the probing laser power with the fluorescence signal to improve stability of the fluorescence signal and study other mechanisms that contribute to this signal. If the change of the fluorescence signal for all ions in the *bright* state is known, for example by ion loss rate, the fluorescence signal collected over full microwaves frequency sweep could be fitted with a function that would be used to scale accordingly the *dip* signals for each individual microwave pulse.

Currently in a vast majority of fluorescence signals the photon count rate does not repump to the initial value $\mathcal{S}_{max}$ before the pulse. To understand whether depletion of ions is directly related to the microwave pulses, ion loss without microwave exposure would have to be understood. The analysis tool could probably be improved by adjusting the fluorescence signal based on the global decay, but what is more important for the correct analysis of the fractional drop signals is the short term variations, which at the moment could not have been characterised.

Fitting electron spin-flip transition lineshapes

Figures 6.11 and 6.12 show examples of electron spin-flip transition lineshapes obtained by fitting the raw signals of the fluorescence dips with *Model II: Curve Fit Function*, which is the model that includes spin-flip dynamics that occurs if the microwave pulse is significantly longer than the Rabi oscillation period. The electron spin-flip peaks obtained this way were fitted using a Gaussian profile (continuous lines) and a Rabi resonance profile that accounts for decoherence in the system as in Equation 3.1.7 (dashed lines). The data points were also fitted with a Voigt profile, but the fit results were worse than for Gaussian profile by overestimating the transition linewidth. Therefore, they are not presented here. The Rabi resonance profile in the limit of long microwave pulses, $t_{pulse} \gg \tau_c$, is constrained to have a maximum value at $F_{flip} \simeq 0.5$, which does not fit well many of the transition lineshapes.

The long microwave pulse limit is justified by the fact that the *Model II: Curve Fit Function* fits the dips in fluorescence signals significantly better than *Model I: Step Fit Function* with an instantaneous drop in the fluorescence signal, which indicates that the microwave pulse duration is significantly longer than the duration of the corresponding π-pulse. During the microwave pulse, beryllium ions are undergoing many Rabi oscillations, so it is expected that they lose coherence during the pulse.

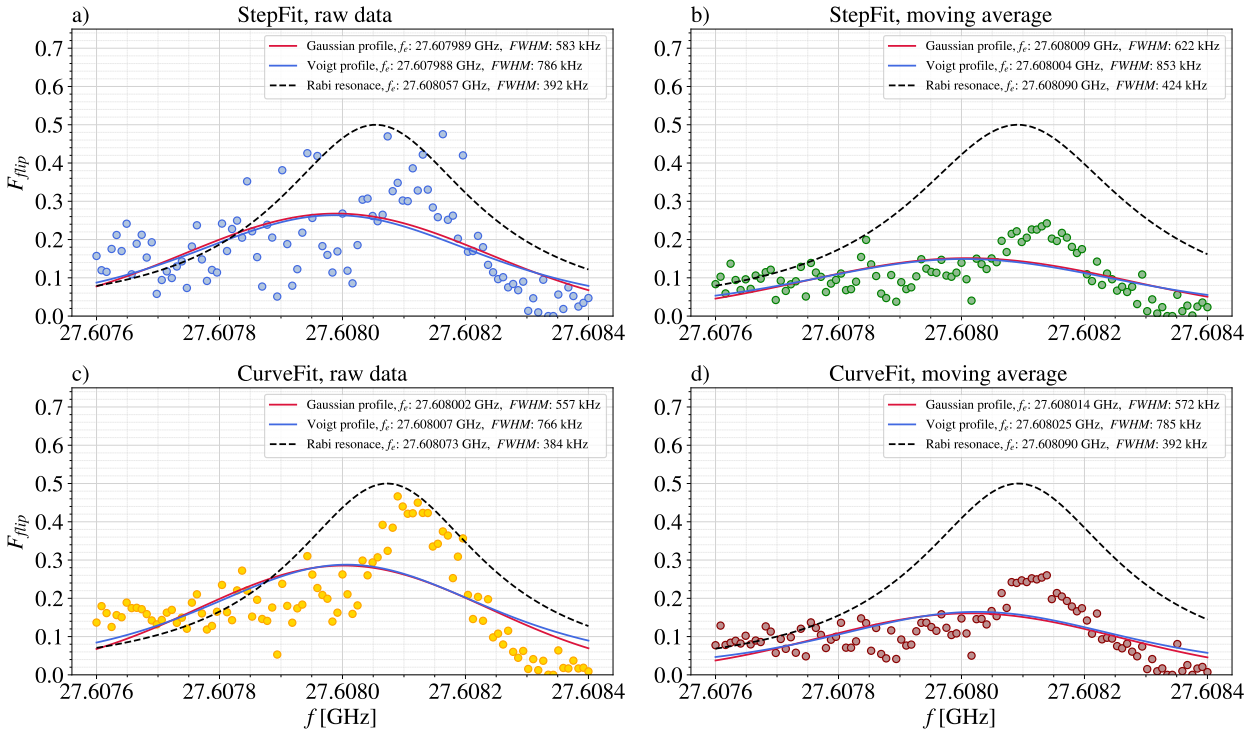

Figure 6.9 – Example of fitting the lineshape with different functions: Gaussian profile, Voigt profiles and with Rabi resonance curve that accounts for the decoherence from Equation 3.1.7 for different methods of extracting fractions of ions in the dark state. This example microwave sweep was collected on 22.07.2022, with the laser on during the 150 ms microwave pulse of 20 dBm power. The Voigt profile fit often overestimated the linewidth of the transition compared to the Gaussian profile fit. The result of the fit with the Rabi resonance profile was highly dependent on the choice of the initial guess parameters, mostly the guess of Rabi frequency. For the Rabi resonance the assumption was made that the time scale of the decoherence is smaller than the microwave pulse duration, so the measured peak is the smeared-out envelope transition frequency and the sidebands. This condition requires that the fraction of ions in the dark state be equal to 0.5 at the resonance frequency, which was not the case for most of the collected data. To satisfy $F_{flip} = 0.5$, the Rabi resonance profile result was often narrower than the measured transition peaks. The conservative approach was taken to use the result of the Gaussian fit and *FWHM* of that fit was associated with the errorbar of the transition frequency.

The fits with the Rabi resonance profile were performed, restricting the decoherence time to be significantly shorter than the microwave pulse duration. Fitting with the Rabi resonance profile required very good guess of initial parameters to fit the points well. In fact, the fit result was strongly dependent upon the initial conditions. Therefore, more understanding about the system, e.g. good estimate of Rabi frequency and decoherence time, must be made in order to use this fit method to extract physical information from the fit parameters. This function is not particularly useful for fitting broad resonance in long-pulse regime, but it will be the function that should be used in *around* π-pulse regime, when the linewidth is narrowed and it manifests the fringe pattern.

The main argument against using the Rabi resonance curve is that, by definition, it restricts the maximum of the peak to be equal $\frac{1}{2}$ in the long-pulse limit, while most of the sweeps resulted in shorter peaks, which means that the Rabi resonance profile results in an underestimated linewidth of the transition.The reason for the decrease in the maximum value of $\mathcal{F}_{flip}$ is unknown. It is possible that this is an error in analysis of not the best quality data or the intensity of microwaves is too low or varies too much across the volume of beryllium ion plasma.

For the few microwave frequency sweeps recorded in the mode, when the laser was switched off during the pulses, a *Model III: Step Fit Function* was used, in which two parts of the piecewise function from *Model I* were disconnected and during the pulse the values of the fit function were set to zero. The fractional drop $\mathcal{F}_{flip}$ obtained by this method was obtained by fitting the raw data and moving average of the data (more than 11 points). These were compared with a simple ratio of the minimum of the fluorescence signal (equal to the first readout after the laser shutter opens) to the average signal recorded before the microwave pulse. The example lineshape comparing these two methods is presented in Figure 6.8.b). $\mathcal{F}_{flip}$ extracted from the *Model III* fit of the raw data was chosen for the final analysis.

Only 7 frequency sweeps with *laser off* were correctly recorded, 6 of which could be fitted with a lineshape, the results are shown in Figure 6.13. Gaussian, Voigt profiles and Rabi resonance curve (with decoherence effect) were fitted to those 6 spectra to find the transition frequency f_e.

Results of the electron spin-flip in Be^+ measurement

The FWHM of f_e varied between around 100-400 kHz. The lineshapes recorded for different lengths and powers of the microwave pulses differ from each other, but not significantly more than the data collected for the same pulse parameters (100 ms and 20 dBm) during the first two and the last day (see comparison of the *laser on* and *laser off* in Figure 6.13). The plasma parameters might change over time, as it has been observed that the time needed for repumping ions from the *dark state* increased from around 1 s on the first day to multiple seconds during last day. This might be the possible source of the transition linewidth broadening observed at the end of the data taking, which caused that the sweeps with laser off during microwave pulses were wider than linewidths collected during the first two days with the laser on during microwave exposure.

The resulting electron spin-flip transition frequencies obtained from the Gaussian fit of all reconstructed lineshapes are plotted in the top Figure 6.10. The magnetic fields calculated from those frequencies are on the lower part of the figure. The error bars of the transition frequencies were conservatively assigned as the *FWHM* of the Gaussian lineshape. We have observed that f_e drifts down over time at a rate similar to that of the ECR frequency, due to the decaying magnetic field of *Carlsberg magnet* [12]. The transition resonance frequency changes by around 1.6 kHz per minute, and the full microwave sweep of 101 frequencies lasts around 8-10 min during the first two days and around 15 min on the last day. For the transition lineshapes measured in this experiment the decay of the magnetic field during the microwave frequency sweep is not significant, but whenever the transition linewidth will be reduced to the order of few kHz, this effect will have to be accounted for. Depending on whether the microwave frequency is swept towards higher or lower values, the resonant frequency f_e would move toward higher or lower values. If the time of the frequency sweep is significantly reduced, this shift will have a proportionally smaller contribution. Additionally, with the changing f_e due to the magnetic field drift, the laser-cooling rate changes accordingly, since the probing laser causes Doppler cooling. Detunings closer to resonance would have a greater effect on the cooling rate change. This effect could be reduced by using a separate probing laser of a power significantly lower than the power of a cooling laser.

[12] This effect is well known and it is a standard behaviour of these type of magnets, caused by the non-zero resistance of the superconducting coil's joint.

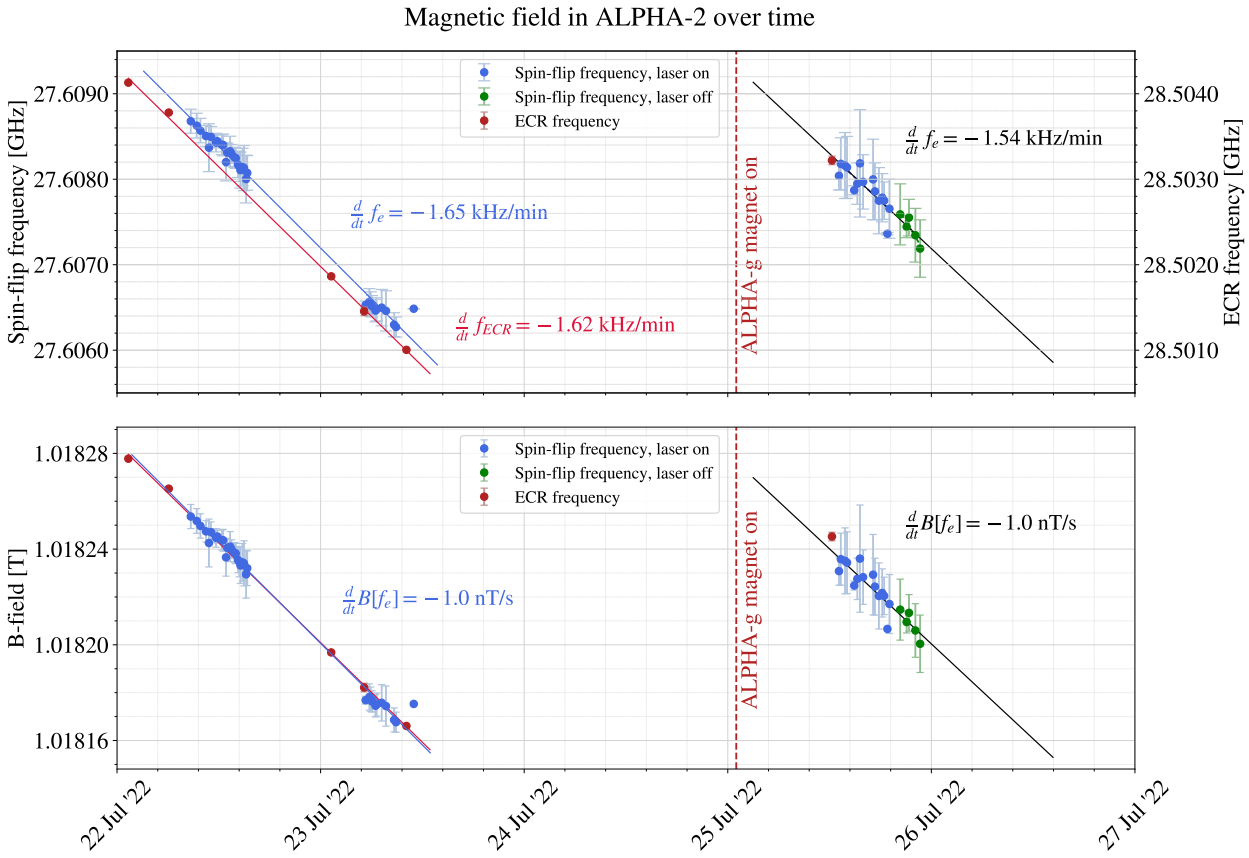

Figure 6.10 – Electron spin-flip transition frequency in Be^+ is changing over time due to decaying magnetic field of the superconducting solenoid magnet. During the experiment, the magnetic field was additionally measured with the *ECR* technique. The magnetic field has increased on the fourth day due to ramping up the ALPHA-g solenoid magnet. The decay rate of the magnetic field was obtained using linear regressions, first linear fit included points collected during the first 2 days and the second fit included points collected during the last day, combining laser on and off runs. In a high field of around 1T, the f_e is well approximated as being linearly dependent on the magnetic field strength (see Figure 6.2).

The initial guess for the resonance frequency f_e was made by running *ECR* sequence to calculate the value of the magnetic field. The electron cyclotron frequency was usually determined within less than 30 kHz, which translates to around 1 μT. The *ECR* frequency was measured a few times in between the f_e measurement for comparison. The errorbars for ECR frequencies were automatically extracted in the analysis tool used in ALPHA. The upper limit for the uncertainty of magnetic field measurements with Be^+ is given by the *FWHM* of the transitions and corresponds to 10-30 μT and accuracies were not assessed due to not having sufficient information about systematic effects, especially concerning plasma effects, which were not possible to study within the limited time we had to perform this experiment.

From Figure 6.10 we can see that the magnetic field values extracted from the central values of the electron spin-flip transition linewidth agree well with measurements performed with the *ECR* technique, so major frequency shifts are not expected. The *ECR* method is more precise than the first results of the electron spin-flip in the Be^+ measurements presented in this work by at least one order of magnitude, but beryllium magnetometry could be improved by systematic study of the system and technical upgrades, which will be discussed in the final chapter in Section 7.2 *Future Prospects*.

At the moment the *Reservoir ECR* technique allows for faster measurement of the external magnetic field than beryllium magnetometry, since 100 electron plasma *scoops* can be extracted and measured over 10 seconds [162]. In the measurement we performed with Be^+ we had to separate each microwave pulse by around 2-8 seconds due to the time required to repump all the ions back to the $|\uparrow\rangle$ state and to collect enough signal prior to each μwave pulse. There is a lot of room for improvement to reduce the repump time by using smaller Be^+ samples, higher laser powers and making use of all of the ion trapping volume overlap with the laser beam. With improved fluorescence detection (increased solid angle of detection, reduced noise of the photon counter), the time before microwave pulse exposure could also be reduced.

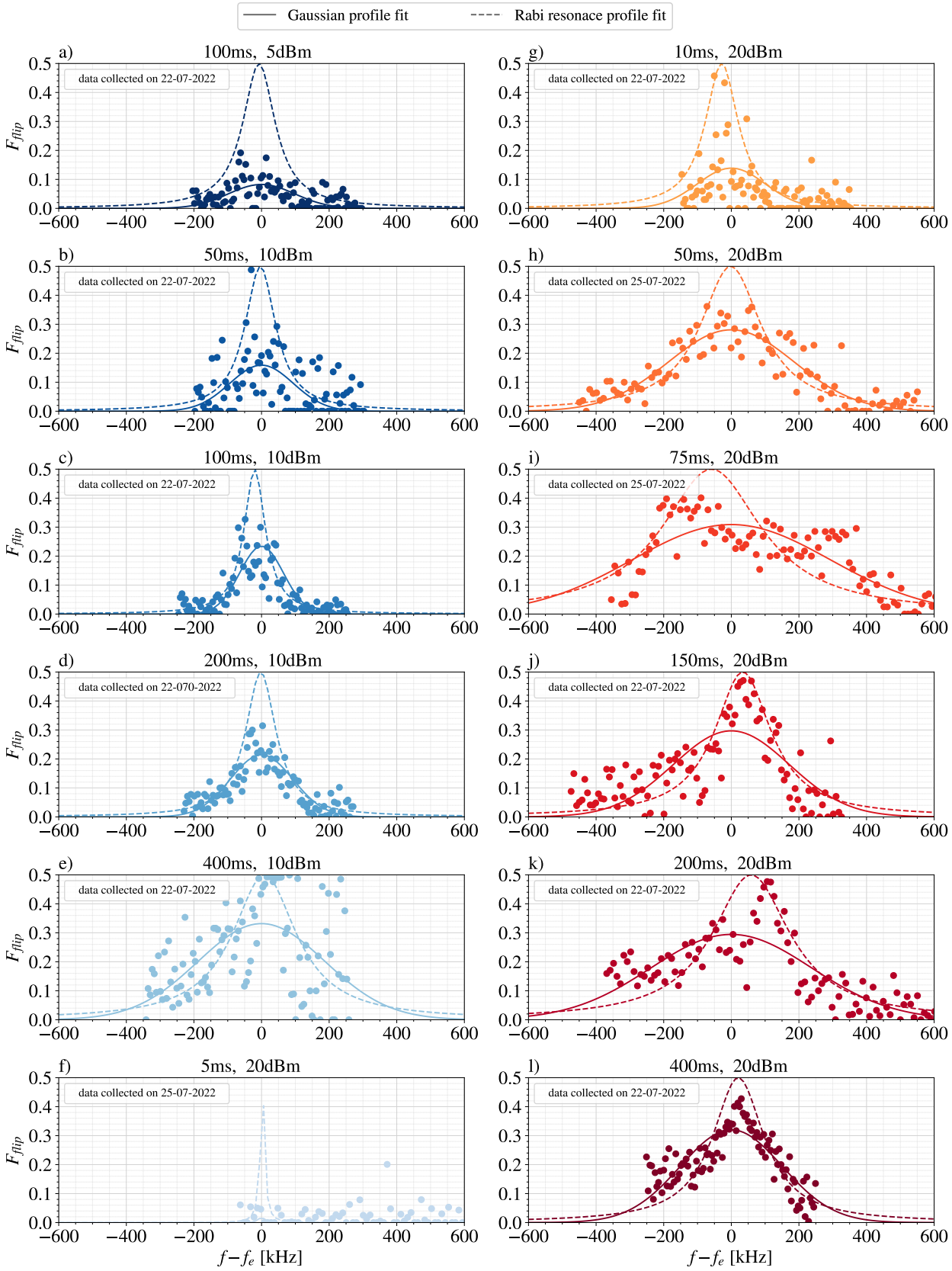

Figure 6.11 – Example lineshapes of electron spin-flip transition in $^9Be^+$ plasma obtained for different duration and power of microwave pulses, that have been tested. Data points are extracted by fitting the *Model II: Curve Fit Function* to the raw data. The offset frequency f_e is the centre of the Gaussian profile.

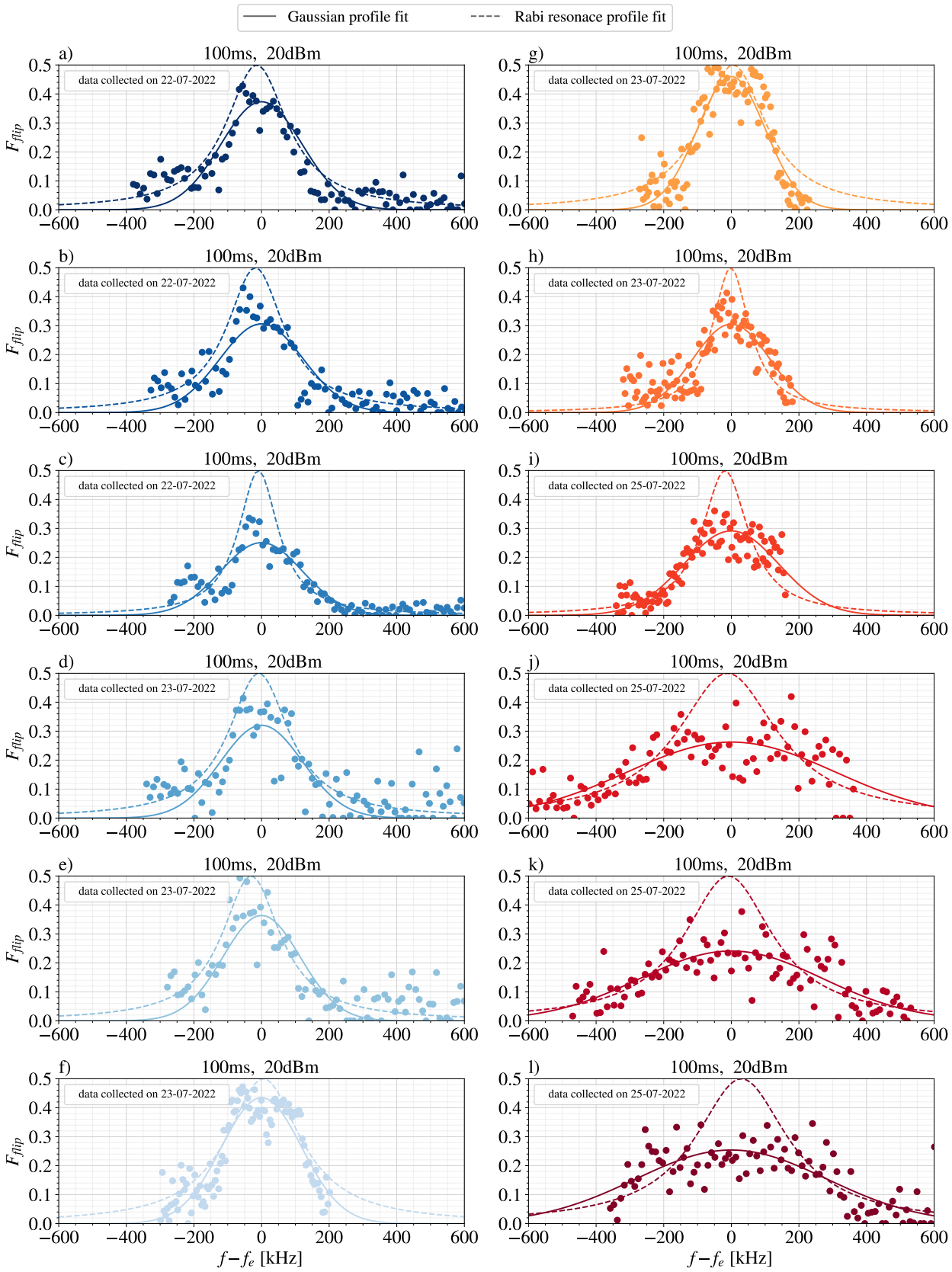

Figure 6.12 – Example lineshapes of electron spin-flip transition in $^9Be^+$ plasma for 100 ms microwave pulses of 20 dBm power, which was used for most of the sweeps. Data points are extracted by fitting the *Model II: Curve Fit Function* to the raw data. The offset frequency f_e is the centre of the Gaussian profile.

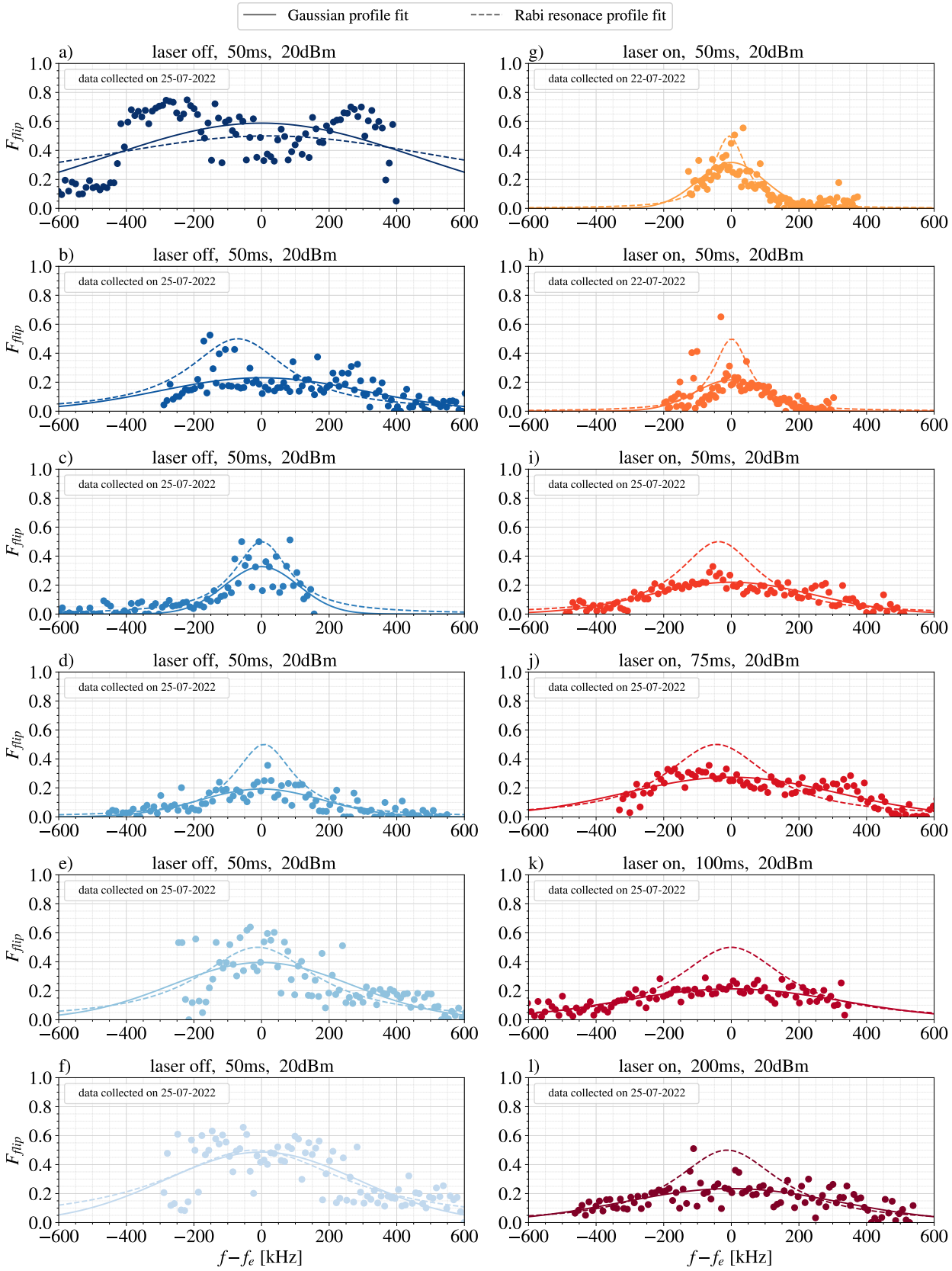

Figure 6.13 – All the lineshapes recorded for the μwave pulse with laser off (left column) compared to examples of μwave pulse when laser was on (right column). The points presented on the plots are extracted using *Model I & III: Step Fit Function*, so the vertical scale differs from Figures 6.11 and 6.12.

Chapter 7

Conclusions and outlook

7.1 Summary and conclusions

Motivation for beryllium magnetometry

The scope of this work was a proof of the concept that beryllium ions could be used for precision magnetometry in ALPHA Penning traps. Precise measurements of the background magnetic (mostly generated by the Penning trap's solenoid magnet) are crucial for the spectroscopic and gravity measurements on the antihydrogen in the ALPHA Experiment. In ALPHA we study properties of antihydrogen that is confined in the magnetic trap by the fields of around 1T. These strong fields cause shifts to the antihydrogen energy level structure due to the Zeeman effect. Antihydrogen is meant to be compared with hydrogen and the most precise measurements of hydrogen performed so far [114, 121] were performed in a low magnetic field of 0.5 mT, so comparing the two results requires precise knowledge of the magnetic field at which the antihydrogen has been measured. To investigate the behaviour of the antihydrogen in Earth's gravitational field, it is also required to characterise the strength of the magnetic forces acting on the anti-atom. Currently, the best method to measure the magnetic field inside the ALPHA Penning traps is *Electron Cyclotron Resonance* (*ECR*) [162, 239], which has been demonstrated to an absolute accuracy 1 ppm and relative precision 26 ppb. This accuracy corresponds to determining the absolute magnetic field within 1 μT. The alternative method to characterise the external magnetic field is to use a well known atomic species and measure the transition between its electronic states in order to extract the magnetic field strength.

In this work it has been proposed to use $^9Be^+$ trapped in the Penning trap to find the frequency of the hyperfine transition in its ground state $2S_{1/2}$, the energy levels of which are well characterised as a function of the magnetic field [132]. The main reason to use beryllium ions for magnetometry was the fact that we have already installed a beryllium source and all necessary hardware to perform this measurement in the ALPHA-2 trap. Laser-cooled beryllium ions were originally intended to sympathetically cool the positron plasma, which is expected to enhance cold antihydrogen production [1, 128].

The proposed magnetometry technique with Be^+ relies on measuring the frequency of the electron spin-flip transition, which is induced by microwave radiation. In the magnetic field of ALPHA-2 trap this frequency is around 27.6 GHz. We could use the same microwave source as for the antihydrogen hyperfine transition or *ECR*. The electron spin-flip transition in $^9Be^+$ is a magnetic dipole transition induced by the oscillating magnetic field component of the microwave, similarly to the positron spin-flip transition in the antihydrogen. This brings an additional and more unique application of beryllium magnetometry, which could allow us to characterise the strength of the microwaves, more precisely the magnetic field components of the microwaves, which are important for antihydrogen hyperfine structure spectroscopy. Microwave radiation does not propagate freely inside the interior of the ALPHA-2 trap, the stack of cylindrical electrodes acts as a cavity, causing microwaves to form irregular pattern of standing waves mixed with freely propagating microwaves. This varies the intensity of microwave radiation along the z-axis of the trap and since the trapped $\bar{H}$ atoms travel within a roughly cylindrical volume of 44 mm diameter and length of 280 mm, they experience different strengths of the microwaves during their motion. In situ measurement with beryllium ions would allow us to probe the oscillating magnetic field from microwaves along the axis of the trap with sub-millimeter resolution. So far this magnetic field component of the microwaves could not be measured at all, since the electron cyclotron resonance is sensitive to the electric field component.

The electron spin-flip transition in Be^+ is studied by measuring the fraction of trapped ions that changed the electron spin state under exposure to a specific microwave frequency f_i. Initially, all beryllium ions are optically pump into the $|\uparrow\rangle$ state, $2S_{1/2}$ ($m_J = +\frac{1}{2}, m_I = +\frac{3}{2}$), with the 313 nm cooling laser tuned to one of the laser-cooling cycling transitions, which also cools down the beryllium ions sample.

Ions in the $|\uparrow\rangle$ state can be detected by a fluorescence emitted while exposed to the laser tuned to the cycling transition $2S_{1/2} \leftrightarrow 2P_{1/2}$ (laser-cooling transition). Trapped Be^+ are exposed to microwave pulses, and the microwave frequency is scanned for consecutive pulses. If the microwave pulse changes the electron spin state of the ion to $|\downarrow\rangle = 2S_{1/2}$ ($m_J = -\frac{1}{2}, m_I = +\frac{3}{2}$), that ion is no longer excited by the laser, so it does not emit fluorescence light. The difference in the fluorescence signal before and after the pulse corresponds to the fraction of ions that changed the spin state. Relating the fraction of ions that undergo the electron spin-flip transition under a given microwave frequency allows us to find the resonance frequency f_e, from which the local strength of the magnetic field can be extracted. To achieve a narrow electron spin-flip transition linewidth, therefore high precision of the magnetic field measurement, a Rabi method could be used. Rabi method relies on exposing the beryllium ions to π-pulses, which means that the microwave pulses duration and intensity are adjusted such that, in principle, the pulse at the resonant frequency should induce the spin-flip of all ions.

This measurement technique was inspired by the measurement performed at NIST (see Ref. [132]) with Be^+ in a Penning trap. The Rabi frequency will have to be found to choose the correct time of the π-pulse. Measuring the Rabi frequency in the electron spin-flip of beryllium ions, so the frequency of oscillation between the *spin-up* and *spin-down* states which depends on the intensity of the electromagnetic field driving the transition, would allow access to information about the strength of the magnetic field component of the microwaves inside the ALPHA's trap. As explained previously, knowledge of the microwave intensity is one of the main parameters determining the hyperfine transition in the antihydrogen.

The electron spin-flip in Be^+ could be measured at different axial positions of the Penning trap, which overlaps with the central axis of the Ioffe-Pritchard trap for confining antihydrogen atoms, to scan the magnetic field and microwave intensity along the z-axis. Due to the nature of the confinement of charged particles within the Penning trap, beryllium ions can only probe radially central positions of the trap, and so far it is not possible to measure the magnetic field for the *off-axis* positions. The same limitation applies to the *Electron Cyclotron Resonance* technique.

Probing *off-axis* positions inside the Penning trap would require developing new techniques, either on the trapped plasma frontier to understand the dynamics of charged particles loaded off-axis of the trap or on the optical trapping frontier to manipulate ions with optical tweezers. An optical dipole trap combined with a radiofrequency trap has already been demonstrated for $^{24}Mg^{+}$ ions by a team from the Max Planck Institute of Quantum Optics in Garching [246]. Developing an optical trap operating together with Penning trap would require research and development such that it will not be a practical solution to our application in the nearest future.

Electron spin-flip in Be^{+} observation

In this work the first observation of the hyperfine transition of the ground state of Be^{+} inside the ALPHA-2 apparatus was reported. The feasibility of using the electron spin-flip in Be^{+} for magnetometry in ALPHA combined Penning trap and Ioffe-Pritchard trap for antihydrogen was studied. A proof of principle experiment was performed in the ALPHA-2 trap, in which the beryllium ions sample was exposed to microwave pulses of varied frequency to find the resonance frequency f_e of the electron spin-flip transition. After each microwave pulse, there is a wait of $1-5$ seconds allowing the laser to repump the $|\downarrow\rangle$ states back to $|\uparrow\rangle$. We did not have separate repumping laser, we used the same laser beam for laser-cooling, probing and repumping, so the repumping process was inefficient. Each sweep of the microwave frequency used 101 microwave pulses and it took in total around $10-15$ min. The experiment was performed over 3 days, during which more than 50 microwave frequency sweeps were performed to measure the transition lineshape. The initial guess of the resonant frequency was made based on magnetic field measurements using the *ECR* technique. Since this was the first attempt to observe the electron spin-flip transition in Be^{+}, for most of the microwave frequency sweeps that were collected, the fluorescence signal was observed during the microwave pulse, such that the spin-flips could be detected as a sudden drop in the recorded signal. Laser light induces an AC Stark shift to the energy levels, which offsets the centre of the transition lineshape and broadens the transition linewidth as reported by *Nakamura et al.* in Ref. [186]. Exposing beryllium ions to microwave radiation simultaneously to laser exposure is a good method to initially search for the resonance, but for precision measurement the laser must be off during probing Be^{+} with microwave pulses.

In the proof-of-concept experiment presented in this work, we did not use π-pulses and we did not manage to characterise the Rabi frequency of the hyperfine transition in the ground state of Be^+. We varied the microwave pulse duration between 10 and 400 ms, which is expected to be significantly longer than π-pulse duration. The maximum signal drop under microwave exposure was not greater than $\frac{1}{2}$. In the long pulse regime, when an ion is exposed to microwave radiation for a time significantly longer than the decoherence time, the number of ions in *spin-up* and *spin-down* should tend toward an even distribution. Therefore, the fraction of ions measured in *spin-up* should always be close to $\mathcal{F}_i = \frac{1}{2}$. In this regime the fringe structure of the resonance curve vanishes and the sidebands around the central frequency reduce to a smooth and wide transition linewidth as shown in the Figure 3.4. For many of the transition linewidths reconstructed from the collected data the maximum fraction of ions in the *spin-down* state was significantly less than $\frac{1}{2}$, but this could be caused by other, not yet understood, sources of systematic errors.

The fraction of ions that underwent the electron spin-flip transition was extracted by fitting the drops in the fluorescence signal with a function that describes the dynamics of transitions between the two spin states due to the interaction with the laser and microwave radiations. The *FWHM* of the transition lines were assigned as the uncertainties of the resonance frequencies f_e, which was a conservative approach. The linewidths were few hundreds of kHz, corresponding to an uncertainty of magnetic field measurement $\leq 30\ \mu$T, which is still at least one order of magnitude worse than the current performance of the *ECR* method [162]. We have tried using a protocol in which the laser was off during the microwave pulses, but this did not produce narrower lineshapes than those with the laser on. The linewidths of the transition have already been broadened because of the fact of using pulses longer than π-pulse. Most likely there are other sources of broadening, which could not be studied due to very limited time we had to use ALPHA-2 apparatus for this experiment. The decay of the magnetic field generated by an external solenoid magnet of the Penning trap has been measured to be around 1 nT/s, which is consistent with the decay rate measured with the *ECR* technique. Further progress on that project was not possible due to the start of the antihydrogen experiment in the ALPHA-g trap, as so far both traps cannot be operated at the same time [1].

[1] The main limitation is the liquid helium consumption to kept the cryostat cold

Implemented upgrades to the laser system

Laser-cooled beryllium ions are primarily meant to be used for sympathetic cooling of positrons, which is expected to produce more of cold and trappable antihydrogen atoms. By interaction with cold Be^+ plasma we have managed to obtain positron plasmas that were at least twice colder than the usual positron samples prepared in ALPHA [1]. ALPHA-2 trap is designed to synthesise, confine and detect the antihydrogen, which means that it is not the most optimal apparatus to perform laser cooling of ion plasma. In the original setup, the laser beam was slightly tilted from the z axis of the Penning trap, which meant that the laser overlaps with the beryllium ions only in the axial centre of the trap. There is no overlap between laser and ions in the position of the *Rotating Wall* electrode, which typically is used to compress plasma and transfer the energy between Penning trap's motional degrees of freedom. In order to sympathetically cool positrons we had to perform initial preparation of beryllium ions in multiple steps of alternating cooling in the centre of the trap and compression under *Rotating Wall*. This made the entire process to cool the positron samples to last around 10 min, which is longer than the ~ 4 min time of the typical antihydrogen production sequence. The next step of this project is to make sympathetic cooling compatible with the antihydrogen synthesis protocol. For this reason, we have introduced an additional laser beam that would be well aligned with the central axis of the Penning trap, which would allow simultaneous cooling and compression under the *Rotating Wall* electrode. This required the installation of mirrors on the motorised translators at both ends of the ALPHA-2 trap. Additionally a new 313 nm laser was purchased, capable of providing 20 more power, performing wider frequency sweeps in the *mode-hop-free* operation (up to 100 GHz) and having an automated and programmable control system that requires significantly less maintenance that need to be performed by a laser expert, to simplify future operation.

Within the postgraduate research project, I worked on setting up a new laser, introducing *on-axis* laser beam and other upgrades to the laser system. A significant part of the project was to introduce optical fibres to deliver the 313 nm laser from the laser lab to the experimental zone. It was expected to simplify the laser setup, reduce the space on the optical tables needed for laser delivery and beam profile shaping, and improve the laser beam quality. UV light is known to degrade photonic crystal fibres and significantly attenuate transmission [212].

The fibres for UV light were not commercially available at that point, but there are know techniques to protect the fibres from the damage caused by the UV radiation. The process relies on the diffusion of hydrogen gas into the fibre's glass core, called *hydrogenation*, and then exposing the fibre to ultraviolet (UV) light, called *curing* the fibre. We have used *LMA-PM-10* by *NKT Photonics*, but unlike other research groups we know, we used jacketed fibres instead of bare fibres. We also required 10 m long fibre, while others typically use ~ 1 m fibres. Although the hydrogenation and curing processes were most likely successful, the operation with the fibre installed between the laser lab and the ALPHA-2 trap in the experimental area was very problematic. In principle the transmission was poor and it was necessary to manoeuvre the fibre in space, change the shapes of the bends, and twist to find a decent transmission of at least 10%. Even if higher transmission was achieved, it was a very short-lasting effect. The fibre position required at least daily realignment, but often even more frequent. The power loss through the fibre and the instability of the transmission made those fibres very unpractical to use in our application. We tried 4 fibres and they all showed the same result. The possible explanation is that the plastic jacketing of the fibre plastically deformed during hydrogenation at increased temperature ($\gtrsim 60^\circ$ C) and that the deformation could not be removed during the stretching of the fibre. In our setup we only fixed the fibre in a few points along the 10 metres-long path, and most of the fibre has a freedom to twist and hang on its own. Therefore, the shape changes over time were attenuating the light transmission. We stretched the fibres as suggested by *Marciniak et al.* [215], but the straightening effect was only temporary and after a few days the fibres regained their previous contortion. We have observed that a great gain in transmission could be achieved by applying significant tension to the fibre ends, especially on the input side. It is possible that tensioning the fibre along the full length during the operation could improve transmission stability, although this has never been tried. The idea of using optical fibres to transmit the 313 nm laser to the ALPHA-2 trap was abandoned after the beryllium magnetometry experiment in 2022.

7.2 Future prospects

7.2.1 Beryllium magnetometry

Measurement of the of the electron spin-flip in Be^+ with the transition linewidth of a few *kHz* trapped in the Penning trap, similar to our experiment, has been reported [132], so we believe the same order of magnitude precision should also be achievable in the ALPHA traps, if the Rabi method is applied. A lot of development needs to be done before this method can be used reliably in the ALPHA Experiment. The most important steps would be:

1. **Reproducibility of Be^+ sample** would aid any systematic study of the system. This could possibly be achieved with the *SDREVC* technique [164], thanks to the new *on-axis* laser beam that allows simultaneous laser-cooling and *Rotating Wall* compression.
2. **Reduce or characterise the ion loss rate**: in principle we could confine the beryllium ions sample in the ALPHA-2 Penning trap for multiple hours
3. **Laser beam and ions overlap**: make sure that all trapped ions are overlapping with the laser beam and there is no change in the overlap over time
4. **Laser power stabilisation**: the fluctuations of the recorded fluorescence signal level might be due to changing power of the 313 nm laser if saturation of the laser cooling transition is not reached. Study the transition linewidth dependence on laser power.
5. **Reduction of the noise in the photon counter**: verify that there is no external electrical noise present in the detector. We have already improved the optical shielding, which removed the periodic noise due to background light in the experimental area.
6. **Introduce repump laser** detuned from the laser cooling resonance to repump ions from the *spin-down* state after the microwave pulse faster; this could reduce the repumping time by possibly even a factor of 1000. This could be achieved either by using the other laser source (at the moment we have two lasers, the old *Toptica* laser was not used in this experiment) or by sweeping the frequency of the laser further away from the resonance after probing the spin states.
7. **Correlate the number of trapped ions with the number of photons counted by the detector**: this would help to study the dependence of electron spin-flip resonance as a function of number of ions and sample size.

8. **Introduce a probing beam** for state detection after the microwave pulse, this beam could have a lower intensity but be detuned very close to the resonance of the laser cooling transition. This could be done either by adding a new laser beam or simply by fast switching of the *Acusto-Optical Modulator* present in the system to attenuate power and frequency (140-280 MHz frequency sweeps available).

9. **Lower number of Be^+ ions**: small samples would probe lower volume of the trap and the broadening due to the magnetic and electric fields non-uniformity would be reduced. Ultimately, to reduce collective effects, one could use only a single Be^+ ion, but this requires improved fluorescence detection (*SiPM* inside the Penning trap as in the BASE at Heidelberg design [247]), which is currently being developed in ALPHA [117].

10. **Account for the magnetic field change during the microwave frequency sweep**: The *Carlsberg magnet* decays at a rate of ~ 1.6 kHz/min. When the linewidth narrows to ~ 1 kHz, this frequency shift during the sweep would have to be taken into account.

As reported by the NIST group, relative accuracies on the level of 10^{-10} can be achieved if the electron spin-flip is combined with nuclear spin-flip measurement. This would require a radiofrequency wave source, which currently does not exist in the ALPHA-2 trap. Alternatively, a Raman transition could be performed between the two hyperfine levels in the ground state [248]. This requires using two 313 nm laser beams equally detuned from the transition between each of the hyperfine levels and the excited level. The feasibility of using the Raman transition in Be^+ for magnetometry in the ALPHA Experiment would have to be studied.

7.2.2 Cold Be^+ for antihydrogen synthesis

Positron plasma of parameters comparable to samples used for antihydrogen synthesis has been cooled to ~ 7 K by interaction with laser-cooled Be^+. The next steps would involve integrating this technique into the antihydrogen production sequence. The same experimental procedure as presented in Ref. [1, 131] could be used to study the mixing of positrons with antiprotons. We expect that beryllium ions could remain in the trap and continue to provide cooling during mixing. The currently used mixing scheme is the so-called *slow merge*, during which the positron and antiproton plasmas are slowly overlapped by manipulating the shape of the trapping potential wells. Positrons and Be^+ in their thermal equilibrium state are

radially split by a centrifugal separation effect, with heavier species forming a shell around lighter ones. In this situation, positrons could be mixed with antiprotons, while beryllium ions on the outside would still provide a cooling mechanism as long as cooling laser is present. This would be an experiment to see whether colder positrons indeed increase the antihydrogen production rate, but to make this technique practical for antihydrogen precision experiments, the procedure of cooling of positrons would have to be upgraded. The first limitation is the fact that preparing the Be^+ sample is too lengthy, around 10 minutes, so we would miss roughly 4 out of the 5 antiproton bunches from *ELENA*. The long preparation was caused by nonefficient laser-cooling of Be^+ due to the too large radial size of the beryllium plasma, while the too hot plasma was not efficiently compressed by the *Rotating Wall* method. Laser-cooling should become more efficient thanks to the higher power of the new cooling laser. Now it is also possible to implement a dedicated repumping laser in ALPHA-2, but this has not been done so far. With the new *on-axis* laser beam, Be^+ could be laser-cooled and compressed at the same time, so this issue should be possible to overcome. Compression of beryllium ion plasma should also allow positron cooling on standard plasmas of $\sim$ 3 million of positrons, while the magnetic minimum trap for antihydrogen is energised, which would allow for antihydrogen accumulation [105]. The octupole magnet, which provides radial confinement of the antihydrogen atoms, alternates the magnetic field at higher radii, so the greater the radial size of the plasma, the more heating it would experience. We have demonstrated sympathetic cooling with the octupole magnet on only for radially small positron plasmas, with only 0.1 million positrons. Finally, simultaneous laser-cooling and compression by the *Rotating Wall* technique opens a path towards applying the *SDREVC* method on the beryllium plasma, which would allow us to control plasma size and density. This would greatly improve and accelerate all systematic studies involving to beryllium ions. Recently, *Beryllium Team* has made progress towards using SDREVC on Be^+ plasma.

Laser-cooled $^9Be^+$ ions are a very promising tool for future improvements in the field of antihydrogen research. We have proved their potential to reduce the temperature of positron plasma and an improved laser cooling setup allows us to apply this technique to the antihydrogen synthesis procedure. In this work, it has been shown that Be^+ could also be used in the ALPHA Penning trap for precision magnetometry and could potentially be used to characterise the intensity distribution of the microwaves along the trap axis.

List of symbols

Physical constants [7]

$c = 299792458\ \frac{m}{s}$	speed of light in vacuum
$h = 6.62607015 \cdot 10^{34}\ J \cdot s$	Planck constant
$\hbar = 1.054571817\ldots \cdot 10^{34}\ J \cdot s$	reduced Planck constant
$m_p = 1.67262192369(51) \cdot 10^{-27}\ kg$	proton mass
$m_e = 9.1093837015(28) \cdot 10^{-31}\ kg$	electron mass
$e = 1.602176634 \cdot 10^{19}\ C$	elementary charge
$eV = 1.602176634 \cdot 10^{19}\ J$	electronvolt
$k_B = 1.380649 \cdot 10^{23}\ J/K$	Boltzmann constant
$\epsilon_0 = 8.8541878128(13) \cdot 10^{-12}\ F/m$	vacuum electric permittivity
$\mu_0 = 1.25663706212(19) \cdot 10^{6}\ H/m$	vacuum magnetic permeability
$\mu_B = 9.2740100783(28) \cdot 10^{-24}\ J/T$	Bohr magnetron
$\mu_N = 5.0507837461(27) \cdot 10^{-27}\ J/T$	nuclear magnetron
$g_e = 2.00231930436256(35)$	electron g-factor
$\alpha = 7.2973525693(11) \cdot 10^{-3}$	fine-structure constant

Physical variables

E	electric field intensity
$\bar{E}$	electric field vector
B	magnetic field intensity
$\bar{B} = \mu_0 \bar{H}$	magnetic field vector
$\bar{r}$	position vector
$\bar{p}$	momentum vector
$\bar{k} = 2\pi\hat{k}/\lambda$	wave vector
t	time
P	power
ω	angular frequency
f	frequency
Δ, δ	frequency detuning
Ω	Rabi frequency
t_π	time of the π-pulse
f_e	electron spin-flip frequency
f_c	cyclotron frequency
f_{ECR}	Electron Cyclotron Resonance frequency
ω_z	axial (angular) frequency
ω_c	cyclotron (angular) frequency
ω_c'	modified cyclotron (angular) frequency
ω_m	magnetron (angular) frequency
ω_0	optical transition (angular) frequency
γ_0	natural linewidth of the transition
Γ	Coulomb coupling constant
Ω	solid angle
$\bar{d}_{ge} \equiv \langle g\|\bar{d}\|e\rangle$	electric dipole moment of the transition
$\mathcal{P}$	probability
M_J	total angular momentum quantum number
γ_s	scattering rate of photon on the two-level atom

Acronyms used in ALPHA Experiment

AD	Antiproton Decelerator
ALPHA-2	Atom Trap for spectroscopic measurements (Atom Trap + Re-Catching trap)
ALPHA-g	Atom Trap(s) for gravity measurement (Atom Trap + Re-Catching trap)
AOM	Acusto-Optic Modulator
AT	Atom Trap
Beam	packet of particles provided by accelerator; in the context of this work, it usually refers to the beam of $\bar{p}$ from the Antiproton Decelerator
Beryllium Experiment	all the hardware, software, and experiments involving the use of beryllium ions
Carlsberg magnet	ALPHA-2 Penning Trap solenoid, named after Carlsberg Foundation funding ALPHA research
CPT	Charge-Parity-Time (symmetry or transformation)
CT	Catching Trap, a Penning trap used to cool antiprotons
DL	Diode Laser
DOF	degree of freedom
DSAT	Downstream Atom Trap
ECR	Electron Cyclotron Resonance
ECDL	Extended/External Cavity Diode Laser
egun	electron gun, electron emitter
EVC	Evaporative cooling
FHG	Fourth Harmonic Generation
FPGA	Field Programmable Gate Array
FSR	Free Spectral Range
HTS	High Temperature Superconductor leads
IR	infrared
LHe	liquid helium

LN_2	liquid nitrogen
LS2	Long Shutdown no.2 (2019 - August 2021), period of technical break with no particle beams at CERN
MCP	Micro-Channel Plate detector
MHF	Mode-Hop-Free (tuning range)
ODE	ordinary differential equation
OVC	Outer Vacuum Chamber
PDH	Pound–Drever–Hall technique
PID	Proportional–Integral–Derivative controller
PLA	Pulsed Laser Ablation
RCT	Re-Catching Trap
SDR	Strong Drive Regime
SGH	Second Harmonic Generation
SME	Standard Model Extension
SolA	Solenoid A
SolB	Solenoid B
SVD	Silicon Vertex Detector
TA	Tapered Amplifier
UHV	Ultra High Vacuum ($< 10^{-8}$ mbar)
ULE	Ultra Low Expansion cavity
USAT	Upstream Atom Trap
UV	ultraviolet
VIS	visible (optical) radiation
VUV	vacuum ultraviolet
WEP	Weak Equivalence Principle
WLM	Wavelength Meter, also called Wavemeter

References

[1] ALPHA Collaboration, *Sympathetic cooling of positrons to cryogenic temperatures for antihydrogen production*. Nat Commun 12, 6139 (2021). doi: 10.1038/s41467-021-26086-1

[2] ALPHA Collaboration, *Laser cooling of antihydrogen atoms*, Nature 592, 35–42 (2021). doi:10.1038/s41586-021-03289-6

[3] ALPHA Collaboration, *Observation of the effect of gravity on the motion of antimatter*, Nature 621, 716–722 (2023). doi: 10.1038/s41586-023-06527-1

[4] ALPHA Collaboration, *Design and performance of a novel low energy multispecies beamline for an antihydrogen experiment*, Phys. Rev. Accel. Beams 26, 040101 (2023). doi: 10.1103/PhysRevAccelBeams.26.040101

[5] ALPHA Collaboration, *Precision spectroscopy of the 1S-2S transition in antihydrogen: hyperfine structure and CPT invariance*, in review by Nature Physics

[6] ALPHA Collaboration, *Measurements of Penning-Malmberg trap patch potentials and associated performance degradation*, in review by Physical Review Letters

[7] Tiesinga, E. , Mohr, P. , Newell, D. and Taylor, B. (2021), *CODATA Recommended Values of the Fundamental Physical Constants: 2018*, Reviews of Modern Physics, [online], https://doi.org/10.1103/RevModPhys.93.025010,

[8] P. A. M. Dirac. *The quantum theory of the electron*. Proceedings of the Royal Society of London. Series A, Containing Papers of a Mathematical and Physical Character 117.778 (Feb. 1928), pp. 610–624. doi: 10.1098/rspa.1928.0023

[9] J. R. Oppenheimer. *On the Theory of Electrons and Protons*. Physical Review 35.5 (Mar. 1, 1930), pp. 562–563. 10.1103/PhysRev.35.562

[10] C. D. Anderson. *The Positive Electron*. Phys. Rev. 43, 491 (1933) doi: 10.1103/PhysRev.43.491

[11] Owen Chamberlain, Emilio Segrè, Clyde Wiegand, and Thomas Ypsilantis, *Observation of Antiprotons*, Phys. Rev. 100, 947 (1955). doi: 10.1103/PhysRev.100.947

[12] K. Orrman-Rossiter, *Observation and Annihilation: The Discovery of the Antiproton*. Phys. Perspect. 23, 3–24 (2021). doi: 10.1007/s00016-021-00271-7

[13] B. Cork, G. R. Lambertson, O. Piccioni, W. A. Wenzel, *Antineutrons Produced from Antiprotons in Charge-Exchange Collisions*, Phys. Rev. 104, 1193(1956). doi: 10.1103/PhysRev.104.119

[14] Owen Chamberlain, Donald V. Keller, Emilio Segrè, Herbert M. Steiner, Clyde Wiegand, and Thomas Ypsilantis, *Antiproton Interaction Cross Sections*, Phys. Rev. 102, 1637 (1956). doi: 10.1103/PhysRev.102.1637

[15] P. B. Schwinberg, R. S. Van Dyck, Jr., and H. G. Dehmelt, *New Comparison of the Positron and Electron g Factors*, Phys. Rev. Lett. 47, 1679. doi: 10.1103/PhysRevLett.47.1679

[16] F.J Wysocki, M Leventhal, A. Passner, C. M. Surko, *Accumulation and storage of low energy positrons*. Hyperfine Interact 44, 185–200 (1989). doi: 10.1007/BF02398669

[17] G. Gabrielse, X. Fei, K. Helmerson, S. L. Rolston, R. Tjoelker, T. A. Trainor, H. Kalinowsky, J. Haas, and W. Kells, *First Capture of Antiprotons in a Penning Trap: A Kilo-electronvolt Source*, Phys. Rev. Lett. 57, 2504 (1986) doi: 10.1103/PhysRevLett.57.2504

[18] G. Gabrielse, X. Fei, L. A. Orozco, R. L. Tjoelker, J. Haas, H. Kalinowsky, T. A. Trainor, and W. Kells, *Cooling and slowing of trapped antiprotons below 100 meV*, Phys. Rev. Lett. 63, 1360 (1989) doi: 10.1103/PhysRevLett.63.1360

[19] G. Gabrielse, A. Khabbaz, D. S. Hall, C. Heimann, H. Kalinowsky, and W. Jhe, *Precision Mass Spectroscopy of the Antiproton and Proton Using Simultaneously Trapped Particles*, Phys. Rev. Lett. 82, 3198 (1999) doi: 10.1103/PhysRevLett.82.3198

[20] ATRAP Collaboration, *One-Particle Measurement of the Antiproton Magnetic Moment*, Phys. Rev. Lett. 110, 130801 (2013). doi: 10.1103/PhysRevLett.110.130801

[21] Borchert, M.J., Devlin, J.A., Erlewein, S.R. et al. *A 16-parts-per-trillion measurement of the antiproton-to-proton charge–mass ratio*. Nature 601, 53–57 (2022). doi: 10.1038/s41586-021-04203-w

[22] Smorra, C., Sellner, S., Borchert, M. et al. *A parts-per-billion measurement of the antiproton magnetic moment*. Nature 550, 371–374 (2017). doi: 10.1038/nature24048

[23] G. Gabrielse, S.L. Rolston, L. Haarsma, W. Kells, *Antihydrogen production using trapped plasmas*, Phys. Lett. A, 1291 (1988), doi: 10.1016/0375-9601(88)90470-7

[24] G. Baur et al., *Production of antihydrogen*, Physics Letters B 368.3 (Feb. 1996), pp. 251–258. doi:10.1016/0370-2693(96)00005-6

[25] G. Blanford, D. C. Christian, K. Gollwitzer, M. Mandelkern, C. T. Munger, J. Schultz, and G. Zioulas, *Observation of Atomic Antihydrogen*, Phys. Rev. Lett. 80, 3037 (1997). doi: 10.1103/PhysRevLett.80.3037

[26] Latacz, B.M., Arndt, B.P., Bauer, B.B. et al. *BASE—high-precision comparisons of the fundamental properties of protons and antiprotons*. Eur. Phys. J. D 77, 94 (2023). doi: 10.1140/epjd/s10053-023-00672-y

[27] W. A. Bertsche, E. Butler, M. Charlton and N. Madsen, *Physics with antihydrogen*, 2014 J. Phys. B: At. Mol. Opt. Phys. 48 232001, doi: 10.1088/0953-4075/48/23/232001

[28] Hori, M., Sótér, A., Barna, D. et al. *Two-photon laser spectroscopy of antiprotonic helium and the antiproton-to-electron mass ratio*. Nature 475, 484–488 (2011). 10.1038/nature10260

[29] E. Widmann, *Low-energy antiprotons physics and the FLAIR facility*, Phys. Scr. 2015 014074 (2015). doi: 10.1088/0031-8949/2015/T166/014074

[30] ATHENA Collaboration, *Production and detection of cold antihydrogen atoms*, Nature 419, 456–459 (2002). 10.1038/nature01096

[31] The ALPHA Collaboration, *Trapped antihydrogen*. Nature 468, 673–676 (2010). 10.1038/nature09610

[32] The ALPHA Collaboration, *Confinement of antihydrogen for 1,000 seconds*. Nature Phys 7, 558–564 (2011). doi: 10.1038/nphys2025

[33] The ALPHA Collaboration, *Characterization of the 1S–2S transition in antihydrogen*. Nature 557, 71–75 (2018). doi: 10.1038/s41586-018-0017-2

[34] The ALPHA Collaboration, *Observation of the 1S–2P Lyman-α transition in antihydrogen*. Nature 561, 211–215 (2018). doi: 10.1038/s41586-018-0435-1

[35] The ALPHA Collaboration, *Observation of the hyperfine spectrum of antihydrogen*. Nature 548, 66–69 (2017). doi: 10.1038/nature23446

[36] The ALPHA Collaboration, *Investigation of the fine structure of antihydrogen*. Nature 578, 375–380 (2020). doi: 10.1038/s41586-020-2006-5

[37] M. Diermaier, C. Jepsen, B. Kolbinger, C.Malbrunot, O. Massiczek, C. Sauerzopf, M. C. Simon, J. Zmeskal, E. Widmann, *In-beam measurement of the hydrogen hyperfine splitting and prospects for antihydrogen spectroscopy*. Nat Commun 8, 15749 (2017). 10.1038/ncomms15749

[38] AEgIS Collaboration, *AEgIS at ELENA: outlook for physics with a pulsed cold antihydrogen beam*, Phil. Trans. R. Soc. A.376 (2018), doi: 10.1098/rsta.2017.0274

[39] AEgIS Collaboration, *Toward a pulsed antihydrogen beam for WEP tests in AEgIS*, EPJ Web of Conferences 282, 01005 (2023). doi: 10.1051/epjconf/202328201005

[40] P. Pérez and A. Rosowsky *A new path toward gravity experiments with antihydrogen*, Nucl. Instr. Meth. A 545, 20-30 (2005). doi: 10.1016/j.nima.2005.01.301

[41] P. Pérez, Y. Sacquin, *The GBAR experiment: gravitional behaviour of antihydrogen at rest*, Quantum Grav. 29 (2012) 184008. doi: 10.1088/0264-9381/29/18/184008

[42] S. A. Jones, *An ion trap source of cold atomic hydrogen via photodissociation of the BaH^+ molecular ion*, 2022 New J. Phys. 24 023016. doi: 10.1088/1367-2630/ac4ef3

[43] Azevedo, L.O.A., Costa, R.J.S., Wolff, W. et al. *Adaptable platform for trapped cold electrons, hydrogen and lithium anions and cations*. Commun Phys 6, 112 (2023). doi: 10.1038/s42005-023-01228-7

[44] Patrick Stephen Mullan, *A proton source in the ALPHA apparatus for precision measurements of antihydrogen and hydrogen*, Ph.D. thesis, Swansea University, 2023. doi: 10.23889/SUthesis.63617

[45] Tseng, C.H., Gabrielse, G. Portable trap carries particles 5000 kilometers. Hyperfine Interact 76, 381–386 (1993). doi: 10.1007/BF02316739

[46] C. Smorra et al., *BASE-STEP: A transportable antiproton reservoir for fundamental interaction studies*, arXiv:2304.09555 (2023). arXiv:2304.09555

[47] PUMA Collaboration, *PUMA, antiProton unstable matter annihilation*, Eur. Phys. J. A 58, 88 (2022). doi: 10.1140/epja/s10050-022-00713-x

[48] Lewis, R., Smith, G. & Howe, S. *Antiproton portable traps and medical applications.* Hyperfine Interactions 109, 155–164 (1997). doi: 10.1023/A:1012653416870

[49] Holzscheiter MH et al., *The Biological Effectiveness of Antiproton Irradiation*, Radiother Oncol (2006), doi:10.1016/j.radonc.2006.09.012

[50] N. Bassler, et al. (2008). *Antiproton radiotherapy.* Radiotherapy and Oncology, Volume 86, Issue 1, 2008. doi: 10.1016/j.radonc.2007.11.028

[51] Masaki Hori et al., *Buffer-gas cooling of antiprotonic helium to 1.5 to 1.7K, and antiproton-to–electron mass ratio.* Science 354, 610-614 (2016). doi: 10.1126/science.aaf6702

[52] A.P. Mills, M. Leventhal, *Can we measure the gravitational free fall of cold Rydberg state positronium?*, Nucl. Instrum. Methods Phys. Res., Sect. B 192, 102 (2002). doi: 10.1016/S0168-583X(02)00789-9

[53] D. B. Cassidy and S. D. Hogan, *Atom control and gravity measurements using Rydberg positronium*, Int. J. Mod. Phys.: Conf. Ser.30, 1460259 (2014). doi: 10.1142/S2010194514602592

[54] K. Kirch, *Testing gravity with muonium*, arXiv preprint physics/0702143 (2007). https://arxiv.org/abs/physics/0702143v1

[55] A. Antognini, D. M. Kaplan, K. Kirch, A. Knecht, D. C. Mancini, J. D. Phillips, T. J. Phillips, R. D. Reasenberg, T. J. Roberts and A. Soter, *Studying Antimatter Gravity with Muonium*, Atoms 6, 17 (2018). doi: 10.3390/atoms6020017

[56] Simon Dupourqué, Luigi Tibaldo, and Peter von Ballmoos, *Constraints on the antistar fraction in the Solar System neighborhood from the 10-year Fermi Large Area Telescope gamma-ray source catalog*, Phys. Rev. D 103, 083016 (2021). doi: 10.1103/PhysRevD.103.083016

[57] Joshua Sokol, *Giant space magnet may have trapped antihelium, raising idea of lingering pools of antimatter in the cosmos*. Science (19 April 2017). doi: 10.1126/science.aal1067

[58] Andrei D Sakharov, *Violation of CP invariance, C asymmetry, and baryon asymmetry of the universe*, 1991 Sov. Phys. Usp. 34 392. doi: 10.1070/PU1991v034n05ABEH002497

[59] A. Riotto; M. Trodden, *Recent progress in baryogenesis*, Annual Review of Nuclear and Particle Science, Vol. 49:35-75 (1999) doi: 10.1146/annurev.nucl.49.1.35

[60] T. D. Lee and C. N. Yang, *Question of Parity Conservation in Weak Interactions*, Phys. Rev. 104, 254 (1957). doi: 10.1103/PhysRev.104.254

[61] C. S. Wu, E. Ambler, R. W. Hayward, D. D. Hoppes, and R. P. Hudson, *Experimental Test of Parity Conservation in Beta Decay*, Phys. Rev. 105, 1413 (1957). doi: 10.1103/PhysRev.105.1413

[62] L. Landau, *On the conservation laws for weak interactions*, Nuclear Physics 3, no. 1 (1957): 127-131. doi: 10.1016/0029-5582(57)90061-5

[63] J. H. Christenson, J. W. Cronin, V. L. Fitch, and R. Turlay, *Evidence for the* 2π *Decay of the* K_2^0 *Meson*, Phys. Rev. Lett. 13, 138 (1964). doi: 10.1103/PhysRevLett.13.138

[64] G.D. Barr et al., *A New measurement of direct CP violation in the neutral kaon system*, Physics Letters B, 1993, Volume 317, Issues 1–2, pp. 233-242. doi: 10.1016/0370-2693(93)91599-I

[65] Heinrich Wahl, *First observation and precision measurement of direct CP violation: the experiments NA31 and NA48*, Physics Reports, Volumes 403–404, 2004, Pages 19-25. doi: 10.1016/j.physrep.2004.08.007

[66] KTeV Collaboration, *Observation of CP Violation in* $K_L \to \pi^+\pi^-e^+e^-$ *Decays*, Phys. Rev. Lett. 84, 408 (2000). doi: 10.1103/PhysRevLett.84.408

[67] BABAR Collaboration, *Observation of CP Violation in the B0 Meson System*, Phys. Rev. Lett. 87, 091801 (2001). 10.1103/PhysRevLett.87.091801

[68] Belle Collaboration, *Observation of Large CP Violation in the Neutral B Meson System*, Phys. Rev. Lett. 87, 091802 (2001). 10.1103/PhysRevLett.87.091802

[69] Makoto Kobayashi, Toshihide Maskawa, *CP-Violation in the Renormalizable Theory of Weak Interaction*, Progress of Theoretical Physics, Volume 49, Issue 2, February 1973, Pages 652–657. doi: 10.1143/PTP.49.652

[70] Don Colladay and V. Alan Kostelecký, *CPT violation and the standard model*, Phys. Rev. D 55, 6760 (1997) doi: 10.1103/PhysRevD.55.6760

[71] V. Alan Kostelecký and Neil Russell, *Data tables for Lorentz and CPT violation*, Rev. Mod. Phys. 83, 11 (2011). doi: 10.1103/RevModPhys.83.11

[72] M. Charlton, S. Eriksson, and G. M. Shore, *Antihydrogen and Fundamental Physics*, (Springer, Cham, Switzerland, 2020). doi: 10.1007/978-3-030-51713-7

[73] J.D. Tasson, *Antimatter, the SME, and gravity*. Hyperfine Interact 213, 137–146 (2012). doi: 10.1007/s10751-012-0642-3

[74] M. M. Nieto and T. Goldman. *The arguments against "antigravity" and the gravitational acceleration of antimatter*, Physics Reports, 205:221, 1991. doi: 10.1016/0370-1573(91)90138-C

[75] M. Kowitt, *Gravitational repulsion and Dirac antimatter*, Int J Theor Phys 35, 605–631 (1996). doi: 10.1007/BF02082828

[76] R. M. Santilli, *A classical isodual theory of antimatter and its prediction of antigravity*, International Journal of Modern Physics A 14, no. 14 (1999): 2205-2238. doi: 10.1142/S0217751X99001111

[77] Chardin, G., and J-M. Rax. *CP violation. A matter of (anti) gravity?*, Physics Letters B 282, no. 1-2 (1992): 256-262. doi: 10.1016/0370-2693(92)90510-B

[78] F. C. Witteborn and W. M. Fairbank, *Experimental Comparison of the Gravitational Force on Freely Falling Electrons and Metallic Electrons*, Phys. Rev. Lett. 19, 1049 (1967). doi: 10.1103/PhysRevLett.19.1049

[79] The ALPHA Collaboration & A. E. Charman , *Description and first application of a new technique to measure the gravitational mass of antihydrogen*. Nat Commun 4, 1785 (2013). doi: 10.1038/ncomms2787

[80] AEgIS Collaboration, *Pulsed production of antihydrogen*. Commun Phys 4, 19 (2021). 10.1038/s42005-020-00494-z

[81] The AEgIS Collaboration, *Velocity-selected production of 2^3S metastable positronium*, Phys. Rev. A 99, 033405 (2019). doi: 10.1103/PhysRevA.99.033405

[82] G. Janka, B. Ohayon, Z. Burkley, L. Gerchow, N. Kuroda, X. Ni, R. Nishi, Z. Salman, A. Suter, M. Tuzi, C. Vigo, T. Prokscha, P. Crivelli, *Intense beam of metastable Muonium*, Eur. Phys. J. C 80, 804 (2020). doi: 10.1140/epjc/s10052-020-8400-1

[83] A. Antognini, P. Crivelli, L. Gerchow, T. D. Hume, K. Kirch, A. Knecht, J. Nuber, A. Papa, N. Ritjoho, M. Sakurai, A. Soter, D. Taqqu, S. M. Vogiatzi, J. Zhang, and L. Ziegler, *Room-temperature emission of muonium from aerogel and zeolite targets*, Phys. Rev. A 106, 052809 (2022). doi: 10.1103/PhysRevA.106.052809

[84] Precision Physics at Low Energy Group at ETH Zürich, *Muonium production*, website link: *https://edm.ethz.ch/research/muoniumproduction.html* (access on 25/06/2023)

[85] Walz, J., Hänsch, T.W. *A Proposal to Measure Antimatter Gravity Using Ultracold Antihydrogen Atoms*. General Relativity and Gravitation 36, 561–570 (2004). doi: 10.1023/B:GERG.0000010730.93408.87

[86] W. A. Bertsche, *Prospects for comparison of matter and antimatter gravitation with ALPHA-g*, Philosophical Transactions of the Royal Society A: Mathematical, Physical and Engineering Sciences 376.2116 (2018): 20170265. doi: 10.1098/rsta.2017.0265

[87] The GBAR Collaboration, *The GBAR antimatter gravity experiment*. Hyperfine Interact 233, 21–27 (2015). doi: 10.1007/s10751-015-1154-8

[88] Paul Hamilton, Andrey Zhmoginov, Francis Robicheaux, Joel Fajans, Jonathan S. Wurtele, and Holger Müller, *Antimatter Interferometry for Gravity Measurements*, Phys. Rev. Lett. 112, 121102 (2014). doi: 10.1103/PhysRevLett.112.121102

[89] Richard J. Hughes and Michael H. Holzscheiter, *Constraints on the gravitational properties of antiprotons and positrons from cyclotron-frequency measurements*, Phys. Rev. Lett. 66, 854 (1991) doi: 10.1103/PhysRevLett.66.854

[90] Karshenboim, S.G., Pavone, F.S., Bassani, F., Inguscio, M. and Hänsch, T.W. eds., 2007. *The hydrogen atom: precision physics of simple atomic systems* (Vol. 570). Springer. link: Internet Archive

[91] Cooke, D.A., Crivelli, P., Alnis, J. et al. *Observation of positronium annihilation in the 2S state: towards a new measurement of the 1S-2S transition frequency.* Hyperfine Interact 233, 67–73 (2015). doi: 10.1007/s10751-015-1158-4

[92] Jungmann, K. P. (2016). *Precision Muonium Spectroscopy.* Journal of the Physical Society of Japan, 85(9), Article 091004. doi: 10.7566/JPSJ.85.091004

[93] Pohl, Randolf. *Laser spectroscopy of muonic hydrogen and the puzzling proton.* Journal of the Physical Society of Japan 85.9 (2016): 091003. doi: 10.7566/JPSJ.85.091003

[94] M. Doser, *Antiprotonic bound systems.* Progress in Particle and Nuclear Physics 125 (2022): 103964. doi: 10.1016/j.ppnp.2022.103964

[95] Smorra, C., Stadnik, Y.V., Blessing, P.E. et al. *Direct limits on the interaction of antiprotons with axion-like dark matter.* Nature 575, 310–314 (2019). doi: 10.1038/s41586-019-1727-9

[96] S. Gov, S. Shtrikman, H. Thomas. *Magnetic trapping of neutral particles: Classical and quantum-mechanical study of a Ioffe–Pritchard type trap*, Journal of Applied Physics 87, 8 (2000) doi:10.1063/1.372444

[97] ALPHA Collaboration, *The ALPHA antihydrogen trapping apparatus.* Nuclear Instruments and Methods in Physics Research Section A: Accelerators, Spectrometers, Detectors and Associated Equipment 735 (2014): 319-340. doi: 10.1016/j.nima.2013.09.043

[98] P. Granum, *Measuring the Properties of Antihydrogen.* Ph.D. thesis, Aarhus University, 2022. link

[99] R. G. Greaves, C. M. Surko, *Antimatter plasmas and antihydrogen*, Physics of Plasmas 4, 1528–1543 (1997), doi: 10.1063/1.872284

[100] Michael H. Holzscheiter, Michael Charlton, and Michael Martin Nieto. *"The route to ultra-low energy antihydrogen.* Physics reports 402, no. 1-2 (2004): 1-101. doi: 10.1016/j.physrep.2004.08.002

[101] S Jonsell, D P van der Werf, M Charlton, and F Robicheaux, *Simulation ofthe formation of antihydrogen in a nested penning trap: effect of positron density.* 2009 J. Phys. B: At. Mol. Opt. Phys. 42 215002. doi: 10.1088/0953-4075/42/21/215002

[102] Svante Jonsell and Mike Charlton. *On the formation of trappable antihydrogen*, 2018 New J. Phys. 20 043049. doi: 10.1088/1367-2630/aabc71

[103] D. Hodgkinson, *On the Dynamics of Adiabatically Cooled Antihydrogen in an Octupole-Based Ioffe-Pritchard Magnetic Trap*, Ph.D. thesis, The University of Manchester, 2022. link

[104] Tardiff, E., Fan, X., Gabrielse, G., Grzonka, D., Hamley, C., Hessels, E.A., Jones, N., Khatri, G., Kolthammer, W.S., Zambrano, D.M. and Meisenhelder, C., *Two-symmetry Penning-Ioffe trap for antihydrogen cooling and spectroscopy*, Nuclear Instruments and Methods in Physics Research Section A: Accelerators, Spectrometers, Detectors and Associated Equipment 977 (2020): 164279. doi: 10.1016/j.nima.2020.164279

[105] The ALPHA Collaboration, *Antihydrogen accumulation for fundamental symmetry tests*, Nat Commun 8, 681 (2017). doi: 10.1038/s41467-017-00760-9

[106] J. Pérez-Ríos, A. S. Sanz, *How does a magnetic trap work?*, American Journal of Physics 81, 836–843 (2013). doi:10.1119/1.4819167

[107] David E. Pritchard, *Cooling Neutral Atoms in a Magnetic Trap for Precision Spectroscopy*, Phys. Rev. Lett. 51, 1336 (1983). doi: 10.1103/PhysRevLett.51.1336

[108] *BASE Celebrates First Antiproton Birthday* link to BASE Collaboration website

[109] *The BASE antiprotons celebrate their first birthday* CERN Press release

[110] M. Betz, E.A. Veit, V. Mull, K. Holinde, *$p\bar{p}$ annihilation into $\pi^+\pi^-\pi^0$ in a hadron-exchange model*, Phys.Lett.B 398 (1997) 12-17. doi: 10.1016/S0370-2693(97)00197-4

[111] Capra, A., ALPHA collaboration. *Lifetime of magnetically trapped antihydrogen in ALPHA*. Hyperfine Interact 240, 9 (2019). doi: 10.1007/s10751-018-1526-y

[112] J.T.K. McKenna, *Silicon Vertex Detector and it applications in the ALPHA Experiment*, Ph.D. thesis, University of Liverpool, 2014. link

[113] Capra, A., Amaudruz, P., Bishop, D., Fujiwara, M.C., Freeman, S., Gill, D.R., Grant, M.A., Henderson, R., Kurchaninov, L., Lu, P., Menary, S.R., Olchanski, K., & Retière, F., *Design of a Radial TPC for Antihydrogen Gravity Measurement with ALPHA-g.*, In Proceedings of the 12th International Conference on Low Energy Antiproton Physics (LEAP2016) (p. 011015) (2017). doi: 10.48550/arXiv.1609.06656

[114] Arthur Matveev, Christian G. Parthey, Katharina Predehl, Janis Alnis, Axel Beyer, Ronald Holzwarth, Thomas Udem, Tobias Wilken, Nikolai Kolachevsky, Michel Abgrall, Daniele Rovera, Christophe Salomon, Philippe Laurent, Gesine Grosche, Osama Terra, Thomas Legero, Harald Schnatz, Stefan Weyers, Brett Altschul, and Theodor W. Hänsch, *Precision Measurement of the Hydrogen 1S-2S Frequency via a 920-km Fiber Link*, Phys. Rev. Lett. 110, 230801 (2013). doi: 10.1103/PhysRevLett.110.230801

[115] Kolachevsky, N., et al. *2S-4S spectroscopy in hydrogen atom: The new value for the Rydberg constant and the proton charge radius.* AIP Conference Proceedings. Vol. 1936. No. 1. AIP Publishing, 2018. doi: 10.1063/1.5025453

[116] Axel Beyer et al. , *The Rydberg constant and proton size from atomic hydrogen.* Science358,79-85(2017). 10.1126/science.aah6677

[117] J. Schoonwater, *Towards observing antihydrogen fluorescence: characterizing SiPMs down to 6.1 K*, Msc thesis, Eindhoven University of Technology, 2022. link

[118] Alexey Grinin et al., *Two-photon frequency comb spectroscopy of atomic hydrogen.* Science370,1061-1066(2020). DOI:10.1126/science.abc7776

[119] S.A. Jones, *Observation Of The 1S-2S Transition In Trapped Antihydrogen*, Ph.D. thesis, Swansea University, 2017. link

[120] Parthey C.G., Matveev A., Alnis J., Bernhardt B., Beyer A., Holzwarth R., Maistrou A., Pohl R., Predehl K., Udem T., Wilken T., Kolachevsky N., Abgrall M., Rovera D., Salomon C., Laurent P., Hänsch T.W. *Improved measurement of the hydrogen transition frequency*, Phys. Rev. Lett., 107 (2011), Article 203001, doi: 10.1103/PhysRevLett.107.203001

[121] Arthur Matveev, Christian Parthey, Katharina Predehl, Janis Alnis, Axel Beyer, et al.. *Measurement of the Hydrogen 1 S – 2 S Frequency via a 920-km Fiber Link*. Physical Review Letters, American Physical Society, 2013, 110 (23), doi: 10.1103/PhysRevLett.110.230801

[122] T. Lyman, *The spectrum of hydrogen in the region of extremely short wave-length*. Mem. Am. Acad. Arts Sci. New Ser. 13, 125–146 (1906). doi: 10.2307/25058084

[123] C. So, J. Fajans, and W. Bertsche, *The ALPHA-g antihydrogen gravity magnet system*, IEEE transactions on applied superconductivity 30.4 (2020): 1-5. doi: 10.1109/TASC.2020.2981272

[124] ALPHA Collaboration, *Evaporative Cooling of Antiprotons to Cryogenic Temperatures*, Phys. Rev. Lett. 105, 013003 (2010). doi: 10.1103/PhysRevLett.105.013003

[125] D.J. Wineland, C.S. Weimer, J.J. Bollinger, *Laser-cooled positron source*. Hyperfine Interact 76, 115–125 (1993). doi: 10.1007/BF02316710

[126] Jelenković B M, Newbury A S, Bollinger J J, Mitchell T B and Itano W M *Sympathetically laser-cooled positrons*, Nucl. Instrum. Methods Phys. Res. B 192 117–27 (2002). doi: 10.1016/S0168-583X(02)00791-7

[127] B. M. Jelenković, A. S. Newbury, J. J. Bollinger, W. M. Itano, and T. B. Mitchell *Sympathetically cooled and compressed positron plasma*, Phys. Rev. A 67, 063406 (2003). doi: 10.1103/PhysRevA.67.063406

[128] N. Madsen, F. Robicheaux and S. Jonsell *Antihydrogen trapping assisted by sympathetically cooled positrons* 2014 New J. Phys. 16 063046. doi: 10.1088/1367-2630/16/6/063046

[129] M. Sameed, D.Maxwell, & N.Madsen, *Ion generation and loading of a Penning trap using pulsed laser ablation*. New J. Phys. 22 013009 (2020). doi: 10.1088/1367-2630/ab6066

[130] M. Sameed, *Laser-Ablated Beryllium Ions for Cold Antihydrogen in ALPHA*, Ph.D. Thesis, Swansea University, 2017. link

[131] J. McCauley Jones, *Sympathetically Laser-Cooled Positron Plasmas for Antihydrogen Formation*, Ph.D. thesis, Swansea University, 2021. doi: 10.23889/SUthesis.59731

[132] N. Shiga, W. M. Itano, and J. J. Bollinger, *Diamagnetic correction to the 9Be+ ground-state hyperfine constant*, Phys. Rev. A 84, 012510 (2011). doi: 10.1103/PhysRevA.84.012510

[133] W. Paul, H. Steinwedel, *Ein neues massenspektrometer ohne magnetfeld*, Zeitschrift für Naturforschung A 8, 7 (1953). doi:10.1515/zna-1953-0710

[134] H.G. Dehmelt, *Radiofrequency Spectroscopy of Stored Ions I: Storage*, Advances in Atomic and Molecular Physics 3, 53 (1968). doi:10.1016/S0065-2199(08)60170-0

[135] Klaus Blaum, *F47 — Cyclotron frequency in a Penning trap*, lecture notes, "Stored and Cooled Ions" Division at the Max-Planck Institute for Nuclear Physics, October 2022.

[136] Klaus Blaum, *High-accuracy mass spectrometry with stored ions*, Physics Reports, Volume 425, Issue 1, 2006, Pages 1-78, doi:10.1016/j.physrep.2005.10.011

[137] M. Kretzschmar, *Particle motion in a Penning trap*, 1991 Eur. J. Phys. 12 240, doi: 10.1088/0143-0807/12/5/010

[138] Martina Knoop, Niels Madsen, and Richard C. Thompson. *Trapped Charged Particles*. 2016.

[139] Lowell S. Brown, Gerald Gabrielse, (1982-04-01). *Precision spectroscopy of a charged particle in an imperfect Penning trap* Physical Review A. 25 (4): 2423–2425. doi:10.1103/PhysRevA.25.2423

[140] Jens Dilling, Klaus Blaum, Maxime Brodeur, and Sergey Eliseev, *Penning-Trap Mass Measurements in Atomic and Nuclear Physics*, Annual Review of Nuclear and Particle Science, Vol. 68:45-74 (2018), doi: 10.1146/annurev-nucl-102711-094939

[141] Paul D. Lett, Richard N. Watts, Christoph I. Westbrook, William D. Phillips, Phillip L. Gould, and Harold J. Metcalf, *Observation of Atoms Laser Cooled below the Doppler Limit*, Phys. Rev. Lett. 61, 169 (1988). doi: 10.1103/PhysRevLett.61.169

[142] J. Dalibard and C. Cohen-Tannoudji, *Laser cooling below the Doppler limit by polarization gradients: simple theoretical models*, J. Opt. Soc. Am. B 6, 2023-2045 (1989). doi: 10.1364/JOSAB.6.002023

[143] W. M. Itano and D. J. Wineland, *Laser cooling of ions stored in harmonic and Penning traps*, Physical Review A 25, 35–54 (1982). doi: 10.1103/PhysRevA.25.35

[144] Malmberg, J. H.; deGrassie, J. S. (1975). *Properties of Nonneutral Plasma*. Physical Review Letters. 35 (9): 577–580. doi:10.1103/PhysRevLett.35.577

[145] Malmberg, J. H.; Driscoll, C. F. (1980). *Long-Time Containment of a Pure Electron Plasma*. Physical Review Letters. 44 (10): 654–657. doi:10.1103/PhysRevLett.44.654

[146] J. J. Bollinger and D. J. Wineland, *Strongly Coupled Nonneutral Ion Plasma*, Phys. Rev. Lett. 53, 348 doi: 10.1103/PhysRevLett.53.348

[147] J. Bollinger, D. Wineland, D. Dubin, *Non-neutral ion plasmas and crystals, laser cooling, and atomic clocks*, Physics of Plasmas 1, 1403 (1994); doi: 10.1063/1.870690

[148] D. H. E. Dubin and T. M. O'Neil, *Trapped nonneutral plasmas , liquids , and crystals (the thermal equilibrium states)*, Rev. Mod. Phys. 71, 87 (1999). doi: 10.1103/RevModPhys.71.87

[149] C.F. Driscoll, J.H. Malmberg and K.S. Fine, *Observation of Transport to Thermal Equilibrium in Pure Electron Plasmas*, Phys. Rev. Lett. 60, 1290 (1988). doi: 10.1103/PhysRevLett.60.1290

[150] J. R. Danielson, D. H. E. Dubin, R. G. Greaves, and C. M. Surko, *Plasma and trap-based techniques for science with positron*, Rev. Mod. Phys. 87, 247 (2015). doi: 10.1103/RevModPhys.87.247

[151] Lewi Tonks, Irving Langmuir, *Oscillations in ionized gases*, Physical Review. 33 (8): 195–210. (1929) doi:10.1103/PhysRev.33.195

[152] Chukman So, *Antiproton and positron dynamics in antihydrogen production*, Ph.D. thesis, University of California, Berkeley, 2014. link

[153] J. J. Bollinger, D. J. Heinzen, F. L. Moore, W. M. Itano, D. J. Wineland and D. H. E. Dubin, *Electrostatic modes of ion-trap plasmas*. Physical Review A 48, 525–545 (1993). doi: 10.1103/PhysRevA.48.525

[154] L. R. Brewer, J. D. Prestage, J. J. Bollinger, W. M. Itano, D. J. Larson and D. J. Wineland, *Static properties of a non-neutral 9Be+-ion plasma.* Physical Review A 38, 859–873 (1988). doi: 10.1103/PhysRevA.38.859

[155] T.M. O'Neil, *Centrifugal separation of a multispecies pure ion plasma*, Physics of Fluids 24, 1447–1451 (1981). doi: 10.1063/1.863565

[156] D.H.E. Dubin, *Collisional transport in non-neutral plasmas*, Physics of Plasmas 5, 1688–1694 (1998). doi: 10.1063/1.872837

[157] The ALPHA Collaboration, *Centrifugal Separation and Equilibration Dynamics in an Electron-Antiproton Plasma*, Phys. Rev. Lett. 106, 145001. doi: 10.1103/PhysRevLett.106.145001

[158] The ALPHA Collaboration, *Experimental and computational study of the injection of antiprotons into a positron plasma for antihydrogen production*, Physics of Plasmas 20, 043510 (2013). doi: 10.1063/1.4801067

[159] Edward H. Eberhardt, *Gain model for microchannel plates*, Appl. Opt. 18, 1418-1423 (1979). doi: 10.1364/AO.18.001418

[160] E. D. Hunter, J. Fajans, N. A. Lewis, A. P. Povilus, C. Sierra, C. So, and D. Zimmer, *Plasma temperature measurement with a silicon photomultiplier (SiPM)*, Review of Scientific Instruments 91, 103502 (2020), doi: 10.1063/5.0006672

[161] D. L. Eggleston, C. F. Driscoll, B. R. Beck, A. W. Hyatt, J. H. Malmberg, *Parallel energy analyzer for pure electron plasma devices*, Physics of Fluids B: Plasma Physics 4, 3432–3439 (1992). doi: 10.1063/1.860399

[162] E. D. Hunter, A. Christensen, J. Fajans, T. Friesen, E. Kur, J. S. Wurtele, *Electron cyclotron resonance (ECR) magnetometry with a plasma reservoir*, Physics of Plasmas 27, 032106 (2020). doi: 10.1063/1.5141999

[163] The ALPHA Collaboration, *Enhanced Control and Reproducibility of Non-Neutral Plasmas*, Phys. Rev. Lett. 120, 025001 (2018). doi: 10.1103/PhysRevLett.120.025001

[164] Celeste Carruth, *Methods for plasma stabilization and control to improve antihydrogen production*, Ph.D. thesis, University of California, Berkeley, 2018. link

[165] B. R. Beck, J.Fajans, J.H.Malmberg, *Temperature and anisotropic-temperature relaxation measurements in cold, pure-electron plasmas*, Physics of Plasmas 3, 1250–1258 (1996) doi: 10.1063/1.871749

[166] ATRAP Collaboration, *Adiabatic Cooling of Antiprotons*, Phys. Rev. Lett. 106, 073002(2011). doi: 10.1103/PhysRevLett.106.073002

[167] X.-P. Huang, F. Anderegg, E. M. Hollmann, C. F. Driscoll, and T. M. O'Neil, *Steady-State Confinement of Non-neutral Plasmas by Rotating Electric Fields*, Phys. Rev. Lett. 78, 875 (1997). doi: 10.1103/PhysRevLett.78.875

[168] R. G. Greaves and C. M. Surko, *Inward Transport and Compression of a Positron Plasma by a Rotating Electric Field*, Phys. Rev. Lett. 85, 1883 (2000). 10.1103/PhysRevLett.85.1883

[169] J. R. Danielson and C. M. Surko, *Torque-Balanced High-Density Steady States of Single-Component Plasmas*, Phys. Rev. Lett. 94, 035001 (2005). doi: 10.1103/PhysRevLett.94.035001

[170] J. R. Danielson and C. M. Surko, *Radial compression and torque-balanced steady states of single-component plasmas in Penning-Malmberg traps*, Phys. Plasmas 13.5, 055706 (2006), p. 055706. doi: 10.1063/1.2179410

[171] M. Johnson, *Design and Commissioning of Beamlines for the ALPHA Antihydrogen Experiment*, Ph.D. thesis, University of Manchester, 2019. link

[172] Claudio Torregrosa Martin, Antonio Perillo-Marcone, Marco Calviani, and José-Luis Muñoz-Cobo, *CERN antiproton target: Hydrocode analysis of its core material dynamic response under proton beam impact*, Phys. Rev. Accel. Beams 19, 073402 (2016). doi: 10.1103/PhysRevAccelBeams.19.073402

[173] D. Möhl, *Production of low-energy antiprotons.* Hyperfine Interactions 109, 33–41 (1997). 10.1023/A:1012680728257

[174] Hémery, J. Y., and S. Maury. *The antiproton decelerator: overview.* Nuclear Physics A 655.1-2 (1999): c345-c352. doi: 10.1016/S0375-9474(99)00223-7

[175] L. Ponce, L. Bojtár, C. Carli, B. Dupuy, Y. Dutheil, P. Freyermuth, D. Gamba, L.V. Jørgensen, B. Lefort, S. Pasinelli, *ELENA - From Commissioning to Operation*, JACoW IPAC 2022 (2022): 2391-2394. doi: 10.18429/JACoW-IPAC2022-THOXGD1

[176] S. Fabbri, *Optimization of Antiproton Capture and Delivery for the ALPHA Antihydrogen Experiment*, Ph.D. thesis, The University of Manchester, 2021. link

[177] Houtermans, H., O. Milosevic, and F. Reichel. *Half-lives of 35 radionuclides*. The International Journal of Applied Radiation and Isotopes 31.3 (1980): 153-154. doi: 10.1016/0020-708X(80)90139-8

[178] GBAR Collaboration, *Positron production using a 9 MeV electron linac for the GBAR experiment*, Nuclear Instruments and Methods in Physics Research Section A: Accelerators, Spectrometers, Detectors and Associated Equipment 985 (2021): 164657. doi: 10.1016/j.nima.2020.164657

[179] Greaves, R. G., and C. M. Surko. *Solid neon moderator for positron-trapping experiments*, Canadian Journal of Physics 74.7-8 (1996): 445-448. doi: 10.1139/p96-063

[180] Van Der Werf, D. P., Jørgensen, L. V., Watson, T. L., Charlton, M., Collier, M. J. T., Doser, M., & Funakoshi, R., *The ATHENA positron accumulator*. Applied surface science, 194(1-4), 312-316 (2002). doi: 10.1016/S0169-4332(02)00141-1

[181] The ALPHA Collaboration, *Autoresonant-spectrometric determination of the residual gas composition in the ALPHA experiment apparatus.*, Review of Scientific Instruments 84.6 (2013). doi: 10.1063/1.4811527

[182] B.H.Bransden and C.J. Joachain, *Physics of Atoms and Molecules*, Prentice-Hall, 2003

[183] Hahn, H., Zarantonello, G., Schulte, M. et al. *Integrated 9Be+ multi-qubit gate device for the ion-trap quantum computer*, npj Quantum Inf 5, 70 (2019). doi:10.1038/s41534-019-0184-5

[184] Jain, S. and Alonso, J. and Grau, M. and Home, J. P. *Scalable Arrays of Micro-Penning Traps for Quantum Computing and Simulation*, Phys. Rev. X 10, 22 (2020) doi:10.1103/PhysRevX.10.031027

[185] Harold J. Metcalf, Peter van der Straten. *Laser Cooling and Trapping*, Springer 1999.

[186] Takashi Nakamura, Michiharu Wada, Kunihiro Okada, Ichiro Katayama, Shunsuke Ohtani, H.A. Schuessler, *Precision spectroscopy of the Zeeman splittings of the* $^9Be^+2S_{1/2}$ *hyperfine structure for nuclear structure studies* Optics Communications 205 (2002) 329–336. doi: 10.1016/S0030-4018(02)01259-2

[187] The ALPHA Collaboration, *Resonant quantum transition in trapped antihydrogen atoms*, Nature 483, 439–443 (2012). doi: 10.1038/nature10942

[188] D. J. Wineland and W. M. Itano, *Laser cooling of atoms*, Physical Review A 20, 1521 (1979) doi: 10.1103/PhysRevA.20.1521

[189] C. Foot, *Atomic Physics*, Oxford University Press, 2005

[190] C. Cohen-Tannoudji, B. Diu, F. Laloë, *Quantum Mechanics*, Wiley-VCH; 1st edition, 2019

[191] J. Mielke, *Thermometry of* $^9Be^+$ *ions in a cryogenic Penning trap*, Ph.D. thesis, Leibniz Universität Hannover (2021). doi: 10.15488/11511

[192] H. F. Powell, D. M. Segal, and R. C. Thompson, *Axialization of Laser Cooled Magnesium Ions in a Penning Trap*, Phys. Rev. Lett. 89, 093003 (2002). doi: 10.1103/PhysRevLett.89.093003

[193] Wayne M. Itano, L. R. Brewer, D. J. Larson, and D. J. Wineland, *Perpendicular laser cooling of a rotating ion plasma in a Penning trap*, Phys. Rev. A 38, 5698 (1988). doi: 10.1103/PhysRevA.38.5698

[194] M. E. Glinsky, T. M. O'Neil, M. N. Rosenbluth, K. Tsuruta S. Ichimaru, *Collisional equipartition rate for a magnetized pure electron plasma*, Physics of Fluids B: Plasma Physics 4, 1156–1166 (1992). doi: 10.1063/1.860124

[195] Dieter Bäuerle, *Nanosecond-laser ablation*, Laser Processing and Chemistry, 237 (2011). doi: 10.1007/978-3-642-17613-$5_1$2

[196] Butt, Muhammad Zakria. *Laser ablation characteristics of metallic materials: Role of Debye-Waller thermal parameter.* In IOP Conference Series: Materials Science and Engineering, vol. 60, no. 1, p. 012068. IOP publishing, 2014. doi: 10.1088/1757-899X/60/1/012068

[197] L. Torrisi et al., *Comparison of nanosecond laser ablation at 1064 and 308 nm wavelength*, Applied surface science 210, 262 (2003). doi: 10.1016/S0169-4332(02)01467-8

[198] https://www.quantel-laser.com/en/products/item/ultra-50-100-mj–134.html

[199] https://www.rp-photonics.com/q_switching.html

[200] W. Nörtershäuser, C. Geppert, A. Krieger, K. Pachucki, M., K. Blaum, M.L. Bissell, N. Frömmgen, M. Hammen, M. Kowalska, J. Krämer, K. Kreim, R. Neugart, G. Neyens, R. Sánchez, and D.T. Yordanov, *Precision Test of Many-Body QED in the Be^+ 2p Fine Structure Doublet Using Short-Lived Isotopes*, Phys. Rev. Lett. 115, 033002 (2015). doi: 10.1103/PhysRevLett.115.033002

[201] Bollinger, J. J. and Wells, J. S. and Wineland, D. J. and Itano, Wayne M., *Hyperfine structure of the $2p^2P_{1/2}$ state in $^9Be^+$*, Phys. Rev. A 31, 2711, April 1985. doi: 10.1103/physreva.31.2711

[202] W. Nörtershäuser, D. Tiedemann, M. Žáková, Z. Andjelkovic, K. Blaum, M. L. Bissell, R. Cazan, G. W. F. Drake, Ch. Geppert, M. Kowalska, J. Krämer, A. Krieger, R. Neugart, R. Sánchez, F. Schmidt-Kaler, Z.-C. Yan, D. T. Yordanov, and C. Zimmermann, *Nuclear Charge Radii of $^{7,9,10}Be$ and the One-Neutron Halo Nucleus ^{11}Be*, Phys. Rev. Lett. 102, 062503 (2009). doi: 10.1103/PhysRevLett.102.062503

[203] Mariusz Puchalski and Krzysztof Pachucki, *Fine and hyperfine splitting of the 2P state in Li and Be+*, Physical Review A 79, 032510 (2009). doi: 10.1103/PhysRevA.79.032510

[204] V. A. Yerokhin, *Hyperfine structure of Li and Be^+*, Phys. Rev. A 78, 012513 (2008). doi: 10.1103/PhysRevA.78.012513

[205] Gregory Breit, Isidor Isaac Rabi: *Measurement of Nuclear Spin.* In: Physical Review Letters. Band 38, Nr. 11, November 1931, S. 2082–2083, doi:10.1103/PhysRev.38.2082.2

[206] P. J. Mohr, B. N. Taylor, and D. B. Newell, *CODATA Recommended Values of the Fundamental Physical Constants: 2018*, Rev. Mod. Phys. 80(2), 633-730 (2008). doi: 10.1103/RevModPhys.80.633

[207] S. J. Lipson, G. D. Fletcher, and D. J. Larson, *Observation of Quadrupole and Dipole Diamagnetic Shifts in Atomic Ground-State Hyperfine Structure*, Phys. Rev. Lett. 57, 567 (1986). doi: 10.1103/PhysRevLett.57.567

[208] T. Andersen, K. A. Jessen, and G. Sørensen, *Mean-Life Measurements of Excited Electronic States in Neutral and Ionic Species of Beryllium and Boron*, Phys. Rev. 188, 76 (1969). doi: 10.1103/PhysRev.188.76

[209] *https://www.toptica.com/products/tunable-diode-lasers/frequency-converted-lasers/ta-fhg-pro*

[210] *https://www.toptica.com/technology/technical-tutorials/tapered-amplifiers*

[211] *https://www.toptica.com/products/tunable-diode-lasers/laser-driving-electronics/dlc-pro-digital-control*

[212] Linards Skuja, Hideo Hosono, and Masahiro Hirano. *Laser-induced color centers in silica*, Proceedings of SPIE - The International Society for Optical Engineering, 4347, 04 2001 doi: 10.1117/12.425020

[213] P. Karlitschek, G. Hillrichs, and K.-F. Klein, *Influence of hydrogen on the colour center formation in optical fibers induced by pulsed UV-laser radiation.*
Part 1: All-silica fibers with low-OH undoped core, Opt. Commun. 155, 386–397 (1998). doi: 10.1016/S0030-4018(98)00409-X
Part 2: All-silica fibers with low-OH undoped core, Opt. Commun. 155, 386–397 (1998). doi: 0.1016/S0030-4018(98)00408-8

[214] Y. Colombe, D. H. Slichter, A. C. Wilson, D. Leibfried, and D. Wineland, *Single-mode optical fiber for high-power, low-loss UV transmission*, Opt. Express 2222, 1401–1409 (2014) doi: 10.1364/OE.22.019783

[215] Christian D. Marciniak, Harrison B. Ball, Alex T.-H. Hung, and Michael J. Biercuk. *Towards fully commercial, UV-compatible fiber patch cords*, Opt. Express, 25(14):15643–15661, Jul 2017. doi: 10.1364/oe.25.015643

[216] https://www.sukhamburg.com/products/fiberoptics/fibercoupler/series/60fc-xv.html

[217] https://www.fiberlabs.com/glossary/polarization-maintaining-fiber/

[218] B. Mroziewicz, *External cavity wavelength tunable semiconductor lasers - a review.* Opto-Electron. Rev. 16, 347–366 (2008). https://doi.org/10.2478/s11772-008-0045-9

[219] Paul Zorabedian (1995), *Tunable External-Cavity Semiconductor Lasers* in F.Duarte, *Tunable Lasers Handbook*, Elsevier Science, 1996, p.385-430. doi: 10.1016/B978-0-12-222695-3.X5000-4

[220] S.C. Doret, *Simple, low-noise piezo driver with feed-forward for broad tuning of external cavity diode lasers*, Review of Scientific Instruments 89, 023102 (2018). doi: 10.1063/1.5009643

[221] D. D. Cook and F. R. Nash, *Gain-induced guiding and astigmatic output beam of GaAs lasers*, Journal of Applied Physics 46, 1660 (1975); doi: 10.1063/1.321769

[222] GS Pandian, S Dilwali, *On the thermal FM response of a semiconductor laser diode*, IEEE Photonics Technology Letters 4 (2), 130-133, 1992. doi: 10.1109/68.122338

[223] https://www.toptica.com/application-notes/phase-and-frequency-locking-of-diode-lasers/phase-and-frequency-of-laser-light

[224] Drever, R. W. P., Hall, J. L., Kowalski, F. V., Hough, J., Ford, G. M., Munley, A. J., & Ward, H. (1983). *Laser phase and frequency stabilization using an optical resonator.* Applied Physics B, 31(2), 97-105. doi: 10.1007/BF00702605

[225] *https://www.toptica.com/application-notes/phase-and-frequency-locking-of-diode-lasers*

[226] U. Eismann, M. Enderlein, K. Simeonidis, F. Keller, F. Rohde, D. Opalevs, M. Scholz, W. Kaenders, J. Stuhler, *Active and passive stabilization of a high-power UV frequency-doubled diode laser*, CLEO, OSA Technical Digest (Optical Society of America, 2016). arXiv:1606.07670

[227] Fabry, C; Perot, A (1899). *Theorie et applications d'une nouvelle methode de spectroscopie interferentielle*. Ann. Chim. Phys. 16 (7) doi: 10.1051/jphysrad:01958001903018700

[228] Perot, A; Fabry, C (1899). *On the Application of Interference Phenomena to the Solution of Various Problems of Spectroscopy and Metrology*. Astrophysical Journal. 9: 87 doi: 10.1086/140557

[229] R. W. P. Drever, G. M. Ford, J. Hough, I. M. Kerr, A. J. Munley, J. R. Pugh, N. A. Robertson, and H. Ward, *A gravity wave detector using optical cavity sensing*, Proceedings of the Ninth International Conference on General Relativity and Gravitation, Jena, July 1980, p. 265–267, 1980 link

[230] R. V. Pound, *Electronic frequency stabilization of microwave oscillators*, Review of Scientific Instruments, vol. 17, no. 11, pp. 490–505, 1946. doi: 10.1063/1.1770414

[231] E. D. Black, *An introduction to Pound-Drever-Hall laser frequency stabilization*, American Journal of Physics, vol. 69, no. 1, pp. 79–87, 2001. doi: 10.1119/1.1286663

[232] Black, Eric. *Notes on the Pound-Drever-Hall technique*. LIGO Technical Note. PDF download

[233] Bahaa E A Saleh and Malvin Carl Teich, *Fundamentals of Photonics, 1st ed.*; Wiley, New York, NY, 1991.

[234] *https://www.fiberoptics4sale.com/blogs/wave-optics/acousto-optic-diffraction*

[235] *https://www.fiberoptics4sale.com/blogs/wave-optics/acousto-optic-modulators*

[236] E. A. Donley, T. P. Heavner, F. Levi, M. O. Tataw, and S. R. Jefferts, *Double-pass acousto-optic modulator system*, Rev. Sci. Instrum. 76, 063112 (2005). doi: 10.1063/1.1930095

[237] *https://ethz.ch/content/dam/ethz/special-interest/phys/quantum-electronics/tiqi-dam/documents/semester_theses/semesterthesis-mathieu_chanson.pdf*

[238] L. R. Brewer, J. D. Prestage, J. J. Bollinger, W. M. Itano, D. J. Larson, and D. J. Wineland, *Static properties of a non-neutral* $^9Be^+$*-ion plasma*, Phys.Rev.A 38, 859 (1988). doi:10.1103/PhysRevA.38.859

[239] ALPHA Collaboration, *In situ electromagnetic field diagnostics with an electron plasma in a Penning–Malmberg trap*, 2014 New J. Phys. 16 013037. doi: 10.1088/1367-2630/16/1/013037

[240] N. Evetts, *Solid-State Nuclear Magnetic Resonance Magnetometry at Low Temperature with application to antimatter gravity experiments by ALPHA*, Ph.D. thesis, The University of British Columbia, 2021. doi: 10.14288/1.0396355

[241] E. Hunter, *Cavity and Microwave Experiments on Electron Plasma*, Ph.D. thesis, University of California, Berkeley (2019). link

[242] S. George, S. Baruah, B. Blank, K. Blaum, M. Breitenfeldt, U. Hager, F. Herfurth, A. Herlert, A. Kellerbauer, H.-J. Kluge, M. Kretzschmar, D. Lunney, R. Savreux, S. Schwarz, L. Schweikhard, and C. Yazidjian, *Ramsey Method of Separated Oscillatory Fields for High-Precision Penning Trap Mass Spectrometry*, Phys. Rev. Lett. 98, 162501 (2007). doi: 10.1103/PhysRevLett.98.162501

[243] N. Evetts, *Cavity cooling of leptons for increased antihydrogen production at ALPHA*. Master thesis, The University of British Columbia, 2015. link

[244] T. Friesen, *Probing Trapped Antihydrogen: In Situ Diagnostics and Observations of Quantum Transitions*. Ph.D. thesis, University of Calgary, 2014. link

[245] Agilent E8257D PSG Analog Signal Generator, datasheet: https://www.keysight.com/us/en/product/E8257D/psg-analog-signal-generator-100-khz-67-ghz.html

[246] Ch. Schneider, M. Enderlein, T. Huber and T. Schaetz, *Optical trapping of an ion*, Nature Photon 4, 772–775 (2010). doi: 10.1038/nphoton.2010.236

[247] M. Bohman, *Sympathetic Cooling of a Proton with Resonant Image Current Coupling*, Ph.D. thesis, Heidelberg University, 2021. doi: 10.11588/heidok.00029319

[248] A.-G. Paschke, *$^9Be^+$ ion qubit control using an optical frequency comb*. Hannover : Gottfried Wilhelm Leibniz Universität Hannover, Diss., 2017, VI, 162 S. doi: 10.15488/9036